

University of Windsor

## Scholarship at UWindor

---

Electronic Theses and Dissertations

Theses, Dissertations, and Major Papers

---

2018

# Effective Ignition Control in Advanced Combustion Engines

Kelvin Xie

*University of Windsor*

Follow this and additional works at: <https://scholar.uwindsor.ca/etd>



Part of the [Engineering Commons](#)

---

### Recommended Citation

Xie, Kelvin, "Effective Ignition Control in Advanced Combustion Engines" (2018). *Electronic Theses and Dissertations*. 7486.

<https://scholar.uwindsor.ca/etd/7486>

This online database contains the full-text of PhD dissertations and Masters' theses of University of Windsor students from 1954 forward. These documents are made available for personal study and research purposes only, in accordance with the Canadian Copyright Act and the Creative Commons license—CC BY-NC-ND (Attribution, Non-Commercial, No Derivative Works). Under this license, works must always be attributed to the copyright holder (original author), cannot be used for any commercial purposes, and may not be altered. Any other use would require the permission of the copyright holder. Students may inquire about withdrawing their dissertation and/or thesis from this database. For additional inquiries, please contact the repository administrator via email ([scholarship@uwindsor.ca](mailto:scholarship@uwindsor.ca)) or by telephone at 519-253-3000ext. 3208.

Effective Ignition Control in Advanced Combustion Engines

by

Kelvin Xie

A Dissertation  
Submitted to the Faculty of Graduate Studies  
through the Department of Mechanical, Automotive and Materials Engineering  
in Partial Fulfillment of the Requirements for  
the Degree of Doctor of Philosophy at the  
University of Windsor

Windsor, Ontario, Canada

2018

© 2018 Kelvin Xie

EFFECTIVE IGNITION CONTROL IN ADVANCED COMBUSTION ENGINES

by

Kelvin Xie

APPROVED BY:

---

S. Habibi, External Examiner  
McMaster University

---

X. Chen  
Department of Electrical and Computer Engineering

---

J. Tjong  
Department of Mechanical, Automotive and Materials Engineering

---

G.T. Reader  
Department of Mechanical, Automotive and Materials Engineering

---

M. Zheng, Advisor  
Department of Mechanical, Automotive and Materials Engineering

May 29, 2018

## **DECLARATION OF ORIGINALITY**

I hereby certify that I am the sole author of this thesis and that no part of this thesis has been published or submitted for publication.

I certify that, to the best of my knowledge, my thesis does not infringe upon anyone's copyright nor violate any proprietary rights and that any ideas, techniques, quotations, or any other material from the work of other people included in my thesis, published or otherwise, are fully acknowledged in accordance with the standard referencing practices. Furthermore, to the extent that I have included copyrighted material that surpasses the bounds of fair dealing within the meaning of the Canada Copyright Act, I certify that I have obtained a written permission from the copyright owner(s) to include such material(s) in my thesis and have included copies of such copyright clearances to my appendix.

I declare that this is a true copy of my thesis, including any final revisions, as approved by my thesis committee and the Graduate Studies office, and that this thesis has not been submitted for a higher degree to any other University or Institution.

## **ABSTRACT**

The primary objective of the research was to study the limitations of the conventional spark ignition architecture with respect to ultra-lean and dilute combustion and develop ignition technologies and strategies that can facilitate such combustion strategies. A range of strategies using conventional and modified ignition coil systems were used in combustion chamber and engine tests to understand the effectiveness of the energy delivery mechanisms and different energy profiles. At operating conditions where the conventional ignition strategies had difficulties in achieving adequate ignition stability, the use of enhanced energy levels with different energy profiles for the achievement of effective ignition under high dilution ratio engine operating conditions was found to be necessary. A novel multiple-site ignition system was developed. It has been demonstrated to effectively deliver of ignition energy and achieved higher tolerance for lean combustion and high-dilution modes of combustion.

A radio-frequency non-thermal plasma ignition system was developed to investigate its ability to address some of the deficiencies of the spark ignition architecture. Compared to the conventional spark ignition architecture, the ignition volume induced by the corona discharge was greater in size and its growth was less impeded with the absence of a close ground electrode. The rapid energization and discharge characteristics additionally offered a more flexible control path. The formation of multiple ignition sites was possible, although implementation of the system in the engine environment has proven to be a continuing challenge.

## **DEDICATION**

*This work is dedicated to my mom and dad.*

## ACKNOWLEDGEMENTS

The work presented in this manuscript was made possible through the combined contributions of many current and former research associates. I would like to thank Dr. Raj Kumar, Dr. Clarence Mulenga, Dr. Usman Asad, Dr. Xiaoye Han, and Yuyu Tan for their previous work on setting up the engine test cells. I would like to thank all my colleagues, Dr. Meiping Wang, Dr. Shui Yu, Dr. Marko Jestic, Dr. Tongyang Gao, Dr. Prasad Divekar, Dr. Xiao Yu, Shouvik Dev, Qingyuan Tan, and Zhenyi Yang for the many things they have taught me through our insightful discussions.

I am immensely grateful for the guidance of my primary advisor, Dr. Ming Zheng, and his influence on my intellectual and professional development. In addition, I am thankful to Dr. Xiang Chen, Dr. Jimi Tjong, Dr. Graham T. Reader, and Dr. Saeid Habibi for their advisory roles to this work.

## TABLE OF CONTENTS

<b>DECLARATION OF ORIGINALITY</b> .....	iii
<b>ABSTRACT</b> .....	iv
<b>DEDICATION</b> .....	v
<b>ACKNOWLEDGEMENTS</b> .....	vi
<b>LIST OF TABLES</b> .....	x
<b>LIST OF FIGURES</b> .....	xi
<b>NOMENCLATURE</b> .....	xv
<b>1. CHAPTER I INTRODUCTION</b> .....	1
1.1 The Engine Cycle .....	2
1.2 Dilute Combustion for Spark Ignition Engines .....	7
1.3 Spark Ignition.....	10
1.4 Diesel Low-Temperature Combustion.....	14
1.5 Trends of Advanced Combustion Engines.....	16
<b>2. CHAPTER II OBJECTIVES</b> .....	19
2.1 Research Objective.....	19
2.2 Research Motivation .....	19
<b>3. CHAPTER III LITERATURE REVIEW</b> .....	24
3.1 Advanced Ignition Systems.....	24
3.2 Electrical Breakdown .....	28
3.3 Transient Plasma Ignition.....	30
3.4 Radio-Frequency Plasma.....	30
<b>4. CHAPTER IV METHODOLOGY</b> .....	32
4.1 Combustion Vessels .....	32
4.2 Optical Imaging.....	36



4.3	Spark Control and Diagnostics.....	38
4.4	Spark Ignition Components.....	38
4.5	Corona Ignition System.....	42
4.6	Single-Cylinder Test Engine .....	43
<b>5.</b>	<b>CHAPTER V EFFECT OF ENERGY AND ENERGY PROFILE ON SPARK IGNITION .....</b>	<b>50</b>
5.1	Effect of Discharge Energy .....	50
5.1.1	Quiescent Conditions .....	50
5.1.2	Flow Conditions.....	56
5.1.3	Engine Conditions.....	59
5.2	Energy Profile Strategies.....	67
5.2.1	Multi-coil Ignition.....	67
5.2.2	Capacitor Discharge.....	73
5.2.3	Pre-chamber Igniter .....	83
<b>6.</b>	<b>CHAPTER VI MULTIPLE SITE SPARK IGNITION .....</b>	<b>88</b>
6.1	Multi-pole Ignition .....	88
6.2	Extension of Dilution Limit .....	92
6.2.1	Lean Combustion .....	93
6.2.2	EGR Dilution Combustion.....	96
<b>7.</b>	<b>CHAPTER VII VOLUME IGNITION WITH NON-THERMAL PLASMA DISCHARGE .....</b>	<b>101</b>
7.1	Non-thermal Plasma Discharge.....	101
7.1.1	Electrical Power Control Characteristics .....	101
7.1.2	Physical Discharge Characteristics .....	106
7.2	Control of Discharge in Air.....	113
7.2.1	Discharge Voltage Control .....	113

7.2.2	Discharge Duration Control .....	116
7.3	Non-thermal Plasma Ignition .....	117
7.3.1	Flame Kernel Formation Process.....	117
7.3.2	Effect of Discharge Voltage.....	120
7.3.3	Effect of Discharge Duration .....	122
7.3.4	Minimum Discharge Durations for Ignition .....	125
7.4	Plasma and Flame Interactions.....	128
7.4.1	Post-Ignition Flame Kernel Acceleration .....	128
<b>8.</b>	<b>CHAPTER VIII CONCLUSIONS AND RECOMMENDATIONS .....</b>	<b>132</b>
8.1	Effect of Spark Ignition Energy and Energy Profile .....	132
8.2	Multiple-Site Spark Ignition .....	132
8.3	Non-thermal Plasma Ignition .....	133
8.4	Application to Ultra-lean or High Dilution Ignition .....	134
8.5	Recommendations for Future Work.....	134
	<b>REFERENCES.....</b>	<b>136</b>
	<b>APPENDIX A: GASOLINE HCCI COMBUSTION .....</b>	<b>146</b>
	<b>APPENDIX B: NUMERICAL SIMULATION OF DIESEL AUTO-IGNITION ...</b>	<b>153</b>
B.1	Chemical Description of Ignition.....	153
B.2	Sensitivity of Ignition to Physical Parameters .....	155
	<b>APPENDIX C: NUMERICAL SIMULATION OF LAMINAR FLAME SPEED..</b>	<b>161</b>
	<b>APPENDIX D: NOX GENERATION UNDER ELECTRICAL DISCHARGE.....</b>	<b>163</b>
	<b>APPENDIX E: EFFECT OF SPARK GAP SIZE ON KERNEL FORMATION ...</b>	<b>166</b>
	<b>VITA AUCTORIS .....</b>	<b>170</b>
	<b>LIST OF PUBLICATIONS .....</b>	<b>171</b>

## LIST OF TABLES

Table 1-1: Specific Heat Ratios of Select Gas Species.....	9
Table 4-1: Engine Specifications .....	45
Table 4-2: Gas Analyzer Model and Measurement Range .....	49

## LIST OF FIGURES

Figure 1-1: The Piston-Crank Mechanism and Engine Cycle .....	3
Figure 1-2: Effect of Compression and Specific Heat Ratios on Ideal Cycle Efficiency... 5	5
Figure 1-3: P-V Diagram of an Engine Cycle .....	6
Figure 1-4: Heat-Release Analysis of Combustion .....	7
Figure 1-5: Reducing Pumping Work with EGR.....	8
Figure 1-6: Simplified Spark Ignition Circuit.....	10
Figure 1-7: Primary Coil Charging Characteristics .....	12
Figure 1-8: Sample Voltage and Current Profiles for Conventional Spark Ignition .....	13
Figure 1-9: Discharge and Power Profiles for Conventional Spark Ignition.....	14
Figure 2-1: Fundamental Aspects of Combustion and Available Controls .....	20
Figure 2-2: Impact of Dilution of Spark Timing and Flame Development .....	22
Figure 2-3: Comparison of Cycle-to-Cycle Variations.....	23
Figure 3-1: Potential for Brake Thermal Efficiency Gains [4] .....	26
Figure 3-2: Paschen Curve for Air, adapted from [44].....	29
Figure 4-1: CV1 Small Optical Combustion Vessel.....	33
Figure 4-2: CV2 Intermediate Combustion Vessel.....	33
Figure 4-3: CV3 Large Optical Combustion Vessel.....	34
Figure 4-4: Schematic Diagram of Gas Preparation Systems.....	36
Figure 4-5: Z-type Shadowgraph Optical Setup .....	37
Figure 4-6: Photos of Spark Plugs .....	39
Figure 4-7: Later Generation Manufacturing Prototype Multi-pole Spark Plug .....	40
Figure 4-8: Earlier Generation Lab Prototype Multi-pole Spark Plug .....	41
Figure 4-9: Simplified Schematic of Corona Ignition System.....	43
Figure 4-10: Corona Igniter .....	43
Figure 4-11: Engine Igniter Adaption and Combustion Chamber Shape .....	44
Figure 4-12: Photo of Engine Setup.....	45
Figure 4-13: Engine Test Cell Setup.....	47
Figure 5-1: Discharge Characteristics in Conventional System at Different Energies.....	51
Figure 5-2: Discharge Energy Effect under Stoichiometric Conditions.....	52
Figure 5-3: Discharge Energy Effect under Lean Conditions .....	53

Figure 5-4: Flame Kernel Growth under Stoichiometric Case .....	54
Figure 5-5: Flame Kernel Growth under Lean Ignition Cases .....	55
Figure 5-6: Effect of Energy on Ignition Success Rate under Quiescent Conditions.....	56
Figure 5-7: Effect of Cross-flow Velocity on Discharge Characteristics .....	57
Figure 5-8: Restrike Behavior Under Air Flow .....	58
Figure 5-9: Spark Breakdown Voltage at Various Spark Timings .....	61
Figure 5-10: Spark Breakdown Voltage as a Function of Gas Density .....	62
Figure 5-11: Calculated In-Cylinder Temperature and Laminar Flame Speed .....	63
Figure 5-12: Effect of Spark Energy on Engine Operation .....	64
Figure 5-13: Comparison of Spark Energy .....	64
Figure 5-14: Effect of Spark Energy at Lean Conditions .....	66
Figure 5-15: Comparison of Spark Energy at Lean Conditions .....	66
Figure 5-16: Effect of Spark Energy up to Lean Limit.....	67
Figure 5-17: Current Enhancement with Multi-coil Discharge .....	68
Figure 5-18: Discharge Parameters of Multi-coil Strategy.....	69
Figure 5-19: Multi-coil Ignition Effect.....	70
Figure 5-20: Single Coil vs Multi-coil Ignition .....	71
Figure 5-21: Combustion Phasing Stability Scatter Plot .....	72
Figure 5-22: Load Stability Scatter Plot .....	72
Figure 5-23: High Energy Capacitor Discharge Configuration .....	74
Figure 5-24: High Power Capacitor Discharge Configuration .....	74
Figure 5-25: Comparison of Capacitor Discharge Power.....	75
Figure 5-26: Capacitor Discharge Effect on Combustion Parameters.....	76
Figure 5-27: Capacitive Discharge Effect on Pressure .....	77
Figure 5-28: Combustion Phasing Stability Scatter Plot at Lambda 1.2 .....	78
Figure 5-29: Load Stability Scatter Plot at Lambda 1.2 .....	78
Figure 5-30: Capacitive Discharge Effect on Combustion Parameters .....	79
Figure 5-31: Combustion Phasing Stability Scatter Plot at Lambda 1.7 .....	81
Figure 5-32: Load Stability Scatter Plot at Lambda 1.7 .....	82
Figure 5-33: Adjacent-cycle Impacts on IMEP .....	83
Figure 5-34: Images of Pre-chamber Flame Jet in Combustion Vessel.....	84

Figure 5-35: Pre-chamber Combustion Comparison .....	85
Figure 5-36: Pre-chamber Igniter Pressure Trace .....	85
Figure 5-37: Difference in Spark Timing for Pre-chamber Igniter.....	86
Figure 5-38: Comparison of Pre-chamber Igniter Test Engine Load and Emissions .....	87
Figure 6-1: Location and Orientation of Spark Poles in Multi-pole Configuration .....	89
Figure 6-2: Comparison between Single Pole and Multi-pole Ignition .....	90
Figure 6-3: Combustion Phasing Stability Scatter Plot at Lambda 1.4 .....	91
Figure 6-4: Load Stability Scatter Plot at Lambda 1.4 .....	91
Figure 6-5: Multi-pole Ignition Effect .....	92
Figure 6-6: Lean Extension Using Multi-pole Ignition .....	94
Figure 6-7: Efficiency and Emissions of Lean Combustion.....	95
Figure 6-8: EGR Dilution Limit Extension Using Multi-pole Ignition .....	97
Figure 6-9: Efficiency and Emissions of EGR Combustion.....	98
Figure 6-10: Lean and EGR Dilution Comparison.....	100
Figure 7-1: Voltage Buildup Profile in Corona Igniter.....	102
Figure 7-2: Effect of Primary Voltage on Discharge Voltage and Power .....	104
Figure 7-3: Corona Discharge Power Curve.....	105
Figure 7-4: Discharge Voltage as a Function of Frequency .....	106
Figure 7-5: Image Field and Recording Parameters .....	107
Figure 7-6: High-speed Image Sequence of Corona Discharge.....	109
Figure 7-7: High-speed Image Sequence of Corona Transition to Arcing .....	110
Figure 7-8: Formation of Corona Streamer at Higher Pressure .....	111
Figure 7-9: Corona Wind Effect in Air and Combusting Mixture.....	113
Figure 7-10: Image Field and Recording Parameters .....	114
Figure 7-11: Pressure and Voltage Effect on Corona Discharge .....	115
Figure 7-12: Examples of Arcing Conditions.....	116
Figure 7-13: Pressure and Duration Effect on Corona Discharge .....	117
Figure 7-14: Image Field and Recording Parameters .....	118
Figure 7-15: Direct Image Overlaid with Shadowgraph of Corona Ignition Event .....	119
Figure 7-16: Shadowgraph Images of Corona Voltage Effect on Ignition .....	121
Figure 7-17: Shadowgraph Area of Corona under Different Voltage Conditions.....	122

Figure 7-18: Shadowgraph Images of Corona Duration Effect on Ignition .....	124
Figure 7-19: Shadowgraph Area of Corona under Different Discharge Durations .....	125
Figure 7-20: Effect of Corona Voltage on Minimum Ignition Energy .....	126
Figure 7-21: Effect of Lambda on Corona Ignition Energy .....	127
Figure 7-22: Influence of Corona Duration on Ignition Success Rate of Lean Mixtures	128
Figure 7-23: Discharge Profile of Post-Ignition Corona Pulse Strategy.....	129
Figure 7-24: Shadowgraph Images of Post-Ignition Pulse Effect .....	130
Figure 7-25: Shadowgraph Area of Post-Ignition Corona Pulses.....	131

## NOMENCLATURE

$\gamma$	Isentropic ratio
$\lambda$	Excess air ratio
$\theta$	Engine crank position
abs	Absolute
ATDC	After top dead centre
BDC	Bottom dead centre
BMEP	Brake mean effective pressure
CA5	Crank angle of 5% heat release
CA50	Crank angle of 50% heat release
CAD	Crank angle degree
CR	Compression ratio
CRP	Common-rail pressure
CV	Combustion vessel
CVC	Constant volume chamber
DSO	Digital storage oscilloscope
E	Energy
EGR	Exhaust gas recirculation
EVO	Exhaust valve opening
FOV	Field of view
FID	Flame ionization detector
FSN	Filter smoke number



FTIR	Fourier transform infrared
g/kW·h	Unit of quantity normalized by engine work output
HC	Hydrocarbon
i	Current
IGBT	Insulated-gate bipolar transistor
IMEP	Indicated mean effective pressure
IVO	Intake valve opening
ISFC	Indicated specific fuel consumption
L	Inductance
LNV	Least numerical value
m	mass
MAF	Mass air flow
$\eta$	Indicated thermal efficiency
NO <sub>x</sub>	Nitrogen oxides
p	Pressure
ppb	Parts per billion
ppm	Parts per million
Q	Heat energy
R	1) Resistance 2) ideal gas constant
RPM	Revolutions per minute
T	Temperature
t	Time
TDC	Top dead centre

THC	Total hydrocarbon
V	1) Volume 2) voltage
V <sub>d</sub>	Displacement volume
WOT	Wide open throttle

## **CHAPTER I**

### **INTRODUCTION**

The continuing need to improve the efficiency and emissions of the internal combustion engines, which currently power the vast majority of the more than twenty two million light-duty vehicles and one million heavy-duty vehicles in Canada, is an important part of the public policy to address the issues of climate change and urban air quality [1]. Regulations that have been enacted over the last four decades have driven very significant innovations. Technologies such as variable valve actuation, direct fuel injection, downsized and turbocharged engines, are being increasingly deployed into vehicles [2]. The latest fuel economy standards, announced in 2011 by the United States Environmental Protection Agency, have set annual improvement targets of approximately 5% per year, from the 2016 baseline of 225 g/mile of carbon dioxide emissions to 143 g/mile for 2025 passenger cars [3]. A wide array of technologies, such as improved aerodynamics, hybridization and electrification, lightweight materials, and more advanced transmissions will contribute to the targeted goal. The majority of the improvements, however, are expected to come from internal combustion engines. In order to achieve the long-term targets, major improvements are necessary in the combustion systems. For spark-ignition engines, achieving dilute combustion with cooled exhaust gas recirculation or lean burn combustion is seen as a key pathway to the enhancement of efficiency [4]. For diesel compression-ignition engines, minimizing nitrogen oxide and particulate matter emissions without sacrificing thermal efficiency is the challenge.

## 1.1 The Engine Cycle

The combustion volume of a modern engine is formed by the cylinder head on the top, the piston on the bottom, and the cylinder bore in the radial direction. The piston, linked to the engine crank-shaft by a connecting rod and crank-arm, sweeps up and down the cylinder bore as the engine crankshaft rotates. A schematic of the piston and crank mechanism is shown in Figure 1-1. The cylinder volume with respect to the engine crank-arm angular position,  $\theta$ , follows the relation:

$$V(\theta) = V_d \times \left( \frac{1}{CR - 1} + 0.5 \times \left( 1 + \frac{l}{a} \cos(\theta) - \left( \left( \frac{l}{a} \right)^2 - \sin^2(\theta) \right)^{\frac{1}{2}} \right) \right) \quad (1.1)$$

where  $l$  is the connecting rod length,  $a$  is half the engine stroke length,  $CR$  is the engine compression ratio, and  $V_d$  is the cylinder displacement volume. The cylinder displacement volume is the product of the bore area and the stroke length. The compression ratio is the ratio of the maximum to minimum cylinder volume. Conventionally,  $\theta$  is referenced from the axis formed by the crank-shaft and the piston. At a  $\theta$  of zero crank angle degree (CAD), the piston is at its top-most position and the cylinder volume is at a minimum. This position is known as the piston top-dead centre (TDC) position. As  $\theta$  increases to 180° CAD, the piston moves to its bottom-most position and the cylinder volume is at its maximum. The relevant engine cycle is defined by four of such strokes over two revolutions of the crank. In the intake stroke, an intake valve is opened to draw in fresh air charge into the cylinder as the piston moves downward ( $\theta$  from 0 to 180° CAD). In the compression stroke ( $\theta$  from 180 to 360° CAD), the intake valve closes and the charge is compressed. The charge is expanded in

the expansion stroke ( $\theta$  from 360 to 540° CAD). Finally, the charge is expelled from the cylinder by holding open an exhaust valve while the piston moves upward ( $\theta$  from 540 to 720° CAD).

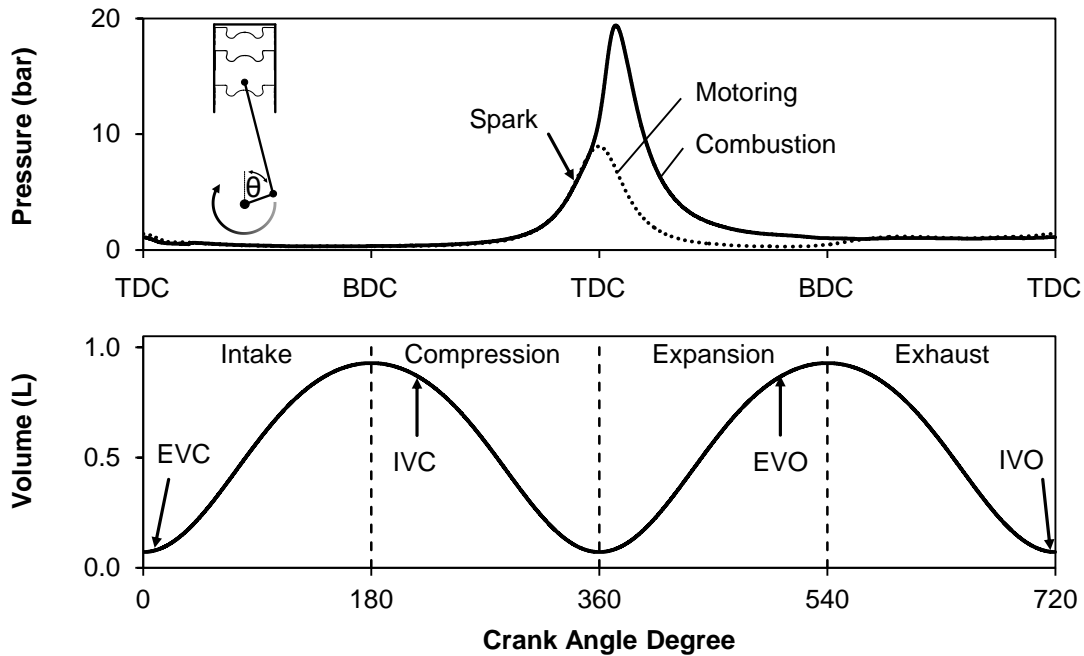


Figure 1-1: The Piston-Crank Mechanism and Engine Cycle

The compression and expansion of the in-cylinder working fluid, in the absence of combustion, approximates the relation:

$$pV^\gamma = \text{constant} \quad (1.2)$$

where  $p$  is the pressure in the cylinder,  $V$  is cylinder volume, and  $\gamma$  is the ratio of the heat capacities  $\frac{c_p}{c_v}$ . The conditions of one point of an adiabatic process can be used to define

subsequent points by the relation:

$$p_0V_0^\gamma = p_1V_1^\gamma \quad (1.3)$$

The mean gas temperature in the cylinder is approximated by the ideal gas law:

$$pV = mRT \quad (1.4)$$

In diesel engines, the compression ratios typically range from 16:1 to 19:1, resulting in peak compression temperatures of 850 K – 1000 K. This high temperature is utilized to vaporize and ignite the liquid diesel fuel. In spark-ignition engines lower compression ratios, typically from 9:1 to 13:1, are used. The compression temperatures are significantly lower and below the typical ignition temperatures of the fuel. Instead, a spark discharge initiates a flame front that propagates through the cylinder volume. In both cases, the heat released by the combustion of the fuel raises the pressure and temperature of the working fluid. Expansion of the working fluid converts a part of the combustion thermal energy into work, which is transferred to the engine crank-shaft. The limit to the thermodynamic efficiency of this process is dependent on the degree of expansion possible, aside from the inevitable energy losses [5]. Figure 1-2 plots this efficiency limit for a range of compression ratios and specific heat ratios. In engine designs that have symmetrical compression and expansion ratios, gains in cycle efficiency by increasing the expansion ratio have a consequence of higher cylinder pressures and temperatures. The high in-cylinder pressures may require stronger mechanical designs, which translate into higher masses and larger bearing surfaces, at the cost of weight and friction. For diesel engines, the high temperatures shorten the ignition delay and potentially lead to higher NO<sub>x</sub> production and smoke production [6-7]. For spark-ignition engines, the higher pressures and temperatures constrain the engine operation range by the onset of engine knock [8].

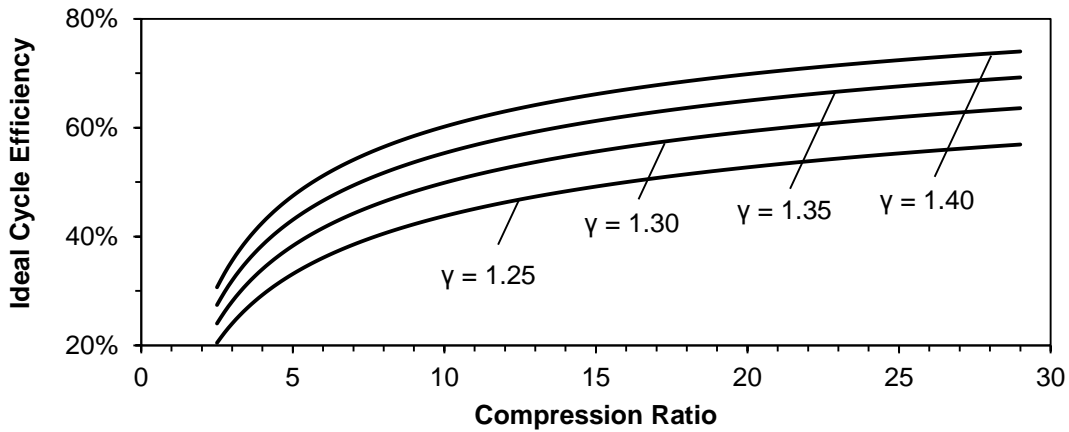


Figure 1-2: Effect of Compression and Specific Heat Ratios on Ideal Cycle Efficiency

Figure 1-3 shows the pressure trace of an engine cycle plotted against the instantaneous cylinder volume. The larger loop in the pressure-volume diagram is the result of the departure of the expansion stroke pressure from the compression stroke pressure as a result of combustion. The smaller loop arise from the pumping work performed when throttling the intake to control the engine load and then subsequently pushing the exhaust out against the atmospheric pressure. The net area of the two loops is the total cycle indicated work. The term *indicated* work refers to the p-V work performed by the working fluid. This is in contrast with *brake* work, which is work available at the engine crank-shaft after friction and consumption by auxiliary engine equipment (such as water pump, fuel pump, oil pump, valve cams, etc.) are subtracted from the indicated work. A measure of the indicated cycle work normalized to the engine displacement size is the *indicated mean effective pressure* (IMEP). The IMEP of an engine is calculated by the expression:

$$IMEP = \frac{\int_{0^{\circ}}^{720^{\circ}} pdV}{V_d} \quad (1.5)$$

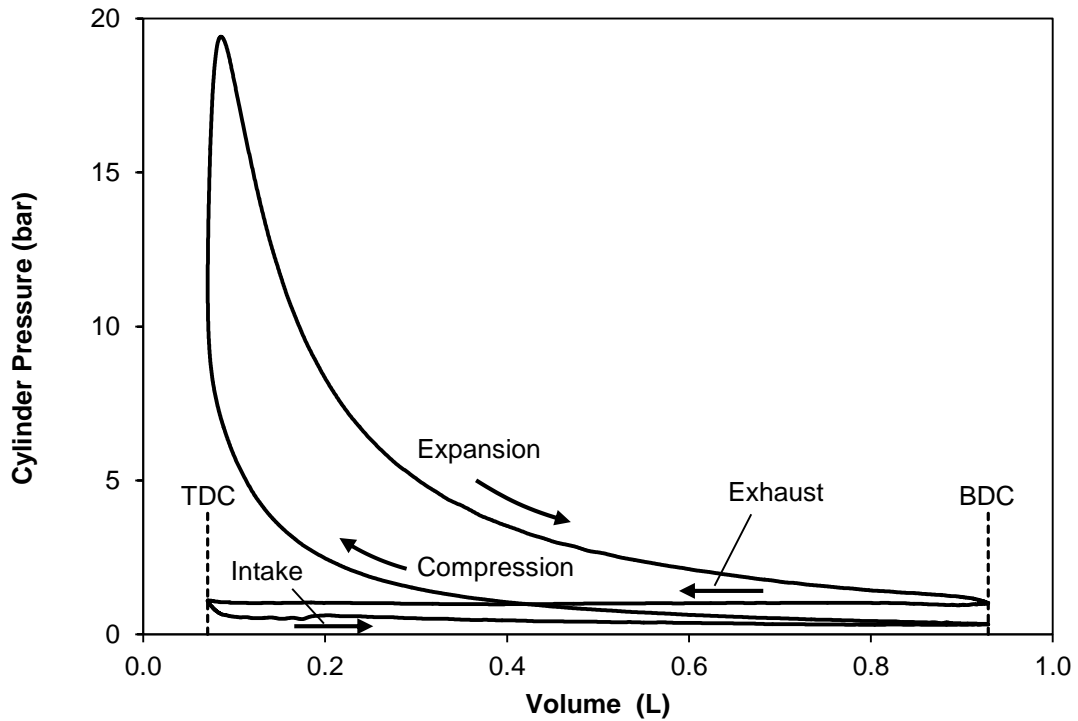


Figure 1-3: P-V Diagram of an Engine Cycle

An analysis of the pressure trace can be performed to identify the changes in the in-cylinder pressure as a result of the combustion process as opposed to the cyclic compression and expansion processes. This is the apparent heat-release analysis [9]. Figure 1-4 shows an example heat-release trace. The heat-released rate in this example is calculated using the expression:

$$\frac{dQ}{d\theta} = \frac{1}{\gamma - 1} \left[ \gamma p \frac{dV}{d\theta} + V \frac{dp}{d\theta} \right] \quad (1.6)$$

where  $p$  is the cylinder pressure,  $V$  is the cylinder volume at crank angle  $\theta$ , and  $Q$  is the apparent heat-release rate. A derivation this expression can be found in the dissertation of Jetric [10].

The heat release can be integrated through the combustion process and normalized to the total heat-release to result in a mass fraction burned function. The



parameters of CA5, CA50, and CA95 are computed from the heat release to indicate the crank angles of 5%, 50%, and 95% total heat-release. These parameters serve as practical quantifiers of the timings of the start of combustion, the midpoint of combustion, and the end of combustion.

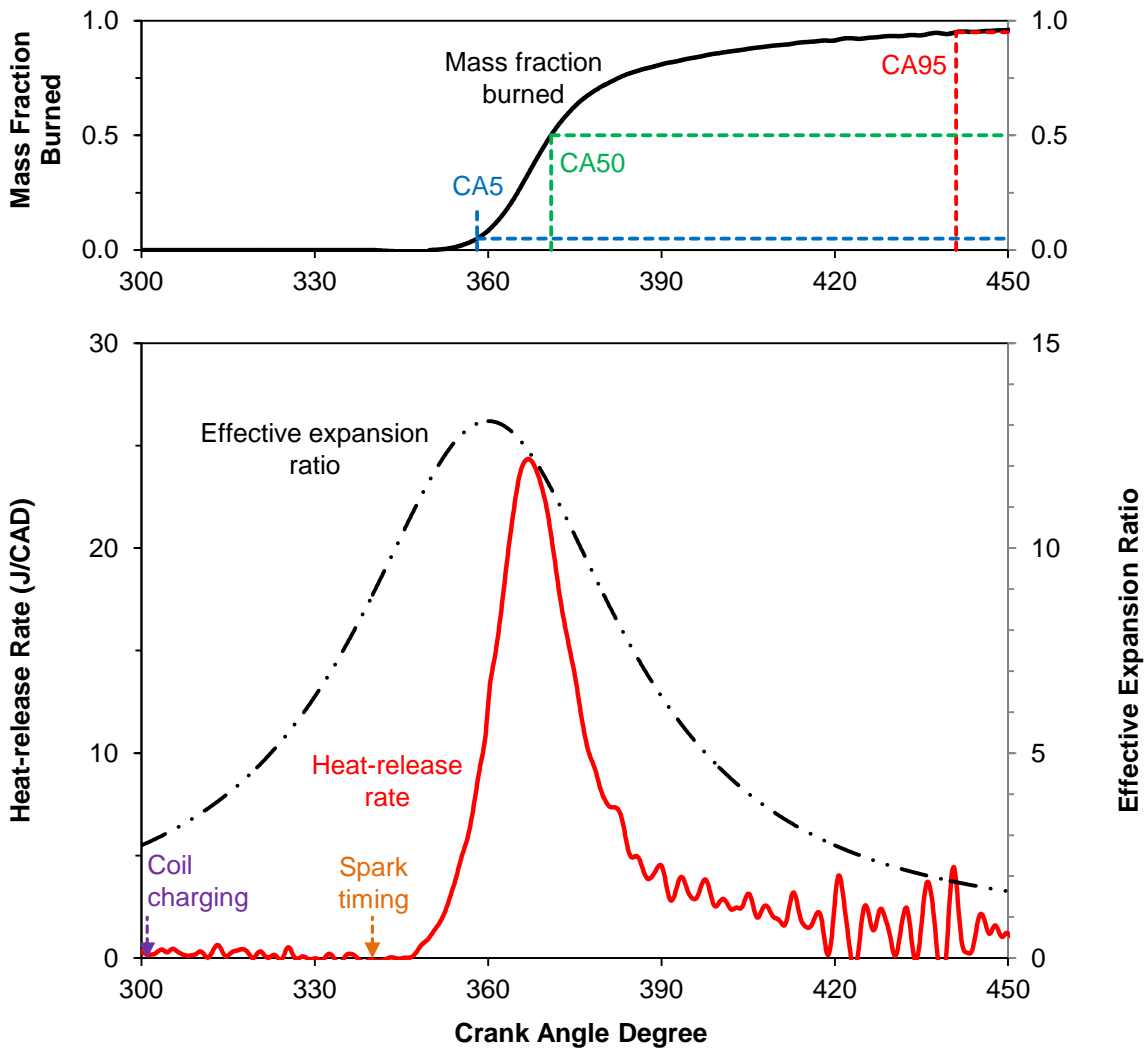


Figure 1-4: Heat-Release Analysis of Combustion

## 1.2 Dilute Combustion for Spark Ignition Engines

The conventional spark ignition engine utilizes air-fuel ratio control near the stoichiometric ratio throughout most of its operation range (at high-load operation, fuel

enrichment may be used for charge cooling purposes to control knocking and exhaust temperatures). At part-load operation, the throttling of the intake air for load control creates a pumping work penalty in the intake stroke of the engine. The introduction of an inert diluent such as recirculated exhaust can reduce this pumping work loss while maintaining the stoichiometric air-fuel ratio requirement. A p-V trace showing the differences in the pumping loop with exhaust gas recirculation is shown in Figure 1-5. At the part-load condition shown, approximately 0.5 bar of vacuum is drawn during the intake stroke. When a portion of the exhaust gases is added back to the air-fuel charge, the amount of vacuum during the intake stroke reduces and the associated pumping work penalty is lower.

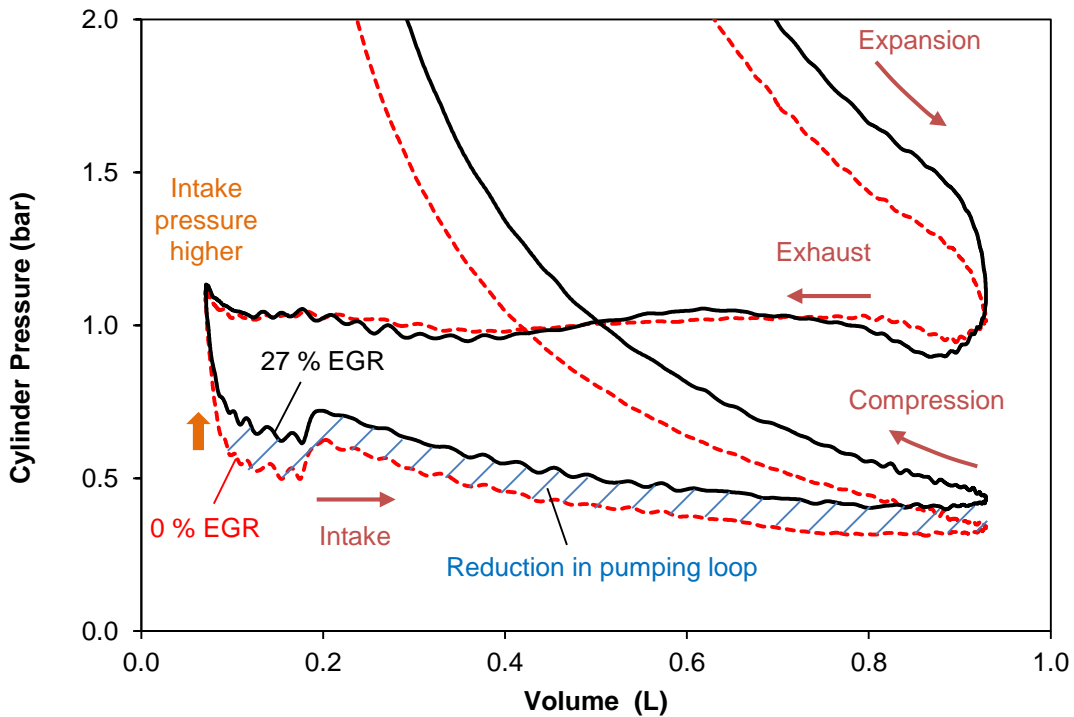


Figure 1-5: Reducing Pumping Work with EGR

If the requirement of stoichiometric operation is relaxed, additional fresh air can be used as the diluent. The amount of dilution that can be applied in lean combustion typically exceeds the amount possible with exhaust gas recirculation. In addition to the reduction of throttling losses, lower combustion temperatures as a result of the heat sink action diluent gases result in lower heat-transfer losses to the combustion chamber surfaces.

It was previously shown in Figure 1-2 that the ideal cycle efficiency is a function of the specific heat ratio  $\gamma$ . The value  $\gamma$  of air is 1.40 at ambient temperature and decreases at higher temperatures (for example, 1.34 at 1000 K) [11]. The values of  $\gamma$  for typical hydrocarbon fuels are lower than that of air, as can be seen in Table 1-1 [12].

Table 1-1: Specific Heat Ratios of Select Gas Species

Substance Name	Molecular Formula	Heat Capacity Ratio @ 298 K	Heat Capacity Ratio @ 1000 K
Nitrogen	N <sub>2</sub>	1.400	1.341
Oxygen	O <sub>2</sub>	1.401	1.313
Water	H <sub>2</sub> O	1.329	1.251
Carbon Dioxide	CO <sub>2</sub>	1.289	1.181
Methane	CH <sub>4</sub>	1.335	1.129
Octane	C <sub>8</sub> H <sub>18</sub>	1.046	1.020
Hexadecane	C <sub>16</sub> H <sub>34</sub>	1.022	1.010

Mixtures of fuel and air have a specific heat ratio intermediate of air and the pure fuel. A higher mixture average  $\gamma$  is achieved with a larger portion of air, which directionally indicates the leanest possible combustion as being desirable. This effect is also present with exhaust gas dilution, but the carbon dioxide constituent has a notably lower specific heat ratio ( $\gamma = 1.29$ ) than air.

### 1.3 Spark Ignition

A simplified spark ignition circuit representative of an inductive ignition system is shown in Figure 1-6 [13]. This basic configuration has been widely used in automobiles since the second half of the twentieth century. The switching that was once accomplished by distributors and rotary contacts is now performed by electronic insulated-gate bipolar transistors (IGBT).

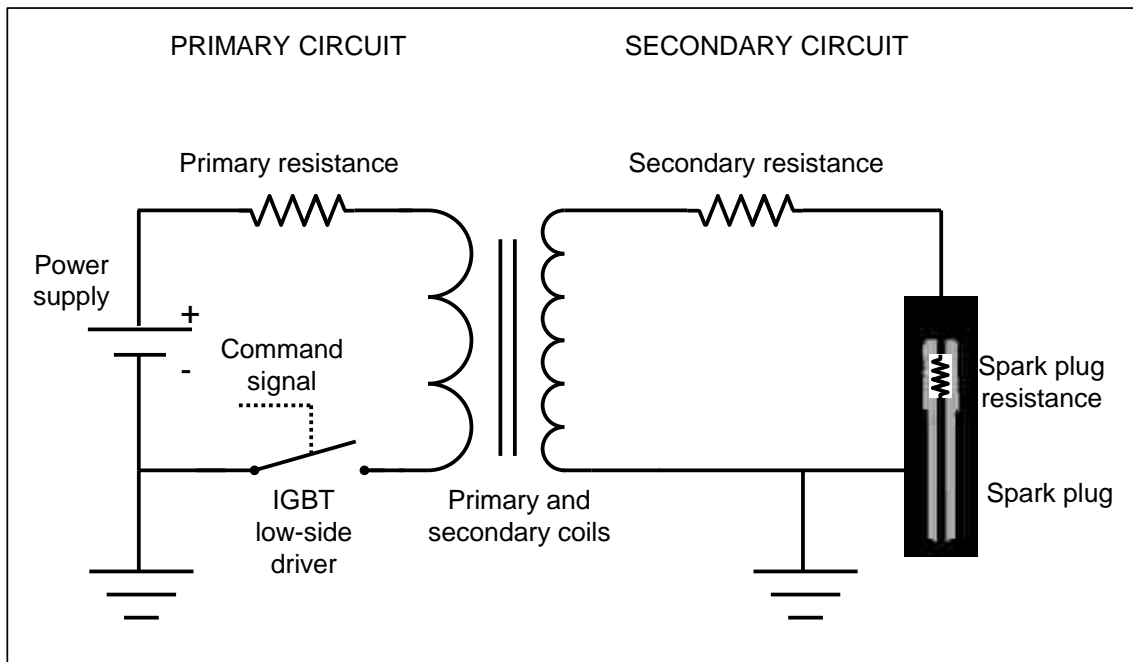


Figure 1-6: Simplified Spark Ignition Circuit

The primary coil circuit can be modelled as a resistance and an inductance in series [14], with the current,  $i$ , expressed by:

$$i = \left(\frac{V}{R}\right) \left[1 - \exp\left(-\frac{Rt}{L}\right)\right] \quad (1.6)$$

where  $V$  is the supply voltage,  $R$  is the coil resistance, and  $L$  is the coil inductance. The cumulative energy input in the primary circuit can be expressed as the integration of the product of the current and voltage:

$$E = \int_0^t iV dt \quad (1.7)$$

The energy stored in the primary coil is expressed by:

$$E = 0.5Li^2 \quad (1.8)$$

The energy available in the secondary coil is considerably lower because of imperfect magnetic coupling and the resistance in the secondary coil winding. The overall transfer efficiency is in the order of 10 to 50% [14].

The model prediction of the primary coil current and a recorded current trace of an ignition coil are shown in Figure 1-7, based on the nominal circuit parameters of  $V = 12.5$  V,  $R = 0.55$   $\Omega$ , and  $L = 5.8$  mH. The energy supplied to the coil and the energy stored are also shown. The supplied energy is higher than the stored energy. This is attributed by Stone to the internal resistance of the coil drive unit, the resistance of the current shunt, and the lower coil inductance at higher currents [14].

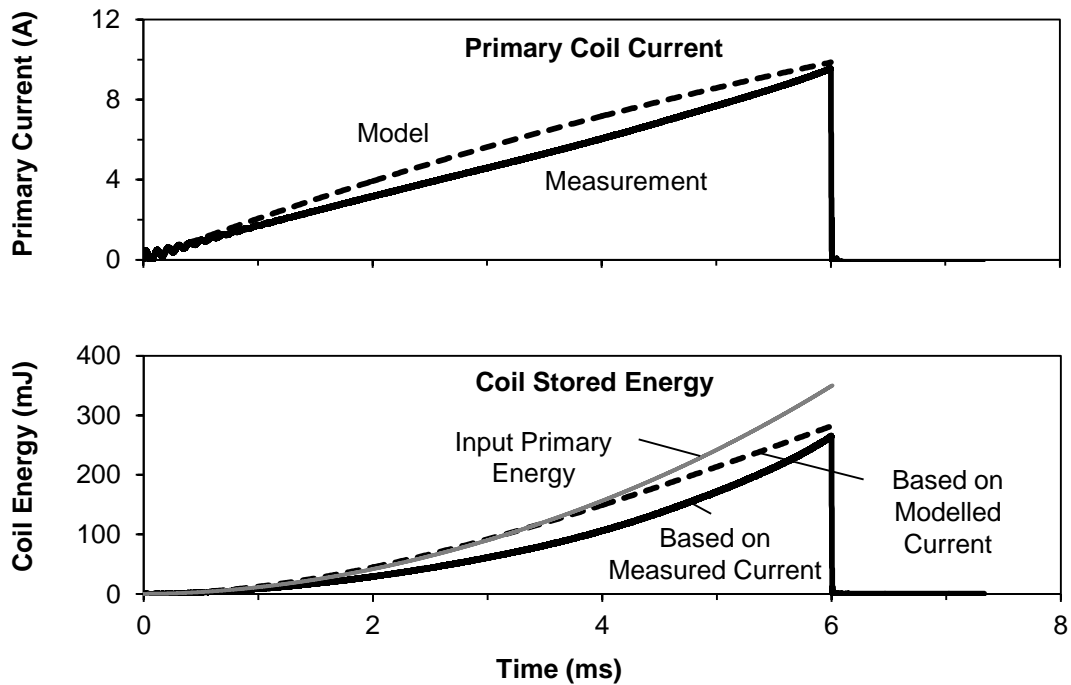


Figure 1-7: Primary Coil Charging Characteristics

The induced voltage buildup in the secondary circuit upon the opening of the primary circuit and the subsequent discharge is shown in Figure 1-8. The pre-breakdown phase lasts a number of microseconds, where the voltage increases up to the point of electrical breakdown in the spark gap. During the pre-breakdown phase, the small capacitances present in the spark plug and secondary cable serve as local energy storage. As the electric field strength in the gap increases during the voltage buildup, the gas begins to ionize. The strong electric field rapidly accelerates free ions and the subsequent collisions of the electrons generate more ion pairs in an avalanche mechanism [15]. The breakdown phase is characterized by extremely short durations on the order of  $\sim 10$  ns, a high degree of ionization, and high currents on the order of  $\sim 200$  A [5]. The next phase of the discharge is the arc phase, which is characterized by a relatively low discharge voltage, a hot cathode, and a degree of ionization on the order of 1 percent of the gas

molecules. As the available current decreases over time, the discharge transitions to the glow phase, where the lower current sustains a more diffuse discharge channel with a low degree of ionization on the order of 0.01 percent [5].

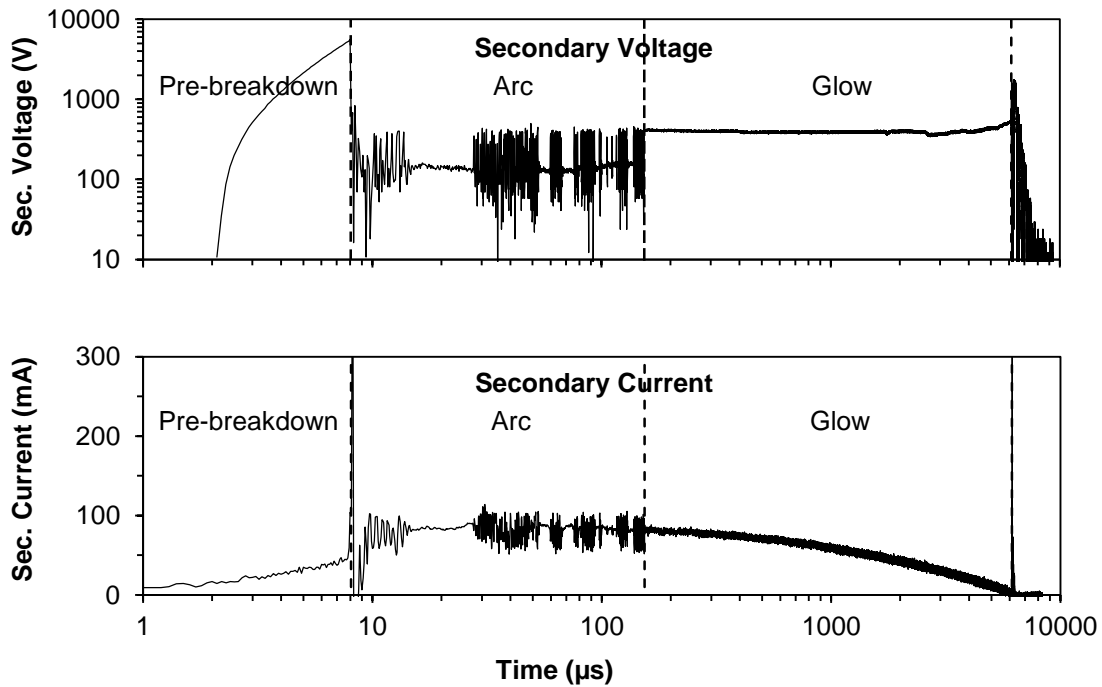


Figure 1-8: Sample Voltage and Current Profiles for Conventional Spark Ignition

The discharge power and cumulative energy profiles of the example trace are shown in Figure 1-9. The power during the breakdown phase is not accurately captured by the electrical recording; the discharge power is on the order of ~100 kW to ~1 MW [5]. The discharge energy during the breakdown phase is low. Most of the discharge energy is released during the long glow phase at a relatively low power on the order of tens of watts.

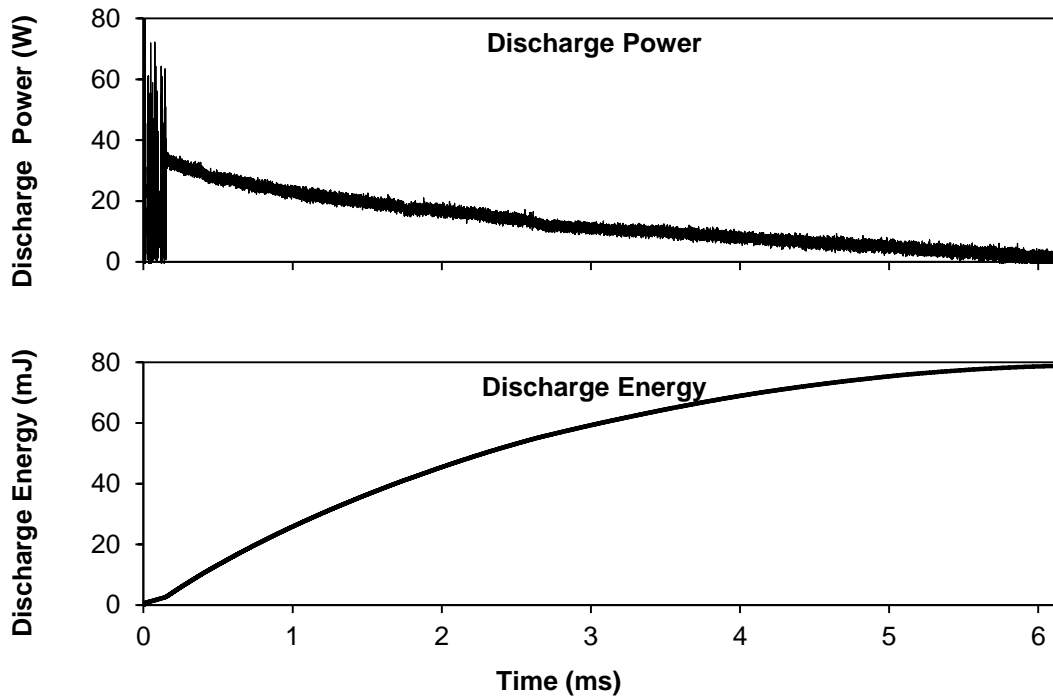


Figure 1-9: Discharge and Power Profiles for Conventional Spark Ignition

The discharge energy deposition forms a pool of radical species and an energetic plasma core. The radical species and thermal energy initiate combustion reactions in the gas mixture. The general criterion for a successful ignition event is that the heat release by chemical reaction at the flame kernel surface exceeds the rate of heat loss. Thus the attainment of a sufficient kernel size is important for successful ignition. The continuing supply of energy to the flame kernel during the glow phase can aid the kernel growth rate [15].

#### 1.4 Diesel Low-Temperature Combustion

Modern diesel engines employ direct injection of a liquid diesel fuel under high pressures into the hot cylinder air. Depending on the fuel injection system type, engine load, and boost level, the injection pressures may range from several hundred bars at low



load to approximately 2,000 bars at high load for common-rail systems. Higher pressures in the range of 3,000 bars can be achieved for unit injectors and hydraulically intensified injection systems. The fuel is delivered through a series of nozzles 0.1 to 0.2 mm in diameter arranged radially around the injector tip, which protrudes into the combustion chamber. The spray is shattered by shear forces during the high-pressure injection process, forming a dense cloud of fuel droplets [16]. The droplets undergo evaporation under the compression temperatures as heat is transferred from the surrounding gas to the liquid. The evaporated fuel is in part carried away from the droplet surface by diffusion and convection, forming mixtures of decreasing richness radiating from the droplet surface [17]. The fuel vapour when mixed with air undergoes the reaction chemistry described in more detail in Appendix B. The ignition tends to initiate in zones where the mixture is near stoichiometric. If ignition starts prior to complete evaporation of the fuel, a stable flame zone may develop where fuel vapour is continuously transported into the flame zone from the droplet surface and air is transported into the flame zone from the surrounding gas mixture. This is referred to as a diffusion or non-premixed flame. Under these conditions, the local stoichiometry may approach  $\lambda = 1$  even though the global stoichiometry may be significantly lean. The impact of near stoichiometric burning is high flame temperatures leading to high NO<sub>x</sub> production. For example, while the mean gas temperature of an engine cycle may not exceed 1500 K and is insufficient for NO<sub>x</sub> formation, flame temperatures where  $\lambda = 1$  are calculated to exceed 2600 K. Dilution of the flame to  $\lambda = 2$  reduces the flame temperature to under 2000 K, closer to a low-NO<sub>x</sub> condition. Thus delaying the ignition to allow more time for evaporation of the fuel and mixing with air or recirculated exhaust is a necessary measure to control NO<sub>x</sub> production in diesel engines.

## 1.5 Trends of Advanced Combustion Engines

In comparison to compression ignition engines, spark ignited engines have lower efficiencies at both low and high loads. The requirement to operate at stoichiometric conditions to enable the three-way catalyst to treat exhaust emissions is a limitation to the achievable efficiency [5]. If the requirement of stoichiometric operation is relaxed, excess air can be used as the diluent and this would increase efficiency at low and medium engine loads. The lean limit of conventional gasoline spark ignition and combustion would however limit the practical dilution level. Alternative combustion strategies such as homogeneous charge compression ignition or stratified charge combustion address some aspects of this, however not without their own challenges for implementation.

One strategy currently being adopted is to reduce the engine displacement and use a turbocharger to maintain the engine power output. This leads to a shift in the engine operating range to a higher level of specific power, thereby reducing the effects of the pumping and frictional losses. A complementary technology is to employ variable valve-train configurations, such as cam phasing, variable valve lift, or variable valve duration.

Knock is the term given to the noise associated with the auto-ignition of a portion of the fuel-air mixture ahead of the propagating flame front [8]. In practice knock limits raising the compression ratio to improve thermal efficiency because sustained auto-ignition of the end-gas, when forceful enough, can lead to damage to the engine. The knock tendency can be even more pronounced in turbocharged applications, where the temperature and pressure of the initial charge is higher than in normally aspirated engines. The use of cooled exhaust gas recirculation is a potential source of efficiency and

emission improvement in this application. Knock reduction using exhaust gas recirculation can have advantages over the use of fuel enrichment (fuel economy penalty, high hydrocarbon and carbon monoxide emissions) or delayed combustion phasing (fuel economy penalty, high exhaust temperatures) [18].

A trend that is occurring in the field of internal combustion engines is the coming together or merging of what were conventionally two different combustion systems, the diesel compression ignition system and the spark ignition system [19]. The spark ignition gasoline engine designs are adopting what were traditionally aspects of diesel engines, namely turbocharging, direct fuel injection, and diluted combustion. The diesel engines, on the other hand, are moving toward more moderate compression ratios and homogeneous combustion to control NO<sub>x</sub> and smoke emissions.

This trend of engine technology assimilation is exemplified by the Mazda Skyactiv-X generation of engines, announced in 2017 [20]. This engine uses a high base compression ratio of 15:1, cam phasing to control valve timing, cooled exhaust gas recirculation, and a clutched supercharger to boost the air charge. At higher engine loads, the combustion strategy is conventional spark ignition and flame propagation. At lower engine loads, the combustion strategy is what Mazda termed spark-controlled compression ignition. It is a stratified combustion strategy where the bulk cylinder charge is lean and a core charge near the spark plug is enriched to enable reliable ignition and a sufficient combustion rate [21-22]. The bulk cylinder charge is sufficiently close to auto-ignition that the temperature and pressure increase caused by the core charge combustion initiates the compression ignition. In this fashion, a suitably rapid lean combustion is achieved in a significant fraction of the cylinder charge, which combined

the high base compression ratio, result in a higher degree of efficiency than a conventional gasoline engine. A key aspect of the technology is the proper matching of the air flow, fuel injection, and spark to achieve the proper stratification and reliable ignition. The use of in-cylinder pressure sensors to control the combustion phasing and the engine mode switching is also critical.

## **CHAPTER II**

### **OBJECTIVES**

#### **2.1 Research Objective**

The main objective of the research was to demonstrate strategies for the effective delivery of ignition energy for combustion in advanced lean combustion and high-dilution engines. A range of strategies using conventional and modified ignition coil systems were used. The aim was to understand the effectiveness of the energy delivery mechanisms and different energy profiles. The ignition strategies were applied in engine tests to assess their ability to extend the lean and exhaust gas diluted gasoline combustion limits with the aim of fuel efficiency improvement.

#### **2.2 Research Motivation**

Chapter 1 has highlighted the increasingly strict standards for fuel economy that the vehicle manufacturers must achieve across their fleet of vehicles. Advances in engine technology will be required to meet the new requirements. Engine combustion systems that operate substantially under lean combustion or high dilution are one proposed solution to achieve higher engine efficiencies. In this case the performance of the ignition system becomes crucial. A robust ignition process allows stable initiation of the combustion with small cyclic variations. Advanced ignition systems can also be advantageous in potentially reducing knock risk at high loads.

Key fundamental aspects that affect the ignition and flame development and the controls available to influence them are shown as a schematic in Figure 2-1. The fundamental flame speed is primarily a function of the temperature, stoichiometry, and

fuel [23]. The fuel chemistry is typically not readily alterable, but can be modified by chemical reformation through negative valve overlap combustion, EGR fuel reforming, or plasma treatment. The temperature of the mixture is an important aspect affected by a variety of variables. At the time of ignition, the charge temperature is a strong determinant of the fundamental flame speed.

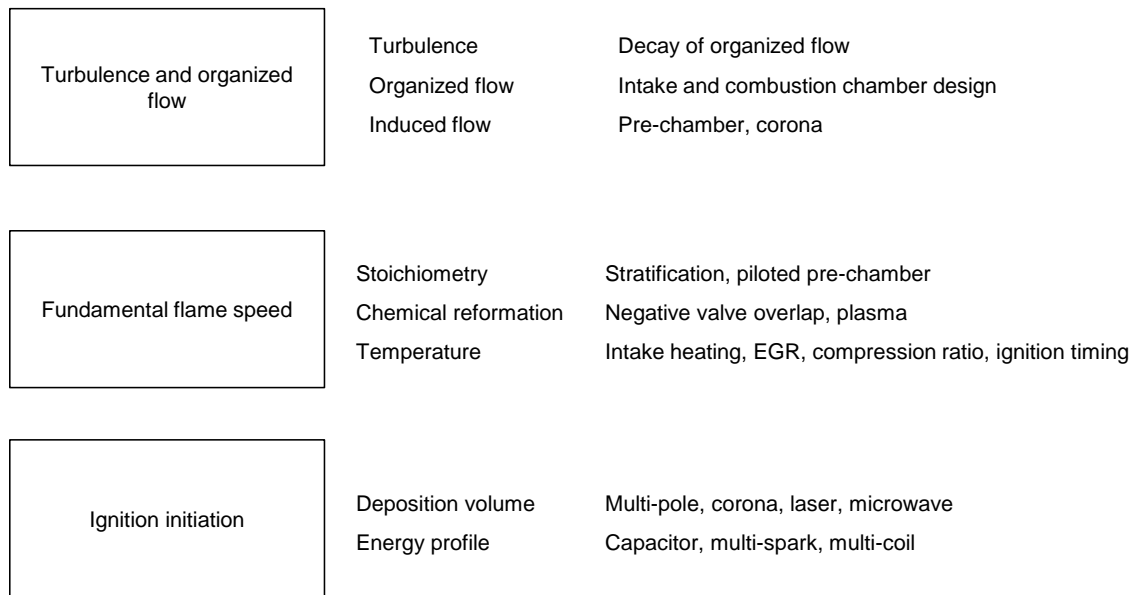


Figure 2-1: Fundamental Aspects of Combustion and Available Controls

In the engine, the actual flame speed is typically more than an order of magnitude greater than the fundamental laminar flame speed. This is primarily attributable to the effect of turbulence, which on a small scale increases the flame surface area and transport rates and therefore the overall combustion rate. The turbulence typically scales with the engine speed, thus enabling the combustion to complete across a range of engine speeds [5]. The organized large-scale flow of the cylinder charge is important in generating turbulence that can increase the burning rate [24]. With respect to the ignition event, a flow across the spark gap is generally regarded as desirable in order to stretch the

discharge channel and expose more of the charge volume to the discharge. However, excessively high flow velocities can cause the discharge channel to blowout and reform prior to the establishment of a stable flame kernel [25]. At conventional levels of energy, motion of the charge induced by the discharge itself is typically small. There are ignition systems such as the pre-chamber igniter which locates the ignition in a partially shrouded volume and uses the ejection of the flame into the main chamber to generate turbulence and increase the combustion rate [5].

The ignition initiation is traditionally achieved through a spark, although advanced systems of such as microwave enhancement, corona discharge, or laser ignition are in development. These systems can alter the energy deposition location, profile, and quantity. The multi-pole ignition strategy uses multiple sites of closely located spark ignited volumes.

In order to address the ignition issue under ultra-lean combustion or high dilution combustion, it is necessary to combine the various controls available to produce an effective combustion system. An example of deficiencies of the conventional ignition system when operating at lean conditions is shown in Figure 2-2, abstracted from the experimental tests performed in this work. The spark timing and measured average combustion phasing of an engine are compared at three different stoichiometry levels, ranging from  $\lambda = 1.1$  to  $\lambda = 1.65$ . At the close to stoichiometric condition, the span from the spark discharge to the CA5 point is 19 CAD. When the  $\lambda$  is increased, the spark timing is correspondingly advanced to maintain the same combustion phasing. The spark timing is pushed to 53 CAD before TDC in the case of  $\lambda = 1.65$ . The slow combustion rate at the lean stoichiometry is compounded by the low charge

temperature at the time of ignition with the highly advanced ignition timing. This results in a substantially long period from the spark to the CA5 point of 48 CAD.

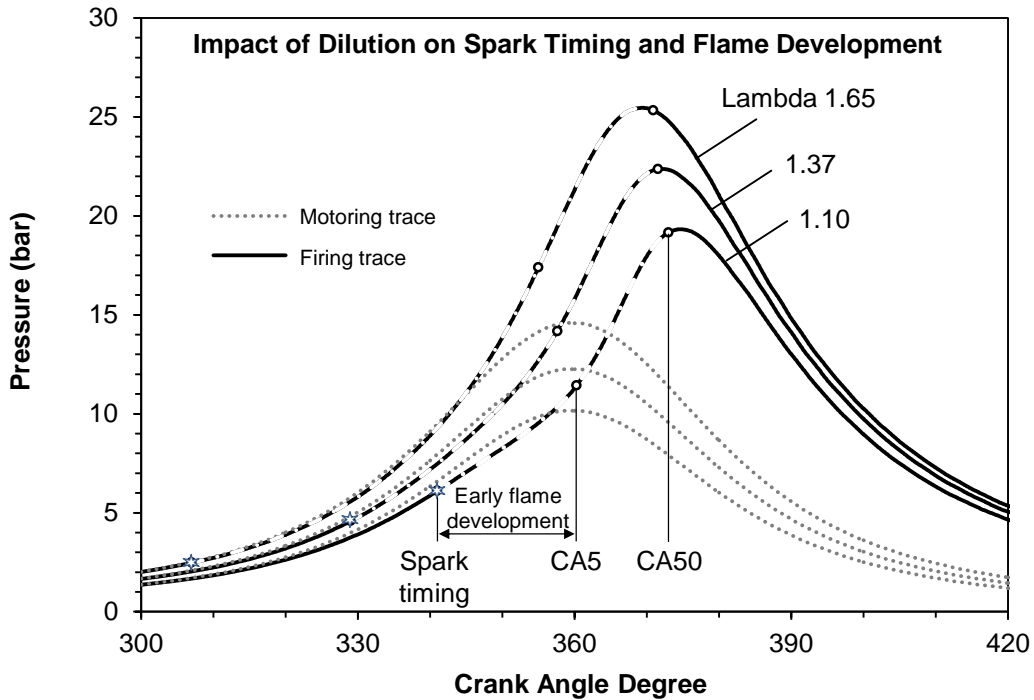


Figure 2-2: Impact of Dilution of Spark Timing and Flame Development

The impact of the early spark and slow initial flame growth is seen in the increased cyclic variations in the combustion. The pressure traces of fifty consecutive engine cycles are shown in Figure 2-3 for the cases of  $\lambda = 1.1$  and  $\lambda = 1.65$ . A notable significant amount of variability is seen at  $\lambda = 1.1$ , attributable to the variability in the cylinder flow motion that strongly influence the early flame kernel development process. This variability is greatly amplified in the case of  $\lambda = 1.65$  by the early spark and slow combustion rate. The outcome even includes two cycles of partial misfires. While the engine can operate with a small percentage of misfires or poor combustion cycles, the loss of efficiency, hydrocarbon emissions, and variability in



torque are undesirable. Thus even though the average engine cycle is apparently controllable by the ignition system, the individual cycle is subject to substantial variability. A more direct and effective control of the ignition process would improve the engine stability, extend the operating limits, and potentially improve the efficiency.

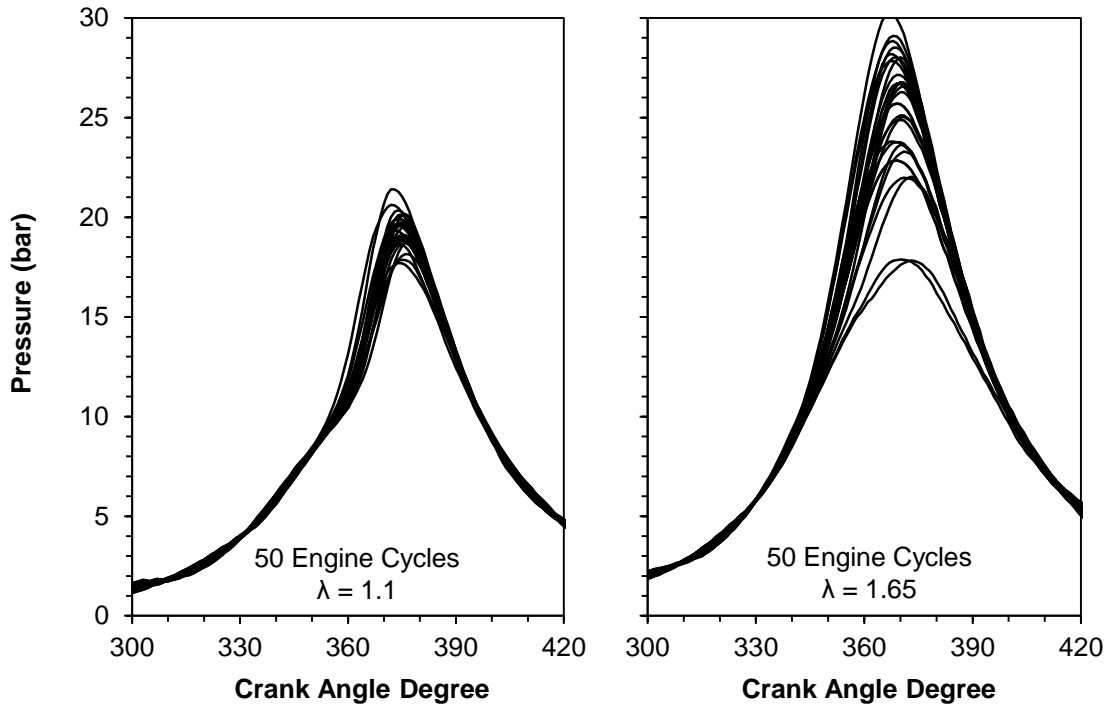


Figure 2-3: Comparison of Cycle-to-Cycle Variations

## CHAPTER III

### LITERATURE REVIEW

#### 3.1 Advanced Ignition Systems

There are a number of ignition and control architectures that can provide benefits in efficiency and emissions compared to conventional stoichiometric spark-ignition engines. However, they are typically constrained in engine operating load and have control challenges. Homogeneous charge compression ignition (HCCI) is a form of low temperature combustion where a premixed or homogeneous fuel-air mixture is compressed to the point of auto-ignition in a process predominately controlled by chemical kinetics [26]. Compared to spark ignition, HCCI combustion is faster and can be operated with leaner mixtures at higher compression ratios. As HCCI lacks a direct ignition trigger, the control of the combustion over a wide range of conditions is a severe challenge [27]. The implementation of HCCI on diesel engine platforms are typically achieved with the selection of a fuel with suitable volatility and reactivity, combined with mixing, engine boost, and exhaust gas recirculation control. In spark ignition engine platforms, the temperatures required to achieve auto-ignition typically cannot be achieved with compression alone. The temperature of the charge is instead typically raised through mixing with hot residual gases, for example by exhaust re-breathing during the intake stroke or trapping of the exhaust with negative valve overlap [28]. A discussion of a set of gasoline HCCI tests conducted on a diesel engine platform is presented in Appendix A.2.

A complement to the HCCI strategy is the spark-assisted compression ignition combustion in which spark-ignition is used to directly initiate bulk auto-ignition and HCCI combustion [28-31]. The spark assist functions by initiating a flame kernel that propagates through a portion of the charge. The release of this combustion energy serves to increase the temperature and pressure of the remaining charge to initiate the auto-ignition. Experimental studies found the use of the spark can alter the phasing of the auto-ignition effect and improve the cycle to cycle combustion stability [31]. The application was most effective under moderate to high loads where the flame speed was adequate to effect significant flame propagation. At the low load limit, however, the spark-assisted combustion was not seen to be effective because of the excessively slow flame speeds.

In both of the above combustion system configurations, the charge may be diluted with excess air or exhaust gas to increase the efficiency, to lower the reactivity, and control knocking and detonation. The potential for efficiency gains was analyzed on a thermodynamic basis by Lavoie [4]. The results are shown in Figure 3-1 for naturally aspirated operation and boosted operation for conventional combustion and advanced combustion modes. In naturally aspirated operation, there is limited potential for efficiency gains at the full load of 10.5 bar BMEP, as the full use of the fresh air intake charge is required to meet the load requirement. At lower load levels, the efficiency of the conventional throttled stoichiometric combustion mode decreased significantly. The use of air dilution or EGR dilution maintained a high level of efficiency to the mid-load region. The switching to an HCCI mode of operation was used in the analysis for low load operation. With the use of turbocharging, the efficiency was calculated to further

increase from the baseline naturally aspirated air full dilution case starting at about 5 bar BMEP.

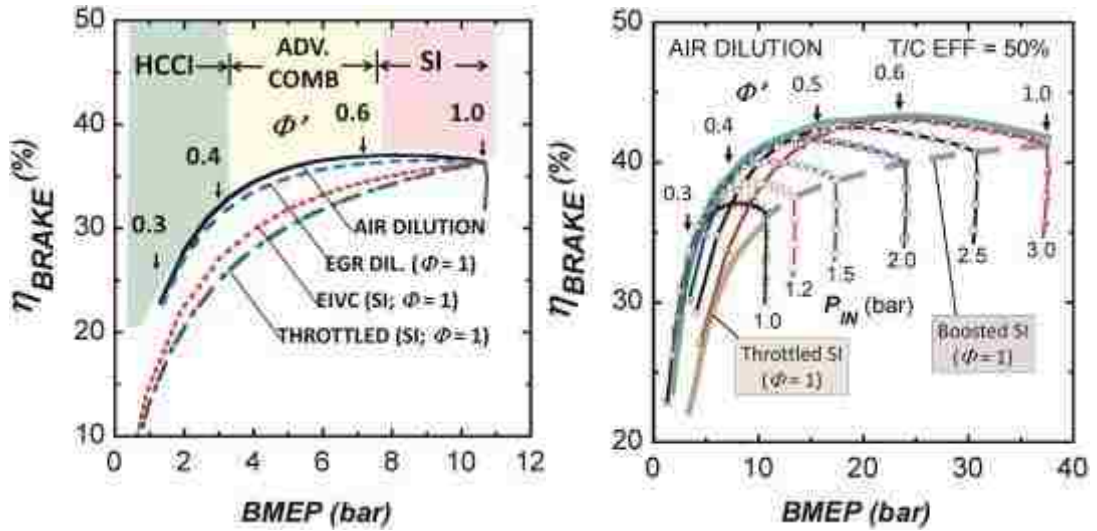


Figure 3-1: Potential for Brake Thermal Efficiency Gains [4]

The thermodynamic analysis by Lavoie gives guidance to the magnitude of gains that may be achievable from advanced combustion modes. The analysis does not, however, address the practical challenges of ignition and combustion at those conditions. As the reactivity and fundamental flame propagation speeds are lowered by dilution, the combustion rate may have to be maintained through the use of enhanced charge motion. Ignition under lean burn, EGR, and high flow conditions can be considerably more challenging. Non-conventional technologies such as laser ignition, microwave generated plasma, and corona aim to broaden the ignition limit and enhance the rate of combustion [32-35]. Compared to conventional inductive system spark plugs, the potential advantages include the ability to deposit higher amounts of energy, the reduction in heat loss to the electrodes, and the reduced blockage by the electrodes.

The principal mechanism of ignition through lasers is electrical breakdown through multi-photon ionization and the inverse bremsstrahlung process (electrons gain energy by absorption of laser radiation) [36]. Multi-photon ionization generates electrons which are further accelerated by photon collision. The accelerated electrons then collide with neutral molecules and ionize them, creating a plasma kernel. The high plasma temperatures and pressures generate a shockwave observable in Schlieren images. The plasma then ignites the combustible mixture through conventional chemical and thermal pathways. The breakdown process is enhanced by pressure due to increased collision frequencies [37]. The laser energy is typically deposited in a few nanoseconds, with the lower bound of pulse energies on the order of 5 – 10 mJ. To date, laser ignition systems have been proven in demonstration combustion systems, for example 100 hours in a stationary natural gas engine running at  $\lambda = 1.8$  ignited by a full-sized external Nd-YAG laser [38]. A solid-state laser in the form factor of a spark plug, coupled to an external pumping laser via fiber optics, was realized by Tauer [32]. The high costs of the laser ignition systems are a current limitation to commercial utilization.

There is still much research activity using conventional or modifications of the inductive coil and spark plug system hardware. The use of twin ignitions coils discharging in an offset fashion to generate a continuous discharge without the typical decay in the current intensity showed increased tolerance to exhaust gas recirculation, which normally slowed combustion progress and reduced engine stability [39]. The continuous nature of the discharge was observed to be better than repetitive restriking at the same spark energy level.

The coupling of a number of ignition coils to discharge simultaneously on one spark plug can increase the discharge energy, with the discharge duration remaining comparable. Work by Yu coupled four coils to enhance the discharge current [40-41]. The multiple coils were also used to generate high frequency discharges up to 20 kHz when the primary coil voltages were raised to decrease the required charging duration.

The coupling of ten ignition coils increased the energy by a factor of five, from 50 mJ to 250 mJ, in work by Jung [42]. The multi-coil system was seen to increase the stability at leaner conditions. The best results were seen when the leaner operation was matched with enhanced in-cylinder turbulence. It was also found that when examining the distribution of the spark energies delivered, the actual energy did not strongly correlate with the cycle combustion characteristics. This indicated that a significant portion of cycle to cycle variations were not directly relatable to the spark energy, but other parameters such as flow conditions, fuel concentration, and temperature. A more powerful spark system using repetitive short discharges (12 ns duration) coupled with a semi-open cavity that generates turbulent jet-like early flame has been used to demonstrate the ability to enhance lean-burn operation limits to achieve fuel economy and NO<sub>x</sub> benefits [43].

### **3.2 Electrical Breakdown**

The process of electrical breakdown is caused by the various processes of ionization. Under moderate electrical strength fields, a free electron may be generated by collisions with background cosmic radiation. Under high strength fields, the ionization may occur as a result of random collisions [44]. The liberated electron and positive ion are accelerated under the electrical field and cause further ionization in subsequent

collisions. The cascading process produces an electron avalanche. The voltage at which breakdown occurs is a function of the gas pressure and contact gap spacing. This relationship is recognized as Paschen's law [44]. A plot of the Paschen curve behavior of air is shown in Figure 3-2. The breakdown voltage increases at higher pressures or wider gap spacing due to the fact that electrons lose energy through more frequent collisions. A high electrical field must be used to allow the electrons to gain sufficient energy between collisions. The curve displays a minimal breakdown voltage and subsequent increase in breakdown voltage at high vacuum conditions. The increase of breakdown voltage in this region is caused by the lower probability of collision and subsequent ionization under the rarified conditions.

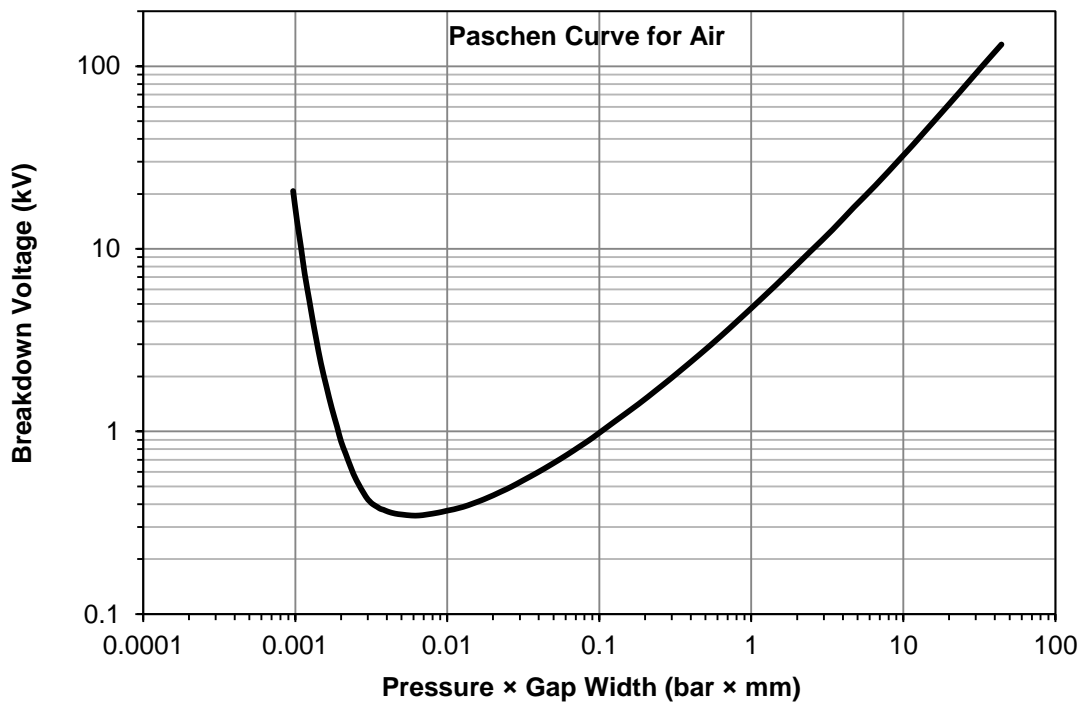


Figure 3-2: Paschen Curve for Air, adapted from [44]

### **3.3 Transient Plasma Ignition**

A highly transient form of plasma discharge is generated by single or repeated nanosecond high voltage pulses. The discharge can provide effective electron impact dissociation at relatively higher pressures for engine applications [45]. The pulse durations typically are 1 to 10 ns in length and generated by high voltage DC generators at 20 to 100 kV. The total energy delivery per pulse is also modest at the short durations. The individual pulses can be coupled together to increase the energy delivered. However, the repeat pulses increase the likelihood of breakdown discharge that result in the high current electrode wear associated with thermal plasma sparks [46].

### **3.4 Radio-Frequency Plasma**

Discharges of a more sustained, continuous can be generated by electric fields with alternate wave frequencies on the order of 1 MHz [47]. The non-equilibrium plasma from the discharge is also a viable ignition method. Starikovskiy attributes the five mechanisms through which a plasma discharge initiates and interacts with the flame kernel. There are two thermal mechanisms: 1) gas heating from the energy deposition, 2) inhomogeneous gas heating leading to perturbations and mixing, and three non-thermal mechanisms: 3) the effect of ionic wind 4) the ion and electron drift in the electric field, and 5) excitation, dissociation, and ionization of the gas by electron impact [48]. An advantage of the radio-frequency plasma is the ability to continuously supplement the ignition energy and affect the flame kernel. One of the key challenges of radio-frequency corona ignition is to ensure the discharge occurs while avoiding breakdown discharge. This is the challenge especially under high density conditions when higher voltages are required for initiate a discharge.



Development of the radio-frequency corona ignition technology toward commercialization has been undertaken by a number of automotive technology companies, the most notable being Federal-Mogul's Advanced Corona Ignition System and Borg Warner's Ecoflash system [49-50]. Published results on research engines with the Advanced Corona Ignition System have shown a larger initial ignition volume, faster times to 5% mass burn fraction, and reduced cycle-to-cycle variations compared to conventional spark ignition [47]. A more systematic follow-up study of the corona ignition voltage and duration effects was also performed [51]. It was found that the discharge parameters influenced the early phases of combustion up to the point of 5% mass fraction burned, beyond which the flame propagation was independent of any action by the igniter. This corresponded to about 300  $\mu\text{s}$  at  $\lambda = 1$  and 500  $\mu\text{s}$  at  $\lambda = 1.4$ . The use of the highest discharge voltage below the arcing threshold was found to be the most effective. When arcing occurred, the discharge was isolated to one arc path instead of the normally four ignition zones generated by the four-pointed igniter. At lower voltages or corona durations, ignition sometimes did not occur at all the igniter points, decreasing the overall combustion stability and speed.

## CHAPTER IV

### METHODOLOGY

This chapter provides a description of the research platforms used in is dissertation. The tests are in general of two categories. The first used a combustion vessel to provide a background gas mixture of controlled pressure and composition to study the electrical discharge, ignition, and flame propagation. The second used a single-cylinder test engine to study the processes in actual engine applications.

#### 4.1 Combustion Vessels

Combustion vessels of three different sizes and functions were used. A small 26 cm<sup>3</sup> optical vessel was used for the majority of tests. This vessel was used for inert and combustible charges up to 8 bar pressure. The layout of this CV1 vessel is shown in Figure 4-1. The vessel has a cylindrical inner volume of 25.4 mm diameter and 51.8 mm length. Two quartz windows provide an optical path through the vessel in the axis of the cylindrical volume. The working fluid of the vessel is filled and discharged through two 1/4 inch ports. The vessel pressure is measured by a Kistler 4075A10 piezoresistive absolute pressure sensor. The vessel is equipped with a pressure relief valve set at 8.3 bar.

An intermediate sized non-optical vessel of 113 cm<sup>3</sup> was used for inert and combustible charges up to 60 bar. This vessel was not instrumented with any optical ports to reduce the design complexity and increase the margin of safety. The layout of this CV2 vessel is shown in Figure 4-2. The vessel cavity is a cylindrical volume of 50.0 mm diameter and 57.6 mm length. The working fluid of the vessel is filled and discharged through two 1/4 inch ports. The static pressure of the vessel was measured by

a Swagelok PTI-S-NG5000-22AQ pressure sensor. The dynamic pressure during a combustion process was measured by an Omega DPX101 pressure sensor. The vessel is equipped with a rupture disk designed to burst at 60 bar pressure.

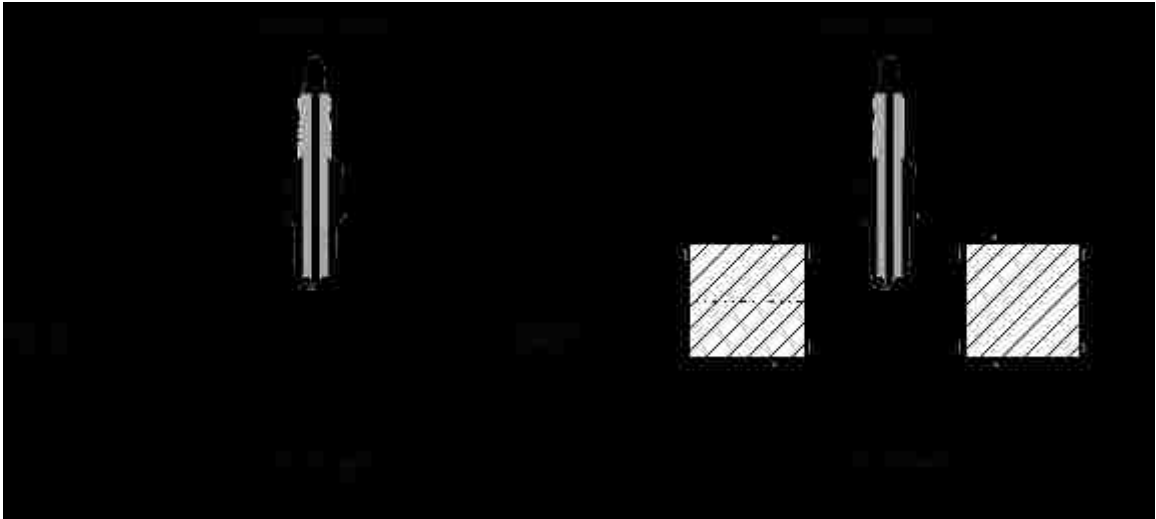


Figure 4-1: CV1 Small Optical Combustion Vessel



Figure 4-2: CV2 Intermediate Combustion Vessel

A large optical vessel of 2.6 litres nominal volume was used to visualize the flame kernel initiation and growth with reduced influence by nearby walls. This vessel, through

the use of different flanges and adapters to accommodate various high-pressure fuel injectors and igniters, was designed for a range of spray visualization and combustion studies. The layout of this CV3 vessel is shown in Figure 4-3.

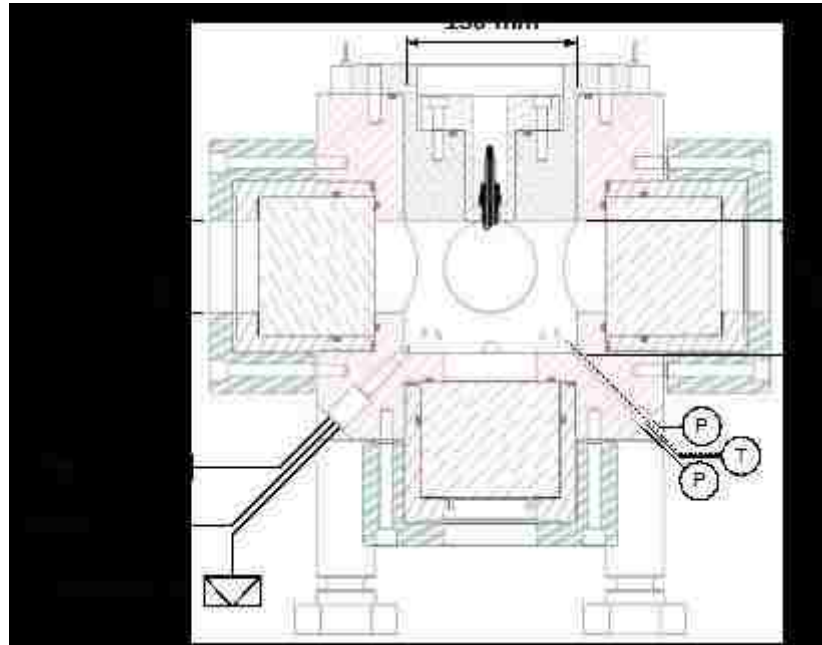


Figure 4-3: CV3 Large Optical Combustion Vessel

The main inner volume of the CV3 vessel is a cylindrical cavity of 150 mm diameter and 115 mm length. Optical access is possible through five of the six orthogonal faces of the vessel. The optical diameter provided by the quartz windows is 80 mm. The working fluid for the vessel is filled through a 3/8 inch port and discharged through two 3/8 inch ports. The static pressure of the vessel was measured by a Swagelok PTI-S-NG5000-22AQ pressure sensor. The dynamic pressure during a combustion process was measured by a Kistler 6043A60 pressure sensor. For the tests undertaken, the vessel was equipped with a rupture disk designed to burst at 60 bar pressure.

Three configurations of gas preparation were used for the charging of the combustion vessels. When a pure gas was required, the vessels were charged directly from the gas bottle using the bottle primary regulator. When the preparation of a certain gas composition was required, such as a stoichiometric methane-air mixture, an Environics 4040 gas divider was used. The gas divider contains four mass-flow controllers that are used to precisely meter two or three sources into one output stream. The output pressure of the gas divider is by design limited to approximately 1.2 bar. The ignition tests conducted at 1 bar gauge pressure used solely the gas divider to pressurize the combustion vessel. With test conditions at higher pressures, the output of the gas divider was pressurized by a two-stage diaphragm pump. This setup was used to prepare charges up to initial pressures of 6 bar gauge. A schematic of the gas preparation configurations is shown in Figure 4-4.

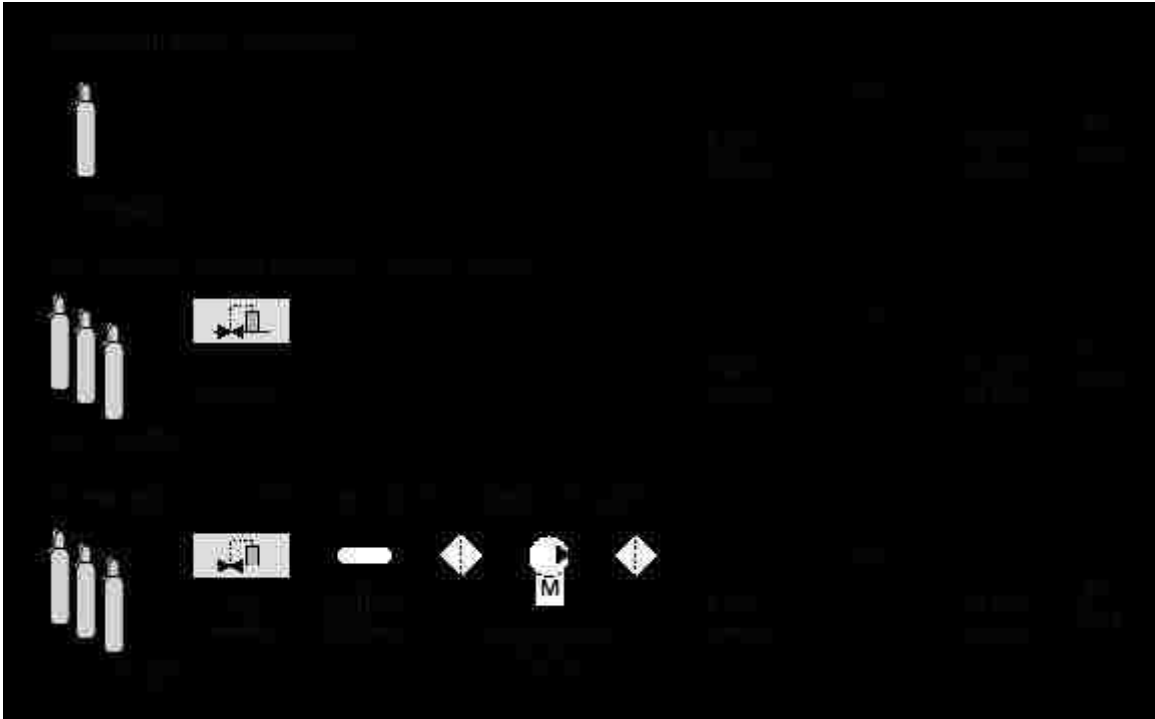


Figure 4-4: Schematic Diagram of Gas Preparation Systems

## 4.2 Optical Imaging

The optical combustion vessels were installed in the test section of Z-type shadowgraph imaging setups. Each setup consists of a Luminous Devices CBT-90 white LED light, a 0.4 mm pinhole aperture, two 6-inch f/8 parabolic mirrors, and a camera. A schematic of the imaging setup is shown in Figure 4-5. The parabolic mirrors were placed approximately nine feet apart on opposing sides of an optical table. The LED light was placed at the focal point of one mirror, four feet away, and approximately  $10.5^\circ$  off axis. The pinhole was placed immediately in front of the LED emitting surface. The camera was placed past the focal point of the second mirror, at an equal angle off the central axis.



A consumer Canon 6D digital single-lens reflex camera was used to capture colour and long-exposure images.

### **4.3 Spark Control and Diagnostics**

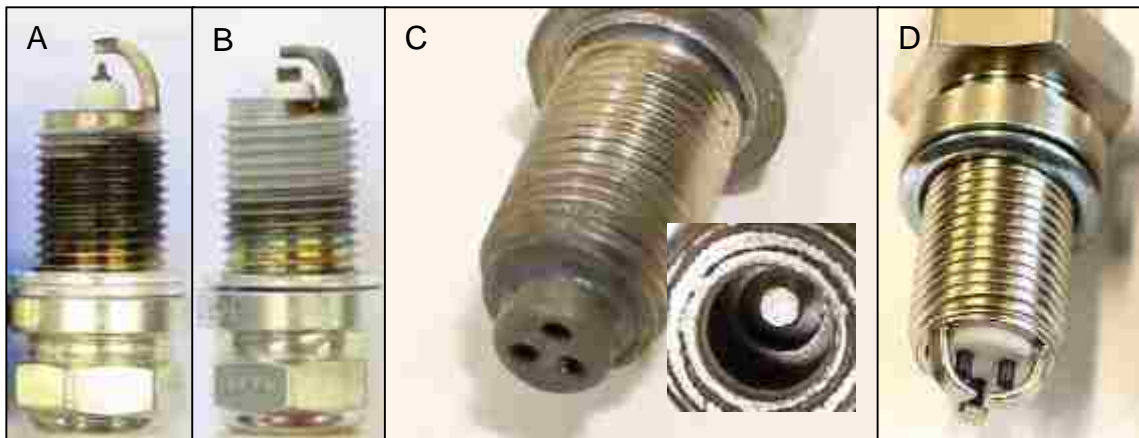
A National Instruments real-time computer with field-programmable gate array (FPGA) resources was programmed to generate the command control signals with 25 ns time resolution. For the spark ignition tests, a multi-channel system of ignition drivers was used to control up to three ignition coils independently. Each ignition coil was driven by an automotive ignition insulated-gate bipolar transistor and a shared 12.7 volt power supply. The control signal to the ignition driver was isolated from the other systems by the use of an optical-isolator. For measurements of the high voltage at the secondary side, a Northstar PVM-6 high-voltage probe with 2000:1 attenuation was used. The discharge current was measured by an inductive Pearson 411 wide-band current monitor probe. The voltage and current signals were recorded by a PicoScope 4824 digital storage oscilloscope.

### **4.4 Spark Ignition Components**

The spark plugs used in this work were a combination of commercially available products and custom fabricated prototypes. The general benchmark spark plug was selected to be the NGK BKR6EIX-11 iridium thin-electrode spark plug [52]. This spark plug design has a comparatively fine 0.6 mm diameter centre electrode, as can be seen in Figure 4-6 (A). This design was selected as the thin centre electrode was expected to reduce heat transfer losses from the flame kernel to the electrode and reduce the blockage by the electrode. The resistance of the spark plug was 4.4 k $\Omega$ . In tests where the spark plug resistance was not desired, a type NGK R5672A-9 V-groove non-resistive design



spark plug was used [53]. This spark plug design has a 2.5 mm diameter nickel centre electrode. The centre electrode design has a triangular groove on its end face, intended to direct the spark discharge to the periphery of the electrode. This spark plug was not selected for this particular feature, but rather because of the limited availability for commercial non-resistive spark plugs. This spark plug is shown in Figure 4-6 (B).



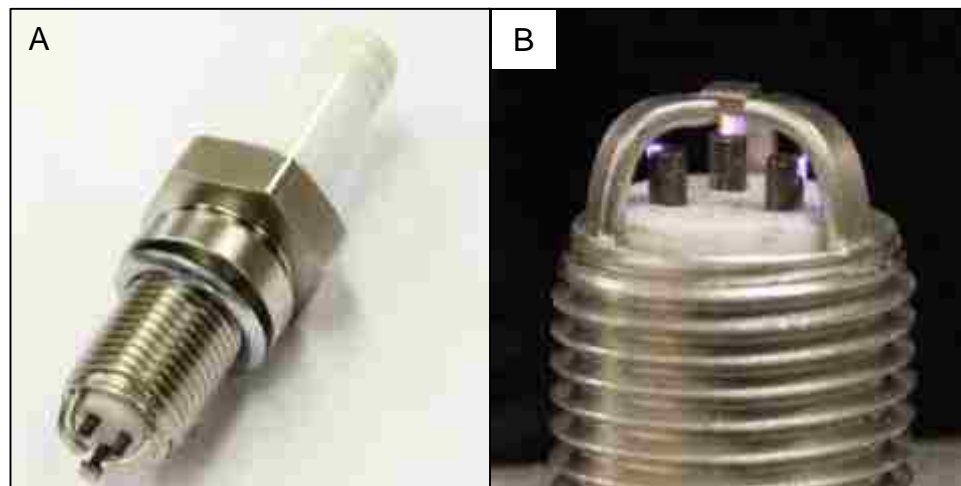
A: NGK BKR6EIX-11 iridium 0.6 mm thin-electrode spark plug  
B: NGK R5672A-9 V-groove non-resistive spark plug  
C: Prototype pre-chamber spark plug. Inset showing pre-chamber interior.  
D: Prototype multi-pole spark plug.

Figure 4-6: Photos of Spark Plugs

A prototype pre-chamber spark plug was also used in this work. The spark plug has a shroud surrounding the core electrode, forming a pre-chamber cavity. The shroud has three circular openings in the axial direction and three smaller openings in the radial direction for passively filling the cavity with the engine charge upon compression and to permit the flame to enter the main combustion chamber. This spark plug is shown in Figure 4-6 (C).

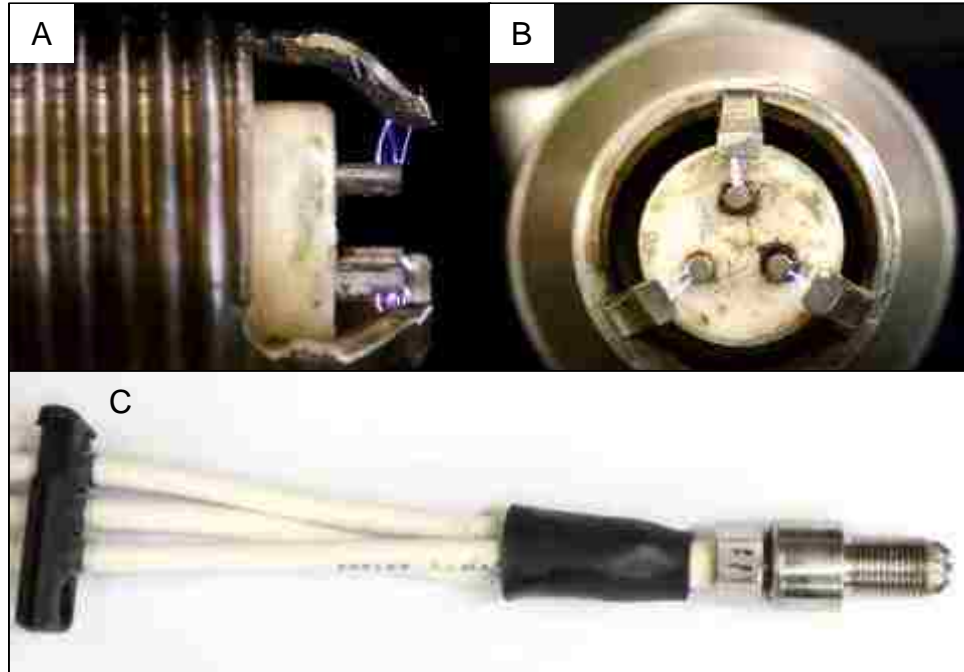
The multiple site spark ignition concept in this work was tested with prototype multi-pole spark plugs consisting of three independent high-voltage electrodes [54-56].

The number of electrodes was selected to be three for the practicality of fabrication, to ensure adequate ceramic thickness for electrical isolation, and to limit the blockage effect of the core and ground electrodes on the flame kernel development. The reported work in this thesis was performed on a manufacturing prototype design made in production-level processes with conventional sintered aluminum oxide processing methods and steel shell fabrication. This spark plug design is shown in Figure 4-6 (D). The M-14 size plug contained three electrically independent 1.5 mm core electrodes arranged in a triangular pattern with a circumradius of 2.3 mm. The conductor used to connect each of the core electrodes to spark wires consisted of 20 American wire gauge high-voltage cable with silicone insulation material. The conductor cable joints were potted with electrical epoxy to insulate the conductors from each other. These spark plugs were not manufactured with any internal resistor.



A: Manufacturing prototype multi-pole spark plug  
B: Spark discharge in air

Figure 4-7: Later Generation Manufacturing Prototype Multi-pole Spark Plug



A: Side view of lab prototype multi-pole spark plug  
B: End view of lab prototype multi-pole spark plug  
C: Lab prototype multi-pole spark plug

Figure 4-8: Earlier Generation Lab Prototype Multi-pole Spark Plug

The manufacturing prototype design was based on proof-of-concept work performed using a laboratory prototype multi-pole spark plug assembled from a custom sintered ceramic core and custom machined shell. The core electrodes were 1 mm diameter stainless steel rods cemented to the ceramic. The ground electrodes used were cut from commercial spark plugs and welded into place. The lab prototype used ground electrodes which were designed for side discharge perpendicular to the high voltage electrode. In contrast, the manufacturing prototype design used conventional J-type ground electrodes. The particular geometry of the ground and centre electrode resulted in the spark channel forming between an edge of the high voltage electrode to the curved portion of the ground electrode under quiescent conditions. Photos of the manufacturing prototype and lab prototype designs are shown in Figure 4-7 and Figure 4-8.

In this work, the spark plug gap sizes were set at 0.86 mm, as measured using a wire-type spark plug gap gauge. While this gap size is on the lower range for modern naturally aspirated automotive gasoline engines, this was selected to limit the peak breakdown voltages under in-cylinder operating conditions. The lower peak voltages reduce the demand on the electrical isolation of the ignition components, particularly the custom fabricated components. In addition, the lower peak voltages reduce the possible interference effects of the ignition system on the engine control system. The effect of spark gap size on the flame kernel development is discussed in Appendix E.

#### **4.5 Corona Ignition System**

The corona ignition system used in this work was developed by post-doctoral researcher Shui Yu at the University of Windsor Clean Combustion Engine Laboratory [57]. A schematic of the corona ignition system is shown in Figure 4-9. The power driver converts a variable direct-current voltage to a sinusoidal alternating-current wave in the primary coil. This induces a higher potential alternating-current wave in the secondary coil. The frequency of the primary waveform is controlled to produce resonance in the secondary circuit, thereby attaining the required voltage amplification.

The high voltage terminal of the secondary circuit is the corona igniter. The combustion chamber surrounding the corona igniter functions as the counter electrode to the igniter center electrode. An example of a corona igniter fabricated for this work is shown in Figure 4-10. The core electrode consists of 1/16<sup>th</sup> inch pure tungsten rods commonly used in TIG welding applications. The core electrode is housed in an insulator body machined from polymers or ceramics. Nylon, Teflon, and machinable ceramics were used for different variations of the igniter design. The polymer designs

were adequate for moderate pressure and near-ambient temperature combustion chamber testing, while the ceramic designs were intended for high pressures and temperatures such as found in the engine environment. The outer shell of the igniter was machined from steel to provide installation into standard M-14 size threads used for spark plugs.

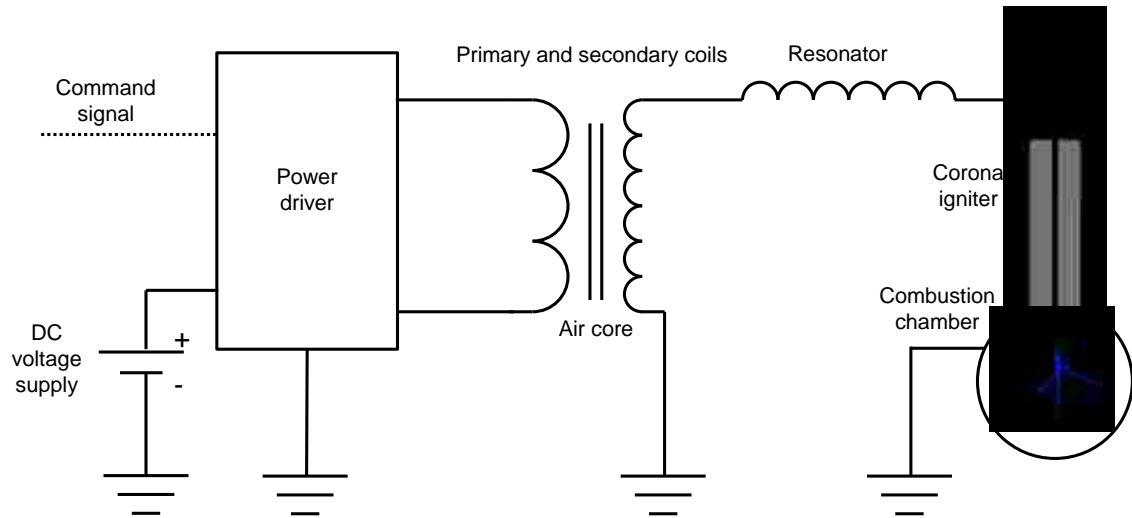


Figure 4-9: Simplified Schematic of Corona Ignition System



Figure 4-10: Corona Igniter

#### 4.6 Single-Cylinder Test Engine

The engine tests were carried out on a single-cylinder engine. Key specifications of the engine are listed in Table 4-1. The engine is a modified Yanmar NFD-170 stationary engine. The base engine was a horizontal, liquid-cooled, two valve single-cylinder direct-injection diesel engine with mechanical fuel injection. The engine was

modified to locate a centrally-mounted spark plug in place of the diesel injector. The igniter axis was  $20^\circ$  from the perpendicular to the cylinder head surface. The nominal depth of installed spark plug center electrodes was set to be 5 mm. When different designs of spark plugs were used, the spark plug reach was kept constant by using different thickness washers to locate the spark gap at a constant depth from the cylinder head surface. The flat design of the original cylinder head necessitated the combustion chamber to be formed primarily by the piston cavity. The omega shape combustion bowl of the original diesel combustion system was retained, but the compression ratio was reduced from the base of 17.8 to 13.1:1 by removing material to form a shallow bowl across approximately 80% of the piston top surface. An intake manifold was fabricated to integrate a low-pressure port fuel injector. The injector was driven by an LM1949 injector driver. Photos of the igniter adaption and combustion chamber shape are shown in Figure 4-11. The engine setup is shown in Figure 4-12.

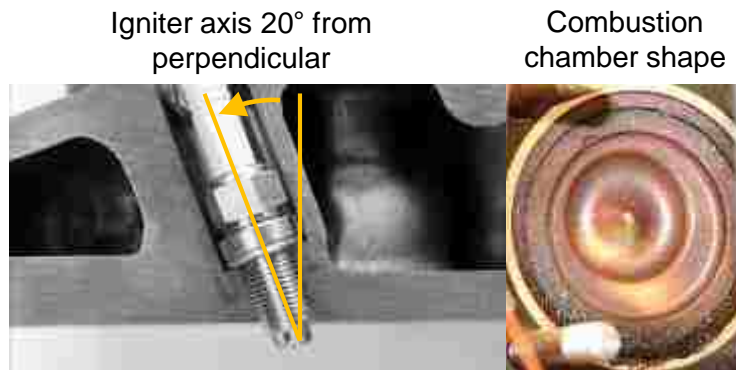


Figure 4-11: Engine Igniter Adaption and Combustion Chamber Shape

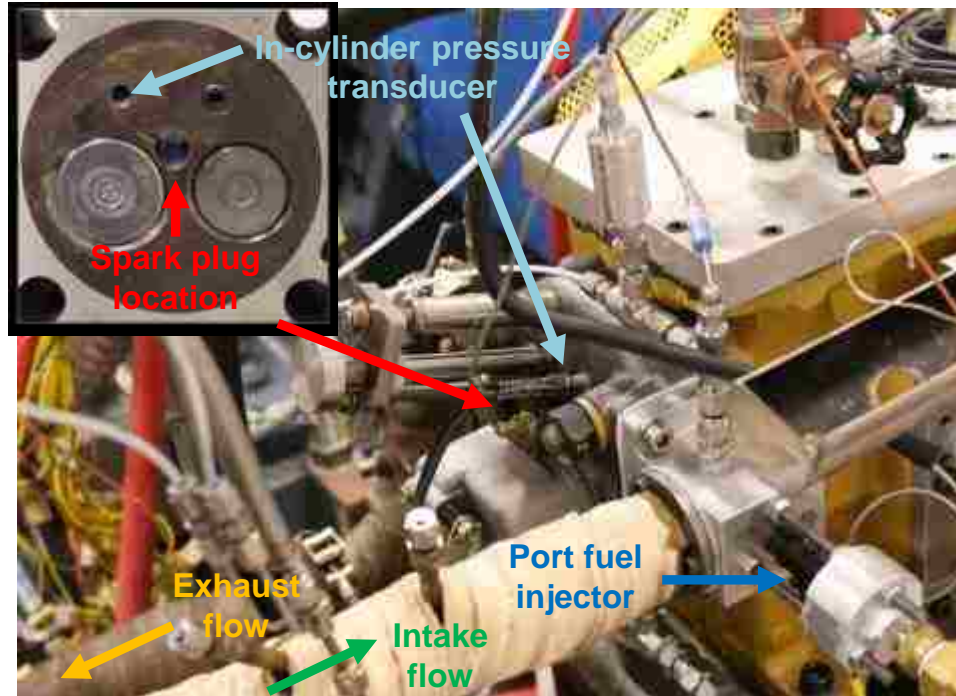


Figure 4-12: Photo of Engine Setup

Table 4-1: Engine Specifications

Research Engine	Modified Yanmar NFD-170
Engine Type	Single-cylinder, 4-stroke
Displacement [cm <sup>3</sup> ]	858
Bore x Stroke [mm]	102 × 105
Compression Ratio [-]	13.1:1
Max. Cylinder Pressure [bar]	120
Piston Bowl	Stepped omega
Port-injection System	Low-pressure rail (5 bar absolute)
Port Injector	1 × gasoline port injector

The test engine was located in a test cell equipped with a double-ended GE 26-G-215 direct-current dynamometer. A DyneSystems Dyn-Loc IV controller was utilized to control the dynamometer in speed mode. A dedicated coolant condition unit was used to control the coolant temperature throughout the experiments. Similarly, a dedicated lubricant system was used to control the engine oil temperature and pressure.

The primary high-speed control of the engine, namely the fuel injection scheduling and spark commands, was performed by a National Instruments real-time computer with field-programmable gate array resources. A desktop personal computer was used for boost and EGR control. A series of additional computers were used for the monitoring and recording of key engine parameters: temperatures, air and fuel flow rates, emissions, and the cylinder pressure. The engine crank angle position was indicated by a crank-shaft aligned rotary incremental encoder (Gurley Precision Instruments 9124S03600H5L01) at  $0.1^\circ$  resolution. The in-cylinder pressure was acquired in synchronization with the encoder. The Yanmar engine used a water-cooled Kistler 6043A60 transducer mounted into engine cylinder head. The transducer was coupled to a Kistler 5010B charge amplifier. The manifold pressure was acquired with a Kistler 4075A10 piezo-resistive absolute pressure transducer. Data recording of the pressures at each condition consisted of 200 consecutive engine cycles.

The intake air for the engine was provided by an off-engine compressor when operating under boosted conditions. The fresh intake flow rate was measured by a Roots rotary-type positive displacement air flow meter. An intake surge tank was installed downstream of the air flow meter to reduce the effects of the intermittent intake valve action on the accuracy of air-flow measurements. The Yanmar engine was primarily



operated in natural aspiration mode and inducted air from the test cell through an airbox filter upstream of the air flow meter. Control of the EGR rate was achieved by the coordinated actions of a manual EGR valve and the throttle valve. A schematic diagram of the engine layout is shown in Figure 4-13.

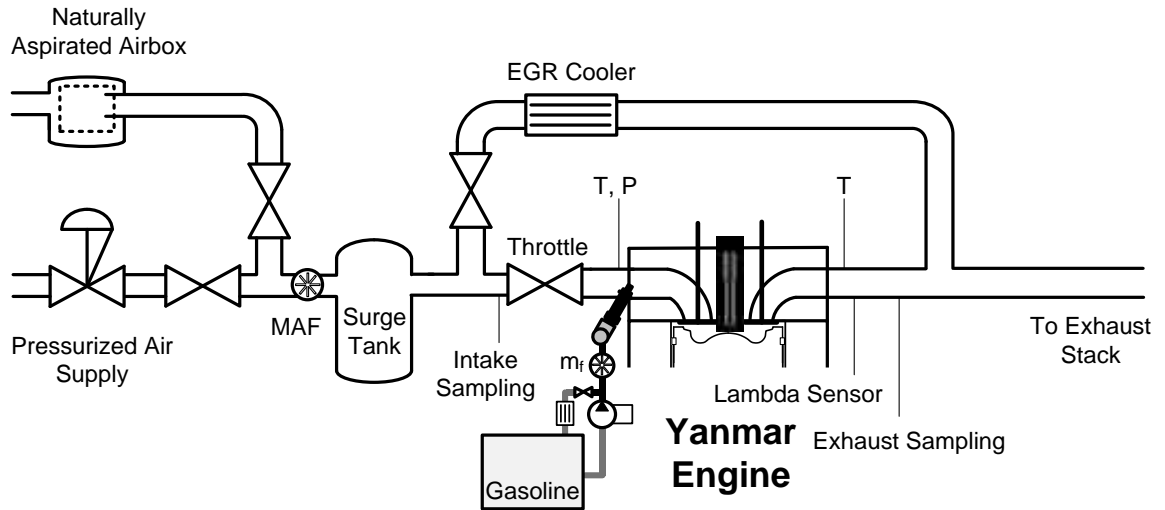


Figure 4-13: Engine Test Cell Setup

A set of exhaust emission analyzers was used to quantify the total hydrocarbons, CO, CO<sub>2</sub>, O<sub>2</sub>, NO<sub>x</sub>, and smoke level. The engine intake composition and EGR rate were quantified by using a second set of O<sub>2</sub> and CO<sub>2</sub> analyzers. The molecular hydrogen was measured with an H-Sense magnetic sector mass spectrometer from V&F Instruments, sensitive at ppm and percent levels. The soot emissions were measured using an AVL 415S smoke meter. The smoke level is nominally reported as FSN (filter smoke number). The FSN unit is related to mg/m<sup>3</sup> soot emissions by estimation using the following correlation [58]:

$$\frac{\text{mg}}{\text{m}^3} = \frac{1}{0.405} \times 4.95 \times \text{FSN} \times e^{(0.38 \times \text{FSN})}$$

A Fourier transform infrared spectrometer was used to allow speciation of the exhaust. Fourier-transform infrared spectroscopy (FTIR) uses interferometry to obtain a scan of infrared absorbencies of the sample gas. The absorption of infrared radiation at specific wavelengths is a property of the molecular composition and structure of each species. The FTIR instrument used was a MKS model 2030HS with a 5.11 metre pathlength gas cell and liquid-nitrogen cooled MCT infrared detector. The gas cell, inlet, and sample line were heated to 191° C. The scan range was configured from 600 to 3500  $\text{cm}^{-1}$  at 0.5  $\text{cm}^{-1}$  resolution and five scans per second. Averages of five scans were recorded at one sample per second.

The full equipment suite used is listed in Table 4-2. The instrument range is shown in the right-hand column where applicable. In instances where the calibrated range differed substantially from the instrument full range, the calibrated range is also listed.

The engine tests were conducted at an engine speed of 1300 RPM. The coolant and engine oil temperatures were set at 80 °C. In general, for each ignition strategy and dilution ratio condition, spark timing sweeps were conducted. This allowed comparisons of different strategies at the same ignition timing as well as comparisons of optimized points of the different strategies.

Table 4-2: Gas Analyzer Model and Measurement Range

<b>EXHAUST ANALYSIS</b>		
Oxygen	CAI 300 paramagnetic detector	0-25%
Carbon Dioxide	CAI 200 NDIR	0-40%
Carbon Monoxide	CAI 300 NDIR	0-5000 ppm
Carbon Monoxide	CAI 600 NDIR	0-10%
THC	CAI 300M HFID	0-30,000 ppm Cal: 3,010 ppm
Nitrogen Oxides	CAI 600 HCLD	0-3000 ppm
Hydrogen	V&F H-Sense mass spectrometer	0-100% Cal: 0-4000 ppm and 0-40%
Smoke	AVL 415S	0-10 FSN
Infrared Spectra	MKS 2030HS FTIR	
<b>INTAKE ANALYSIS</b>		
Oxygen	CAI 602P paramagnetic detector	0-25%
Carbon Dioxide	CAI 602P NDIR	0-10%

## **CHAPTER V**

### **EFFECT OF ENERGY AND ENERGY PROFILE ON SPARK IGNITION**

This chapter presents the results tests on the energy characterization and ignition effectiveness evaluation the conventional ignition coil system. The tests were performed both under quiescent conditions in a combustion vessel and under engine conditions. The conventional energy profiles were then modified to identify the relative impact of energy addition at different phases of the discharge process.

#### **5.1 Effect of Discharge Energy**

##### **5.1.1 Quiescent Conditions**

A set of test was carried out in the CV1 optical combustion chamber to compare the effect of discharge energy in a conventional spark ignition system as specified previously. The discharge energy was varied by changing the coil charging duration, ranging from 0.5 ms to 8 ms. The effects of the coil charging duration on the discharge energy, peak secondary current, discharge duration, and overall current profile are shown in Figure 5-1. The energy delivered to the spark plug increased as the charging duration was increased, up to a measured value of 160 mJ at 8 ms. The rate of energy increase declined at this duration as the primary coil approached current saturation. The measured energy delivered to the spark gap, however, can be significantly lower because of the losses in the spark plug resistor. This fraction of energy consumed by the resistor was less than 15% at low total energy levels, and increased to 67% at the highest energy levels.

The discharge current profile is shown for four cases, ranging from 1 ms charging duration to 8 ms charging duration. The increased primary energy has the effect of increasing the secondary current level and duration. The peak value of the discharge current increases linearly with increasing charging duration. The higher levels of secondary current serves to extend the overall duration of the discharge.

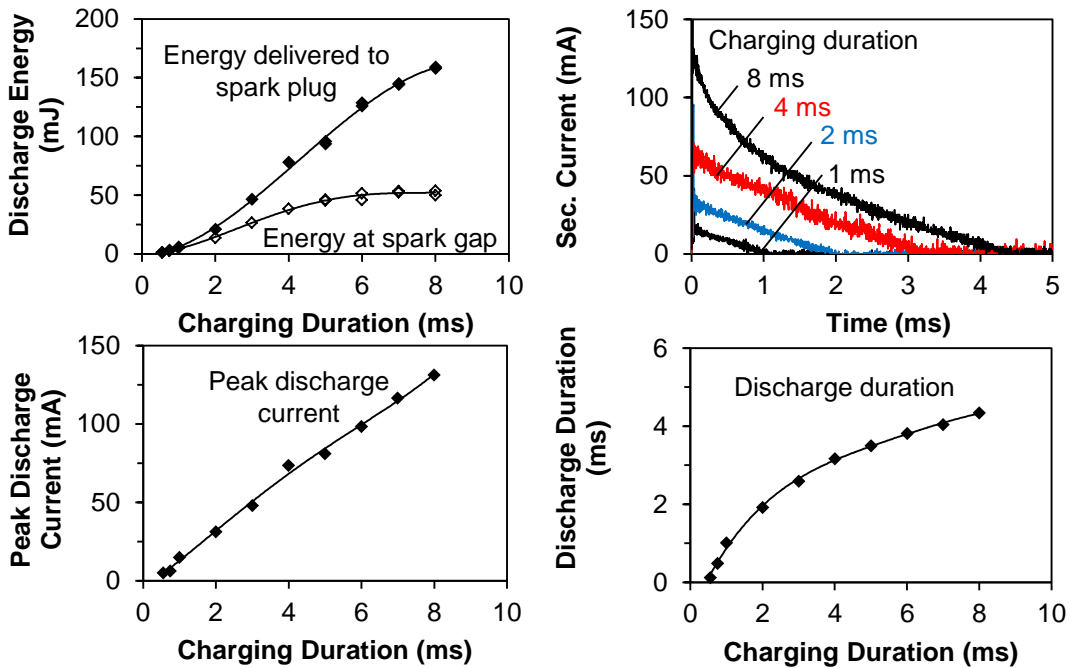


Figure 5-1: Discharge Characteristics in Conventional System at Different Energies

The extracted images from high-speed shadowgraphy video recordings of the ignition process in CV1 are shown in Figure 5-2 for stoichiometric methane-air. Four energy levels of 50 mJ, 15 mJ, 4.9 mJ, and 1.4 mJ, corresponding to charging durations of 8 ms, 2 ms, 1 ms, and 0.55 ms are shown. The lowest energy case corresponds to a misfire case where the spark discharge did not result in a successful flame kernel. In the three cases of successful ignition, the flame front trajectories were very much similar across the energy levels.

A similar set of extracted images is shown in Figure 5-3 for methane-air ignition at a lambda of 1.6. At this leaner condition, the energy threshold for successful ignition was higher and misfire was recorded at 2.9 mJ. Two major differences are apparent at this lean condition compared to the stoichiometric condition. The first difference is that the overall flame kernel growth rate is reduced significantly with the lower laminar flame velocities at lean conditions. The second difference is that the kernel growth trajectory is sensitive to the spark energy at lean conditions. The flame kernel is progressively larger at each time step with higher spark energies.

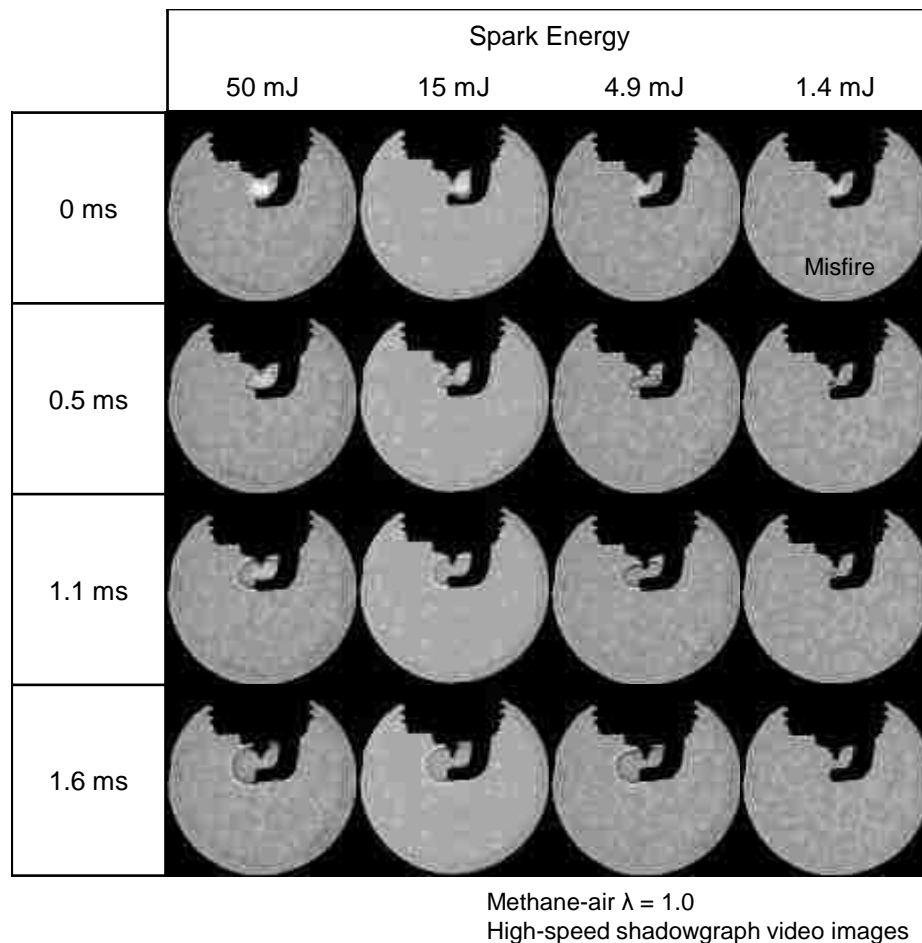


Figure 5-2: Discharge Energy Effect under Stoichiometric Conditions

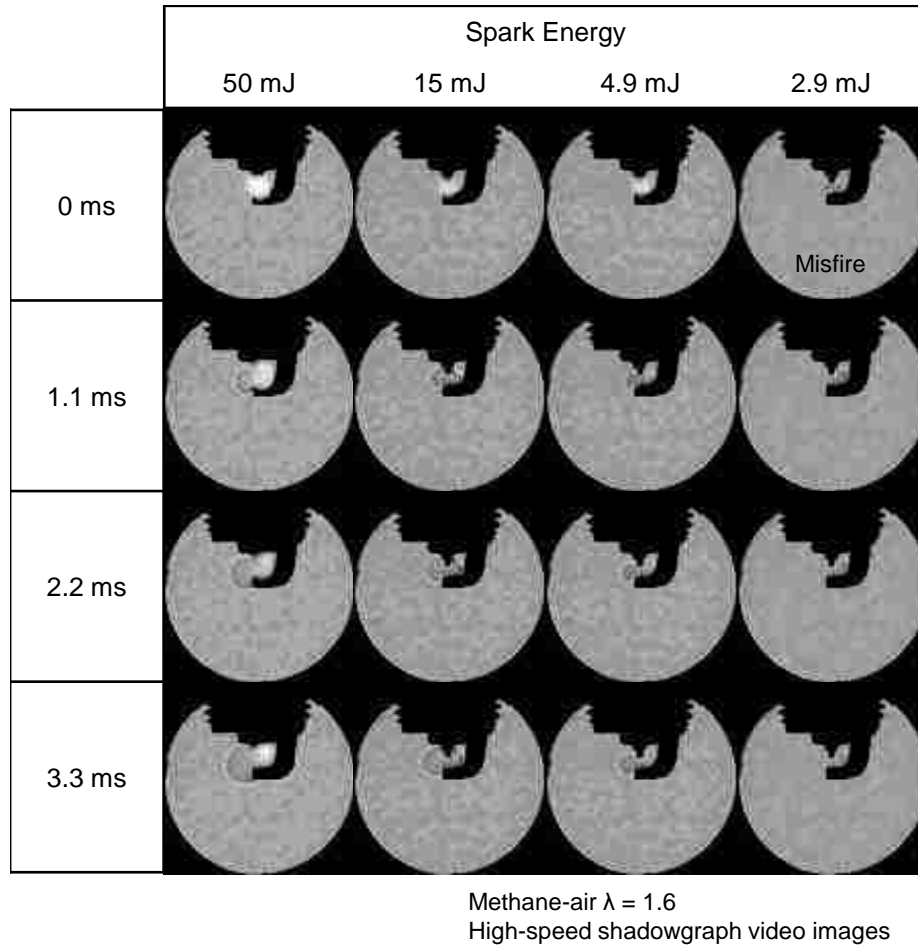


Figure 5-3: Discharge Energy Effect under Lean Conditions

The growth in the flame kernel size is shown in Figure 5-4 plotted against time for the stoichiometric case for two different levels of spark energy. The cumulative spark energy deposited is also plotted. The flame radius was calculated in the direction perpendicular to the spark plug. The flame growth histories were nearly identical in the two cases of different spark energy. The initial high growth rate decayed in the first 0.85 ms and the flame kernel assumed a constant growth rate after 0.85 milliseconds following the spark breakdown. The spark flame radius at this point was 3 mm. The lower energy spark has at this point cumulatively discharged 4.7 mJ of energy, while the higher energy spark has cumulatively discharged 18 mJ. The lower energy spark has discharged 96%

of the of the total spark energy, while the higher energy spark has discharged only 36% of the total spark energy. The power of the discharge was proportional to the slope of the energy deposition curve. The discharge power was the highest during the start of the discharge and decayed thereafter. The additional energy deposited late in the discharge phase had no impact on the flame propagation in this case where the ignition demand was low and the flame front readily propagated beyond the influence of the spark discharge under the favorable stoichiometry.

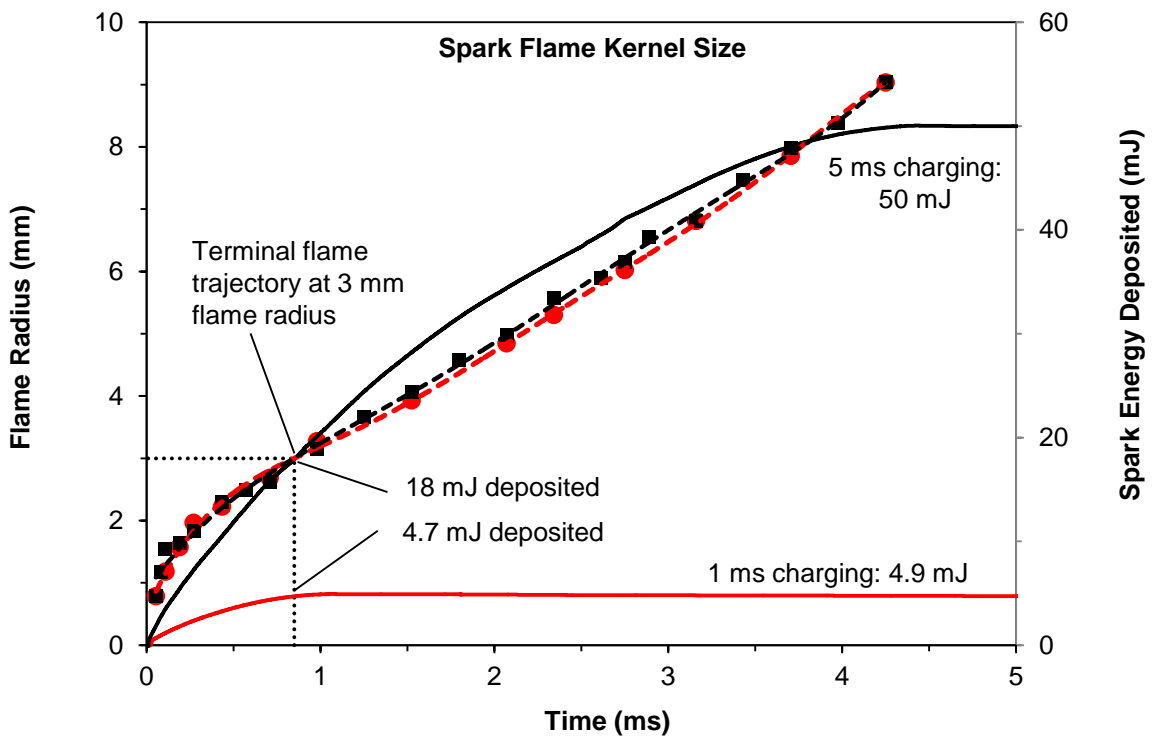


Figure 5-4: Flame Kernel Growth under Stoichiometric Case

The flame growth history in the case of lean ignition at a lambda of 1.6 is compared in Figure 5-5. The stable flame speed at the lean condition is drastically reduced from the stoichiometric case. The time required to reach the stable flame speed, however, occurs at a similar time regardless of the stoichiometry and energy level.



Where the two energy levels did not result in differing flame growth histories in the stoichiometric case, in the lean cases the higher energy level enhanced the early flame growth rate significantly. Thus, the spark energy does impact the flame growth rate under conditions where the fundamental flame speeds are reduced.

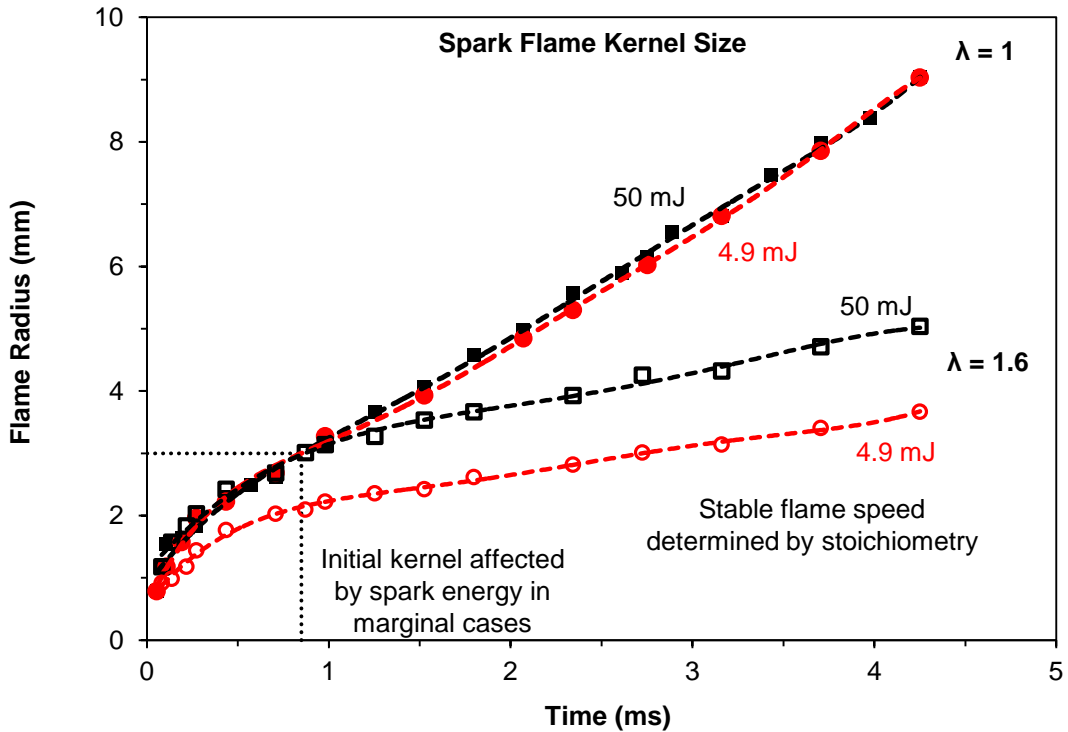


Figure 5-5: Flame Kernel Growth under Lean Ignition Cases

The ignition energy demand for methane-air was low at stoichiometric and moderately lean conditions. Relatively low spark energies of 4.9 mJ was sufficient to ignite the charge. The ignition demands at leaner conditions were examined in a series of ignition success rate tests. Figure 5-6 shows the ignition success rates of three different spark energy levels up to lambda 1.9. The comparison revealed that spark energy was a factor in ignition success at the lean conditions. At a baseline spark energy of 10 mJ, the ignition success rate decayed from 100% at lambda 1.6 to nearly always misfire at

lambda 1.8. Increasing the spark energy to 30 mJ and then 50 mJ progressively increased the ignition success rate. The difference in ignitability between 10 mJ and 50 mJ was approximately 0.1 lambda.

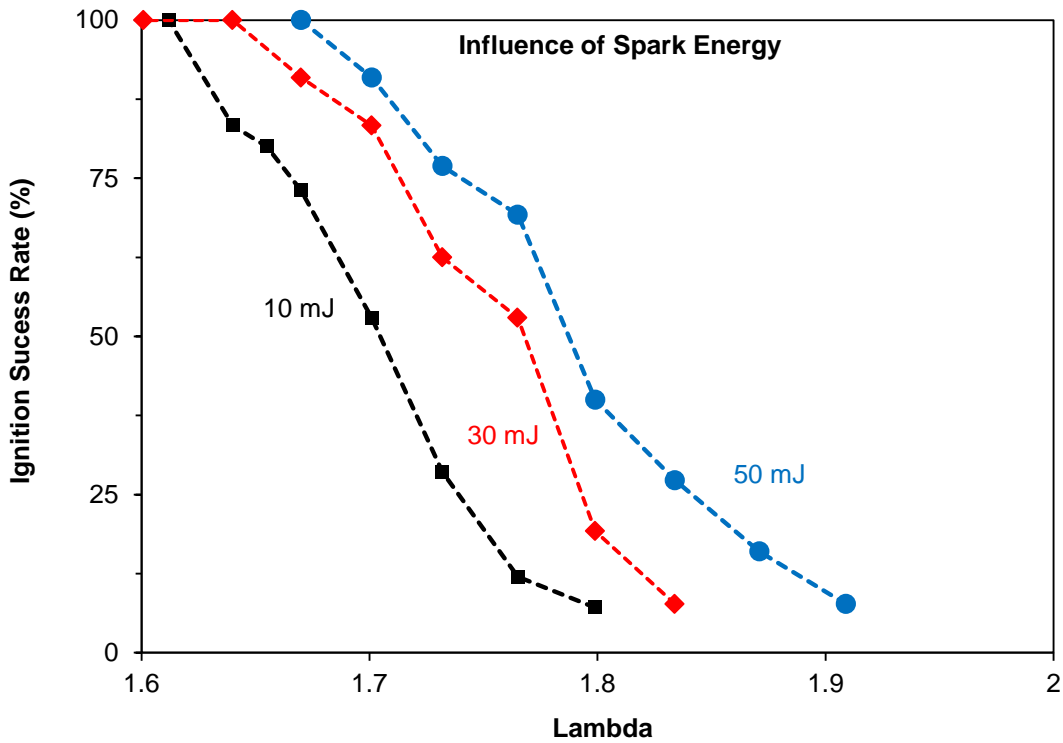


Figure 5-6: Effect of Energy on Ignition Success Rate under Quiescent Conditions

### 5.1.2 Flow Conditions

In the engine environment, the spark is exposed to air flow, which would impact the spark energy delivery and ignition characteristics. Figure 5-7 illustrates a comparison of the flow velocity effect on a spark discharge in air under ambient pressure. The cases shown range from quiescent to 40 m/s. At the quiescent condition, the spark voltage remained largely constant throughout the discharge. With flow, the discharge channel was deflected and progressively stretched. The stretching increased the resistance of the spark channel and a higher discharge voltage was observed. The discharge power was

consequently higher, and led to a faster depletion rate of the coil energy and shorter discharge duration. The shorter discharge duration also resulted in a slight increase in the measured overall spark energy. When the spark was overly stretched and could not be sustained, restrikes occurred to reduce the path-length of the discharge.

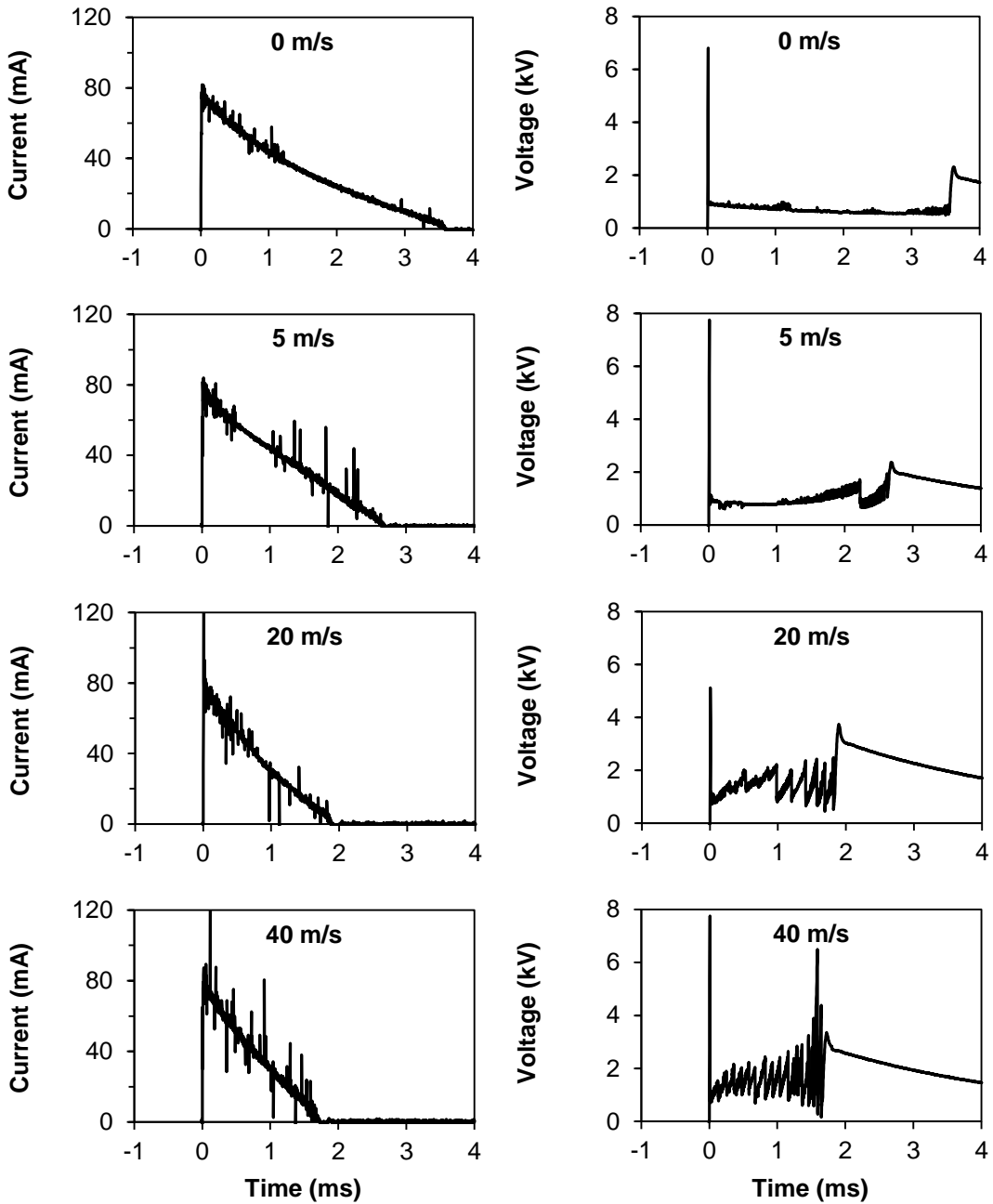


Figure 5-7: Effect of Cross-flow Velocity on Discharge Characteristics

An examination of the spark stretching is shown in Figure 5-8 for the case of 20 m/s flow velocity. From the spark breakdown to 0.3 ms following the breakdown, the spark channel was progressively stretched by the air flow from the left of the image. At 0.3 ms, a slightly reduced discharge path was established, and resulted in a reduction in discharge voltage. Nine more restrike events occurred prior to the end of the discharge after 1.8 ms, ranging from large changes in path-length, for example at restrike event E, to small changes in the path-length, for instance at event C marked in the figure.

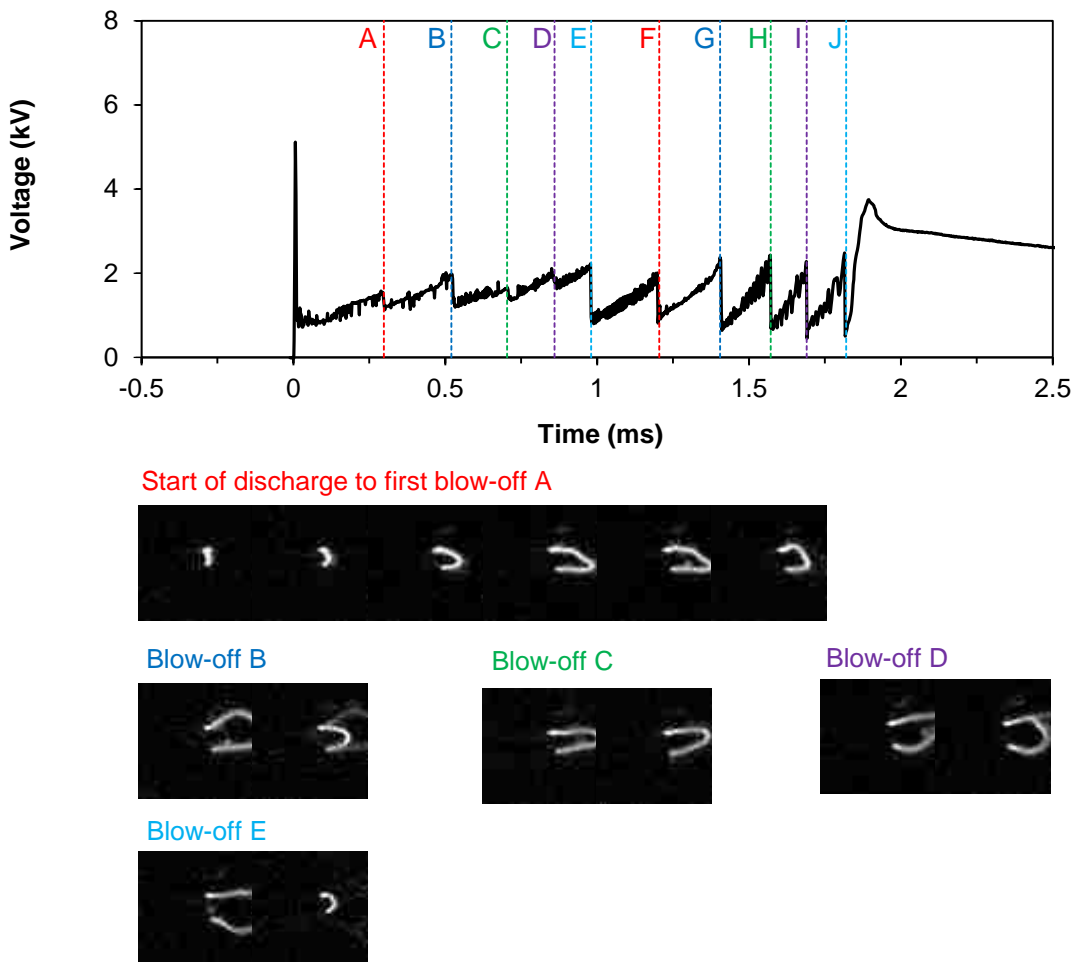


Figure 5-8: Restrike Behavior Under Air Flow

The maximum spark channel length prior to a restrike was not observed to be sensitive to flow velocity, but was sensitive to the discharge current level. With a coil charging duration of 5 ms, the average maximum stretched spark channel length was 8.1 times the geometric minimum gap length. When the coil charging duration was reduced to 3 ms, the average maximum stretched spark channel length was 6.8 times the geometric minimum gap length. The increased energy available with higher charging durations was potentially beneficial when the spark gap was under flow conditions in order to maintain longer spark holding periods and larger stretched gap sizes.

The flow and restrike events impact the ignition process in several ways. Flow can transport the flame kernel away from the vicinity of the spark plug and reduce the heat-loss of the flame kernel to the spark plug electrodes. Stretching of the spark channel increases the volume of the gas in contact with the discharge and can lead to a larger flame kernel. However, the stretching is limited by the ability to sustain the elongated discharge path. When the flow velocity is excessively high and the restrikes occur with high frequency, the individual restrikes may not lead to any successful ignition events.

### **5.1.3 Engine Conditions**

Several tests were conducted to characterize the effect of spark energy on the ignition behavior in fired engine tests. The tests were performed on the Yanmar engine described in Chapter 4. The tests were conducted at 1300 RPM engine speed and low engine load. The effect of engine intake charge dilution was additionally examined by testing at different lambda values.

The engine environment is significantly different from the quiescent chamber conditions in several ways. Besides the effect of charge motion, the temperature and

pressure conditions at the time of ignition influence the spark discharge and the flame propagation processes. The measured average spark gap breakdown voltage is shown in Figure 5-9 for examples of typical throttled and unthrottled operation of the Yanmar engine. During the compression stroke, the pressure and temperature of the in-cylinder charge increases significantly. Thus the breakdown voltage is influenced by the charge thermodynamic conditions in addition to the spark gap size and geometry. Under the testing conditions, the spark timing for optimal efficiency at stoichiometric condition for the throttled case is in the 340 – 345 CAD range and the spark breakdown voltage is in the 8 kV range. Advancing the spark timing results in decreased breakdown voltage as a result of the lower in-cylinder pressure at the time of breakdown. When the throttling restriction on the engine is reduced to the wide-open-throttle (WOT) condition, the breakdown voltage is consequently significantly higher. Thus in diluted charge combustion, increasing dilution typically requires more advanced spark timing, which lowers the breakdown voltage. The increased in-cylinder pressure from the dilution will partially compensate this effect by increasing the breakdown voltage demand.

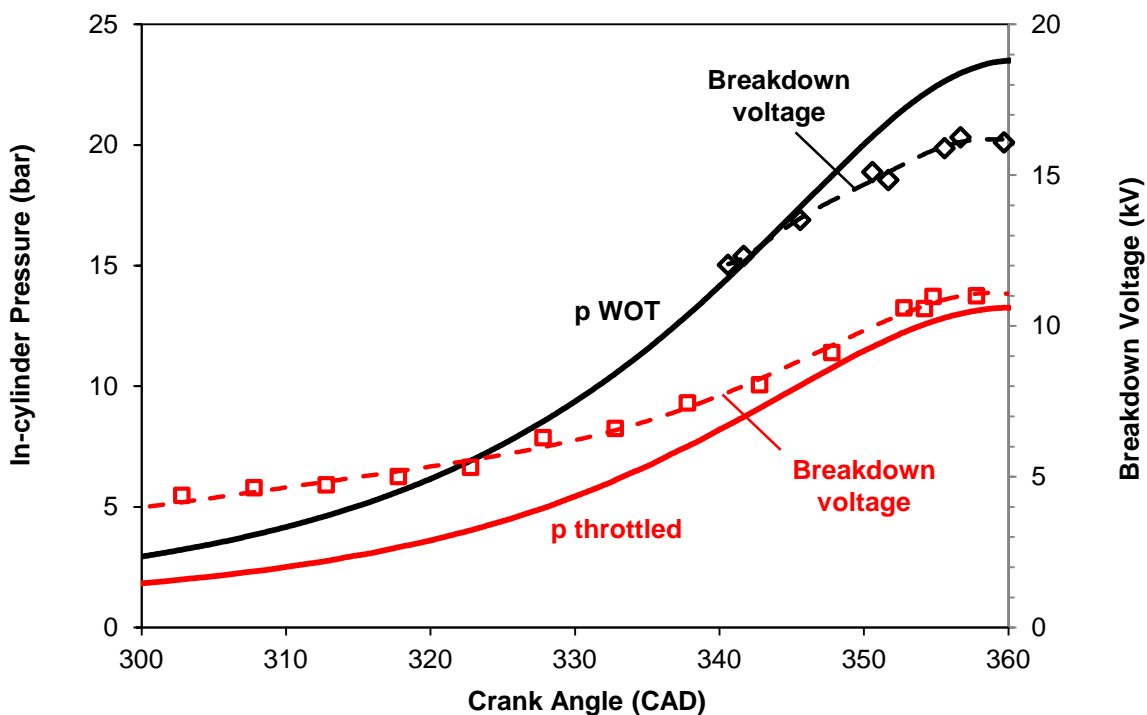


Figure 5-9: Spark Breakdown Voltage at Various Spark Timings

The breakdown voltages above are replotted in Figure 5-10 to show the direct relationship between breakdown voltage and gas density. The breakdown voltages are nearly linear with respect to the in-cylinder gas density. When compared to a measurement of the breakdown voltages in a constant volume chamber with air at ambient temperature, the in-cylinder breakdown voltages are generally only slightly lower, as expected under higher temperatures. The temperature has a relatively minor influence on the breakdown voltage within the relevant conditions.

The breakdown voltage has an impact on the initial discharge due to the capacitive behavior of the spark plug. However, this effect of the small capacitance (~10 – 15 pF) of the spark plug is one aspect of the discharge that is hard to isolate in the experiments. The relative fraction of the discharge energy stored in the capacitance of

the spark plug is small relative to the total discharge energy. However, the energy is released very early in the discharge process, which can have more impact on the ignition [59].

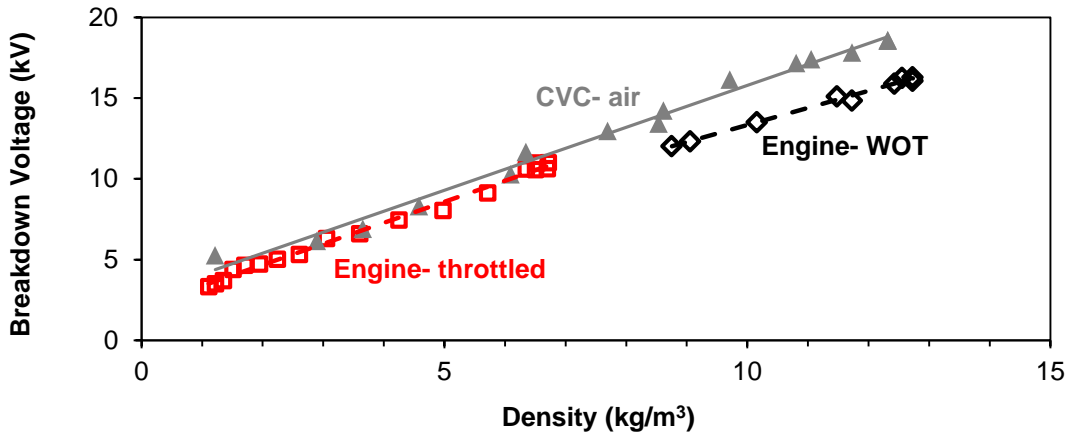


Figure 5-10: Spark Breakdown Voltage as a Function of Gas Density

While the variation of in-cylinder temperature with respect to spark timing has a relatively small impact on the breakdown voltage, its effect on the flame chemistry is significant. The laminar flame speed of stoichiometric methane-air is computed according to the procedure outlined in Appendix C and shown in Figure 5-11. The laminar flame speed reduces under higher pressure, but increases at higher temperatures. Under the engine compression conditions, the temperature effect is dominant and the laminar flame speed is highest at the engine top-dead centre. While the laminar flame speed cannot be taken as a direct indicator of the flame kernel expansion rate, it serves as a qualitative measure of the influence of spark timing on the fundamental flame propagation speed. Thus when compensating for slower combustion rates by advancement of the spark timing, the initial flame kernel growth is negatively affected by the lower temperature at the time of ignition.



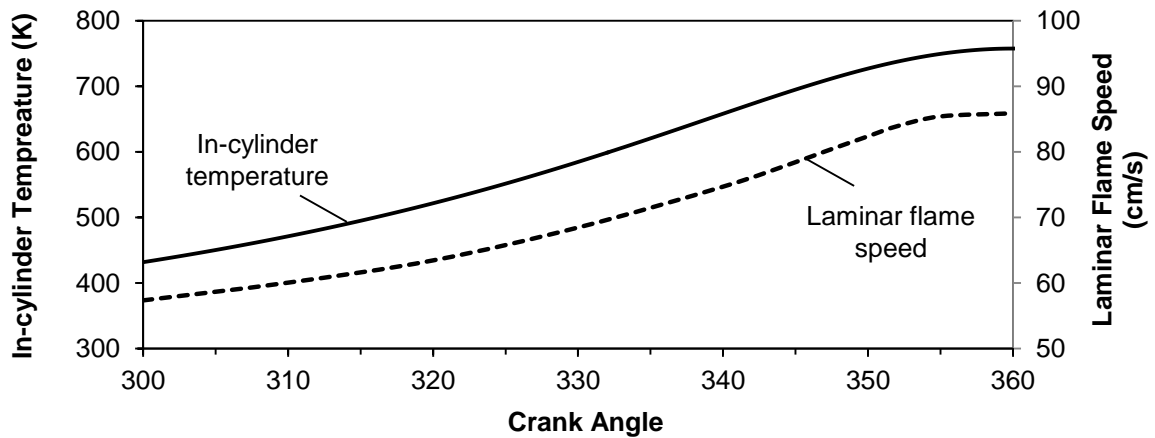


Figure 5-11: Calculated In-Cylinder Temperature and Laminar Flame Speed

The effect of spark energy level on the ignition and combustion behavior is illustrated in Figure 5-12 for a case of spark timing sweep at lambda 1.1, slightly lean of the stoichiometric condition. A longer charging duration of 5 ms resulting in 52 mJ of spark energy is compared to a short 0.8 ms charging duration resulting in 9 mJ of spark energy. The IMEP of the engine exhibited a maxima at which the highest engine efficiency was achieved at a particular spark timing. Delaying the spark timing from this optimal point led to loss of thermal efficiency through late combustion phasing. The combustion phasing of the two cases differed in both the CA5 and CA50 parameters. The difference was approximately 1.5 degrees in the CA5 and CA50 timing. This difference is apparent in the average pressure and mass fraction burned plots of two different energy levels at the same spark timing of 341 CAD, as shown in Figure 5-13.

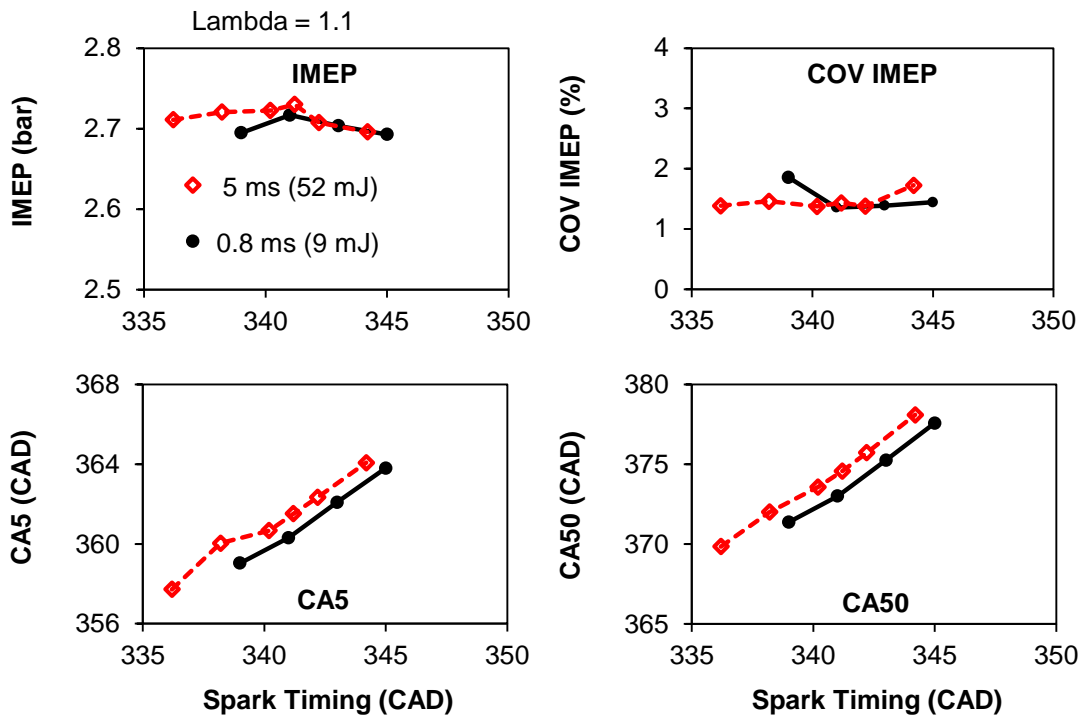


Figure 5-12: Effect of Spark Energy on Engine Operation

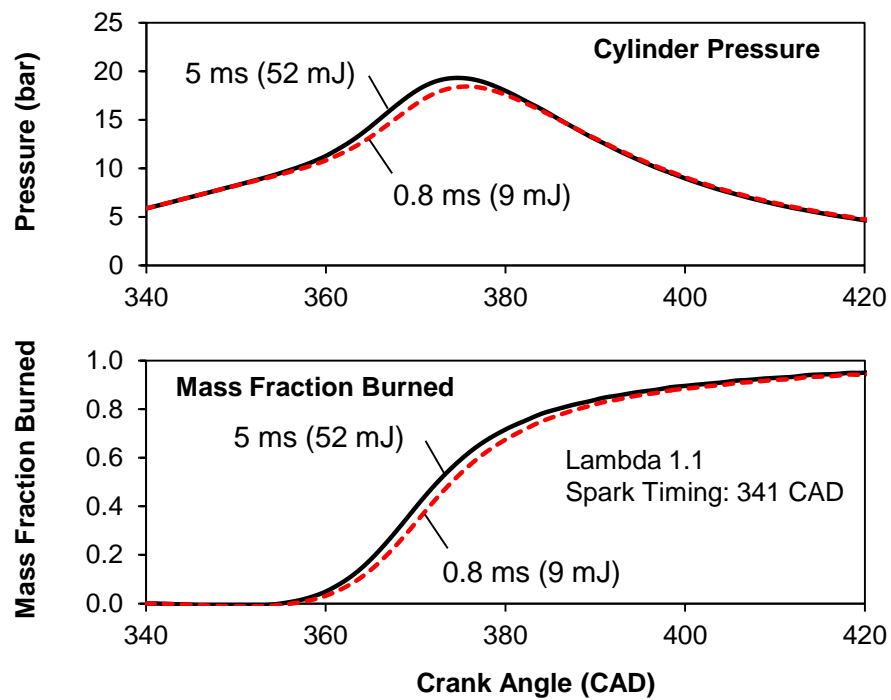


Figure 5-13: Comparison of Spark Energy

While there was a measurable difference in the engine performance between the high energy and low energy cases at lambda 1.1 for the same spark timing, from the overall control perspective the difference could be compensated by a small change in spark timing. An examination of a case at lambda 1.6 will show that under higher dilution the effect of spark energy is more critical.

Figure 5-14 shows a similar sweep of spark timing and spark energy level at a leaner condition of lambda 1.55. The two higher cases of spark energy at 5 ms (52 mJ) and 2.6 ms (30 mJ) charging durations achieved adequate ignition control. The difference in combustion phasing, however, was much more pronounced. There was a notable difference in combustion phasing of 1.3 degrees difference in CA5 and 1.8 degrees difference in CA50. When the spark energy was lowered to 1.5 ms (18 mJ) charging duration, however, the combustion stability suffered drastically and the engine experienced misfires at early spark timings. When the spark timing was delayed, the stability was improved and only 1% of cycles misfired at spark timing of 312 CAD, compared to 6% of the cycles at 307 CAD. However, the reduced flame kernel growth rate at this low energy level resulted in late combustion phasing, which negatively impacted the engine efficiency.

The average pressure and mass fraction burned traces of the three spark energy levels at a spark timing of 309 CAD are shown in Figure 5-15. The slower early flame combustion rate is apparent in the long period between the spark timing and measurable positive heat-release. The impact of the energy at this condition is to increase the early flame growth.

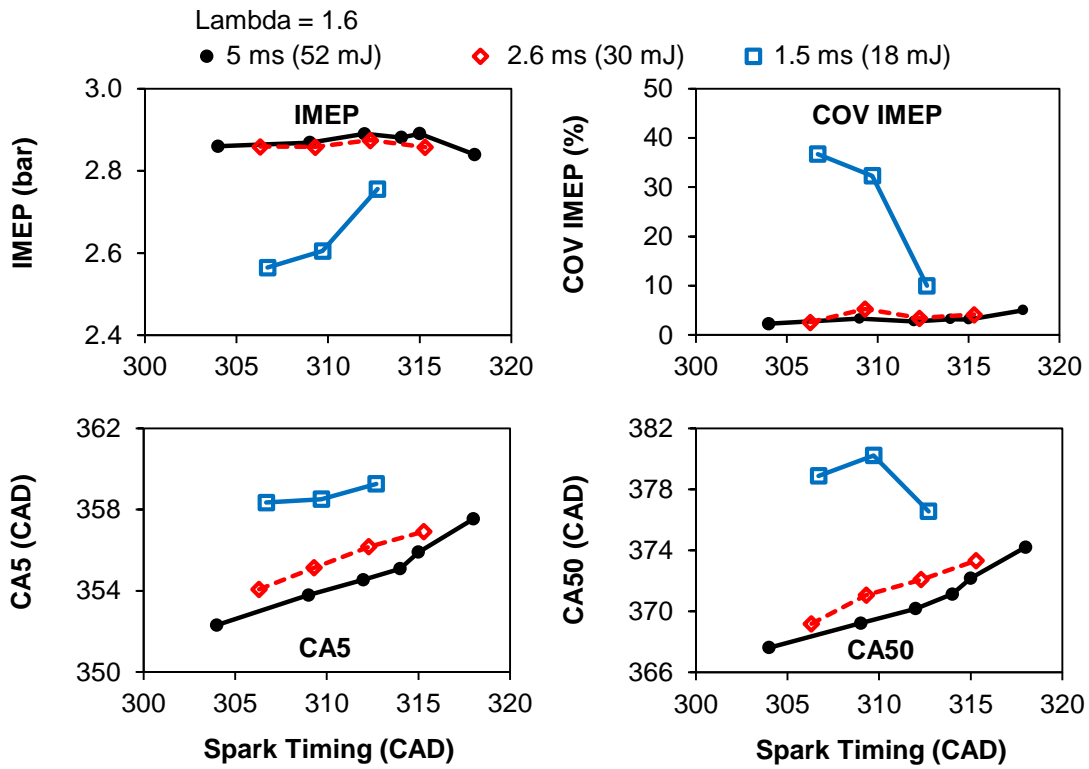


Figure 5-14: Effect of Spark Energy at Lean Conditions

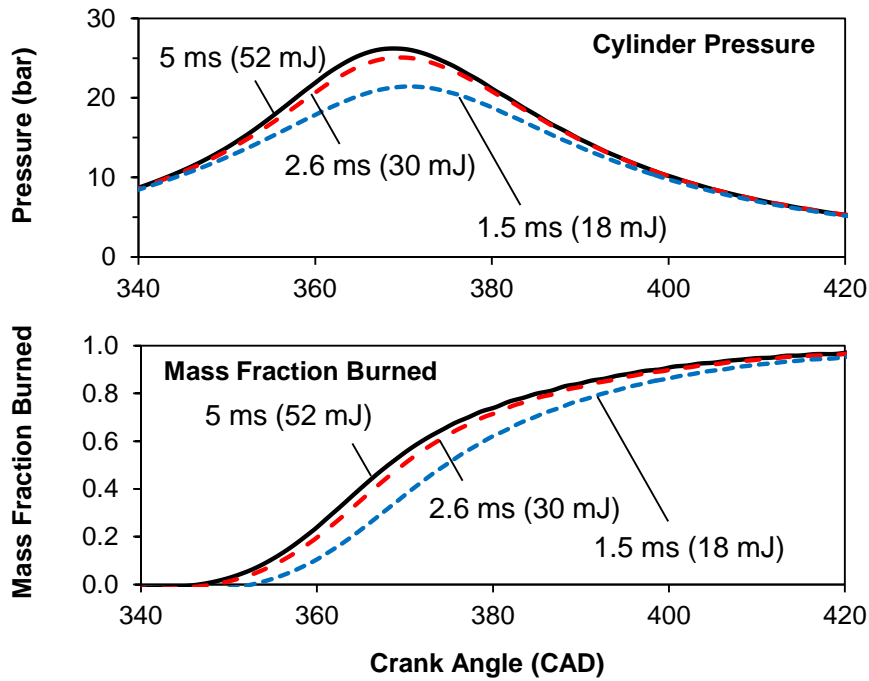


Figure 5-15: Comparison of Spark Energy at Lean Conditions

The impact of the energy up the applicable lean limit is summarized in Figure 5-16. At the tested condition, the sensitivity to energy level is low up to lambda 1.5. At lambda 1.7, the full coil output is no longer sufficient to maintain the engine stability as the combustion duration prolongs and partial misfires occurs.

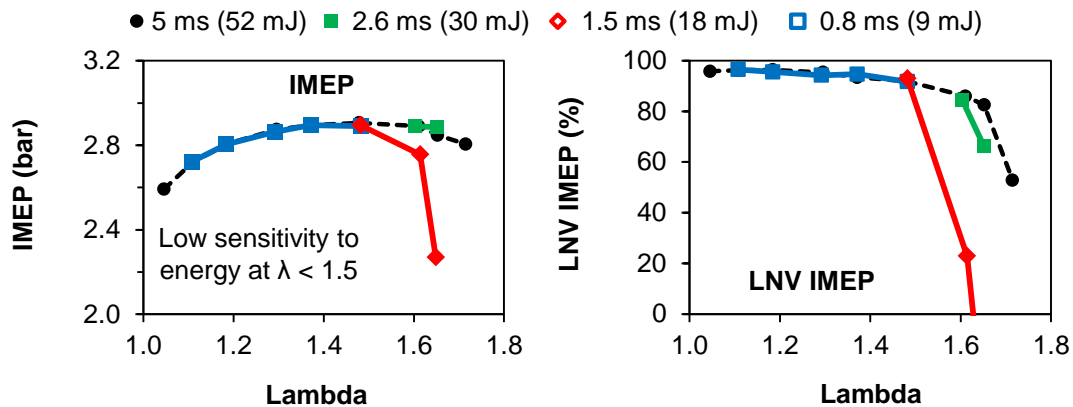


Figure 5-16: Effect of Spark Energy up to Lean Limit

## 5.2 Energy Profile Strategies

A number of strategies to improve the ignition performance were examined to extend the ability of the engine to operate at higher dilution limits. These strategies include multi-coil ignition and capacitor discharge ignition. Additionally, a pre-chamber igniter was tested to examine the effect of a partially enclosed ignition volume.

### 5.2.1 Multi-coil Ignition

A multi-coil ignition system was built to provide additional control over the spark ignition process. The ignition energy could be raised with the multi-coil system. In addition, the discharge mode could in practice be controlled to generate different discharge profiles such as higher current discharge, longer duration discharge, or multi-event spark discharge.

The multi-coil strategy was implemented by setting up three ignition coils in parallel with the secondary output directed to the same spark plug. The discharge current profiles for single and triple coil discharge modes are shown in Figure 5-17 for charging durations of 1.6, 2.0, 2.6, and 3.8 ms. The discharge current was increased over a single coil, typically doubling with the use of three coils. The total discharge durations were comparable, except for the 1.6 ms charging duration case, where the triple coils produced a discharge 73% longer than the baseline. When multiple coils were coupled together, the energy efficiency of the discharge was typically reduced [60]. The discharge energy, peak discharge current, and discharge durations parameters are shown in Figure 5-18.

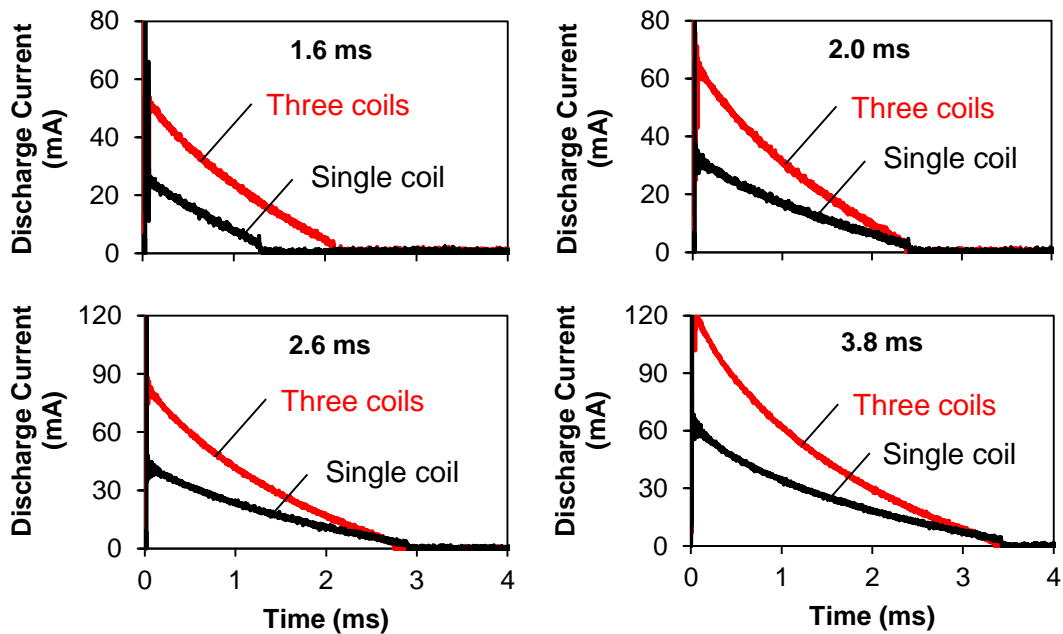


Figure 5-17: Current Enhancement with Multi-coil Discharge

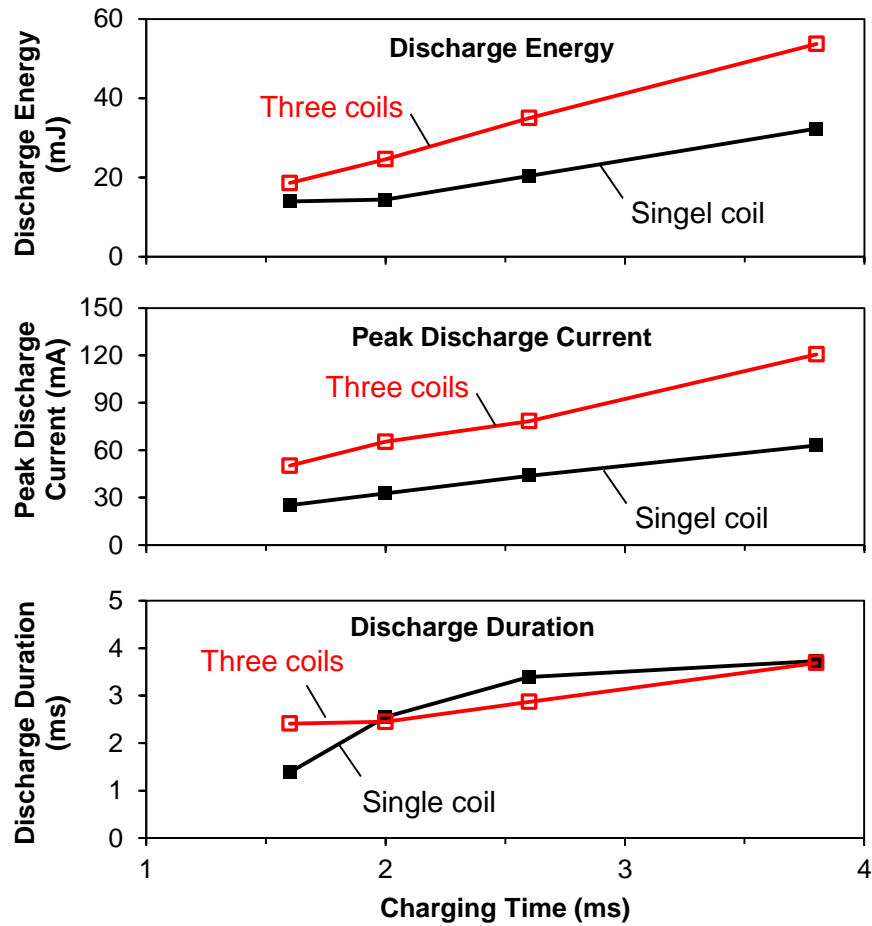


Figure 5-18: Discharge Parameters of Multi-coil Strategy

Engine tests were carried out to investigate the effect of the multi-coil strategy at a nominal load of 3.4 bar IMEP and lambda 1.5. The engine performance in response to the spark timing sweeps is shown in Figure 5-19. The baseline case of a single coil charged to 3.8 ms is compared to triple-coil tests with charging durations of 2.0, 2.6, and 3.8 ms. The single-coil 3.8 ms case has comparable energy as the triple-coil 2.0 ms case, with the difference being that the triple-coil case delivering the energy with higher current and shorter overall discharge duration. Longer charging durations in the triple-

coil configuration increase both the overall energy and discharge current compared to the baseline.

The results show the triple-coil 2.0 ms case resulted in higher coefficient of variation of IMEP and later combustion phasing, indicating poorer ignition performance compared to the baseline single-coil 3.8 ms case. When the charging duration was increased to 2.6 ms, the multi-coil performance exceeded that of the baseline. At the highest charging-duration tested of 3.8 ms, the multi-coil showed a more advanced CA50 of 5 to 10 CAD throughout the spark sweep.

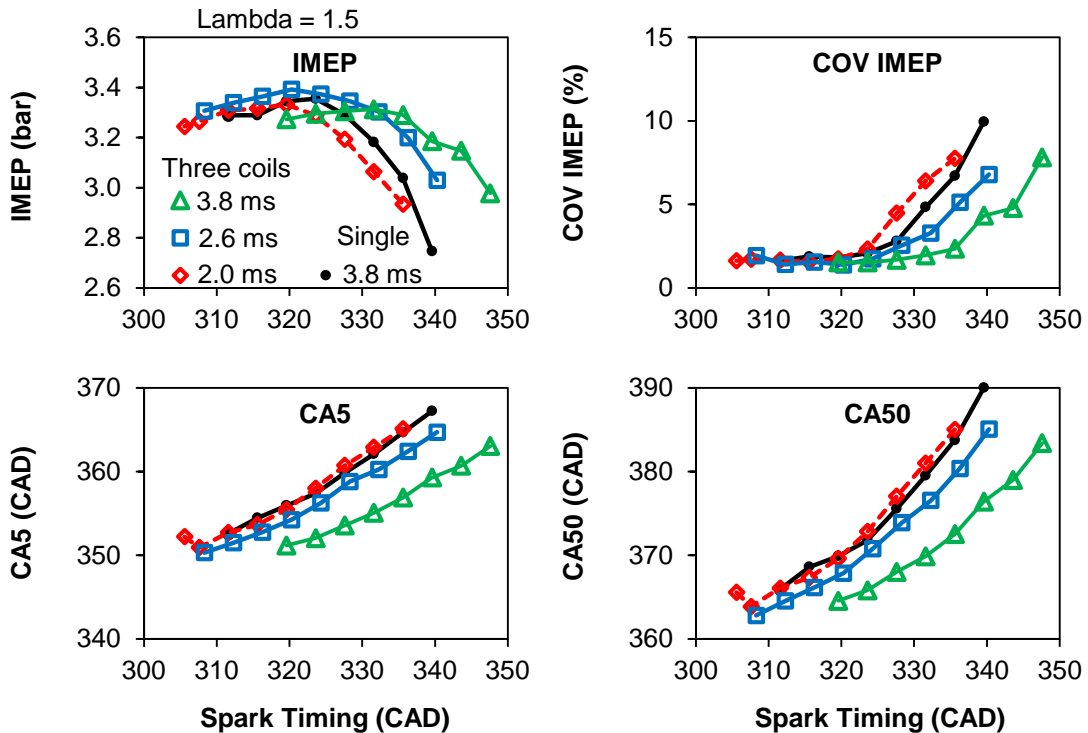


Figure 5-19: Multi-coil Ignition Effect

The pressure and mass fraction burned traces for the single coil and multi-coil comparisons at a comparable spark timing of 324 CAD are shown in Figure 5-20. The combustion phasing is progressively advanced by the increase of the charging duration.



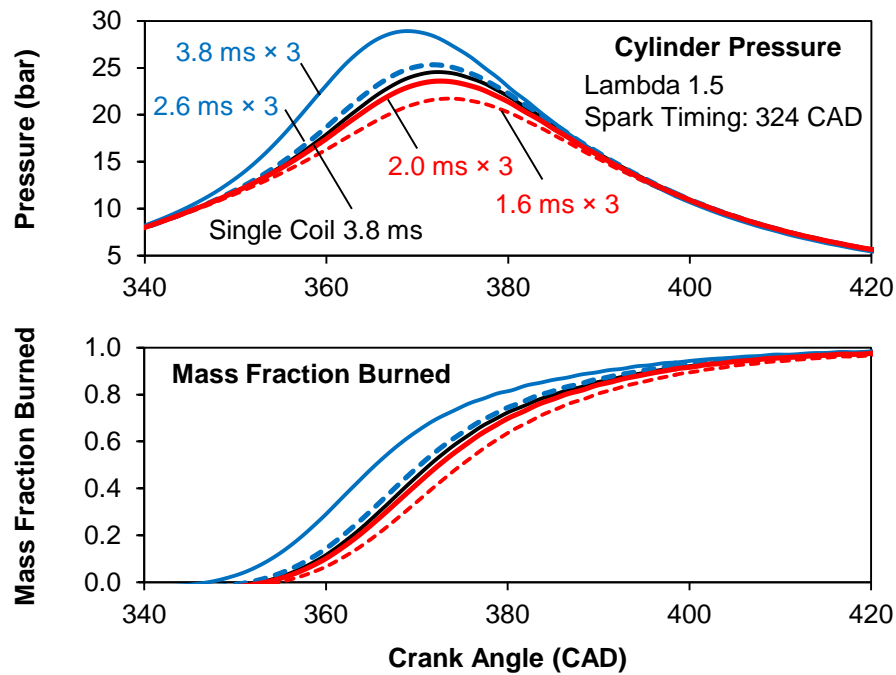


Figure 5-20: Single Coil vs Multi-coil Ignition

The stability characteristics of the strategies are examined in more detail in the following scatter plots of the CA50 versus CA5 and IMEP versus CA50 for 200 engine cycles. Figure 5-21 shows that the CA5 and CA50 are generally well correlated with each other, highlighting the generally linear process of the flame propagation. At a constant spark timing of 324 CAD, the 1.6 ms multi-coil case exhibited later combustion and more variations in combustion phasing than the baseline single coil case. The increase of charging duration to 2.6 ms and 3.8 ms improved the ignition performance from the baseline case. It is shown in Figure 5-22 that the IMEP performance was minimally impacted by variations in the CA50 up to a value as late as approximately 372 CAD. Beyond this value, the efficiency started to decrease. The reduction of the number of late combustion cycles with the appropriate ignition strategy can be realized with the appropriate ignition strategy to avoid the associated efficiency penalty.

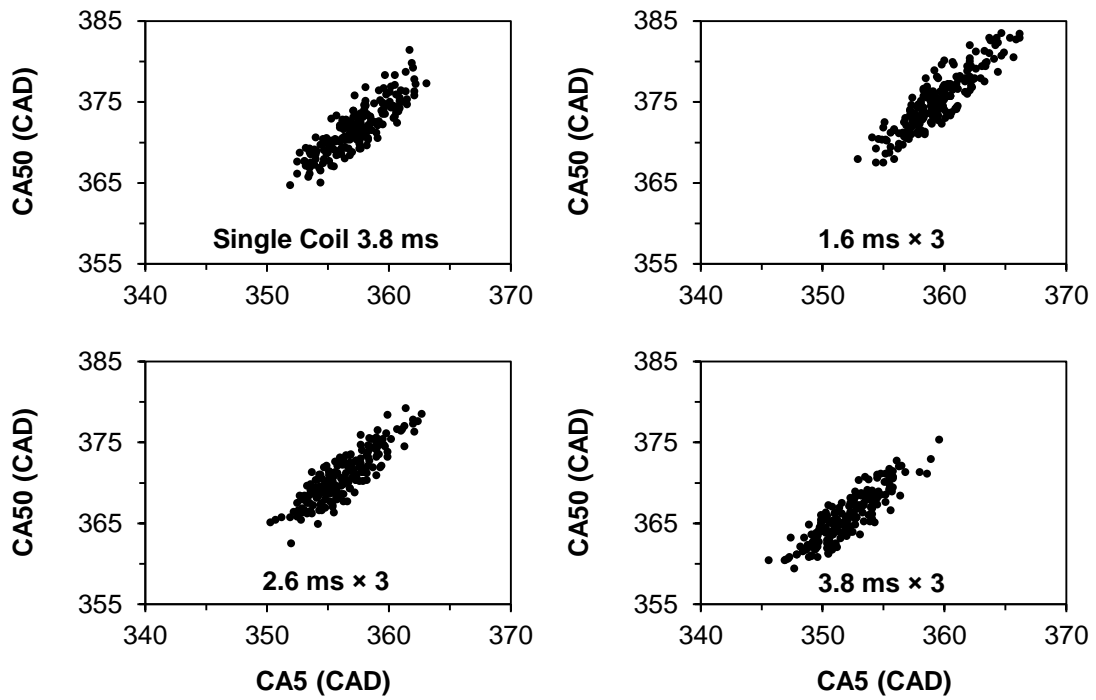


Figure 5-21: Combustion Phasing Stability Scatter Plot

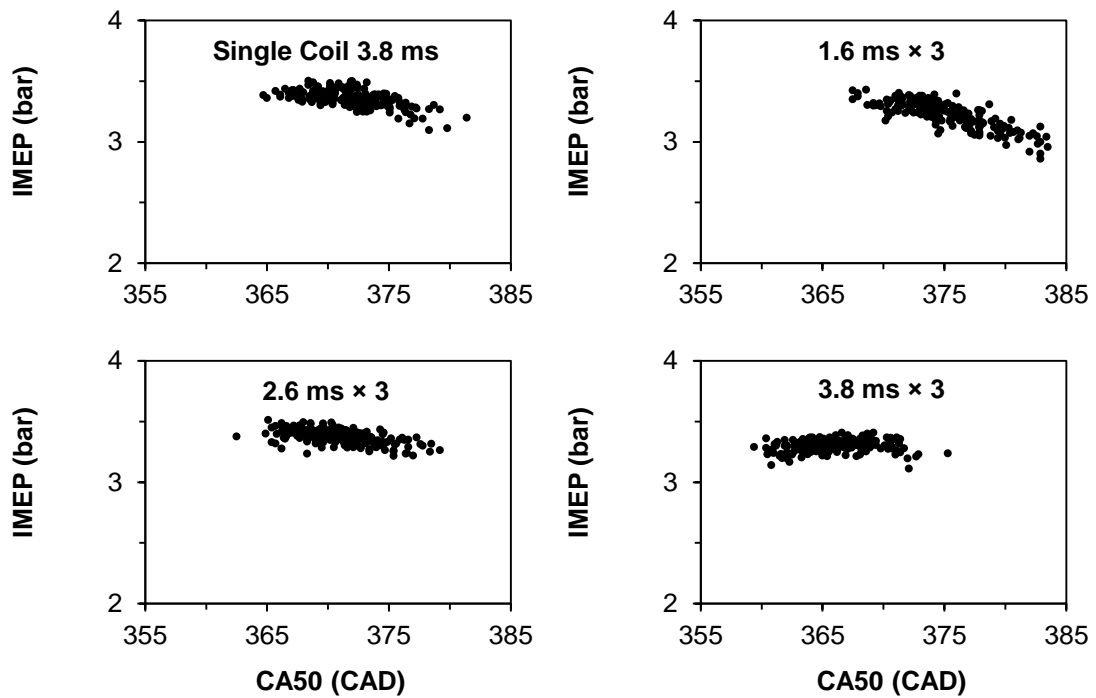


Figure 5-22: Load Stability Scatter Plot

### 5.2.2 Capacitor Discharge

The capacitor coupled ignition system can boost the spark discharge power or energy significantly compared to the conventional inductive system. Two different implementations were used. The capacitor high energy ignition utilizes a relatively large capacitor charged by an external power supply. The charging voltage is lower than the breakdown voltage, but higher than the discharge sustainment voltage. A 2  $\mu\text{F}$  capacitor charged to 575 V was used in this setup. This stored a nominal 330 mJ of energy. The capacitor energy is released over a duration of approximately 20  $\mu\text{s}$  at the beginning of the discharge. The schematic and the electrical waveform recording of this discharge strategy are shown in Figure 5-23. The second implementation, the high power capacitor discharge, uses a small parallel high-voltage capacitor charged directly by the high voltage of the ignition coil. The total energy of this high power capacitor is low, but the stored energy is delivered early in the discharge following the breakdown event, over the course of approximately 0.5  $\mu\text{s}$ . The total discharge energy is not increased by the use of the high power capacitor. The tests coupled 50 pF and 100 pF additional capacitances at the terminal of the spark plug. The schematic and the electrical waveform recording of this discharge strategy are shown in Figure 5-24. A comparison of the differences in discharge power over the first two microseconds of discharge is shown in Figure 5-25. To reduce the resistive losses inside the spark plug, the non-resistive commercial spark plug was used to implement the capacitor discharge methods.

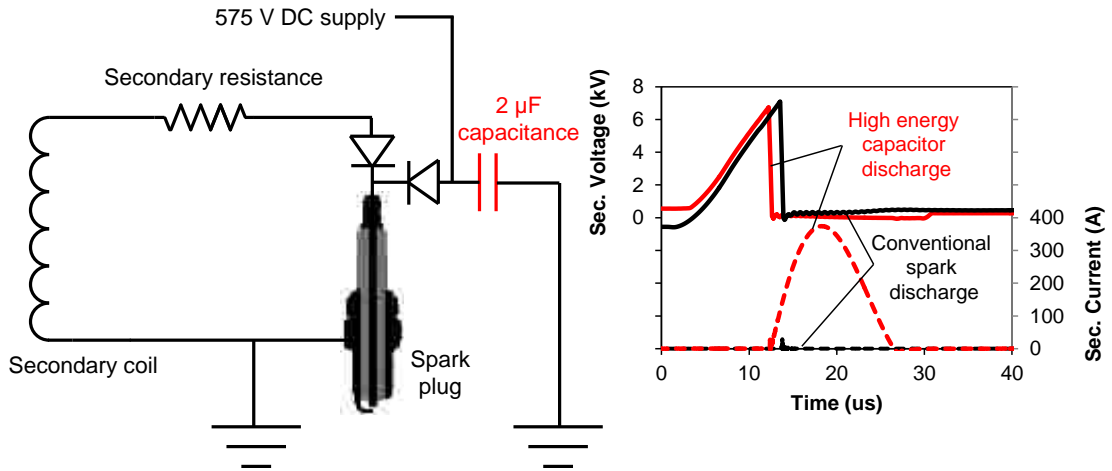


Figure 5-23: High Energy Capacitor Discharge Configuration

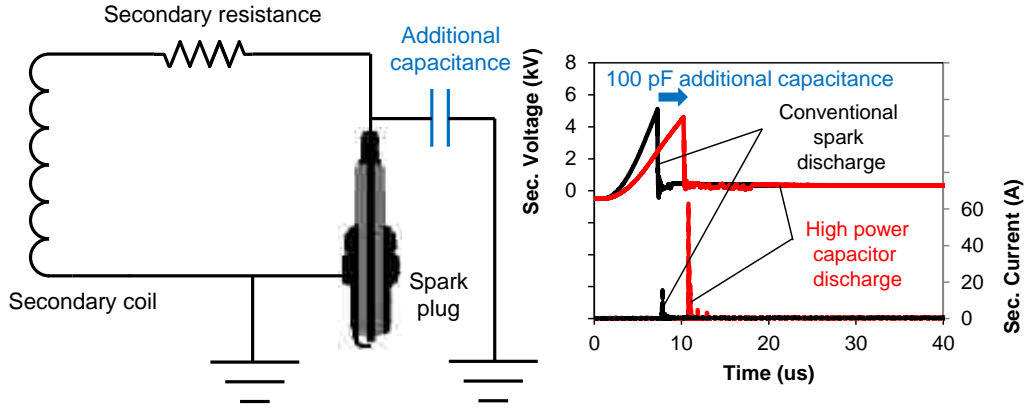


Figure 5-24: High Power Capacitor Discharge Configuration

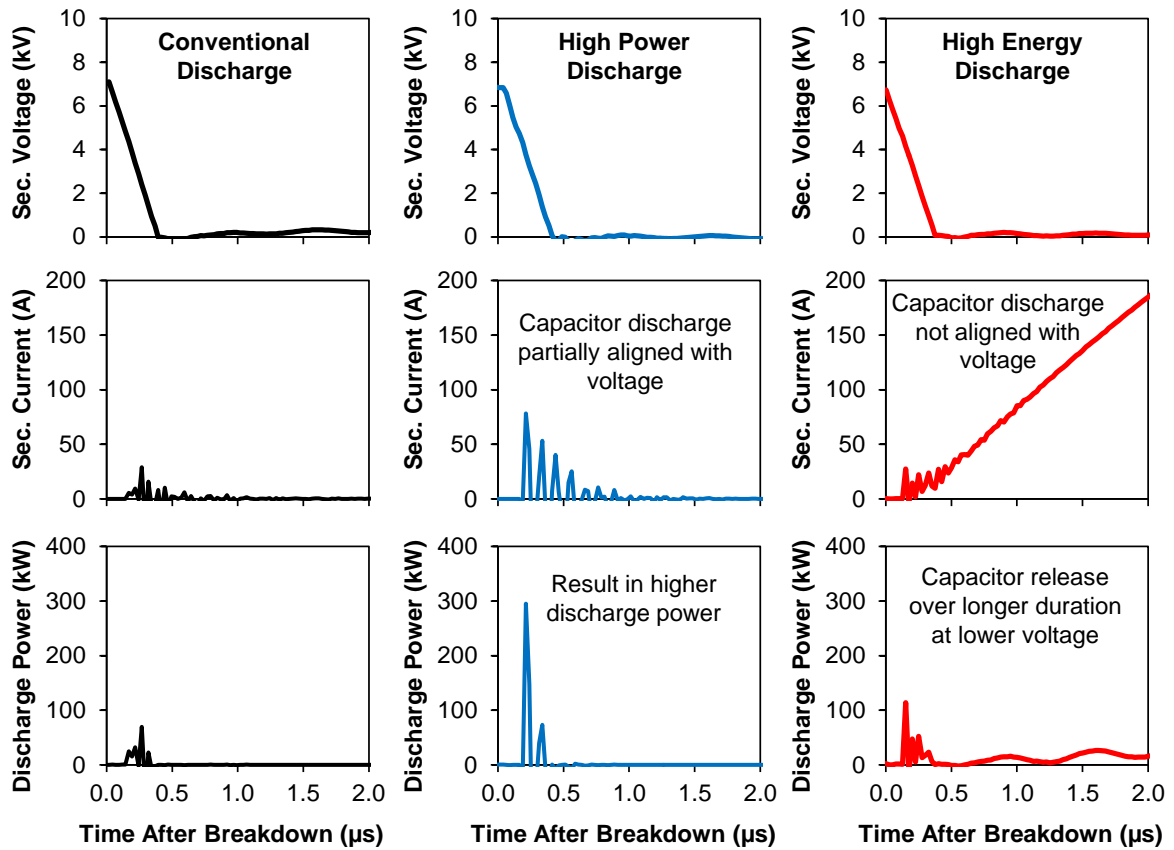


Figure 5-25: Comparison of Capacitor Discharge Power

The effect of the capacitor discharge strategies at a lambda 1.2 is shown in Figure 5-26 in a sweep of spark timing. The capacitor discharge strategies did not result in any discernible difference in the coefficient of variation in IMEP compared to the baseline non-resistive spark plug of the same type or the iridium resistive spark plug.

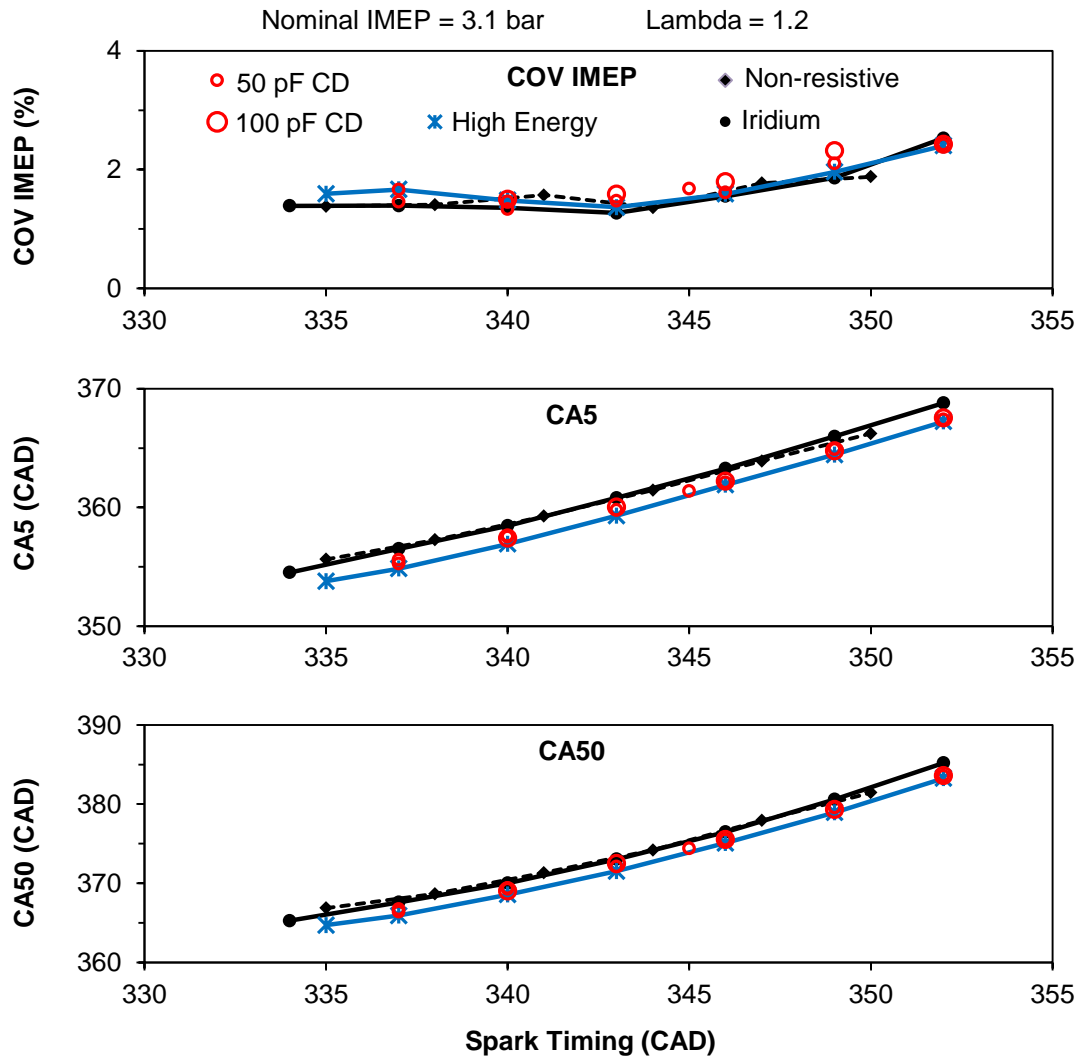


Figure 5-26: Capacitor Discharge Effect on Combustion Parameters

The coefficient of variation for all the strategies at this condition was low at below 2 percent. The combustion phasing was slightly advanced by the use of the high power capacitors. The high energy capacitor strategy resulted in the earliest combustion phasing. The difference in combustion phasing can be seen in the pressure and mass-fraction burned plots, shown in Figure 5-27 at the same spark timing of 340 CAD. The high energy ignition exhibited a CA50 advance of 1.5 degrees compared to the baseline

strategy. The addition of 50 pF capacitance advanced the CA50 by 0.8 degree, while the addition of 100 pF capacitance advanced the CA50 by 1.0 degree.

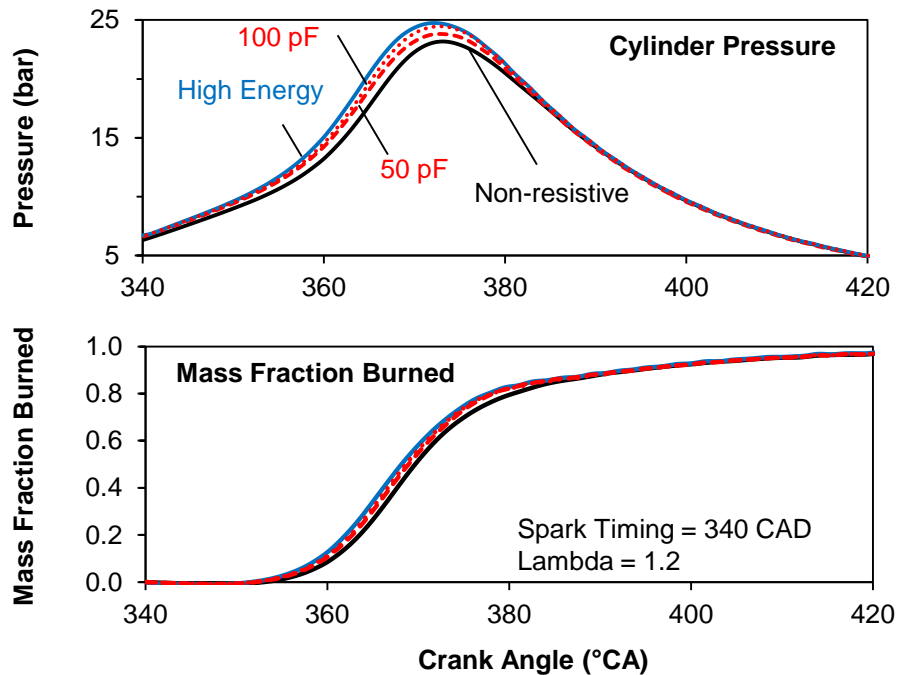


Figure 5-27: Capacitive Discharge Effect on Pressure

The stability characteristics of the strategies are examined in more detail in the following scatter plots of the CA50 versus CA5 and IMEP versus CA50 for 200 engine cycles. Figure 5-28 shows that the CA5 and CA50 are generally well correlated with each other, highlighting the generally linear process of the flame propagation. At a constant spark timing of 340 CAD, the capacitor discharge strategies achieved more advanced CA5 and CA50 timings, but did not significantly reduce the variability of the combustion process. Figure 5-29 shows that although there is variation in the combustion timing, the influence on engine load is negligible. The IMEP displays no correlation with the combustion phasing at this slightly lean condition.

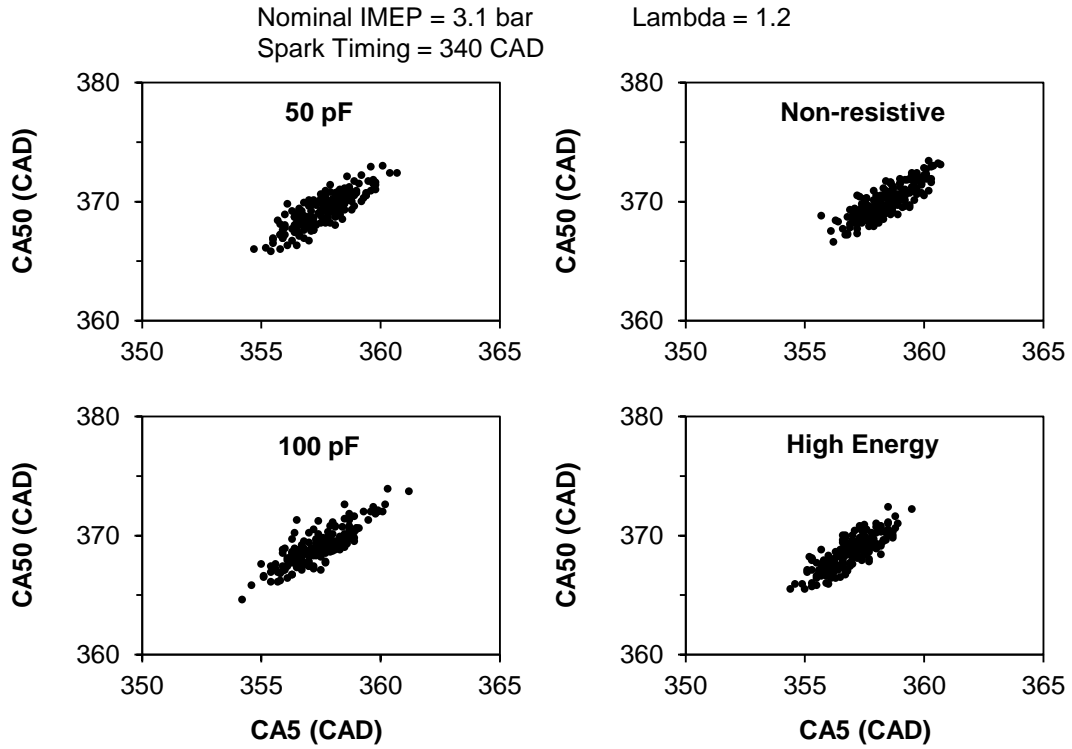


Figure 5-28: Combustion Phasing Stability Scatter Plot at Lambda 1.2

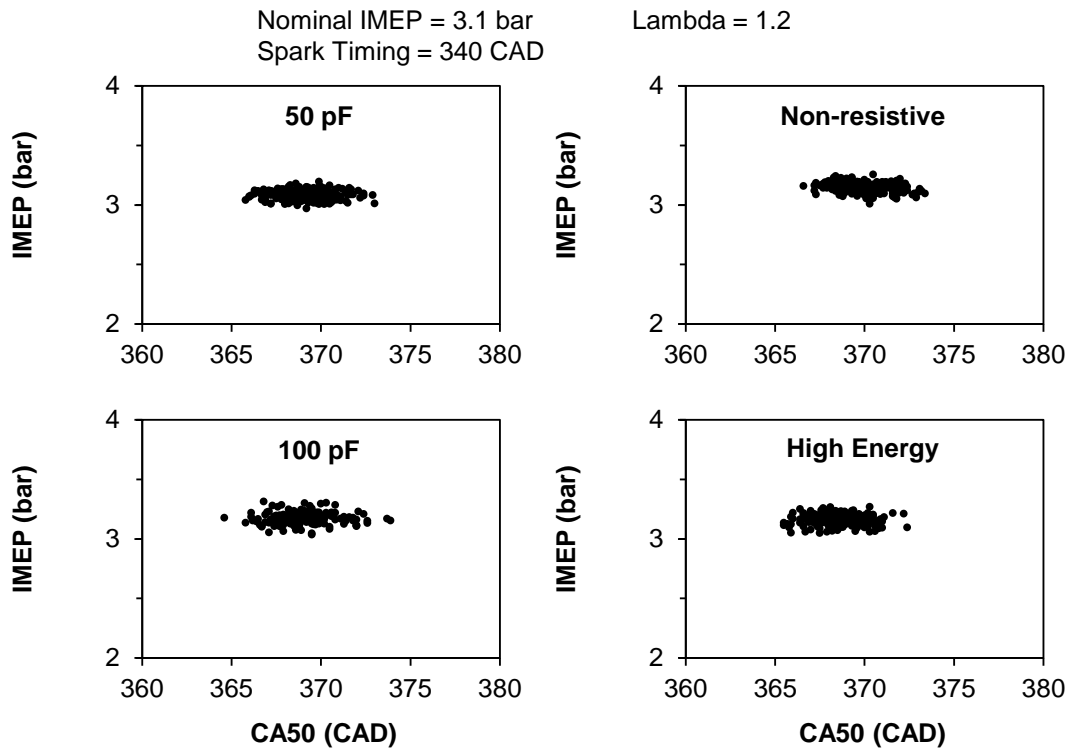


Figure 5-29: Load Stability Scatter Plot at Lambda 1.2



At the higher end of the lean operation boundary, lambda 1.7, the spark timing sweep was repeated. The results are shown in Figure 5-30. The coefficient of variation of IMEP at this condition was generally significantly higher, typically at 5 to 10 percent. The capacitor discharge with 50 pF capacitance exhibited slightly higher coefficient of variation than without the capacitance. The 100 pF capacitance resulted in lower variability in IMEP. The capacitor high energy discharge resulted in generally the lowest variability in IMEP.

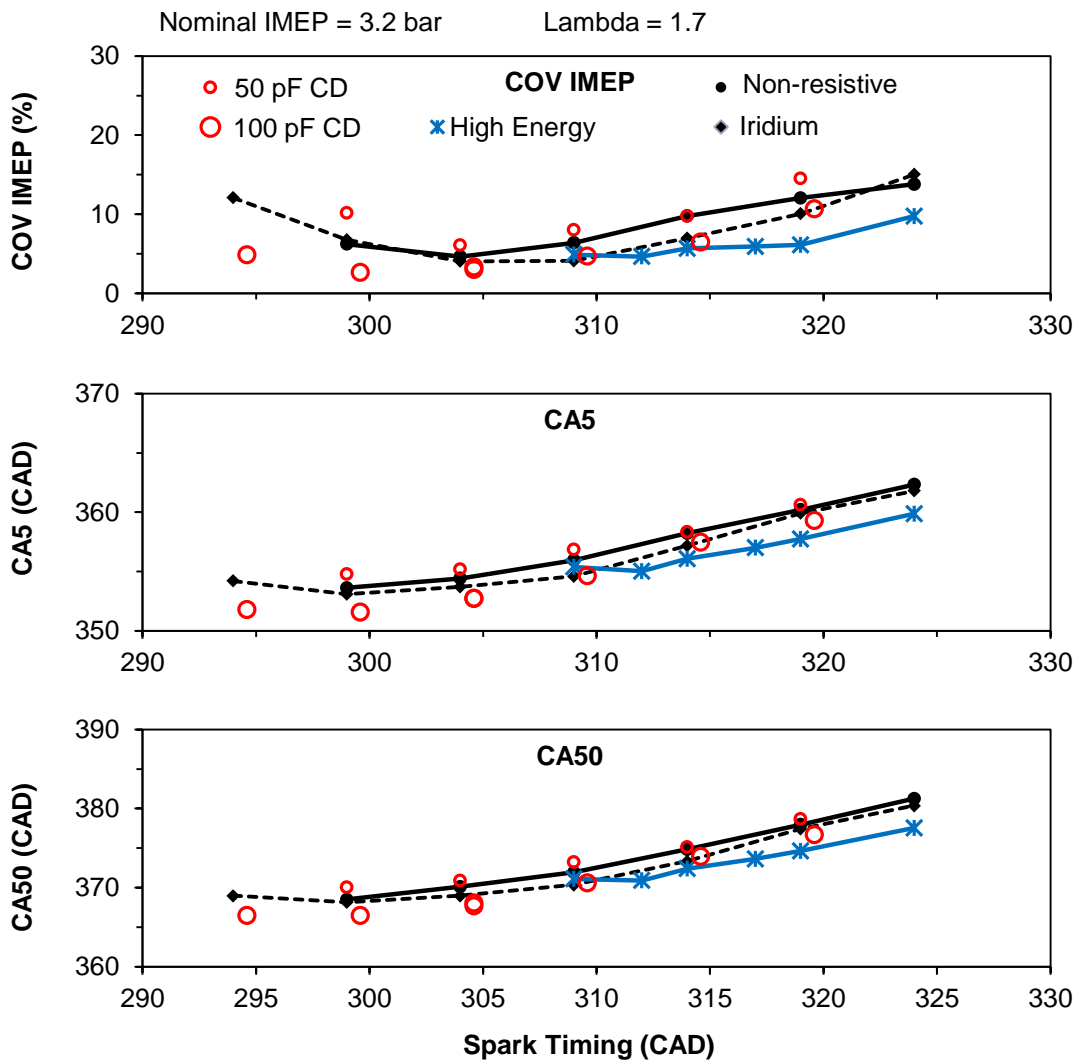


Figure 5-30: Capacitive Discharge Effect on Combustion Parameters

The 50 pF capacitance did not result in any improvements in the ignition when comparing the CA5 and CA50 values to the baseline case. The combustion phasing was similar or even more delayed in several cases. Increasing the capacitance to 100 pF resulted in a slight combustion phasing advancement over the baseline. The capacitor high energy strategy again resulted in generally the earliest combustion phasing.

The scatter plot in Figure 5-31 shows that at this condition, close to the lean limit, the variability in combustion phasing was significantly more pronounced. The range in CA5 and CA50 values over 200 engine cycles was on the order of 20 CAD. The high power capacitor strategies did not reduce the overall magnitude of the variability significantly. The high energy ignition slightly reduced the variability in combustion phasing. The average CA50 was advanced by 0.9 degree with the 100 pF case and 2.4 degrees with the high energy discharge strategy.

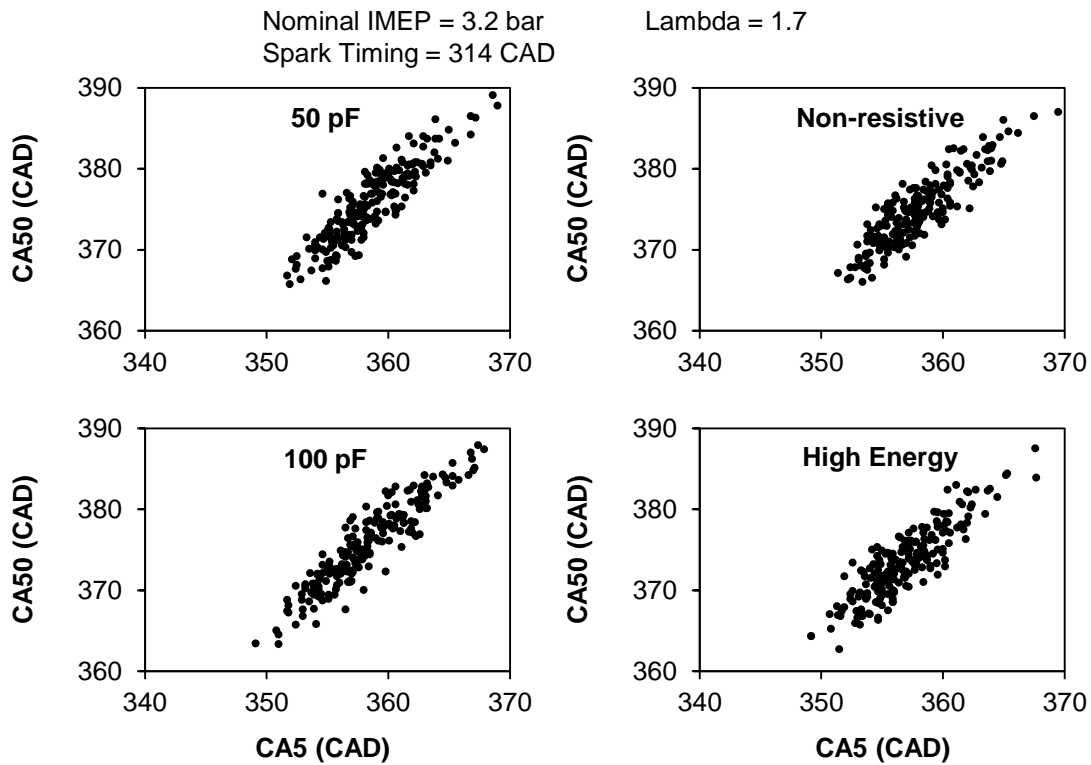


Figure 5-31: Combustion Phasing Stability Scatter Plot at Lambda 1.7

For this fuel lean condition, Figure 5-32 shows that the cycle engine load over 200 cycles had significantly higher scatter than the near-stoichiometric case and was also strongly correlated to the combustion phasing at this condition. However, it should be noted that at least some of the variability can be attributable to the combustion history of the previous engine cycle. As the combustion experiences variabilities in the in-cylinder flow conditions, a given cycle may produce poor, incomplete combustion. If the combustion is significantly late, the exhaust temperature will be correspondingly higher. Upon the next engine cycle, the in-cylinder residuals, having a higher temperature or higher unburned fuel component to enrich the fresh charge, will promote the ignition and combustion of the cycle. This behavior is evident in a plot of the IMEP of adjacent engine cycles in Figure 5-33. At conditions of lambda 1.2 and 1.6, the IMEP for cycle n

and the next cycle  $n+1$  was normally distributed and independent. At lambda 1.7, the distribution became skewed toward lower load levels and began to exhibit correlation between adjacent cycles. This trend was most evident in the case at lambda 1.8, where adjacent cycles exhibited a partial inverse influence to the IMEP.

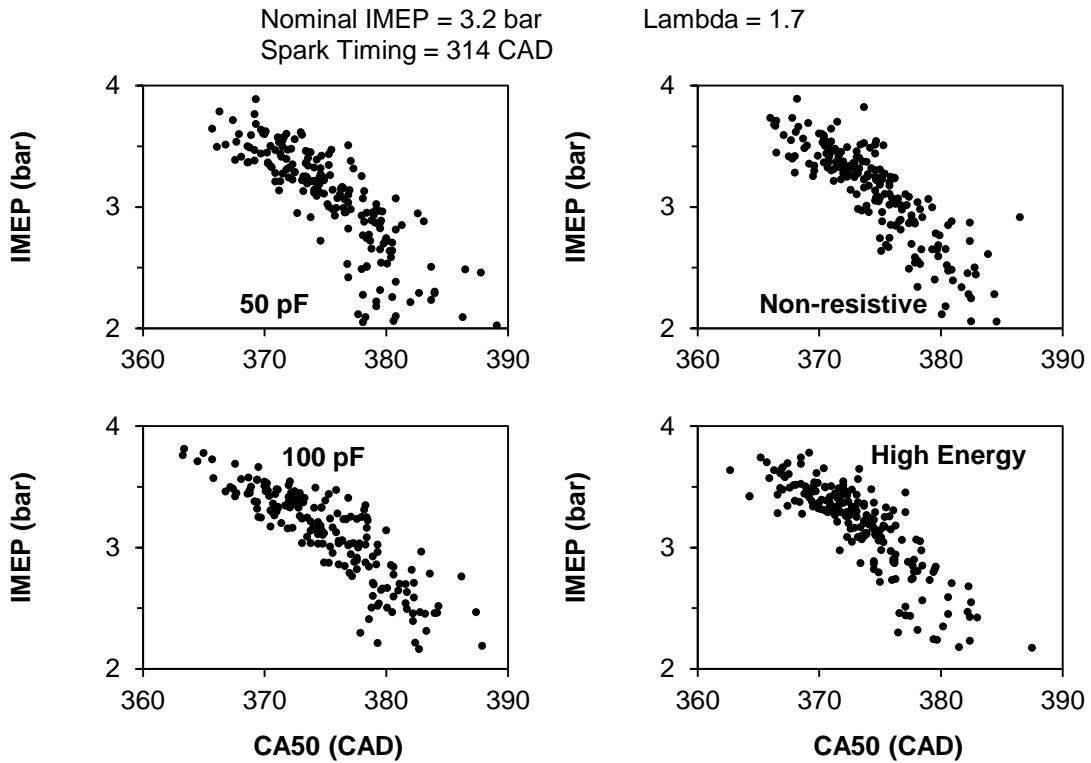


Figure 5-32: Load Stability Scatter Plot at Lambda 1.7

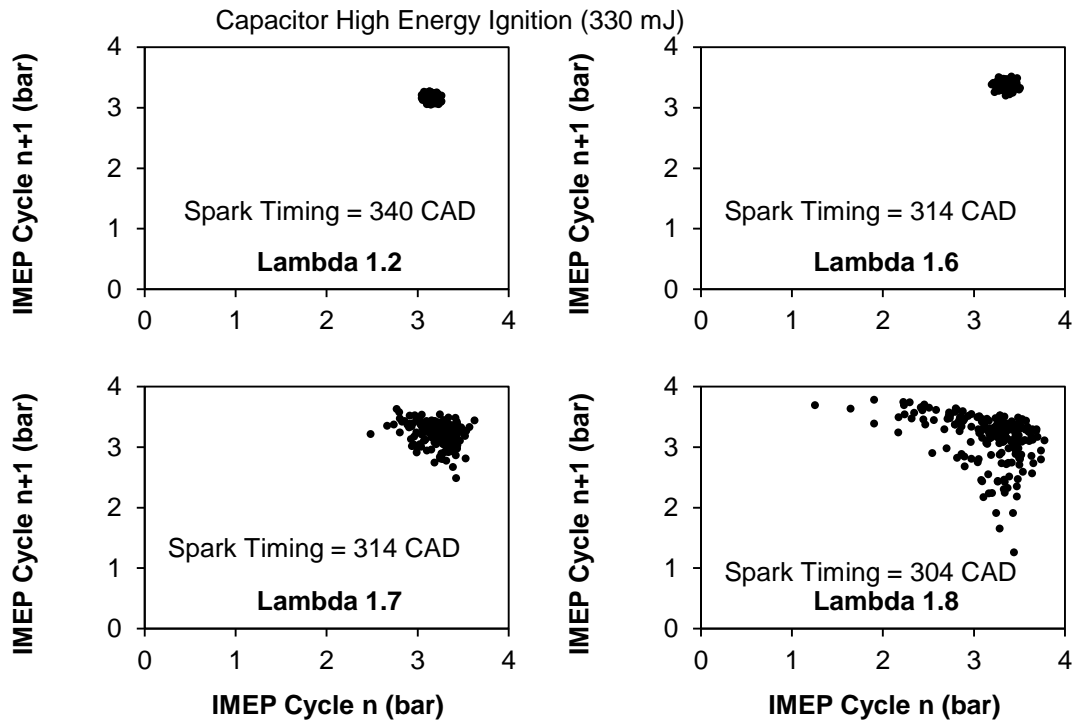


Figure 5-33: Adjacent-cycle Impacts on IMEP

### 5.2.3 Pre-chamber Igniter

A third strategy tested to improve the ignition performance was a pre-chamber spark plug. The spark plug has a shroud surrounding the core electrode, forming a pre-chamber cavity. The shroud has three circular openings in the axial direction and three small openings in the radial direction for passively filling the cavity with the engine charge upon compression and to permit the flame to enter the main combustion chamber. The ejection of the flame from the pre-chamber into the main chamber is typically a turbulent process that can greatly enhance the early combustion rate. An example of this behavior can be seen in Figure 5-34 of shadowgraph images taken in combustion vessel CV1. The initial flame kernel is contained inside the pre-chamber and not visible. The flame growth rate at this stage is slower than that of a conventional spark plug due to the large exposure of the flame kernel to the metal surfaces of the pre-chamber. At 2.45 ms

after the start of discharge, the flame kernel begins to enter the main chamber. The velocity of the jets that emanate from the pre-chamber is significantly faster than the laminar flame expansion speed. The flame surface also shows a high degree of wrinkling and increased surface area indicative of turbulence.

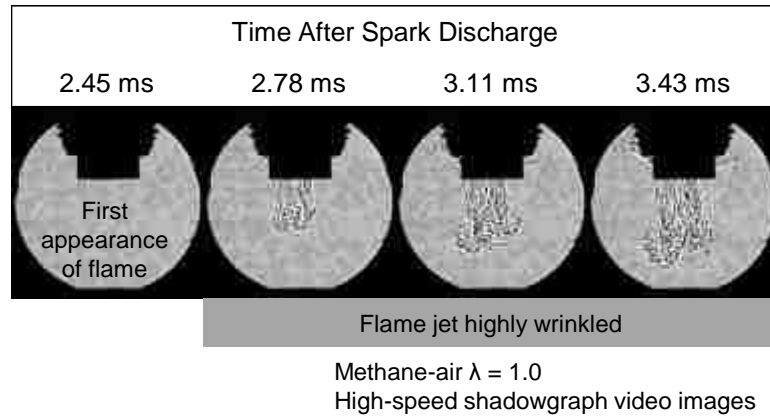


Figure 5-34: Images of Pre-chamber Flame Jet in Combustion Vessel

The prototype pre-chamber igniter was tested in the engine to compare the ignition performance at a range of lambda conditions from 1.0 to 1.5. Figure 5-35 shows a sweep of spark timing at a lean condition of lambda 1.5. The control of the combustion phasing with the pre-chamber spark plug was adequately maintained by the spark timing. However, at the same spark timing, the CA5 and CA50 were well advanced compared to the conventional J-type spark plug. The difference in CA5 and CA50 between the two types of spark plugs was approximately 13 degrees. In response, the spark timing of the pre-chamber igniter needed to be retarded to maintain the CA50 in the range for peak efficiency. This can be seen in Figure 5-36, where the pre-chamber igniter at 337 CAD spark timing achieved similar pressure and mass fraction burned traces as that of the conventional spark plug at 323 CAD spark timing. In contrast, the conventional spark plug at 335 CAD exhibited significantly delayed combustion phasing.

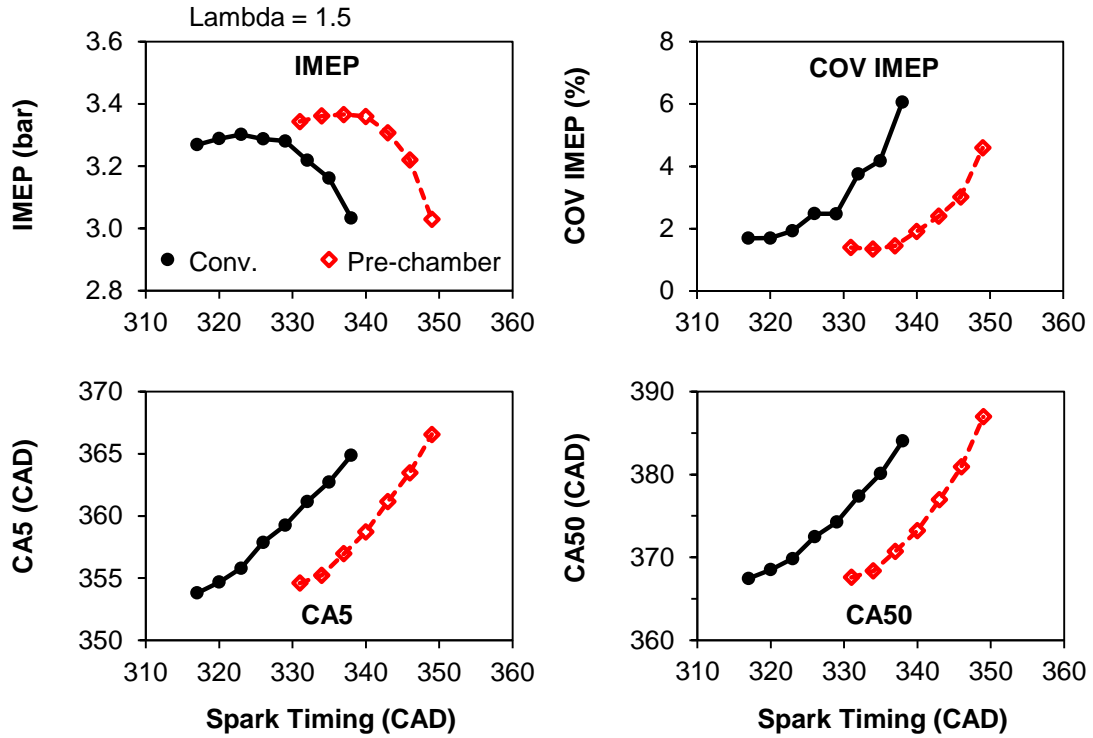


Figure 5-35: Pre-chamber Combustion Comparison

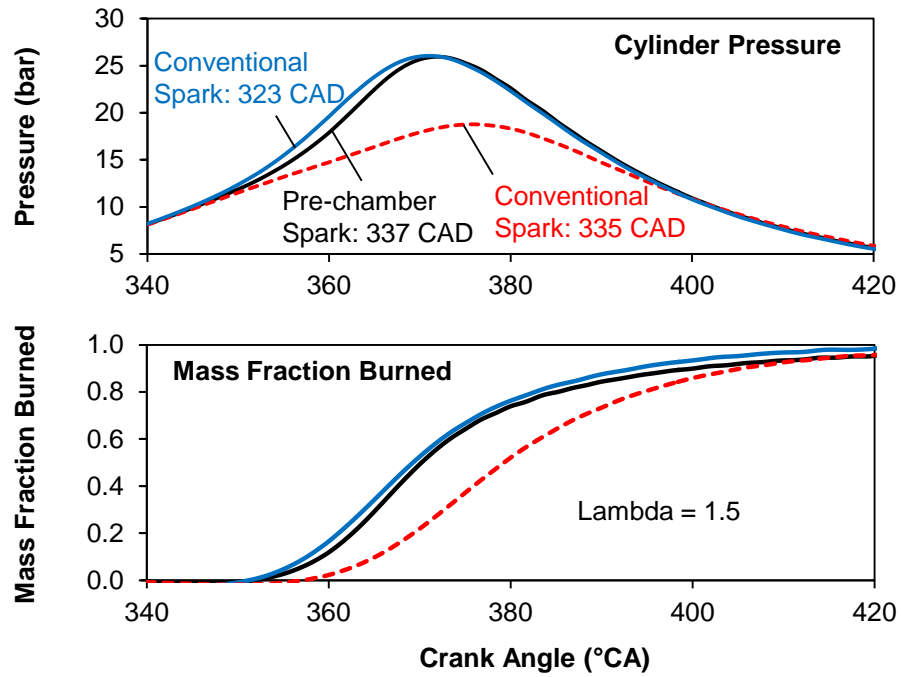


Figure 5-36: Pre-chamber Igniter Pressure Trace

The required change in spark timing control between the conventional and pre-chamber igniters to achieve the same CA50 timing of 370 CAD is plotted in Figure 5-37. This ranged from 4.8 degrees at lambda 1.0 to 13 degrees at lambda 1.5. The difference with respect to the same CA5 was nearly the same, at 5.1 and 12.5 degrees, respectively. The results indicate that the pre-chamber concept was effective in enhancing the earlier flame growth rate. The overall combustion characteristics of the pre-chamber igniter was not different from that of the conventional spark plug when the spark timing was optimized for maximum efficiency, as shown in Figure 5-38.

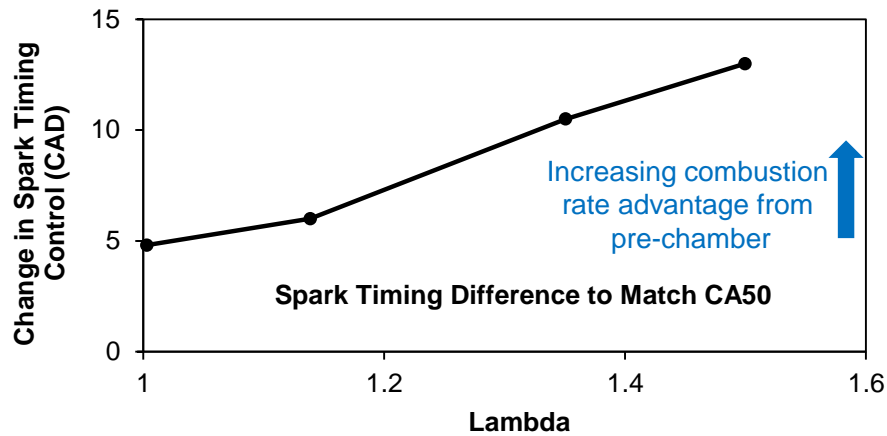


Figure 5-37: Difference in Spark Timing for Pre-chamber Igniter

One issue that was experienced with the pre-chamber spark plug was the greater difficulty in firing the engine from a motored state and typically required more fuel enrichment. The pre-chamber spark plug also had lower tolerance for lean dilution before completely misfiring. Both of these aspects are attributable to the issue of effective filling of the pre-chamber cavity with fresh air-fuel charge, which was also noted by Briggs [61] as a challenge to the successful implementation of pre-chamber designs for automotive engines.



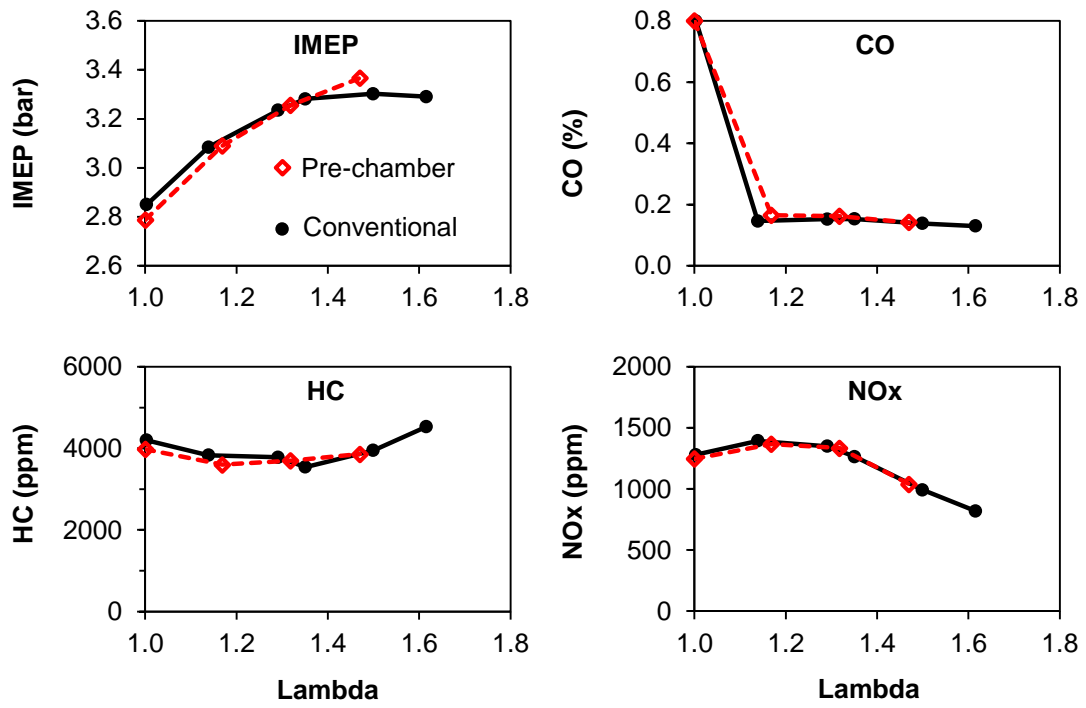


Figure 5-38: Comparison of Pre-chamber Igniter Test Engine Load and Emissions

## CHAPTER VI

### MULTIPLE SITE SPARK IGNITION

This chapter presents the engine test results of a prototype spark plug designed to achieve ignition at multiple sites. This is done using three independent high voltage electrodes, each driven by an ignition coil. The impact on flame development in engine tests is demonstrated. The multipole site ignition strategy is then applied to extend the engine dilution limit.

#### 6.1 Multi-pole Ignition

The multi-pole ignition concept was explored to study the effect of placing multiple independent ignition sites in close proximity, with the same overall packing size as a conventional spark plug. The first test explored the effect of the pole orientation in the three pole design. In conventional spark plugs, the orientation of the ground electrode when installed in the engine can influence the kernel formation because of the interaction of the in-cylinder flows. Similarly, in the installation of the prototype multi-pole spark plug into the engine, the performance of the individual poles can be expected to be affected by the prevalent engine flow patterns, as well as manufacturing variances, and the closeness of the electrode to the center of the combustion chamber. In the present engine tests, the spark plug was installed with the three poles as shown in Figure 6-1. Pole 2 and pole 3 were closer to the center of the cylinder, and with pole 2 closer to the intake valve and pole 3 closer to the exhaust valve. Pole 1 was farther away from the center of the cylinder. As a result of the angled installation of the spark plug, the protrusion depth of the spark poles also varied. Pole 1 protruded approximately 2 mm deeper into the combustion chamber than poles 2 and 3.

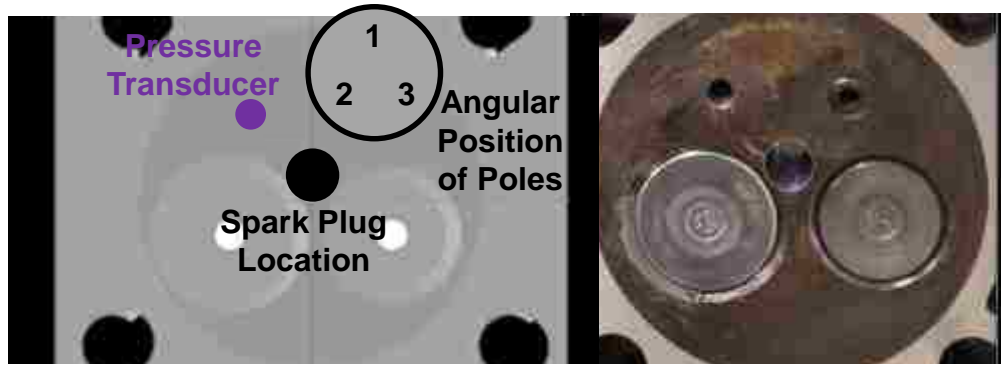


Figure 6-1: Location and Orientation of Spark Poles in Multi-pole Configuration

The effect of the pole position was evaluated in a series of tests. A representative case is shown in Figure 6-2, at a condition of  $\lambda$  1.4 and 3.2 bar nominal IMEP. The impact on IMEP, the coefficient of variation of IMEP, the CA5, and the CA50 are plotted. The tests show that individually, poles 2 and pole 3 behaved similarly with respect to IMEP and combustion stability, but pole 3 showed a slight advantage in terms of CA5 valve. Pole 1, farther away from the cylinder center, had markedly lower IMEP and stability performance with ignition timings in the 332 CAD to 340 CAD range. The CA50 of pole 1 was generally the most delayed of the individual poles. The combined discharge of all three poles in the multi-pole ignition mode showed the most advanced combustion phasing and lowest coefficient of variation in IMEP.

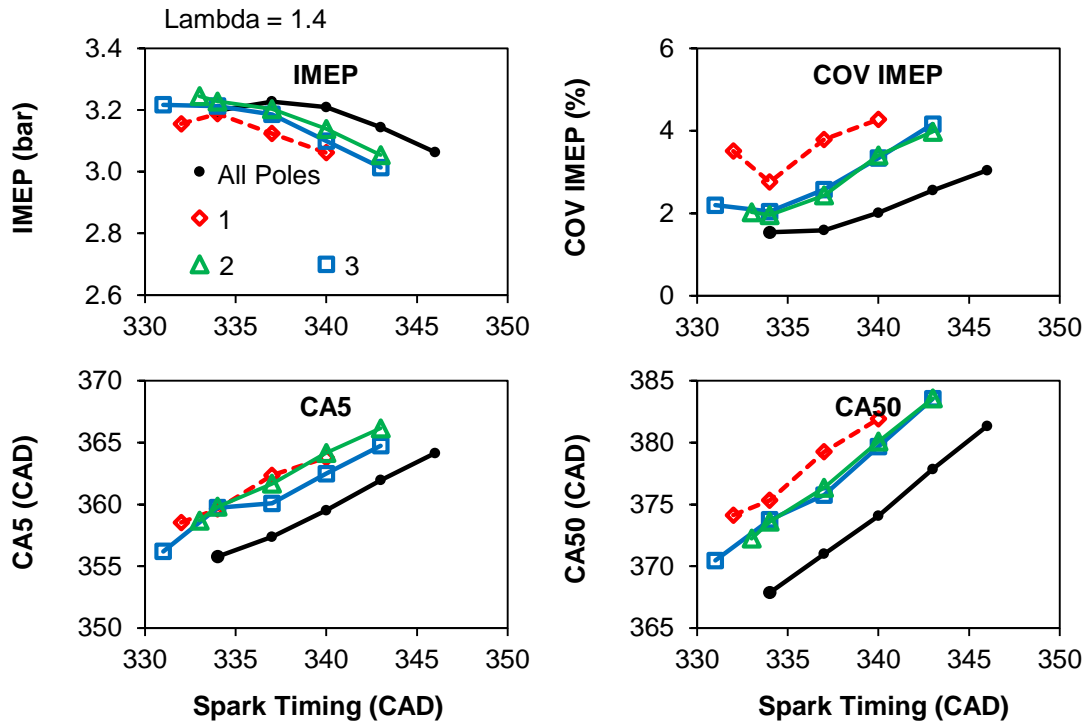


Figure 6-2: Comparison between Single Pole and Multi-pole Ignition

The stability characteristics of the multi-pole ignition cases are examined in more detail in the following scatter plots of CA50 versus CA5, and IMEP versus CA50 for 200 engine cycles, in Figure 6-2 and Figure 6-3, respectively. The cases of discharge of the individual poles and the multi-pole case are shown for spark timing at 337 CAD. There was strong correlation, as expected, between the CA5 and CA50 parameters. Among the single-pole discharge cases, pole 2 exhibited the least amount of scattering. The CA5 and the CA50 can be seen to be considerably more advanced for the multi-pole case.

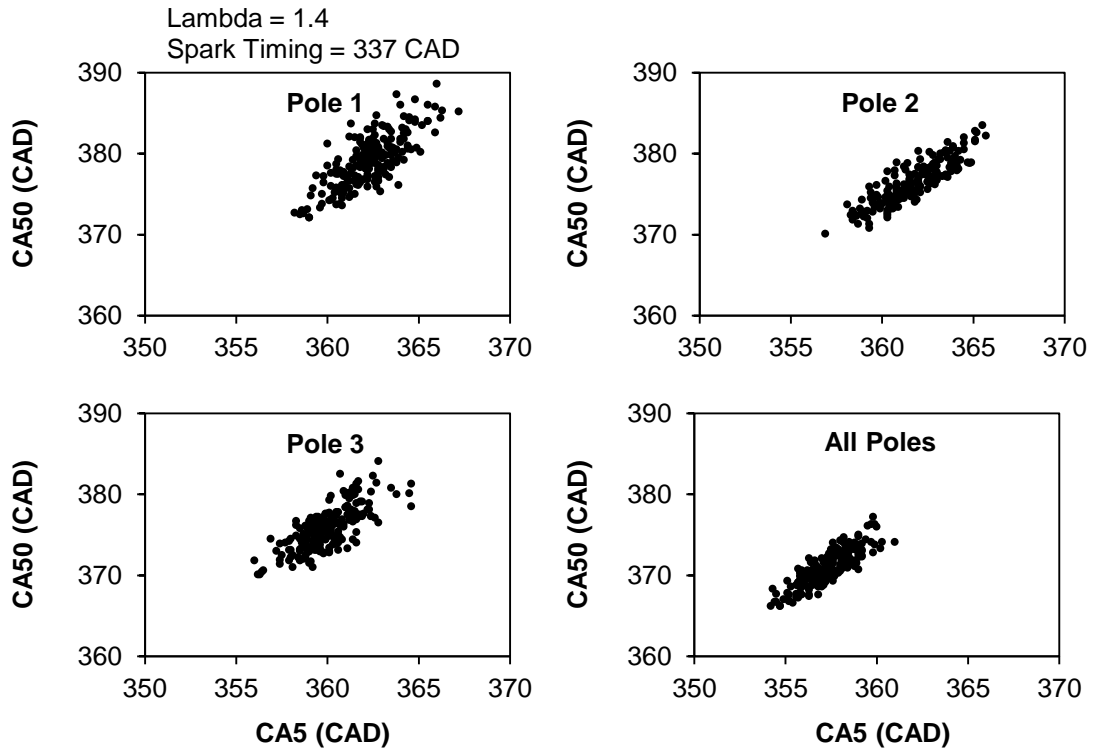


Figure 6-3: Combustion Phasing Stability Scatter Plot at Lambda 1.4

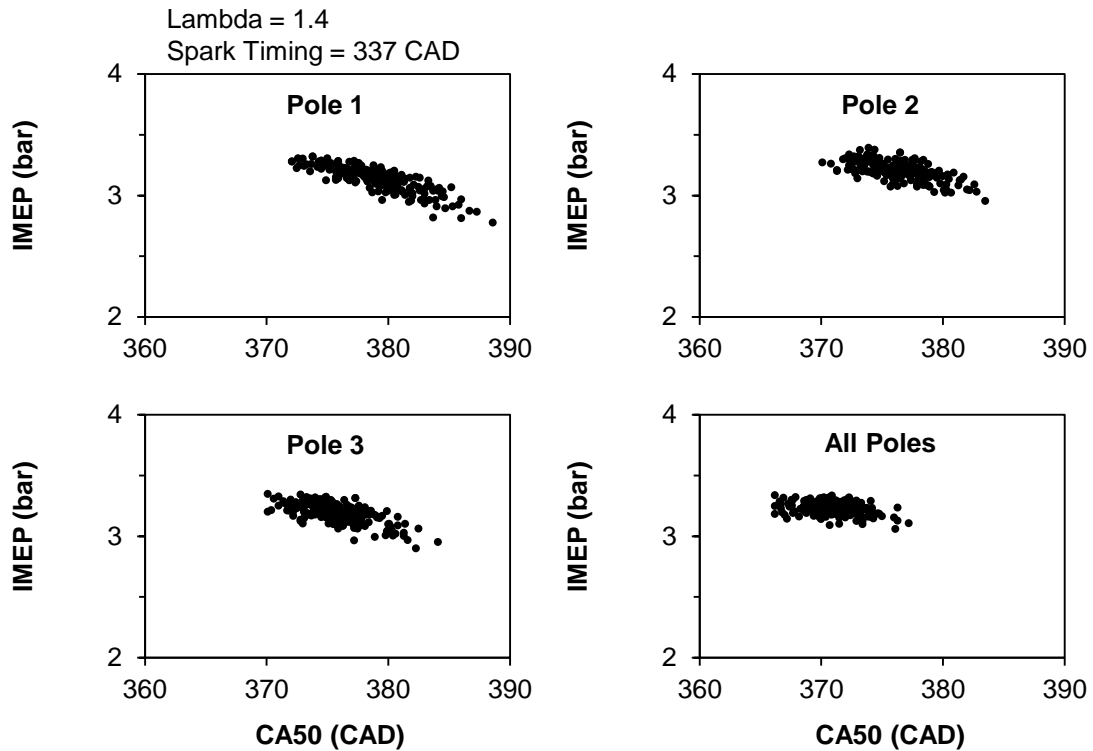


Figure 6-4: Load Stability Scatter Plot at Lambda 1.4

The spark timing of 337 CAD was near the optimal ignition timing for the multi-pole case. The influence of the CA50 variability on IMEP was therefore low. In the individual pole discharge cases, the spark timing was later than optimal as a result of the slower overall flame development. The IMEP consequently displayed considerably higher correlation to the combustion phasing.

The pressure and mass fraction burned traces are shown in Figure 6-5. The difference in combustion phasing between the single pole discharges and the multi-pole discharge are clear. Pole 1 has the slowest combustion rate. Pole 2 has slower initial combustion rate than pole 3, but accelerates later in the process.

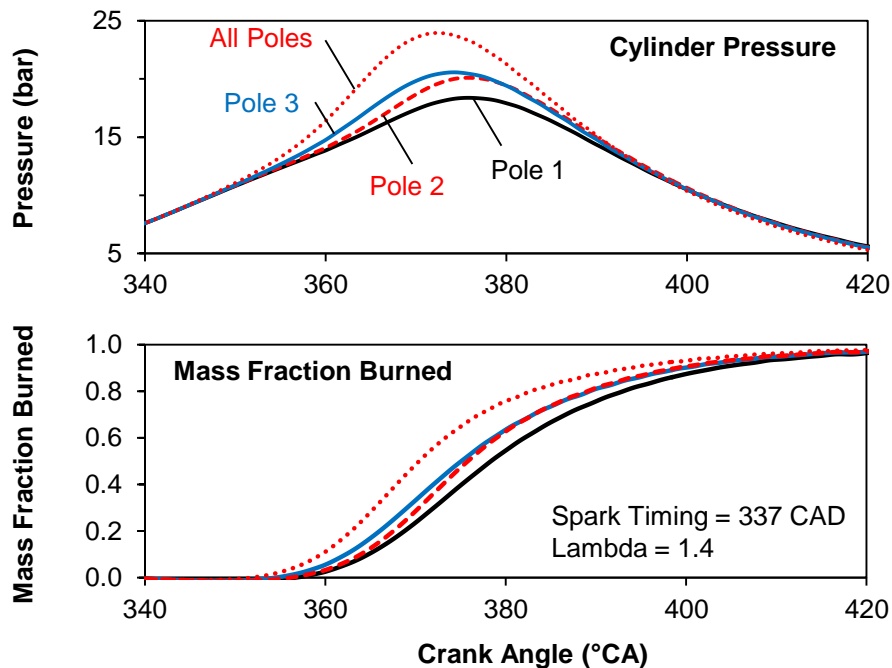


Figure 6-5: Multi-pole Ignition Effect

## 6.2 Extension of Dilution Limit

The multi-pole discharge was previously shown to be more effective when discharged in unison than single discharges of the individual poles. The performance of

the multi-pole strategy was applied to extend the dilution limit of the engine combustion. The dilution of the combustion mixture with excess fresh air and recirculated exhaust gas was also compared. The excess air method is less common on automotive engines because of the inability to use the common three-way catalyst, thereby requiring a different strategy for treatment of nitrogen oxides under lean conditions [62]. Lean combustion is currently used more often in stationary engine applications. In combustion systems where the excess air exceeds fifty percent, the need for NO<sub>x</sub> reduction in the aftertreatment system is greatly reduced or eliminated for stationary engines.

### **6.2.1 Lean Combustion**

The performance of the baseline conventional spark plug under lean combustion is shown in Figure 6-6 below. Two cases of the multi-pole performance are also shown. The energy discharged per pole was approximately 50 mJ in both cases. In the case of the single discharge from the multi-pole spark plug, the performance was similar to that of the conventional spark plug. The stability deteriorated rapidly beyond lambda 1.8. The case of three discharges from the multi-pole could extend the performance limit up to nearly lambda two. Complete mis-fires, which could be recognized by the drop of the least numerical value of IMEP below zero, were not seen until beyond lambda two, whereas complete mis-fires occurred around 1.8 for the single discharge cases. The difference in performance between in single and multi-pole discharges is also seen in the the COV of IMEP and the combustion phasing parameters.

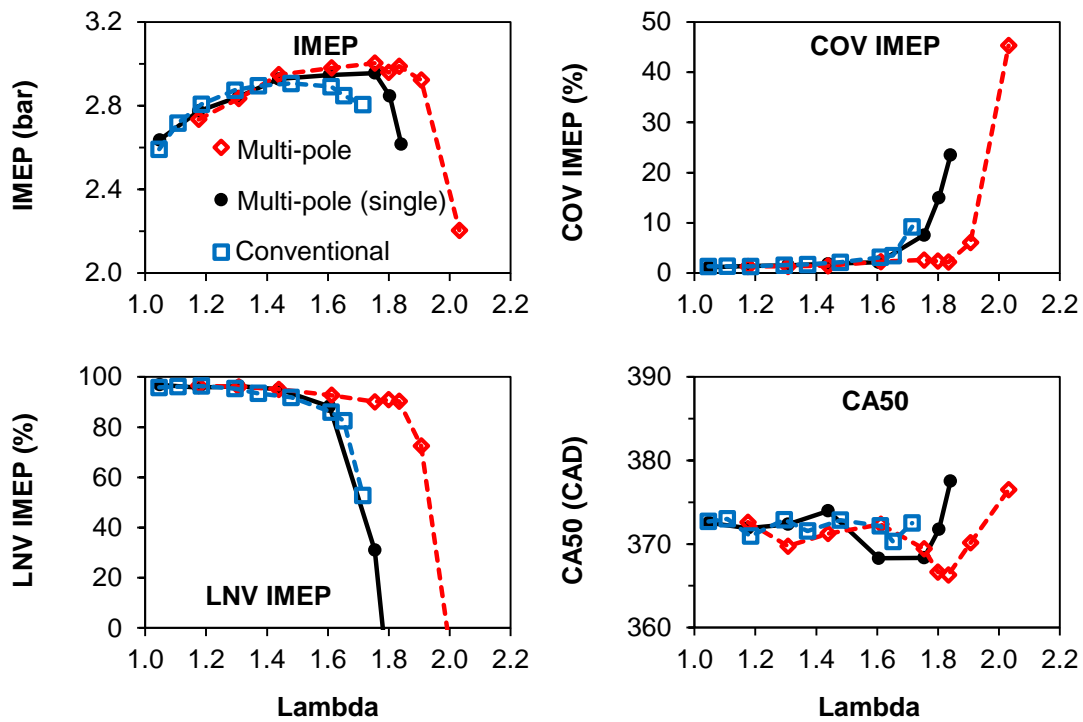


Figure 6-6: Lean Extension Using Multi-pole Ignition

The thermal efficiency of the engine was analyzed on indicated basis using the measurement of the in-cylinder pressure. The change in indicated thermal efficiency, on relative basis, in the pumping loop and closed-cycle portions of the full engine cycle are ascribed separately in Figure 6-7. The lean combustion strategy reduced the negative pumping work as the throttle is opened wider. The maximum gain was an eight percent increase from the baseline IMEP. The closed-cycle portion showed a maximum of eleven percent increase from the baseline IMEP. The window of relatively higher closed-cycle efficiency appeared to range from  $\lambda$  1.3 to 1.7. At excessively lean conditions, the decrease in combustion efficiency and the decrease in combustion rate (and hence prolonged combustion duration) significantly lowered the overall efficiency.



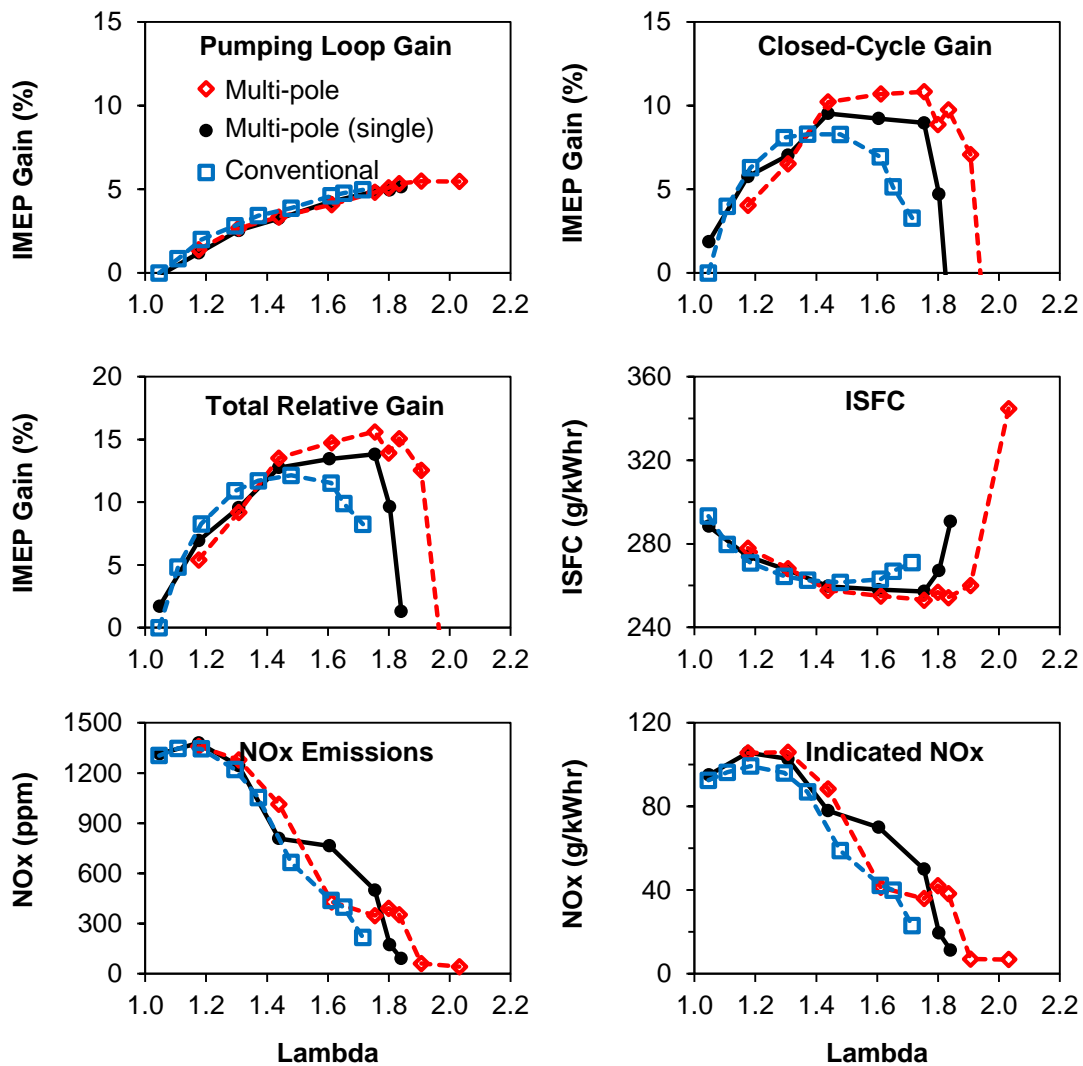


Figure 6-7: Efficiency and Emissions of Lean Combustion

The engine NOx emissions typically decreased on ppm basis from the peak value at lambda 1.3. This was partially offset, however, by the increase in exhaust flow from the use of excess air. The net effect was that significant NOx reduction on an indicated power basis was not achieved until around lambda 1.7. It would take operation approaching lambda two to achieve the lowest levels of NOx, at which point the closed-cycle efficiency would also be compromised.

### 6.2.2 EGR Dilution Combustion

The performance of the multi-pole spark plug under EGR combustion is compared to the baseline conventional spark plug in Figure 6-8. The engine stoichiometry was maintained within a range of  $\lambda$  1.03 to 1.05 in the EGR tests. The energy discharged per pole was 50 mJ in all cases. The black trace shows the case when one pole is discharged. The baseline conventional spark plug case is shown in the blue trace. The red trace shows the case when all three poles were discharged at the same energy level per pole. The single discharge cases from the conventional spark plug and multi-pole spark plug resulted in similar performance. The multiple discharge cases extended the stability curve to higher EGR rates. Misfires were recorded at 32% EGR with the multi-pole case, compared to 26% EGR with the conventional spark plug. Even at low and moderate EGR rates the multiple discharge cases typically also exhibited higher LNV IMEP values.

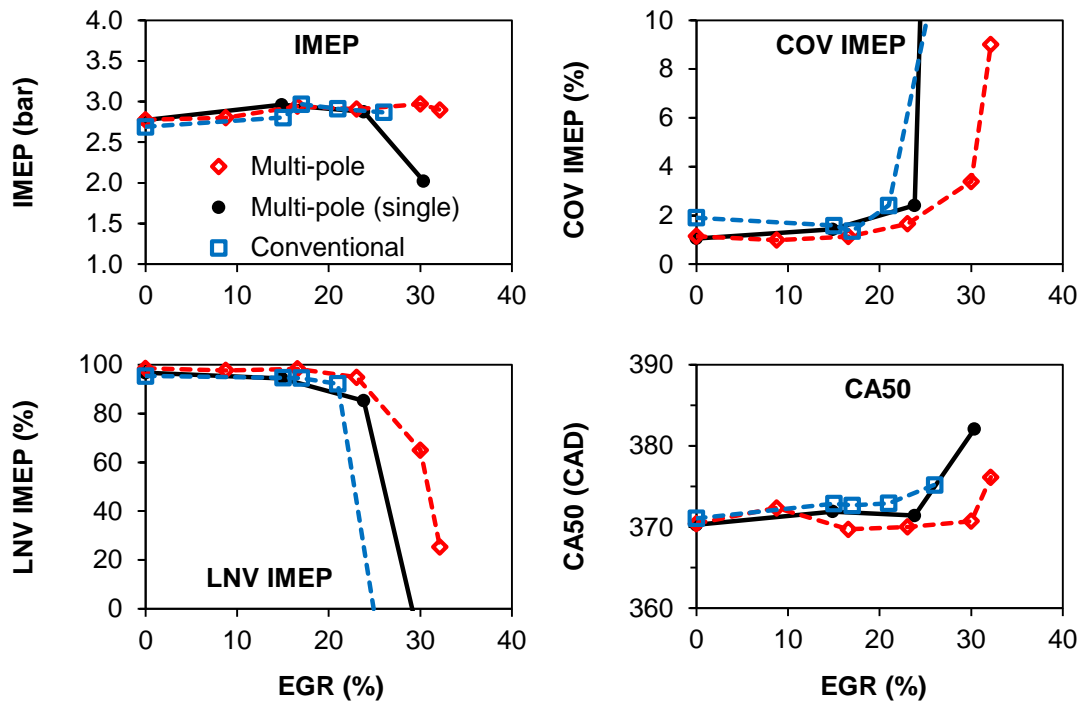


Figure 6-8: EGR Dilution Limit Extension Using Multi-pole Ignition

The rationale for using EGR dilution was in part to increase the part-load thermal efficiency and lower NO<sub>x</sub> emissions. The thermal efficiency of the single-cylinder engine tests was analyzed on indicated basis using the measurement of the in-cylinder pressure. The effect on indicated thermal efficiency, on relative basis, in the pumping loop and closed-cycle portions of the full engine cycle is shown in Figure 6-9. The negative work associated with the pumping loop reduced with higher EGR rates as the throttle was opened wider. The closed-cycle efficiency was mainly affected by the combustion efficiency, heat-transfer losses, and effective expansion ratio (i.e. combustion phasing). The net effect from these changes shows an increase in the closed-cycle efficiency with moderate levels of EGR. At the highest levels of EGR, the efficiency in the closed-cycle portion reduced. Thus the highest increase in the pumping loop and

closed-cycle processes occurred at approximately 30% EGR. This range of optimal EGR from the efficiency perspective is supported by other repeat tests for this engine condition.

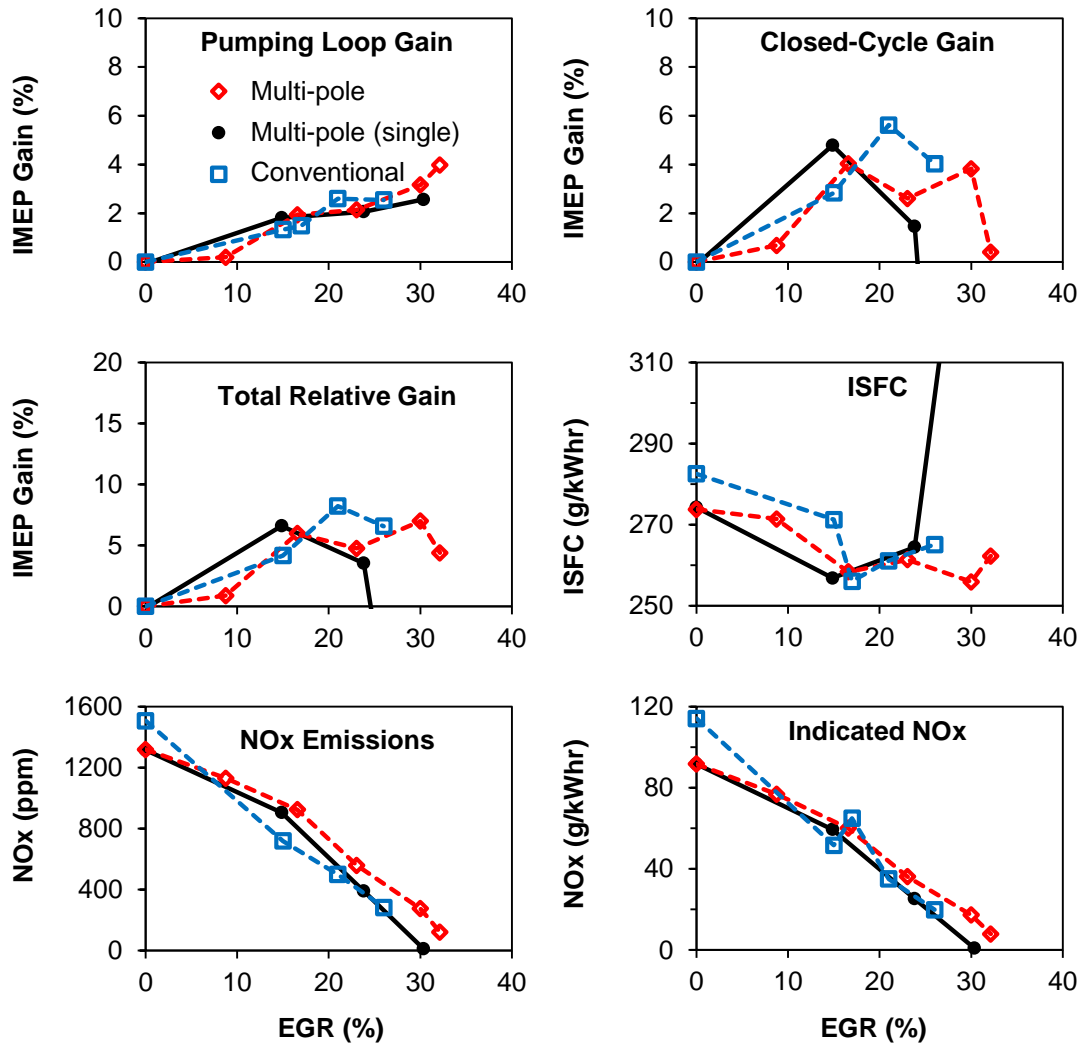


Figure 6-9: Efficiency and Emissions of EGR Combustion

The NOx emissions decreased monotonically with the increase of EGR, mainly attributable to the reduction of peak flame temperatures. Even though the three-way catalyst system can effectively treat NOx emissions, reductions in the engine-out emission levels can still lead to a net efficiency benefit from reducing need to

periodically cycle the engine stoichiometry to rich combustion in order to provide reductants for the catalyst system.

The data from the two different methods of intake mixture dilution are shown on a common basis of dilution ratio in Figure 6-10, using the best cases of the multi-pole discharge strategy. The dilution ratio characterizes the portion of the intake mixture that is either recirculated exhaust or excess air. In the case of EGR, the possible dilution rate was significantly lower than that of excess air, in part because of the strong effects of carbon dioxide in the exhaust. The achievable gains in efficiency from the use of excess air dilution slightly exceed that from exhaust gas recirculation.

The reduction of NO<sub>x</sub> emissions, however, was significantly more effective when using EGR. The use of EGR would also allow the use of a three-way catalyst to effectively reduce all criterion pollutants. This aspect is more challenging in lean combustion systems.

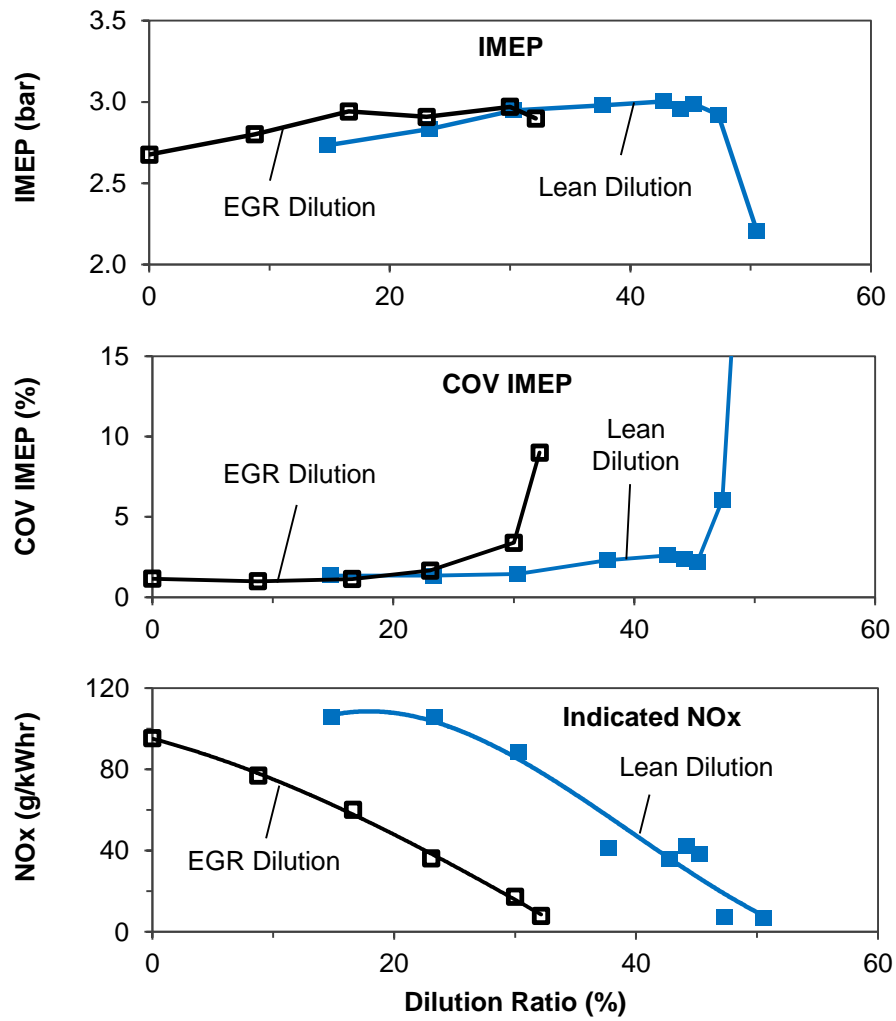


Figure 6-10: Lean and EGR Dilution Comparison

## CHAPTER VII

### VOLUME IGNITION WITH NON-THERMAL PLASMA DISCHARGE

This chapter presents the results of tests to characterize the discharge and ignition behavior of a non-thermal plasma discharge system. The tests were conducted in combustion vessels with the discharge directed into either air or combustible mixtures.

#### 7.1 Non-thermal Plasma Discharge

Plasma is a collection of neutral and ionized particles which are electrically neutral on average [44]. When the plasma is in thermal equilibrium, the electron temperatures, the ions, and neutral molecules are all at elevated temperatures. The degree of ionization required for this to occur is relatively high and the example of a spark discharge approximates this behavior. Non-thermal plasmas have high electron temperatures, but the ion and neutral gas are not in equilibrium and have much lower temperatures [46].

##### 7.1.1 Electrical Power Control Characteristics

The high-frequency (0.4 to 4 MHz) ignition driver circuit contains a primary circuit and a secondary circuit [54]. It supplies the energy required for the alternating electric field at the tip of the corona igniter. The high electric field strength in turn forms streamers that branch out from the igniter tip. The streamers are readily observable in air due to visible light emissions from the excitation of molecular nitrogen [63]. The streamers grow with some preference to existing streamer paths, but will form new branches periodically. The observed frequency of the re-branching is more than an order of magnitude lower than the electrical oscillations.

A sample of the oscilloscope recording of the command signal, secondary current, and secondary voltage acquired from the corona system at 1 bar gauge pressure is shown in Figure 7-1. The command signal to drive the corona circuit turns on and off the power driver at 434.8 kHz and induces resonant voltage amplification in the secondary circuit. The buildup takes several tens of microseconds to reach the threshold of visible discharge. Upon termination of the command signal, the secondary voltage begins to decay within one cycle.

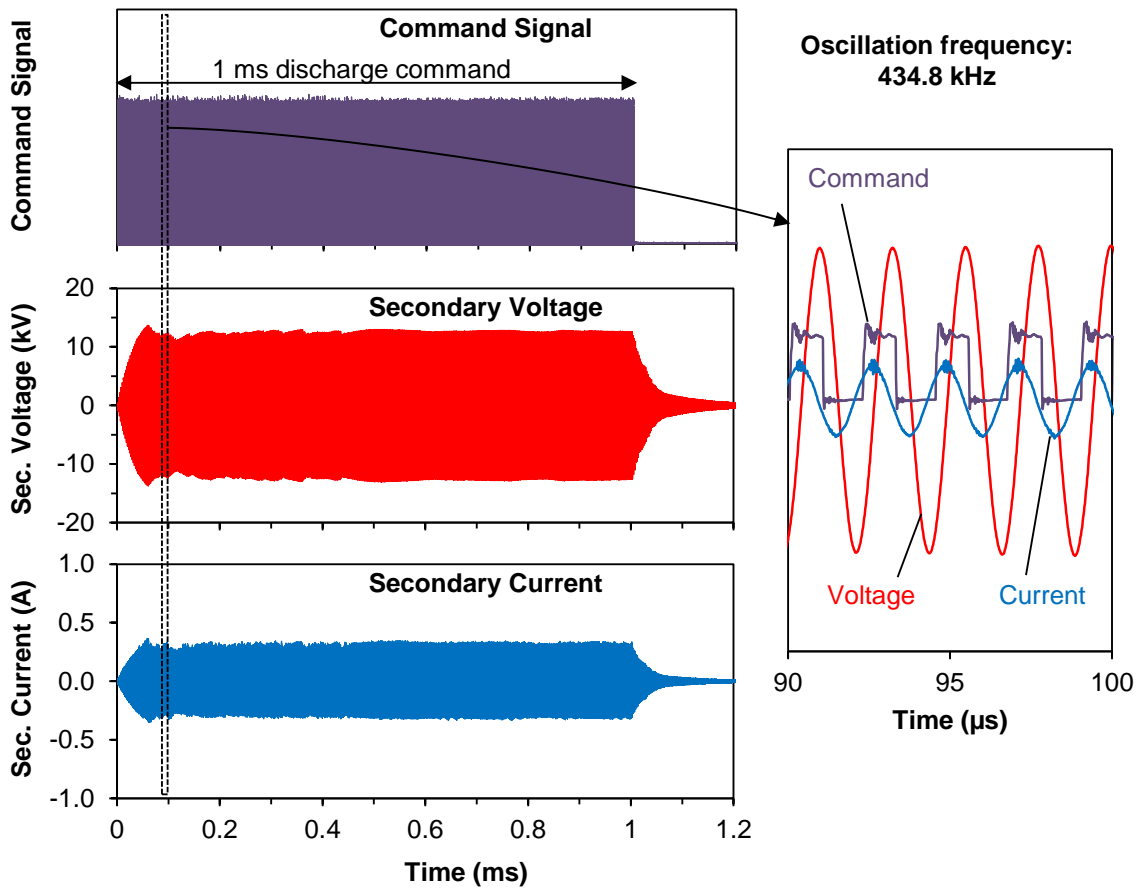


Figure 7-1: Voltage Buildup Profile in Corona Igniter

The effective power of the corona discharge was primarily controlled through the primary voltage. The effect of different primary voltages in the range of 32 V through 56



V on the discharge power, peak secondary voltage, and peak secondary current is shown in Figure 7-2. The measurements were conducted for discharges into air at a pressure of 1 bar gauge. For the sample setup, the average effective power increased from 280 W at 32 V primary input to 518 W at 56 V primary input. The total voltage amplification ratio was approximately 300 at the lower range of primary voltage input and decreased to 230 at the high range. The peak secondary current was in the range of 0.4 to 0.6 A.

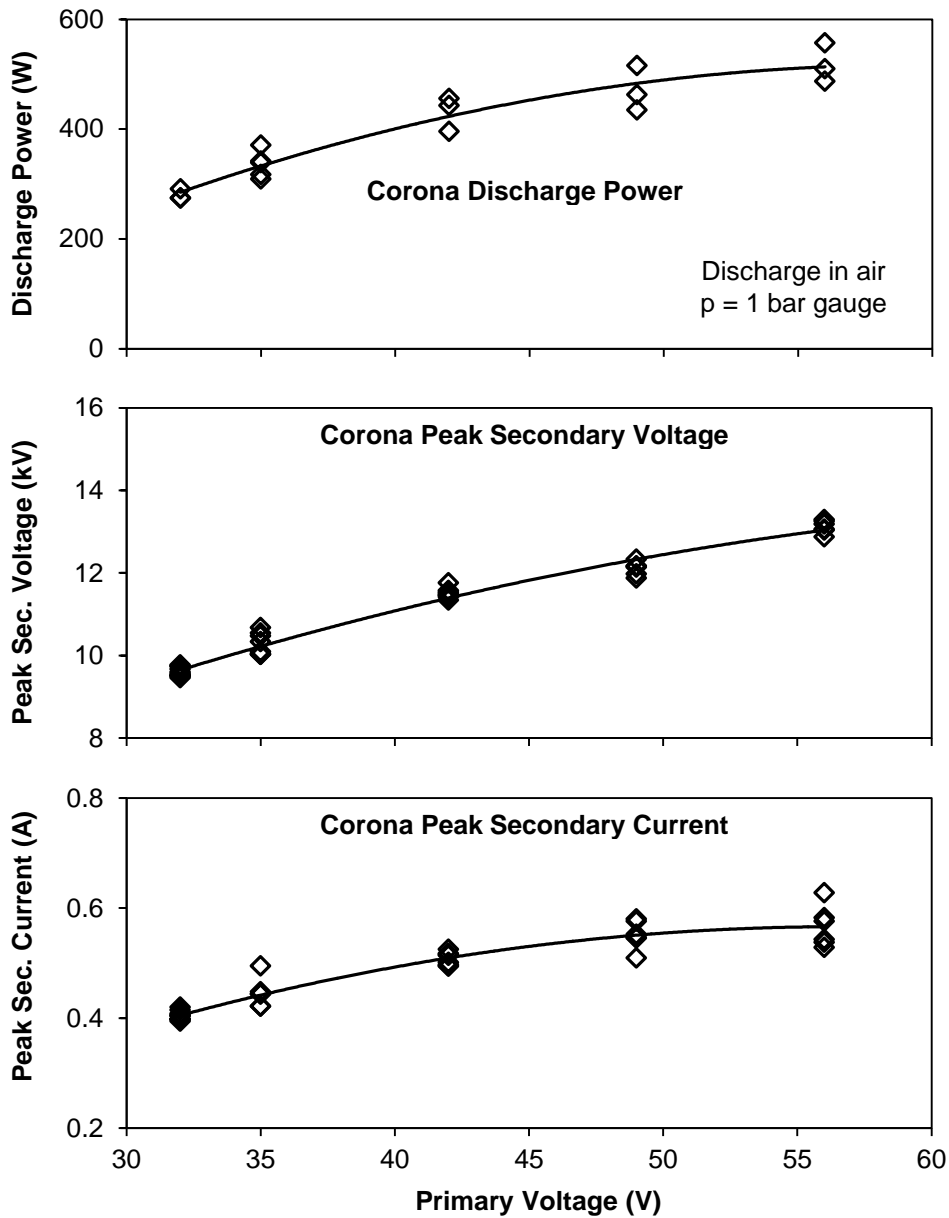


Figure 7-2: Effect of Primary Voltage on Discharge Voltage and Power

The discharge energy profile of a case at 56 V primary voltage is shown in Figure 7-3. The measured electrical discharge power increased over the course of approximately 35  $\mu$ s as the secondary resonance built up. The average peak power of the discharge was 557 W.

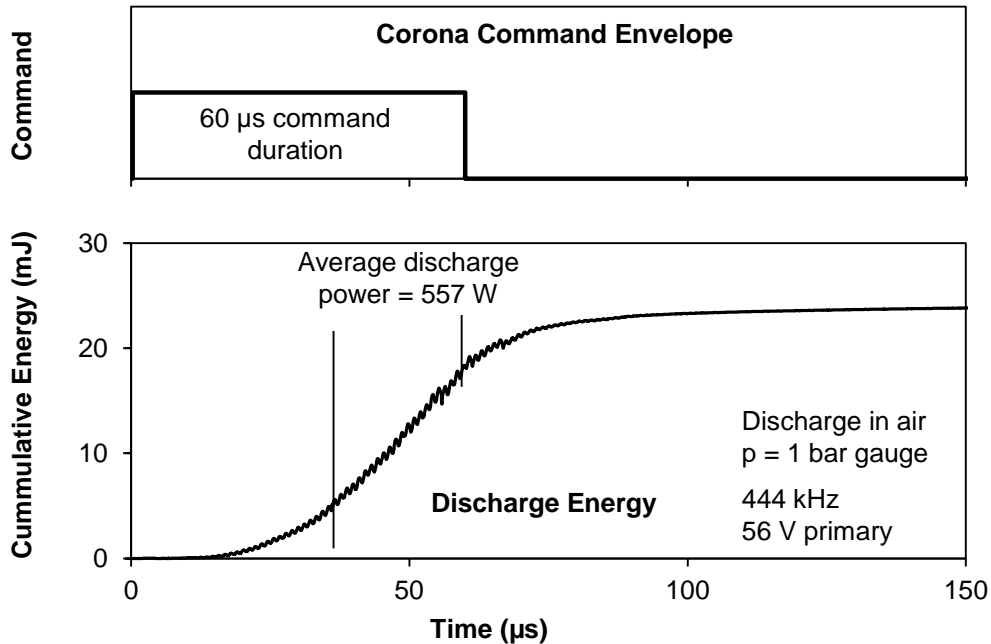


Figure 7-3: Corona Discharge Power Curve

The corona system resonance response to driver frequency is shown in Figure 7-4. The resolution of the control frequency was limited to approximately 10 kHz steps due to the limitations of the FPGA-RT control module for digital control, which operated with 25 ns cycle time. The peak resonance was achieved at 434.8 kHz (46 FPGA-RT cycles). The response curve was sufficient broad that a second control frequency at 444.4 kHz (45 FPGA-RT cycles) was possible with nearly the same voltage amplification potential. The amplitude of resonance response at approximately 10 kHz deviation from the peak frequencies was approximately halved. The driver frequencies in the following tests were generally selected to achieve maximum voltage amplification. The dynamic control of driver frequency control can offer a fast control mechanism for the corona discharge, particularly if the primary voltage control speed is limited by available hardware.

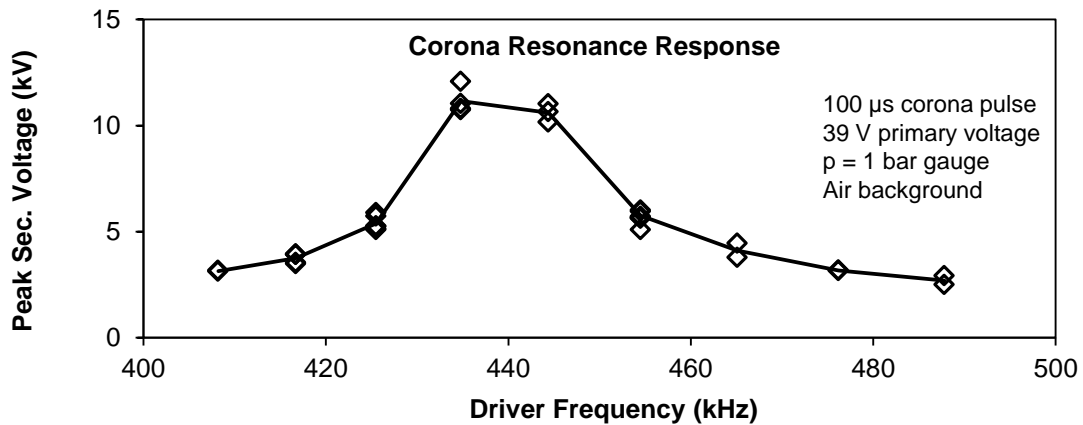


Figure 7-4: Discharge Voltage as a Function of Frequency

### 7.1.2 Physical Discharge Characteristics

The physical appearance of the corona is shown in Figure 7-6. The recording parameters are shown in Figure 7-5. The images were taken in air at 1 bar gauge pressure and with commanded discharge duration of one millisecond. The exposure time of each frame was 9  $\mu$ s, with an interframe time of 11.25  $\mu$ s. The visible field of view (FOV) is a 9 mm by 9 mm. The first visible discharge occurred in the frame 66  $\mu$ s after the start of the command signal and two main streamer branches formed. The visible streamers grew in length over the next few frames, with the full extent of the streamer penetration achieved in the first 150  $\mu$ s. At this pressure and moderate discharge voltage of 12 kV, the persistence of the existing streamer branches was high and relatively little re-branching occurred.

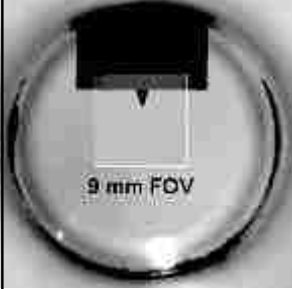
	Recording resolution	128 × 128 pixels
	Nominal spatial resolution	70.3 μm per pixel
	Frame rate	88,888 frames per second
	Interframe time	11.25 μs
	Exposure	9 μs
	Lens	Nikon 105 mm f/2.8

Figure 7-5: Image Field and Recording Parameters

When the voltage is increased, the streamer penetration increases and may reach a grounding surface in the combustion chamber. An example of this behavior is shown in Figure 7-7, when the secondary voltage is increased to 13 kV. The first visible discharge occurred in the frame 49 μs after the start of the corona command and again two main streamer branches were formed. The left streamer branch grew to be longer than the visible field of view, and by 172 μs had reached the chamber opposing surface. This resulted in the establishment of an arc discharge. This disrupted the voltage amplification resonance of the secondary circuit and the discharge ceased in the subsequent image frame. The resonance quickly re-established and a corona streamer reformed by 195 μs. The location of the new streamer channel was the same as the previous streamer and arc path. An arc again formed by 217 μs and this process would repeat a total of 15 times during the discharge.

The achievable streamer penetration and the appearance of the streamers change under increased background pressure. A case of discharge in air at 22 kV with 6 bar gauge pressure is shown in Figure 7-8. The first visible discharge occurred in the frame 31 μs after the start of the corona command. Over the next three frames, the streamer extended in length while at the same time became more convoluted. In the time interval

of 76 – 144  $\mu\text{s}$ , the reach of the streamer began to reduce in length. The discharge thereafter established a new streamer branch and repeated the growth and recession steps. At the time instance of 223  $\mu\text{s}$ , branched streamer profile was observed. Following the cessation of the corona driver input after 1 ms, the streamer gradually reduced and disappeared within 42  $\mu\text{s}$ .

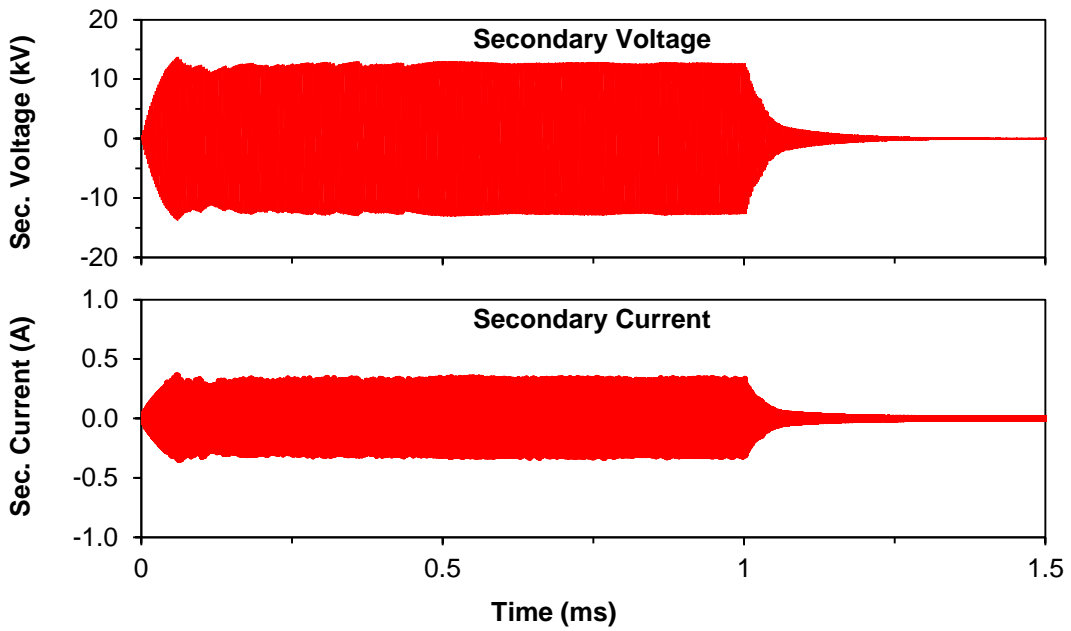
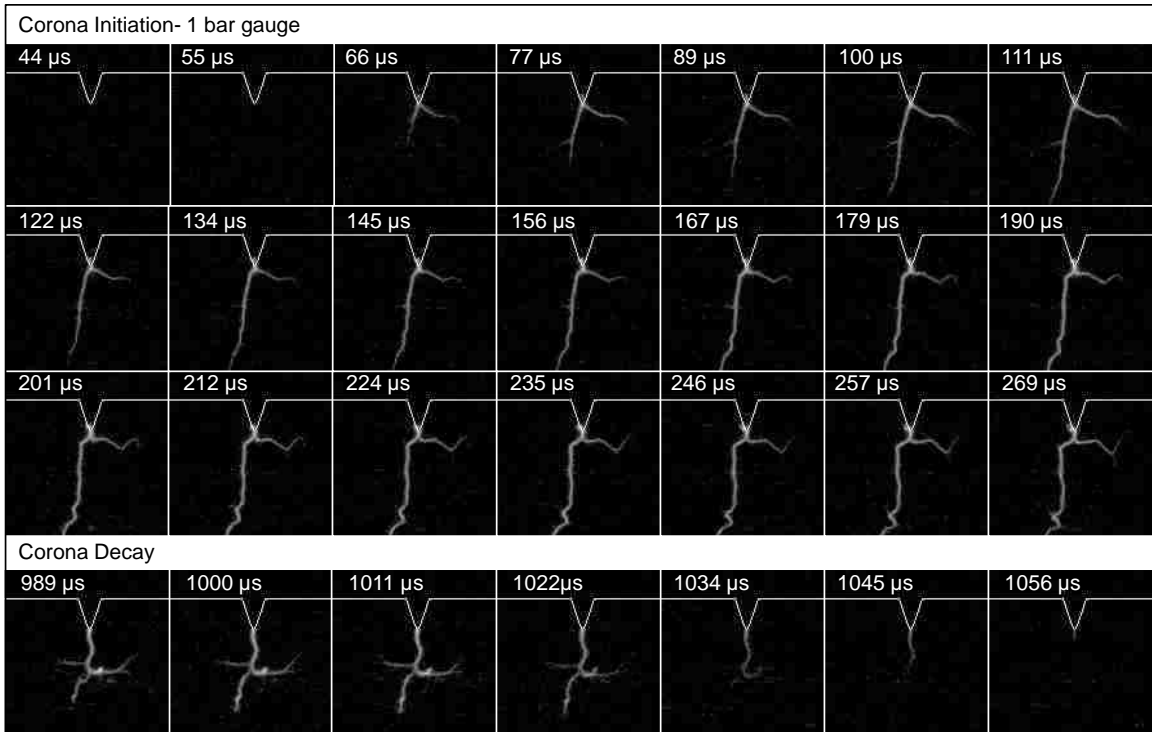


Figure 7-6: High-speed Image Sequence of Corona Discharge

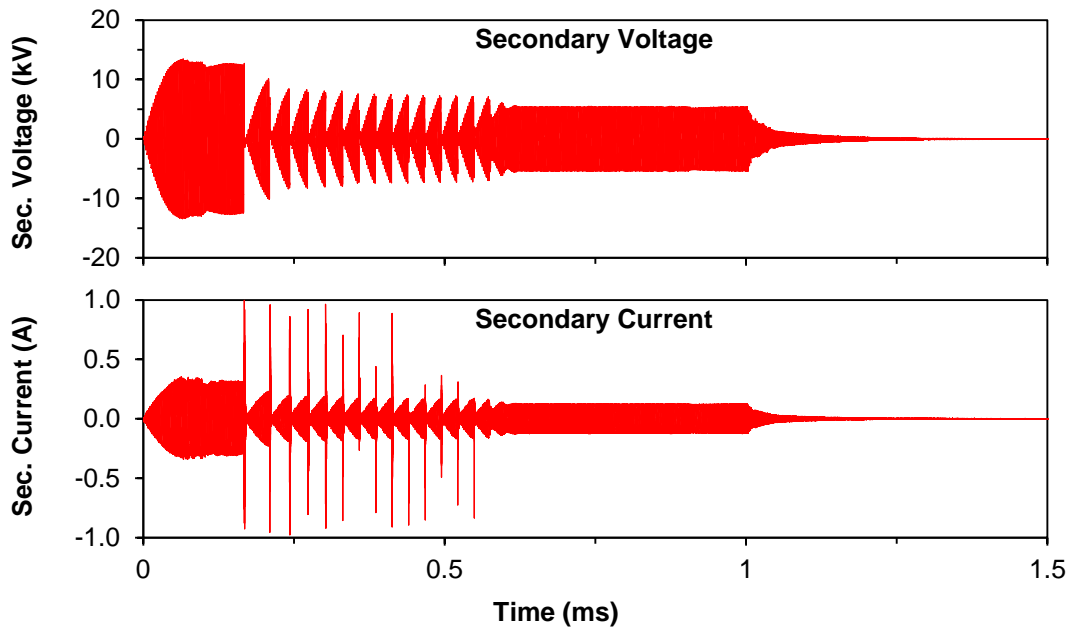
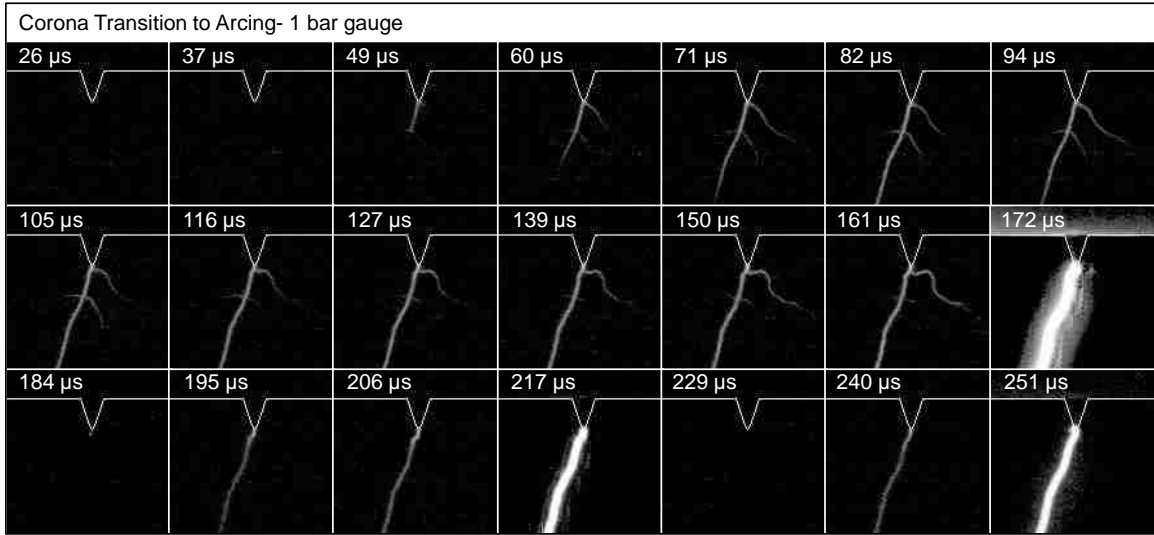


Figure 7-7: High-speed Image Sequence of Corona Transition to Arcing



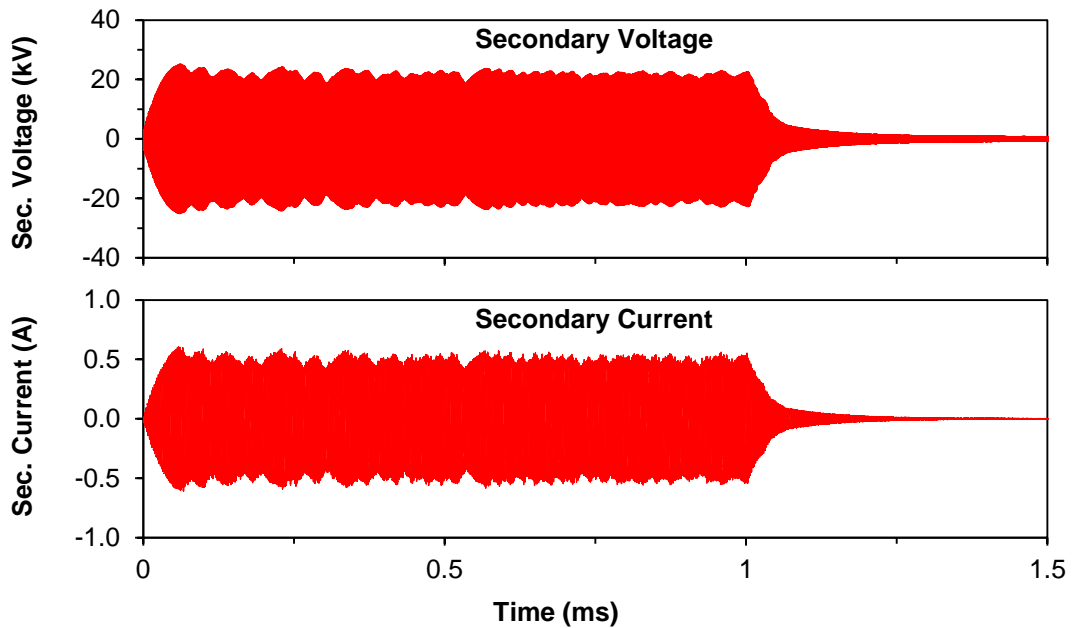
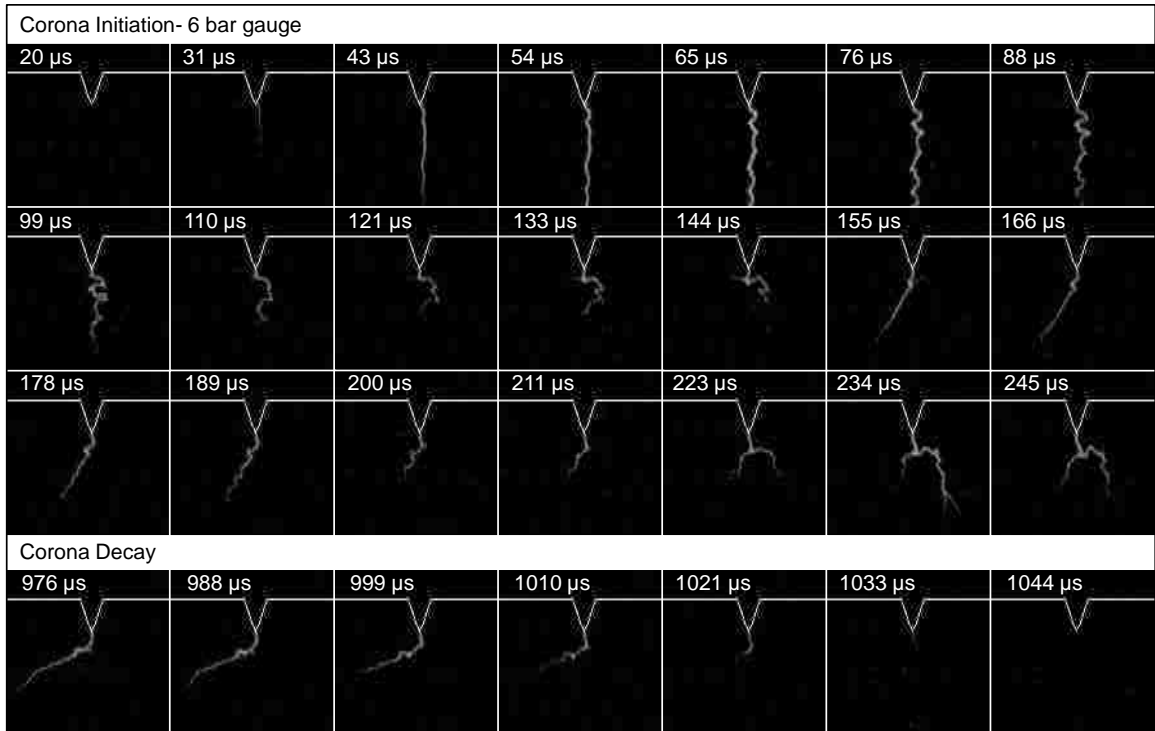


Figure 7-8: Formation of Corona Streamer at Higher Pressure

The visible streamer diameter was typically observed to be on an order of 0.1 – 0.2 mm. The transfer of thermal energy by the streamer to the gas media was observable in shadowgraph imaging. The visible emissions of the streamers were typically not strong enough to appear on the shadowgraph recording, so the captured image was exclusively of the density graduation caused by the heating of the gas media. The size of the thermally influenced zone was significantly larger in diameter than the visible emissions. Under continuous corona discharge, the shadowgraph image had the appearance of a fluid stream emanating from the electrode tip. An example of this effect in pure air is shown in the top strip in Figure 7-9. The phenomenon of corona discharge generated gas flow is called the corona wind [47]. This is caused by the net motion of a flow of ions under the electrical field. This can positively influence the initial flame kernel development by generating a flow field, increasing the turbulence and mixing. The effect can be dramatic under quiescent conditions at longer discharge durations. The presence of the induced flow is shown positively in the bottom strip of Figure 7-9 in its interaction against a laminar flame front. A spark-ignited flame front was initiated opposite of the corona igniter, in a stoichiometric charge of methane-air. A corona discharge of 10 ms duration was used to induce the corona wind. The corona discharge voltage was selected to be below the threshold for ignition. The flow disturbance on the laminar flame front was readily visible in the recorded images. Here the corona wind flow direction acted against the laminar flame propagation. In the case of ignition initiated by the corona, the corona wind effect would have the effect of expanding the flame reaction zone.

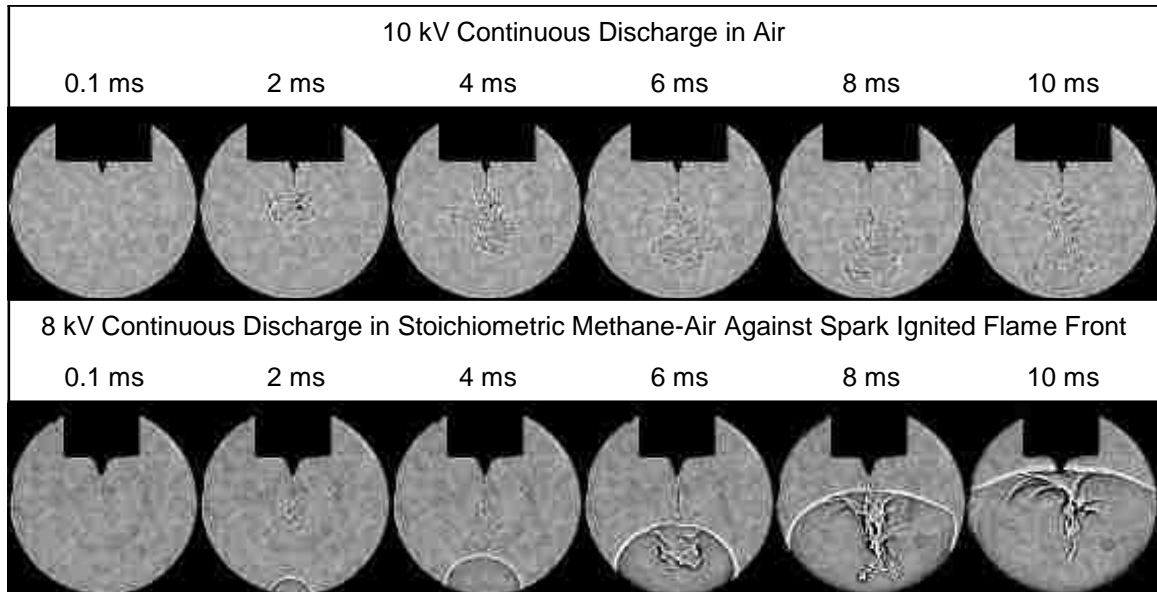


Figure 7-9: Corona Wind Effect in Air and Combusting Mixture

## 7.2 Control of Discharge in Air

### 7.2.1 Discharge Voltage Control

The strength of the streamer discharge is strongly influenced by the background pressure. At a constant voltage, the streamer penetration is shorter under higher pressures. Under higher pressures, electrons and ions lose energy to more frequent collisions and have a reduced likelihood of attaining sufficient kinetic energy for further ionization [44]. This can be partially overcome by increasing the electrical field strength through higher voltage under a fixed oscillation frequency. This can maintain the penetration of the discharge, as shown in Figure 7-11, where the images of the discharge in air at ambient pressure, 1 bar gauge, and 6 bar gauge pressures are compared. The image recording parameters are shown in Figure 7-10. The corona discharge durations were 1 ms in all cases. The primary voltage ranged from 25 V to 63 V. In cases where the streamer

growth rate was high enough that the ground electrode was reached, an arc was formed. A case of arcing discharge is shown for each pressure in Figure 7-12.


	Recording resolution	5472 × 3648 pixels
	Nominal spatial resolution	22.7 μm per pixel
	Frame rate	Single frame
	Exposure	167 μs
	Lens	Nikon 105 mm f/2.8

Figure 7-10: Image Field and Recording Parameters


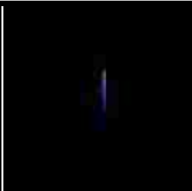


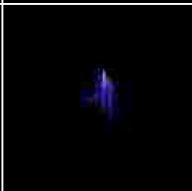





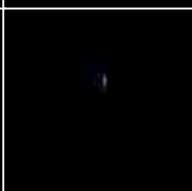
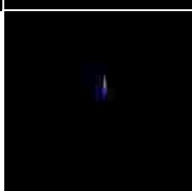
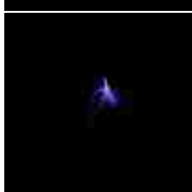

Primary Voltage	Gauge Pressure		
	0 bar	1 bar	6 bar
25 V			
32 V			
35 V			
42 V			
49 V			
56 V			
63 V			

Figure 7-11: Pressure and Voltage Effect on Corona Discharge

Gauge Pressure and Primary Voltage		
0 bar	1 bar	6 bar
35 V	42 V	63 V

Figure 7-12: Examples of Arcing Conditions

### 7.2.2 Discharge Duration Control

In addition to the increase of voltage to achieve greater corona discharge effect, an increase of duration is also a viable way to overcome the effects of pressure and to increase the discharge energy.

Figure 7-13 illustrates the corona discharge at 1 bar and at 6 bar gauge pressure for discharge durations ranging from 0.1 ms to 4 ms. At a discharge duration of 0.1 ms, the discharge was established briefly and only faintly visible. At a discharge duration of 0.25 ms, the full extent of the discharge penetration distance at the pressure and voltage condition was reached. Increasing the duration further resulted in a greater number of sequential streamers and spatial coverage, but not the penetration. The cases at 2 ms and 4 ms discharge duration, at a background of 1 bar pressure, also exhibited some discharge along the bottom surface of the ceramic. This discharge was suppressed at the higher pressure condition.

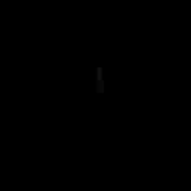

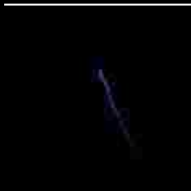
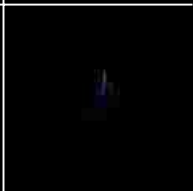

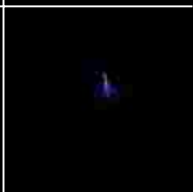

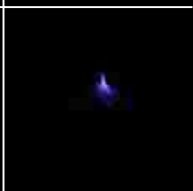




Corona Duration	Gauge Pressure	
	1 bar	6 bar
0.1 ms		
0.25 ms		
0.5 ms		
1 ms		
2 ms		
4 ms		

Figure 7-13: Pressure and Duration Effect on Corona Discharge

### 7.3 Non-thermal Plasma Ignition

#### 7.3.1 Flame Kernel Formation Process

The shadowgraph technique captures well the density gradient caused by the heating of the gas by the corona discharge, but is unable to record the corona streamers

themselves. It is only in the case of arcing that the visible emissions are strong enough to be captured by the shadowgraph setup. Direct imaging of the corona streamers conversely cannot capture the thermal effect of the corona. An experiment was conducted to simultaneously record the visible emissions on the shadowgraph bench by using a mirror splitter and a second high-speed camera in direct imaging configuration. The image recording parameters are shown in Figure 7-14.

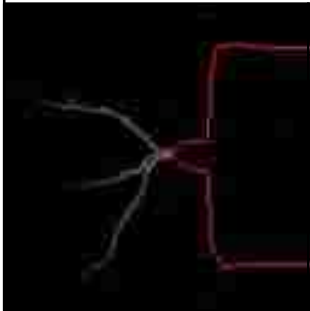

<b>Direct Image</b>		
	Recording resolution	128 × 128 pixels
	Nominal spatial resolution	125 μm per pixel
	Frame rate	50,000 frames per second
	Interframe time	20 μs
	Exposure	19 μs
	Lens	Nikon 50 mm f/1.4
<b>Schlieren Image</b>		
	Recording resolution	256 × 256 pixels
	Nominal spatial resolution	58.5 μm per pixel
	Frame rate	7,750 frames per second
	Interframe time	129 μs
	Exposure	80 μs
	Lens	Nikon 105 mm f/2.8

Figure 7-14: Image Field and Recording Parameters

The corona primary voltage used was 53 V and the discharge duration was 1 ms. The gas mixture was stoichiometric propane-air at 1 bar gauge pressure. The direct images of the discharge and ignition event are shown in Figure 7-15 in green and overlaid with the shadowgraph images in red. The direct image shows the corona appeared in the frame 32 μs after the command. The corona grew to three distinct and stable branches over the next 60 μs. Each visible image did not have a corresponding shadowgraph



image as the frame rate of the shadowgraph images was approximately 1/6<sup>th</sup> of the visible images due to the lower capabilities of the camera. Nonetheless, the emergence of the thermally affected zone was clear over the first three hundred microseconds. The corona streamers remained distinctly identifiable up to the frame at 872  $\mu$ s. The appearance of the later spatially diffuse visible emissions was from the flame luminescence. The electrode tip was a source of visible emissions later in the discharge due to electrode heating.

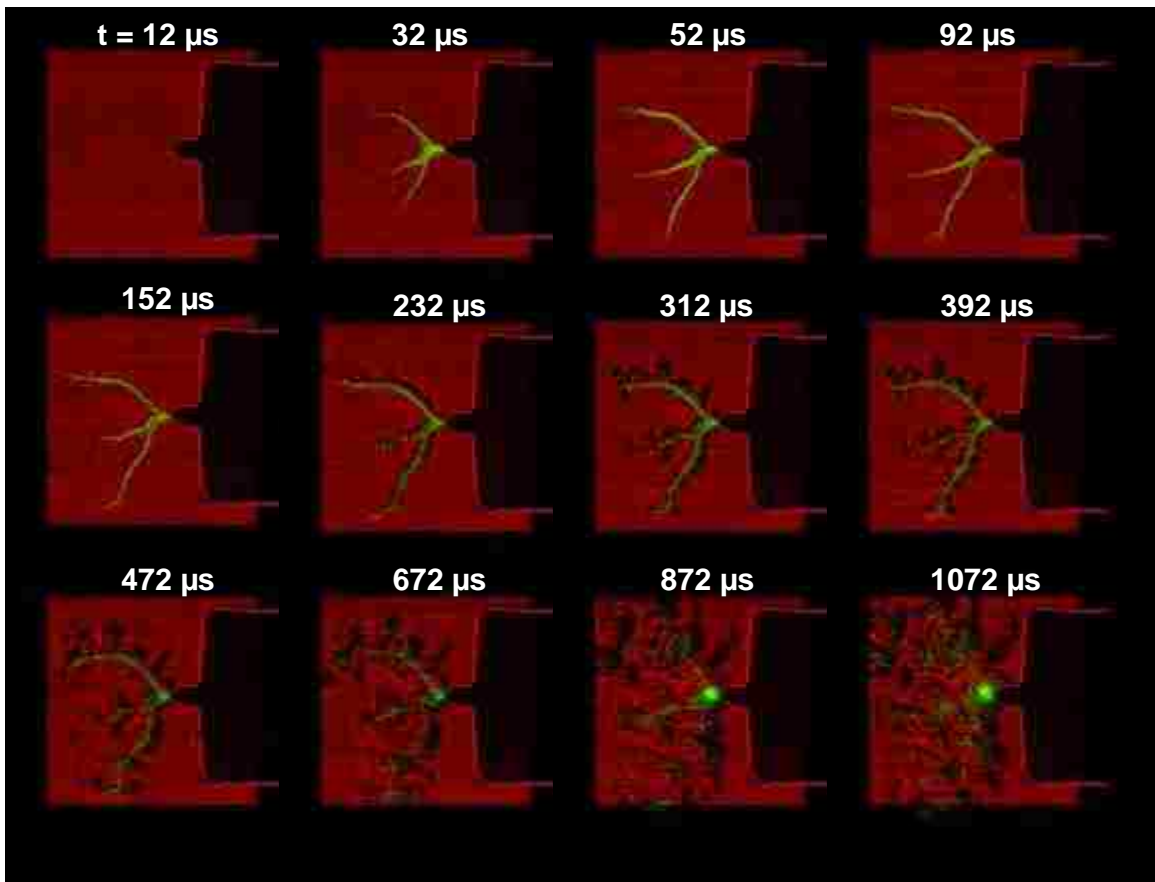


Figure 7-15: Direct Image Overlaid with Shadowgraph of Corona Ignition Event

### 7.3.2 Effect of Discharge Voltage

The effect of the corona control parameters of primary voltage and discharge duration on the ignition event were examined in a series of tests. The corona voltage has an impact on the corona penetration, electrical power, and to a certain extent the degree of streamer branching. The discharge and subsequent flame propagation from a short 80  $\mu$ s corona pulse at primary voltages ranging from 35 V to 53 V are shown in Figure 7-16. A case of conventional spark ignition is shown for comparison. At the lowest primary voltage, three corona streamer branches were formed in the image sequence recorded. However, only one site of ignition occurred, in the main trunk of two streamer branches near the electrode tip. The sustainable flame kernel was formed near the electrode tip because of the higher plasma intensity near the tip. The initial density gradients created in the other branches dissipated after approximately 1 ms as ignition failed. The successfully formed kernel expanded in a smooth, spherical fashion.

When the primary voltage was increased to 45 V and 49 V, ignition was observed to originate from two distinct streamer branches. Furthermore, the flame kernels were elongated in cylindrical fashion along the streamer path. The combined flame expansion from the multiple sites occurred at a significantly faster rate from the increased flame surface area. When the primary voltage was increased to 53 V, the discharge reached the surface of the combustion vessel and an arc discharge occurred. The result was a fully cylindrical flame kernel.

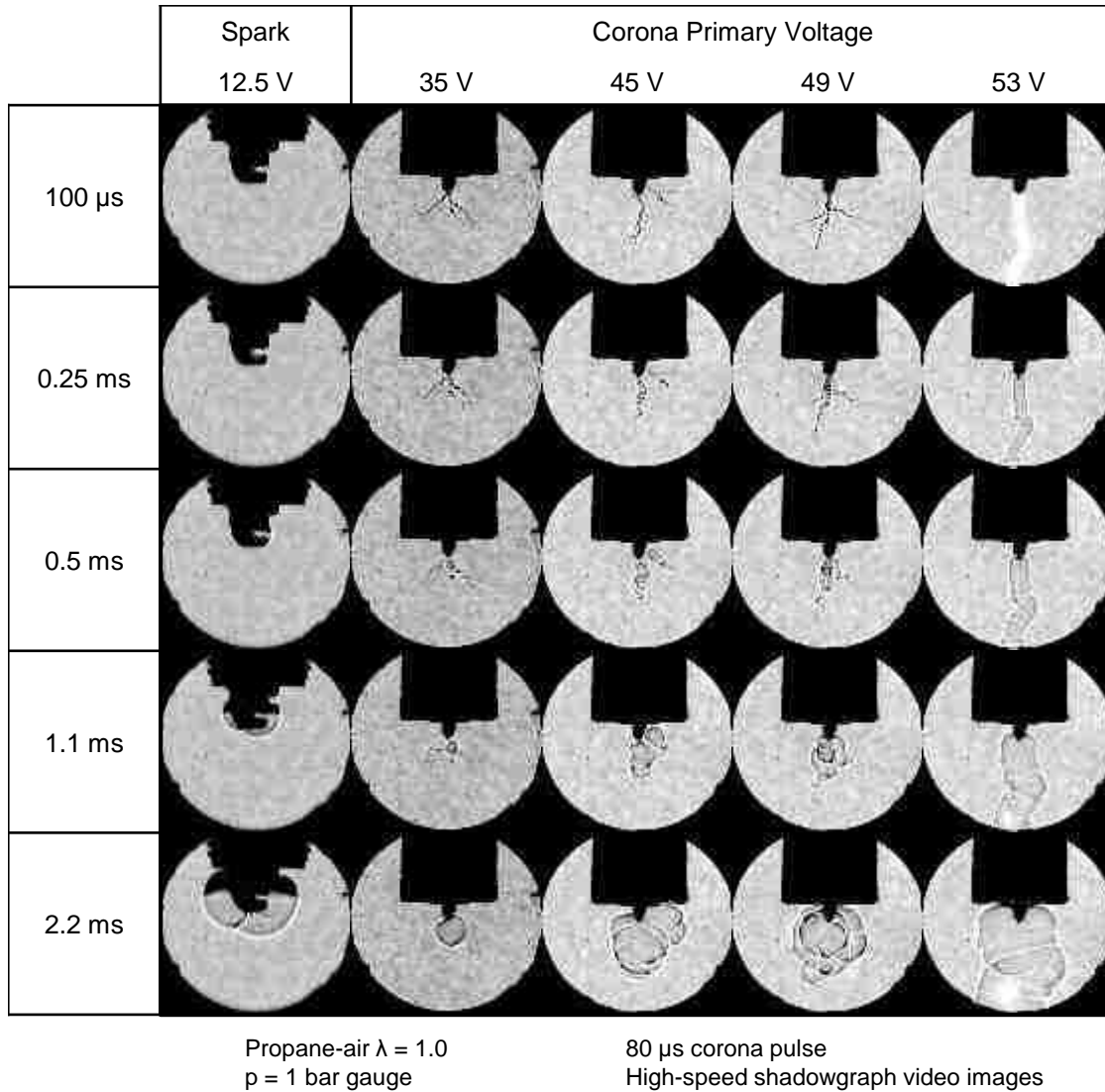


Figure 7-16: Shadowgraph Images of Corona Voltage Effect on Ignition

The cross-sectional area enclosed by the discharge and flame kernel was computed to quantify the different growth rates. The time plot of the flame areas is shown in Figure 7-17. For the 35 V primary voltage case, the shadowgraph discharge envelope grew to 7 mm<sup>2</sup> after 250  $\mu$ s, but shrunk as some of the streamer branches failed to ignite and the thermal gradient dissipated. The single successful kernel was responsible for the increase in the shadowgraph area from the time of 0.5 ms onwards.

With the higher primary voltages of 45 V and 49 V, the discharge immediately achieved a larger shadowgraph area and continued to expand. The flame growth rate of these cases approximated that of the conventional spark plug ignition. The case of the arcing discharge at 53 V primary voltage resulted in the largest initial kernel and fastest flame growth rate due to the extreme length of the initial kernel along the path of the arc.

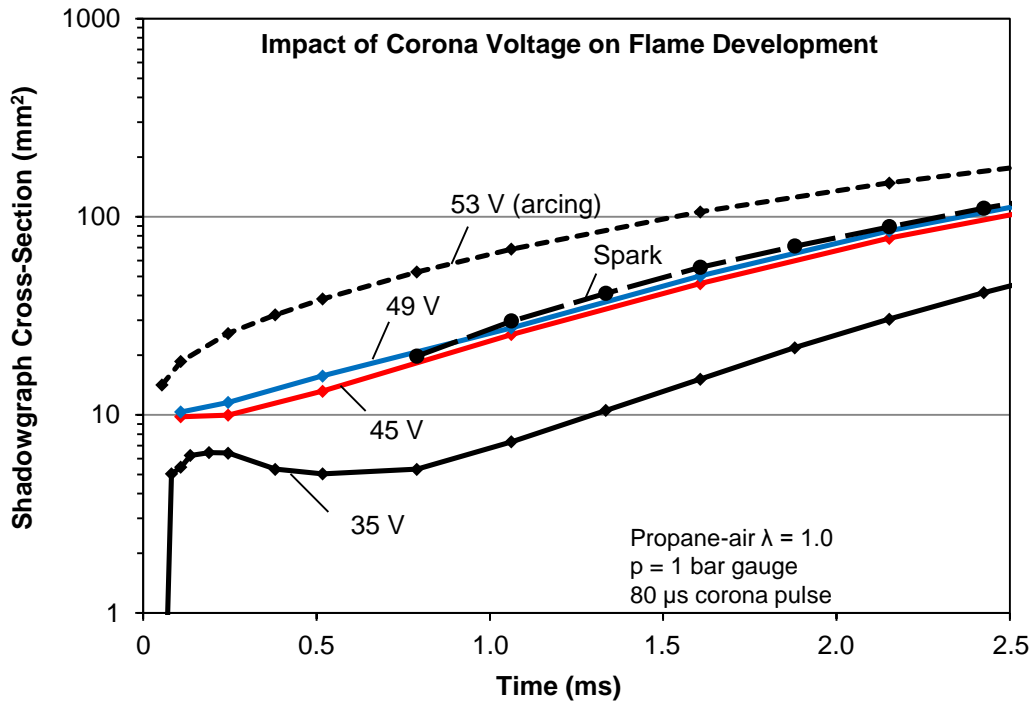


Figure 7-17: Shadowgraph Area of Corona under Different Voltage Conditions

### 7.3.3 Effect of Discharge Duration

When the corona duration is extended beyond the minimum necessary for ignition, the follow-up energy supply enhances the flame growth along the discharge branches. In addition, the flame surface becomes highly wrinkled due to the branched nature of the discharge and the effect of corona wind. The increase in surface area from the wrinkling significantly enhances the flame growth rate. This effect is seen in Figure 7-18 where a

range of discharge durations are compared, from the minimum necessary 80  $\mu\text{s}$  for ignition at this condition to 1 ms duration. When the discharge duration was increased to 100  $\mu\text{s}$ , the initial flame kernel was bigger in size, but still largely smooth and spherical, propagating from one initial site. At durations of 150  $\mu\text{s}$  and 250  $\mu\text{s}$ , the flame kernel formed consisted of the entire streamer length. The flame surface showed more wrinkles and was somewhat cellular in nature. At 1 ms duration, the continued corona discharged caused the flame to be highly convoluted, with the flame wrinkling at small scales.

The computed cross-sectional areas enclosed by the discharge and flame kernel are shown in Figure 7-19. In the previous set of tests at 80  $\mu\text{s}$  duration, increasing the primary voltage increased the flame growth rate of the corona igniter, but only the arcing case exceeded the flame growth rate of the conventional spark. When the duration was increased, it was seen that the performance of the corona igniter exceeded that of the spark discharge at discharge durations as short as 150  $\mu\text{s}$ . When the duration was increased to 250  $\mu\text{s}$ , the flame growth rate achieved was comparable to that of the arc. Further increase of the discharge duration up to 1 ms increased the flame growth rate even more. However, discharge durations beyond 1 ms produced no significant increases in flame growth rate, as the flame growth exceeded the spatial reach of the corona discharge.

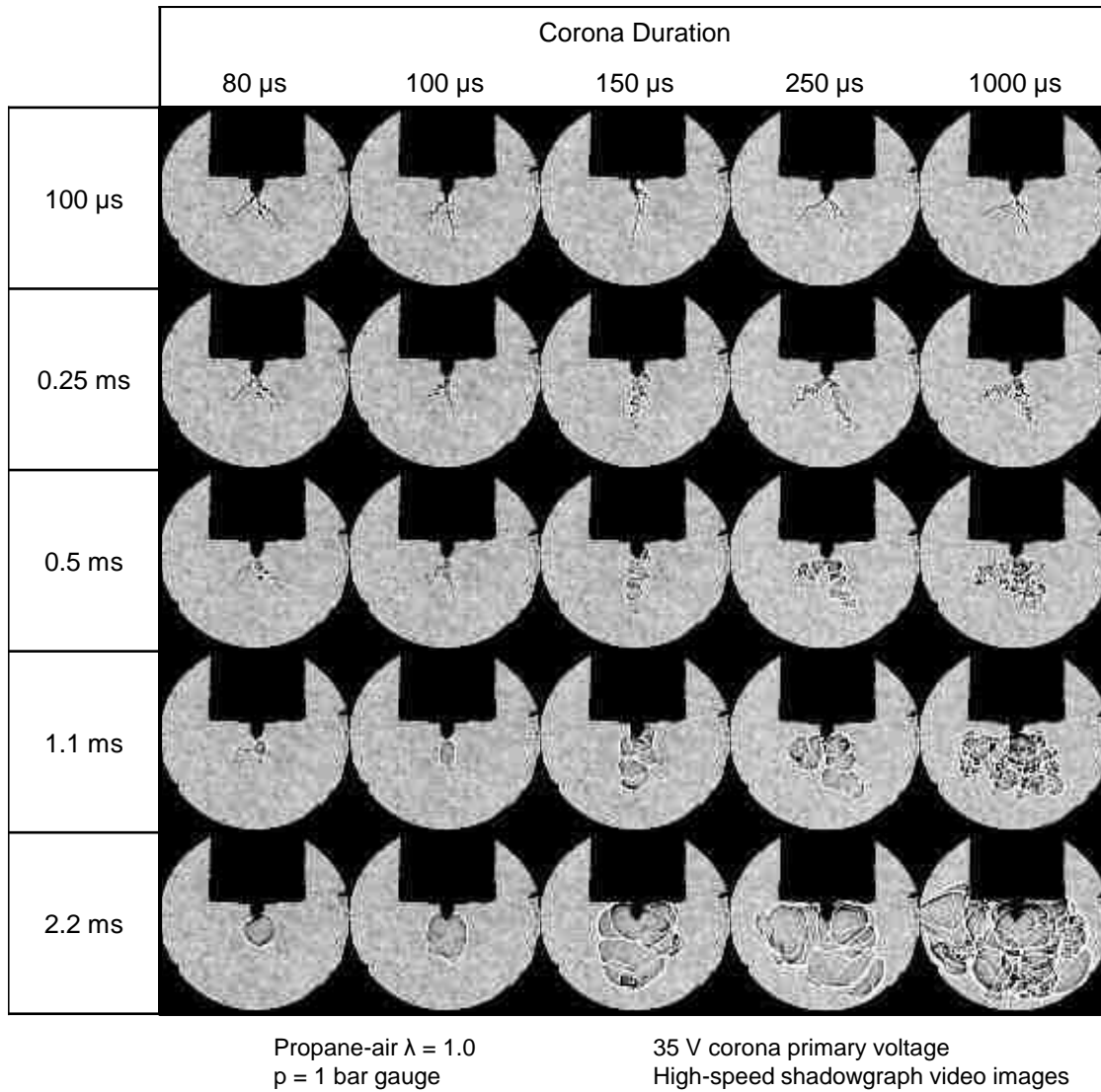


Figure 7-18: Shadowgraph Images of Corona Duration Effect on Ignition

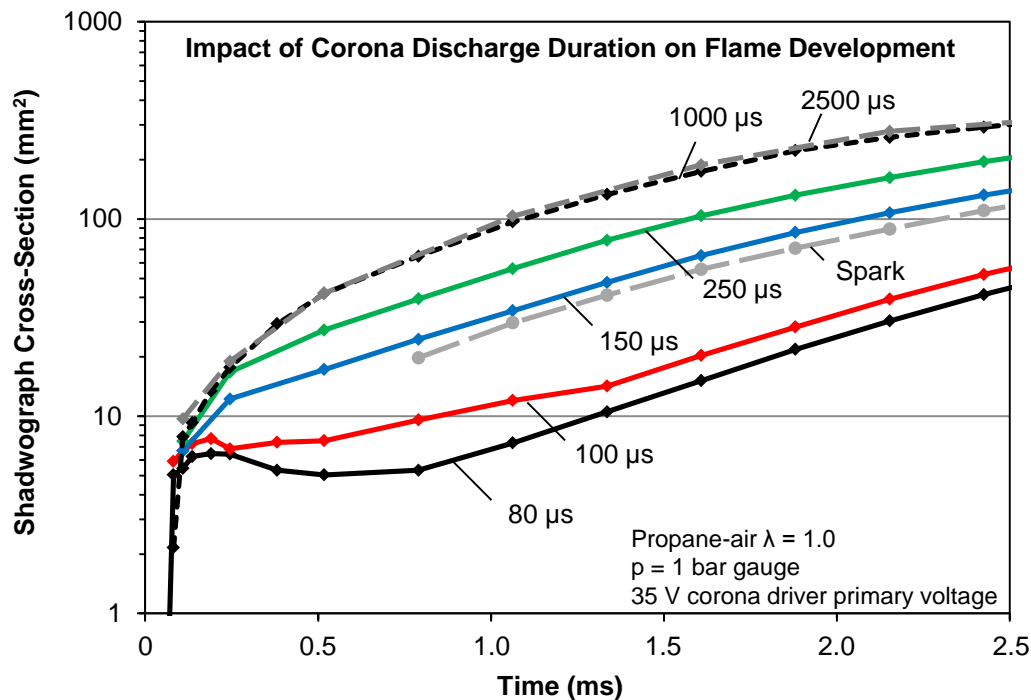


Figure 7-19: Shadowgraph Area of Corona under Different Discharge Durations

### 7.3.4 Minimum Discharge Durations for Ignition

The previous section showed that higher corona primary voltages and longer discharge durations were effective in enhancing the flame growth rate. The effect of voltage and duration at the lower boundary of ignition energy was also explored. At each primary voltage, the minimum discharge duration necessary for ignition was measured. The results for this test using methane-air at lambda 1.3 are shown in Figure 7-20. The required minimum discharge durations were reduced at higher primary voltages. This was expected as the discharge power correspondingly increased. However, the overall discharge energy required was observed to reduce. This indicates that a shorter, higher power discharge was more effective than a longer, lower power discharge. This may be explained by the observation that with lower power discharges, ignition may not form along many of the corona streamers. Thus energy may be dissipated by those streamers,

but do not contribute to the ignition. In the case of higher power discharges, the ignition threshold is reached earlier, thus require shorter discharge duration.

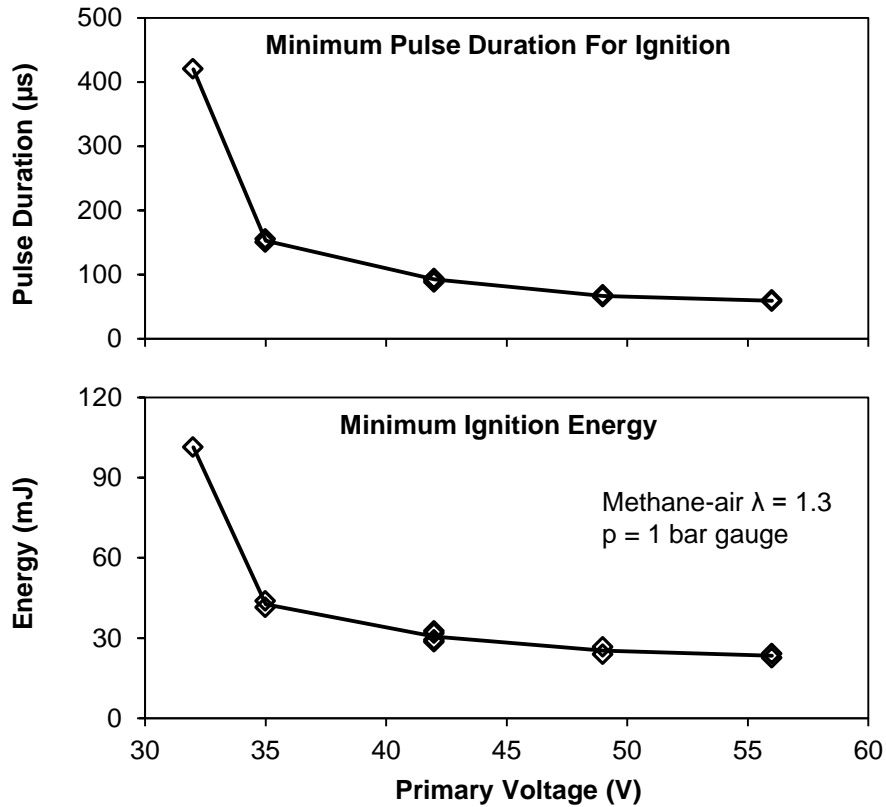


Figure 7-20: Effect of Corona Voltage on Minimum Ignition Energy

The effect of stoichiometry on the lower bound ignition energy was tested at a range of lambda from 0.9 to 1.6. The primary voltage was fixed at 42 V. The results are shown in Figure 7-21. The lowest ignition requirement occurred in the range lambda 1.1 to 1.2, with energy values in the 25 to 28 mJ range. The required ignition energy increased approximately two-fold at lambda 0.9 and 1.6.



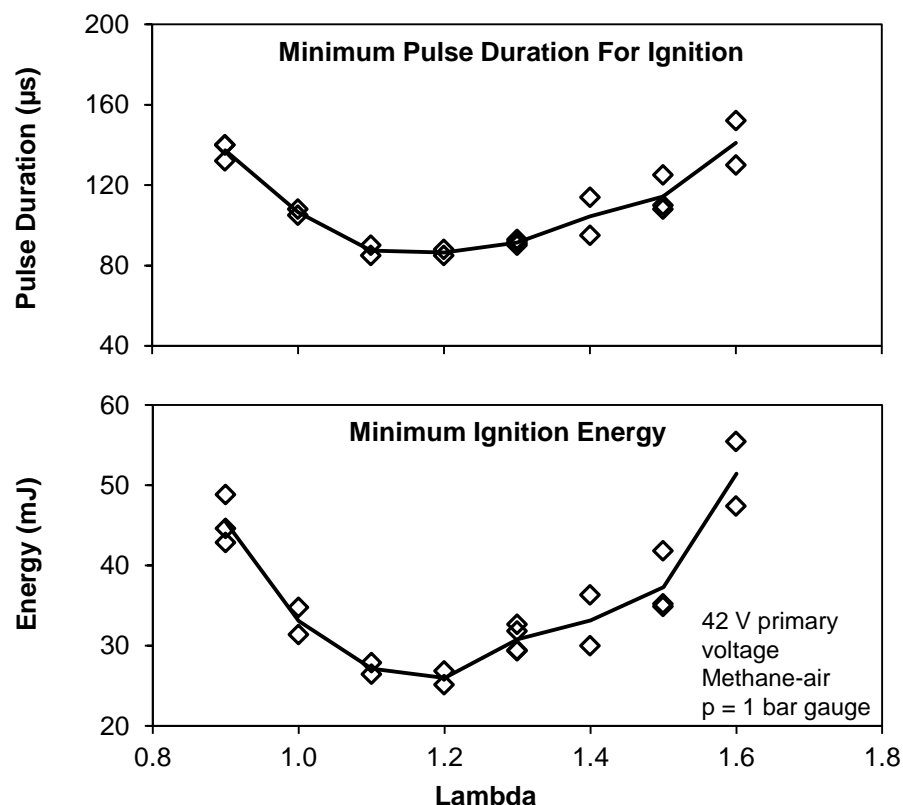


Figure 7-21: Effect of Lambda on Corona Ignition Energy

The effectiveness of corona for the ignition of ultra-lean methane-air mixtures was investigated in the CV1 combustion chamber. A corona duration sweep was conducted at a fixed primary voltage of 35 V. The corona discharge durations were 0.5 ms, 1 ms, and 3 ms. Additionally, a forced arcing condition was intentionally triggered by the use of a 140 µs, 46 V primary voltage pulse. The ignition success rates are shown in Figure 7-22. Increasing the discharge duration progressively increased the ignition success rate at the leaner conditions. The 1 ms condition performance was comparable to the performance of the reference spark plug. The 3 ms condition exceeded the performance of the reference spark plug. The arcing condition, however, had the highest ignition envelope, up to lambda 1.9.

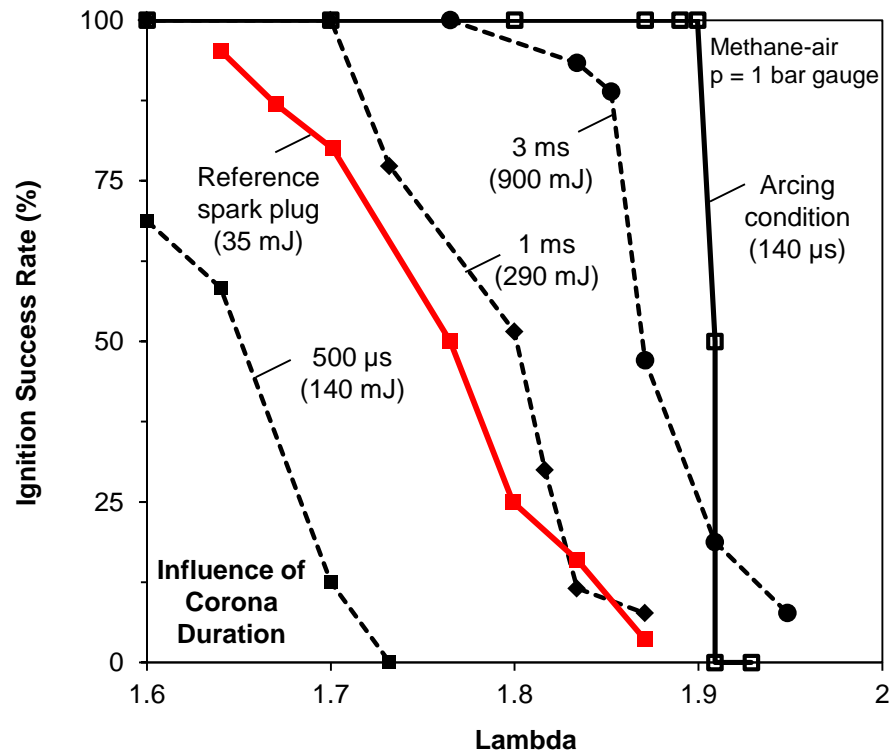


Figure 7-22: Influence of Corona Duration on Ignition Success Rate of Lean Mixtures

## 7.4 Plasma and Flame Interactions

### 7.4.1 Post-Ignition Flame Kernel Acceleration

The control of corona driver input signal frequency can offer a fast control mechanism for the corona discharge. This can be potentially used to prevent or correct the onset of arcing, or to generate a lower intensity of discharge. A test was conducted to examine the corona behavior when purposely offset from the peak resonance frequency. The test compared the effect of varying the voltage and duration of a secondary pulse following a main ignition pulse. The main ignition pulse was 200  $\mu\text{s}$  in duration and 10 kV in amplitude, followed by a 100  $\mu\text{s}$  wait. Then a secondary pulse was supplied. Pulse durations of 500  $\mu\text{s}$  and 1500  $\mu\text{s}$  with amplitudes of 4 kV and 10 kV were compared. Profiles of the discharge sequences are shown in Figure 7-23.

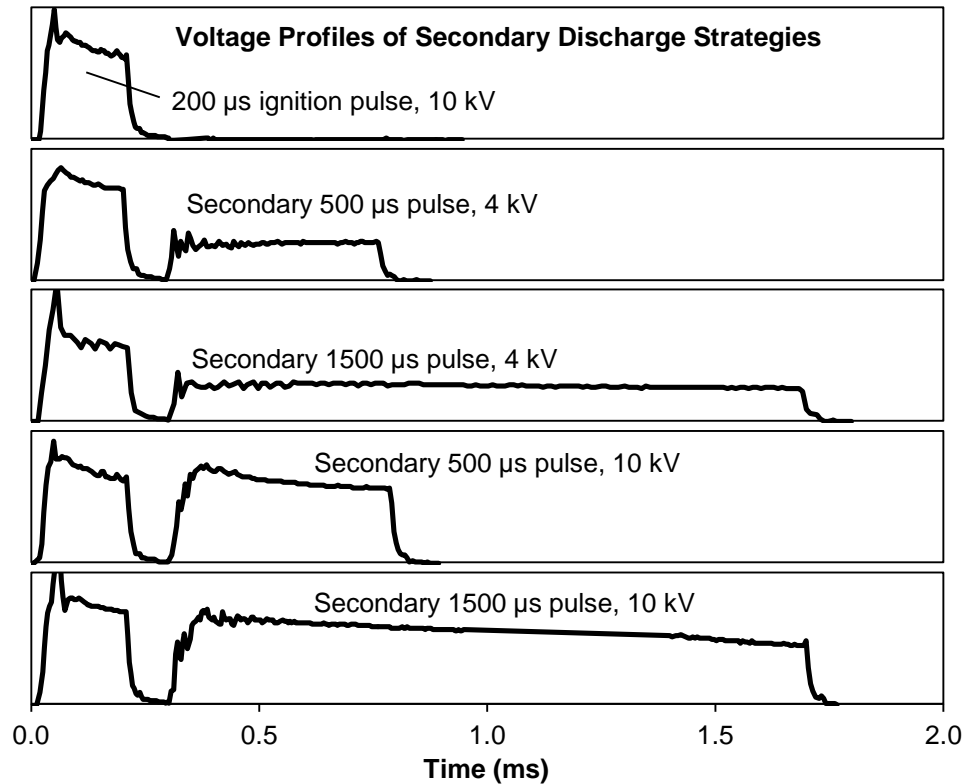


Figure 7-23: Discharge Profile of Post-Ignition Corona Pulse Strategy

Images from the shadowgraph video sequences captured in the test are shown in Figure 7-24. The initial main ignition pulse showed a high level of streamer branching in all cases. In the baseline case without the post-ignition corona pulse, ignition was secured in the larger streamer trunks. The extreme ends and smaller branches did not ignite and the early shadowgraph density gradients from the discharge dissipated. When the discharge was extended by a secondary pulse with 10 kV amplitude, the size of the ignition zone increased significantly. The longer duration discharge of 1500  $\mu$ s exhibited the highest degree of flame surface wrinkling.

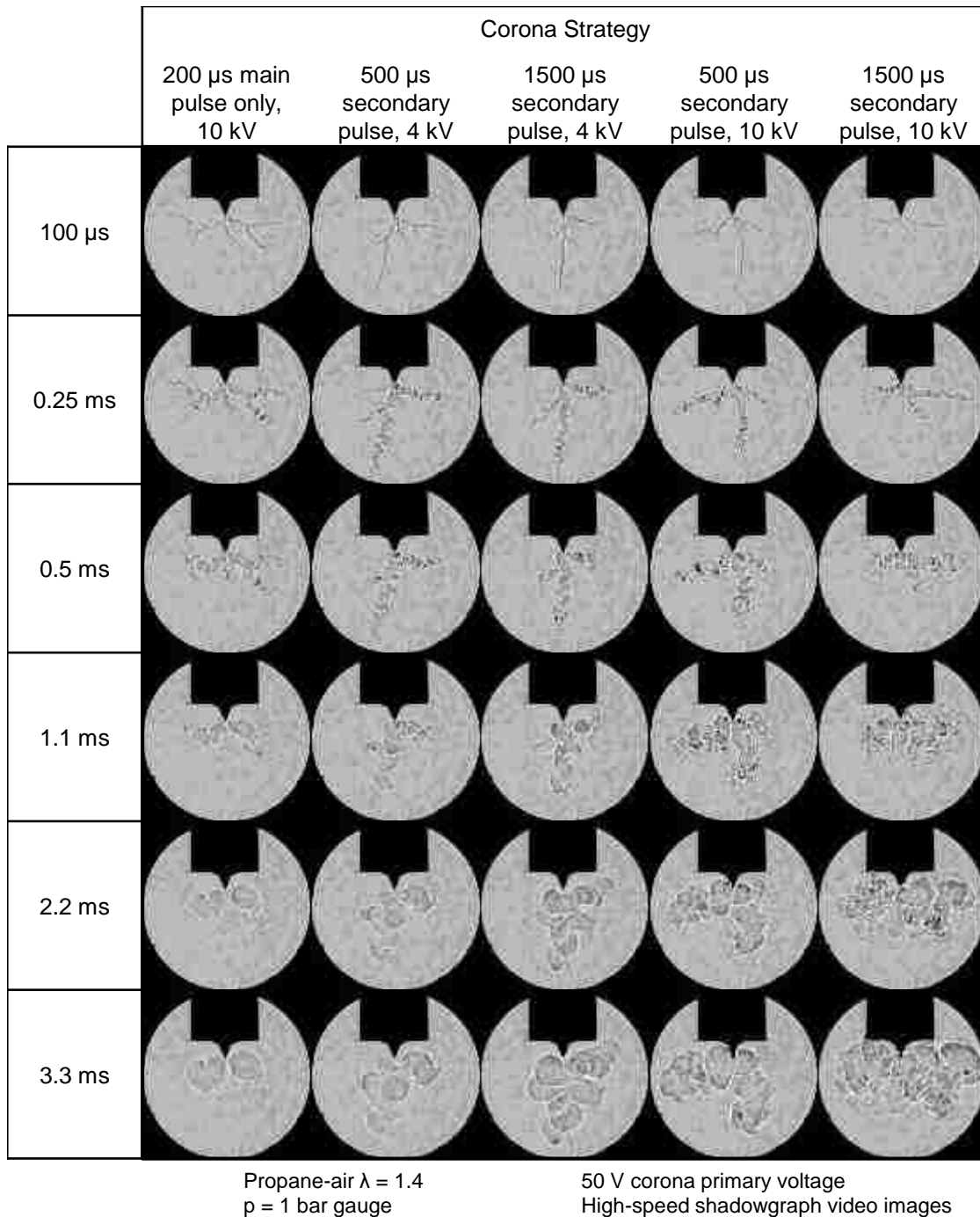


Figure 7-24: Shadowgraph Images of Post-Ignition Pulse Effect

The computed cross-sectional area enclosed by the discharge and flame are shown in Figure 7-25. At the 1.8 ms time step, the 10 kV secondary pulse cases flame areas were more than three times greater than the baseline ignition case. While the 10 kV

secondary pulse was effective, the results showed that even the lower voltage 4 kV secondary pulse was also quite effective. At this lower electrical field strength normally no visible corona discharge or density gradient in the shadowgraph image would be visible. However, in the combustion zone initiated by the main pulse, the chemical and thermal ionization from combustion provide the necessary ionization for the electrical field to transfer energy to the flame. The result was an enhancement of the flame kernel size and wrinkling, to a degree intermediate of the baseline and high voltage potential cases.

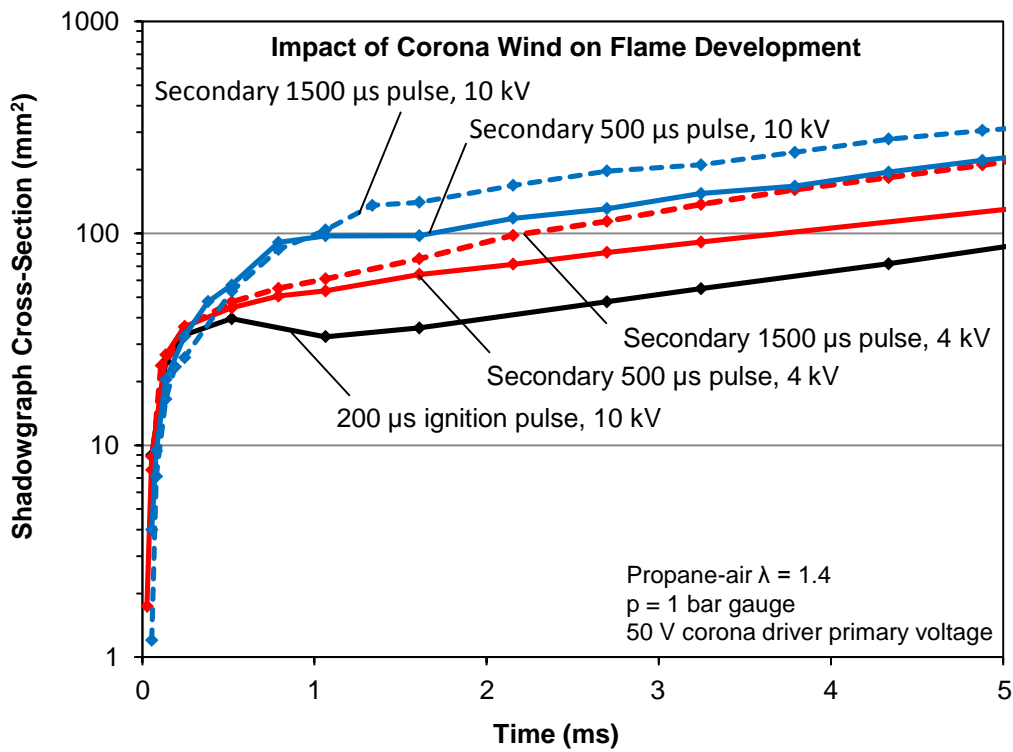


Figure 7-25: Shadowgraph Area of Post-Ignition Corona Pulses

## CHAPTER VIII

### CONCLUSIONS AND RECOMMENDATIONS

This chapter provides a summary of the main research results and the conclusions from the work performed. Recommendations for future research are also provided.

#### **8.1 Effect of Spark Ignition Energy and Energy Profile**

The effects of energy level in conventional inductive spark ignition systems were tested in quiescent combustion vessels. The energy level effects on the flame development by creating a larger initial flame kernel. The ultimate flame growth rate, however, is limited by the stoichiometry of the mixture. In the engine environment, where turbulence and organized flow greatly increase the speed of flame propagation, the effect of the energy level, at conventional quantities, was still measurable. The combustion phasing control afforded by increased energy could in most cases be achieved by the conventional timing control available. In ultra-lean or dilute conditions, however, scheduling the spark discharge very early to compensate for the slow combustion rate led to combustion instabilities and ultimately unreliable ignition. Enhancement of the peak discharge power via capacitor discharge and early spark energy with the high energy capacitor discharge had limited benefit. The multi-coil energy enhancement was more effective, indicating that the delivery of energy over a sufficiently long duration was as key aspect of effective ignition in engines.

#### **8.2 Multiple-Site Spark Ignition**

A prototype design of multi-pole spark plugs with three independent high voltage electrodes was tested in engine operation. The engine was tested with EGR and lean

dilution to identify the potential of the multi-pole spark plug to extend the engine operation limits beyond that of a conventional spark plug. The engine test results showed that when a single pole of the multi-pole spark plug was discharged, its performance was comparable to a conventional spark plug. When the three poles of multi-pole spark plug were commanded to discharge simultaneously, the combustion phasing was notably advanced. In addition, the performance boundaries exceeded those of the conventional spark plug. This enhancement was not entirely caused by the overall increase of total spark energy, as the effect was seen also at reduced spark energies. The result was the ability to operate at higher EGR rates or higher excess air ratios. The cyclic variations of the engine load and combustion phasing were also reduced. This resulted in an increase in thermal efficiency and a decrease in indicated NO<sub>x</sub> emissions in the case of lean dilution. Operation at high EGR rates did not achieve as high a gain in thermal efficiency as excess air dilution, but did result in lower NO<sub>x</sub> emissions.

### **8.3 Non-thermal Plasma Ignition**

A radio frequency non-thermal plasma ignition system developed in-house [54] was tested and its ability to address some of the shortcomings of the conventional ignition system investigated. The ignition volume created by the corona discharge was greater in size and its growth was impeded less because of the absence of a close ground electrode. The rapid energization and continuous discharge characteristic additionally offer a more flexible control path of ignition energy release. In tests under quiescent conditions in combustion chambers, the adjustments of the discharge voltage and duration afforded a high degree of control over the flame kernel initiation and growth. A short duration discharge can provide an ignition kernel that expands in a smooth, spherical fashion.

Longer discharges that continue to supply energy after the initial kernel formation greatly accelerate the flame expansion and create wrinkled flames with larger surface area and burn rates. The degree of streamer branching was found to be a function of the discharge voltage. The formation of multiple ignition sites was most favorable under higher discharge voltages.

#### **8.4 Application to Ultra-lean or High Dilution Ignition**

The multiple-site spark ignition method was most promising for operation at ultra-lean or high dilution ratios. In the comparison of EGR dilution versus excess air dilution, higher thermal efficiencies were possible with lean combustion, in part because of the higher dilution ratios achievable prior to the onset of combustion instability. At similar equivalent dilution ratios, the intake composition in the lean combustion case was more favorable in achieving thermal efficiency gains. However, the increase in fresh air flow and oxygen quantity resulted in little or no improvements to NO<sub>x</sub> emissions until high dilution levels were reached. In contrast, the use of exhaust dilution gas, with the presence of carbon dioxide in particular, was very effective in reducing the NO<sub>x</sub> emissions.

#### **8.5 Recommendations for Future Work**

The present study compared a number of production and new ignition systems for their performance in igniting well-mixed mixtures under high dilution conditions. Both constant volume combustion vessel and engine tests were conducted. There is further research work to be performed to identify the potential of ignition systems for future advanced combustion engines. In particular, the ignition phenomenon for high



turbulence, stratified mixtures are of great importance for future high efficiency engine developments. Future work needs to continue to address those challenging issues.

## REFERENCES

1. Homes, Keith. "A Century of Environmental Technologies for Light-Duty Vehicles," SAE International Journal of Engines, 10(2), 2017. doi:10.4271/2017-01-0119.
2. "Light-Duty Automotive Technology, Carbon Dioxide Emissions, and Fuel Economy Trends: 1975 Through 2017," The United States Environmental Protection Agency, EPA-420-S-18-001, 2018.
3. "EPA and NHTSA Set Standards to Reduce Greenhouse Gases and Improve Fuel Economy for Model Years 2017-2025 Cars and Light Trucks," The United States Environmental Protection Agency, EPA-420-F-12-051, 2012.
4. Lavoie, G., Ortiz-Soto, E., Babajimopoulos, A., Martz, J. B., and Assanis, D. N. "Thermodynamic Sweet Spot for High-Efficiency, Dilute, Boosted Gasoline Engines," International Journal of Engine Research, 14(3), 260-278, 2012. doi:10.1177/1468087412455372.
5. Heywood, John B. Internal Combustion Engine Fundamentals. McGraw-Hill Books, 1988. ISBN 0-07-100499-8.
6. Asad, U., Zheng, M., Han, X., Reader, G.T., Wang, M. "Fuel Injection Strategies to Improve Emissions and Efficiency of High Compression Ratio Diesel Engines," SAE International Journal of Engines, Vol 1, 1220-1233, 2008.
7. Dec, John. "Advanced Compression-Ignition Engines- Understanding the In-cylinder Process," Proceedings of the Combustion Institute, Vol 32, 2727-2742, 2009. doi:10.1016/j.proci.2008.08.008.

8. Wang, Z., Liu, H., Reitz, R. "Knocking Combustion in Spark-Ignition Engines," *Progress in Energy and Combustion Science*, Vol 61, 78-112, 2017. doi:10.1016/j.pecs.2017.03.004.
9. Krieger, R.B., and Borman, G.L. "The Computation of Apparent Heat Release for Internal Combustion Engines," ASME, 66-WA/DGP-4, 1966.
10. Jeftic, Marko. *Strategies for Enhanced After-Treatment Performance: Post Injection Characterization and Long Breathing with Low NOx Combustion*. Doctoral thesis. University of Windsor, 2016.
11. Klein, Marcus. *A Specific Heat Ratio Model and Compression Ratio Estimation*. Doctoral thesis. Linköping University, 2004. ISBN 978-91-628-7578-7.
12. Yaws, Carl. *Yaw's Critical Property Data for Chemical Engineers and Chemical Engineers and Chemists*. Knovel, 2012.
13. Robert Bosch GmbH. *Bosch Automotive Electrics and Automotive Electronics*. ISBN 978-3-658-01783-5. Springer Vieweg, 2007.
14. Stone, C. R., Steele, A. B. "Measurement and Modelling of Ignition System Energy and Its Effect on Engine Performance," *Proceedings of the Institution of Mechanical Engineers*, Vol 203, 277-286, 1989.
15. Van Basshuysen, R., and Schafer, F. *Internal Combustion Engine Handbook: Basics, Components, Systems, and Perspectives*. SAE, 2016. ISBN 978-0-7680-8024-7.
16. Warnatz, Jurgen. *Combustion*. Berlin: Springer, 2006. ISBN 3-540-67751-8.
17. Law, Cheng K. *Combustion Physics*. Cambridge: Cambridge University Press, 2006. ISBN 978-0-521-87052-8.

18. Nakata, K., et al. "Engine Technologies for Achieving 45% Thermal Efficiency of S.I. Engine," SAE International Journal of Engines, Vol 9, 2016. doi:10.4271/2015-01-1896.
19. Lerner, Louise. "Combining Gas and Diesel Engines Could Yield Best of Both Worlds," Argonne National Laboratory, May 4, 2011.
20. Tracy, David. "Mazda's Holy Grail of Gasoline Engines is Completely Fascinating." Jalopnik, September 7, 2017. <https://jalopnik.com/mazda-s-holy-grail-of-gasoline-engines-is-completely-1801820285>.
21. Adcock, Ian. "The Petro Engine That Thinks It's a Diesel: How Mazda's Compression-Ignition Skyactiv-X Engine Works," Car Magazine, September 6, 2017. <http://www.carmagazine.co.uk/car-news/tech/the-petrol-engine-that-thinks-its-a-diesel-how-mazdas-compression-ignition-skyactiv-x-engine-works/>.
22. Stoklosa, Alexander. "Driving Mazda's Next Mazda 3 with Its Skyactiv-X Compression-Ignition Gas Engine." Car and Driver, September 14, 2017. <https://www.yahoo.com/news/driving-mazda-apos-next-mazda-171500129.html>.
23. Kuo, Kenneth. Principles of Combustion. John Wiley & Sons, 2005. ISBN 0-471-04689-2.
24. Lee, K., Bae, C., Kang, K. "The Effects of Tumble and Swirl Flows on Flame Propagation in a Four-Valve S.I. Engine," Applied Thermal Engineering, Vol 27, 2122-2130, 2007. doi:10.1016/j.applthermaleng.2006.011.
25. Schneider, A., Raindl, M., Dumser, F. "Analysis of the Flame Kernel Formation in a SI Engine with Diluted Charge Using Optical Measurement Techniques," Ignition Systems for Gasoline Engines, 3rd International Conference. November 3-4, 2016, Berlin, Germany.

26. Saxena, Samveg, and Bedoya, Ivan. "Fundamentals Phenomena Affecting Low Temperature Combustion and HCCI Engines, High Load Limits and Strategies for Extending These Limits," *Progress in Energy and Combustion Science*, Vol 39, 457-488, 2013. doi:10.1016/j.pecs.2013.05.002.
27. Chang, K., Babajimopoulos, A., Lavoie, G. A., Filipi, Z. S., and Assanis, D. N. "Analysis of Load and Speed Transitions in an HCCI Engine Using 1-D Cycle Simulation and Thermal Networks," SAE Technical Paper, 2006-01-1087, 2006.
28. Persson, Hakan. *Spark Assisted Compression Ignition*. Doctoral thesis. Lund University, 2008. ISBN 978-91-628-7578-7.
29. Weinrotter, M., Wintner, E., Iskra K., et al. "Optical Diagnostics of Laser-Induced and Spark Plug-Assisted HCCI Combustion," SAE Technical Paper, 2005-01-0129, 2005.
30. Persson, H., Hultqvist, A., and Johansson, B. "Investigation of the Early Flame Development in Spark Assisted HCCI Combustion Using High Speed Chemiluminescence Imaging," SAE Technical Paper, 2007-01-0212, 2007.
31. Lavoie, G., Martz, J., Woolridge, M., Assanis, D. "A multi-mode combustion diagram for spark assisted compression ignition," *Combustion and Flame*, 157 (6), 1106-1110, 2010. doi:10.1016/j.combustflame.2010.02.009.
32. Tauer, J, Kofler, H., Iskra, K., Tartar, G., Winter, E. "Laser Plasma-Initiated Ignition of Engines," *Proceedings of the 3<sup>rd</sup> International Conference on the Frontiers of Plasma Physics and Technology*, S6-3, 2007.
33. Wang, Z., Huang, J., Wang, Q., Hou, L., Zhang, G. "Experimental Study of Microwave Resonance Plasma Ignition of Methane-Air Mixture in a Constant

- Volume Cylinder,” *Combustion and Flame*, 162(6), 2561-2568, 2015.  
doi:10.1016/j.combustflame.2015.03.004.
34. Nishiyama, A., Moon, A., Ikeda, Y., Hayashi, J., and Akamatsu, F. “Ignition Characteristics of Methane/Air Premixed Mixture by Microwave-Enhanced Laser-Induced Breakdown Plasma,” *Optics Express*, 21(6), A1094-101, 2013.  
doi:10.1364/oe.21.0a1094.
35. Schenk, A., Rixecker, G., Bohne, S., Becker, M., Budde, M. “The Corona Ignition System EcoFlash®: New Results with CNG Engines and Effects of Engine-Specific Boundary Conditions,” 2nd International Conference on Ignition Systems for Gasoline Engines, November 24–25, 2014, Berlin, Germany.
36. Bradley, D., et al. “Fundamentals of High-Energy Spark Ignition with Lasers,” *Combustion and Flame*, Vol 138, 55-77, 2004.
37. Schwarz, E., Muri, I., Tauer, J., Kofler, H., Winter, E. “Laser-Induced Ignition by Optical Breakdown,” *Laser Physics*, Vol 20 (6), 1543-1553, 2010.
38. Kopecek, H., et al. “Laser Ignition of Methane-Air Mixtures at High Pressures and Diagnostics,” *Journal of Engineering for Gas Turbines and Power*, Vol 127, 213-219, 2005.
39. Alger, T., Gingrich, J., Mangold, B., and Roberts, C. “A Continuous Discharge Ignition System for EGR Limit Extension in SI Engines,” *SAE International Journal of Engines*, 4(1), 677-692, 2011. doi:10.4271/2011-01-0661.
40. US Patent 9441604 (Application number 13/917,054, Provisional Patent filing US 61/702,469). "Multi-coil Spark Ignition System." Inventors: Ming Zheng, Shui Yu, and Kelvin Xie. Priority date: September 25, 2012. Issue date: September 13

2016. US application # US 13/917,054. US divisional Patent 15/238,886, file date Aug 17, 2016.
41. Yu, S., et al. "Multi-Coil High Frequency Spark Ignition to Extend Diluted Combustion Limits," Proceedings of the FISITA 2012 World Automotive Congress. Lecture Notes in Electrical Engineering, Vol 189. Springer-Verlag, 2003. doi:10.1007/978-3-642-33841-0\_17.
42. Jung, D., Sasaki, K., and Iida, N. "Effects of Increased Spark Discharge Energy and Enhanced In-Cylinder Turbulence Level on Lean Limits and Cycle-to-Cycle Variations of Combustion for SI Engine Operation," Applied Energy, 2017. doi:10.1016/j.apenergy.2017.08.043.
43. Sjöberg, M., Zeng, W., Singleton, D., Sanders, J. et al. "Combined Effects of Multi-Pulse Transient Plasma Ignition and Intake Heating on Lean Limits of Well-Mixed E85 DISI Engine Operation," SAE International Journal of Engines, 7(4), 2014. doi:10.4271/2014-01-2615.
44. Slade, Paul G. Electrical Contacts: Principles and Applications, Second Edition. 2013, CRC Press. ISBN 9781439881309.
45. Ju, Yiguang, and Sun, Wenting. "Plasma Assisted Combustion: Dynamics and Chemistry," Progress in Energy and Combustion Science, Vol 48, 21-83, 2015. doi:10.1016/j.pecs.2014.12.002.
46. Wolk, B. and Ekoto, I. "Calorimetry and Imaging of Plasma Produced by a Pulsed Nanosecond Discharge Igniter in EGR Gases at Engine-Relevant Densities," SAE International Journal of Engines, 10(3), 2017. doi:10.4271/2017-01-0674.

47. Cimarello, A., Grimaldi, C., Mariani, F., Battistoni, M. et al. "Analysis of RF Corona Ignition in Lean Operating Conditions Using an Optical Access Engine," SAE Technical Paper 2017-01-0673, 2017. doi:10.4271/2017-01-0673.
48. Starikovskiy, A., and Aleksandrov, N. "Plasma-Assisted Ignition and Combustion," Aeronautics and Astronautics. Intech, 2011. ISBN 978-953-307-473-3.
49. ACIS- Advanced Corona Ignition System. Federal-Mogul. Accessed December 4, 2017, from <http://www.federalmogul.com/en-US/OE/Products/Pages/Product-Details.aspx?CategoryId=15&SubCategoryId=21&ProductId=224>.
50. Ignition Technologies. BorgWarner. Accessed December 5, 2017, from <https://www.borgwarner.com/technologies/ignition-technologies>.
51. Cimarello, A., Cruccolini, V., Discepoli, G., Battistoni, M. et al. "Combustion Behavior of an RF Corona Ignition System with Different Control Strategies," SAE Technical Paper, 2018-01-1132, 2018. doi:10.4271/2018-01-1132.
52. NGK 3764 BKR6EIX-11 IX Iridium Plug. NGK.com (retailer not associated with manufacturer NGK Spark Plugs). Accessed October 12, 2017 from <https://www.ngk.com/product.aspx?zpid=9331>.
53. NGK 7405 R5672A-9 Racing Plug. NGK.com (retailer not associated with manufacturer NGK Spark Plugs). Accessed October 12, 2017 from <https://www.ngk.com/product.aspx?zpid=10048>.
54. Yu, S., Xie, K., Yu, X., Wang, M. et al. "High Energy Ignition Strategies for Diluted Mixtures via a Three-Pole Igniter," SAE Technical Paper, 2016-01-2175, 2016. doi:10.4271/2016-01-2175.



55. Xie, K, Yu, S., Gao, T., Yu, X., Zheng, M, Li, L. "Investigation of Multi-pole Spark Ignition on Flame Kernel Development and in Engine Operation," Proceedings of the ASME 2016 Internal Combustion Engine Division Fall Technical Conference, ASME ICEF2016-9474, October 11, 2016, Greenville, South Carolina, USA.
56. Xie, K., Yu, S., Yu, X., Bryden, G. et al. "Investigation of Multi-Pole Spark Ignition Under Lean Conditions and with EGR," SAE Technical Paper, 2017-01-0679, 2017. doi:10.4271/2017-01-0679.
57. US Patent 9,484,719 (Application 14/329,628). "Active Control Resonant Ignition System." Inventors: Ming Zheng, Shui Yu, Meiping Wang. File date July 3 2014. Issue date Nov 01 2016. US Patent Application 15/286,128 Divisional patent filed Oct 5 2016.
58. Christian, V.R., Knopf, F., Jaschek, A., Schindler, W. "Eine neue Messmethodik der Bosch-Zalh mit erhohter Empfindlichkeit," Motortechnische Zeitschrift, 54, 16-22, 1993.
59. Maly, Rudolf, and Vogel, Manfred. "Initiation and Propagation of Flame Fronts in Lean CH<sub>4</sub>-Air Mixtures by the Three Modes of Spark Ignition," International Symposium on Combustion, Vol 17(1), 821-831, 1979.
60. Yu, X., Yu, S., Yang, Z., et al. "Improvement on Energy Efficiency of the Spark Ignition System," SAE Technical Paper, 2017-01-0678, 2017. doi:10.4271/2017-01-0678.
61. Briggs, T., Alger, T., and Mangold, B. "Advanced Ignition Systems Evaluations for High-Dilution SI Engines," SAE International Journal of Engines, 7(4), 1802-1807, 2014. doi:10.4271/2014-01-2625.

62. Pihl, J., Lewis, J., Topps, T., Parks, J. "Lean NO<sub>x</sub> Trap Chemistry Under Lean-Gasoline Exhaust Conditions: Impact of High NO<sub>x</sub> Concentrations and High Temperature," *Topics in Catalysis*, 26, 89-93, 2013. doi:10.1007/s11244-013-9934-3.
63. Starikovskii, A. "Plasma Supported Combustion," *Proceedings of the Combustion Institute*, 30, 2405-2417, 2005. doi:10.1016/j.prosci.2004.08.272.
64. Hu, E., Li, X., Meng, X., Chen, Y., Xie, Y., Huang, Z. "Laminar Flame Speeds and Ignition Delay Times of Methane-Air Mixtures at Elevated Temperatures and Pressures," *Fuel*, 158, 1-10, 2015. doi:10.1016/j.fuel.2015.05.010.
65. Park, O., Veloo, P., Liu, N., Egolfopoulos, F. "Combustion Characteristics of Alternative Gaseous Fuels," *Proceedings of the Combustion Institute*, 33, 887-894, 2011.
66. Gu, X.J., Haq, M.Z., Lawes, M., Woolley, R. "Laminar Burning Velocity and Markstein Lengths of Methane–Air Mixtures," *Combustion and Flame*, 121, 41-58, 2000.
67. Rozenchan, G., Zhu, D.L., Law, C.K., Tse, S.D. "Outward Propagation, Burning Velocities, and Chemical Effects of Methane Flames up to 60 ATM," *Proceedings of the Combustion Institute*, 29, 1461-1470, 2002.
68. Alger, T., Gingrich, J., Mangold, B., and Roberts, C. "A Continuous Discharge Ignition System for EGR Limit Extension in SI Engines," *SAE International Journal of Engines*, 4(1), 677-692, 2011. doi:10.4271/2011-01-0661.
69. Badawy, T., Bao, X., Xu, H. "Impact of Spark Plug Gap on Flame Kernel Propagation and Engine Performance," *Applied Energy*, 191, 311-327, 2017. doi:10.1016/j.apenergy.2017.01.059.

70. Abe, Y., Sugiura, A., Doi, K., Shibata, M. et al. "Study of Ignition System for Demand Voltage Reduction," SAE Technical Paper, 2015-01-0777, 2015.  
doi:10.4271/2015-01-0777.
71. Seiser, R, Pitsch, H., and Seshadri, K. "n-Heptane, Reduced Mechanism." Lawrence Livermore National Laboratory. Available at:  
<https://combustion.llnl.gov/archived-mechanisms/alkanes/heptane-reduced-mechanism>
72. Goodwin, Dave, et al. "Cantera: An Object-Oriented Software Toolkit for Chemical Kinetics, Thermodynamics, and Transport Processes." Version 2.1a1, available at <https://code.google.com/p/cantera/>
73. Musculus, M. Miles, P., Pickett, L. "Conceptual Models for Partially Premixed Low-Temperature Diesel Combustion," Progress in Energy and Combustion Science, 39, 246-283, 2013. doi:10.1016/j.pecs.2012.09.001.
74. Smith, Gregory P., et al. GRI-MECH 3.0. Available at:  
[http://www.me.berkeley.edu/gri\\_mech/](http://www.me.berkeley.edu/gri_mech/).

## APPENDIX A: GASOLINE HCCI COMBUSTION

The following section details some aspects of gasoline HCCI combustion in a diesel engine platform. Some of the advantages and challenges of the combustion modes are highlighted. In particular, the combustion phasing controllability has the potential to be improved with an effective external ignition source.

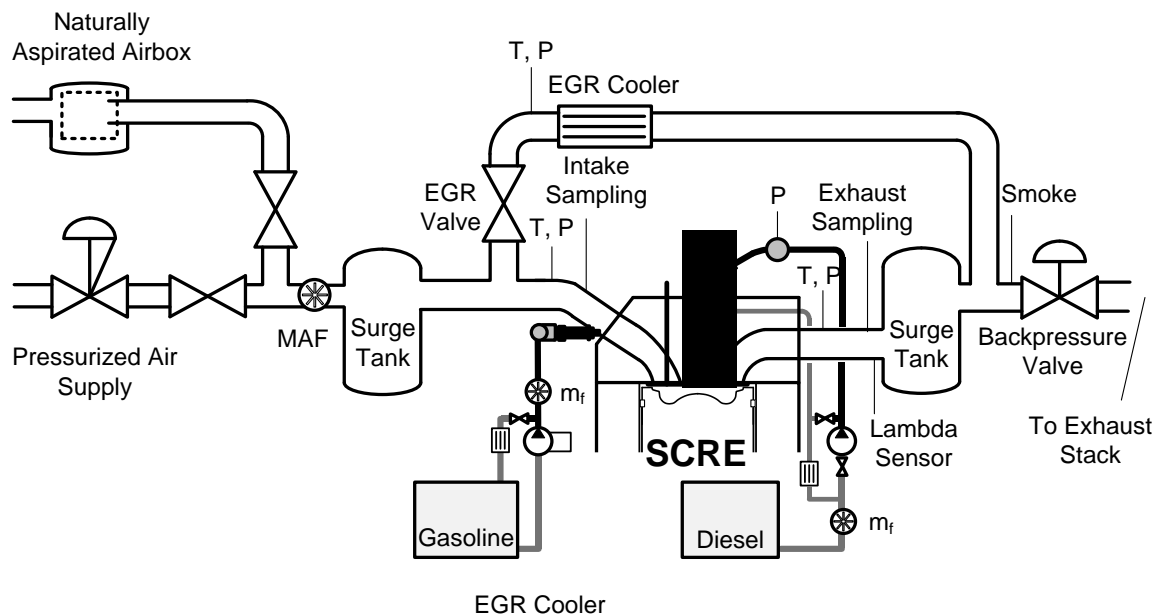


Figure A-1: Engine Test Cell Setup

The compression ignition tests were carried out on a modern common-rail direct-injection single-cylinder research engine (SCRE). The engine utilized production-level systems from a family of commercial medium-duty automotive diesel engines coupled to a dedicated research engine block and crank system. The high-pressure fuel injection system was capable of delivering injection pressures up to 2200 bar. The piezo high-pressure injector was driven by an EFS 8370 IPoD injector power driver. A secondary low-pressure fuel system was integrated into the intake manifold to enable intake port fuel injection of gasoline via two low-pressure solenoid injectors. The injectors were

driven by a pair of LM1949 injector drivers. A diagram of the engine layout is shown in Figure A-1. The key specifications of the engine are shown in Table A-1.

Table A-1: Engine Specifications

Research Engine	FEV built SCRE
Engine Type	Single-cylinder 4-stroke
Displacement [cm <sup>3</sup> ]	744
Bore x Stroke [mm]	95 x 105
Compression Ratio [-]	16.2:1
Max. Cylinder Pressure [bar]	200
Piston Bowl	Stepped omega
Swirl Ratio [-]	~1.5
Direct-injection System	Common-rail (max. 2200 bar)
Direct Injector	Piezo servo, 7 hole, umbrella angle 156°
Port-injection System	Low-pressure rail (5 bar abs)
Port Injector	2 × gasoline type injector

Operation in the homogeneous gasoline-only combustion was explored and the pressure and heat-release profiles of two cases are shown in Figure A-2. The engine loads were 9.6 and 10.4 bar IMEP. The combustion was stable at these two load. The coefficient of variation for IMEP was lower at the higher load case, with a value of 1.7%

versus 2.6%. A minor increase in the gasoline fueling resulted in advancement of the combustion phasing and consequently a large difference in maximal pressure rise rate (16.5 bar/°CA compared to 7.2 bar/°CA). The high combustion intensity is a limitation to high-load operation while conversely, higher cyclic variations indicate a tendency toward misfires. These two issues strongly limit the range of HCCI operation possible unless additional control measures are to be employed. To extend operation toward lower load ranges, strategies such as intake heating, exhaust trapping/rebreathing, or fuel reformation can be employed. Extending the operation toward higher load ranges, on the other hand, can benefit from precise EGR application and fuel stratification. Major changes in the operating envelope, however, may require engine hardware technologies such as variable valve timing or variable compression ratio.

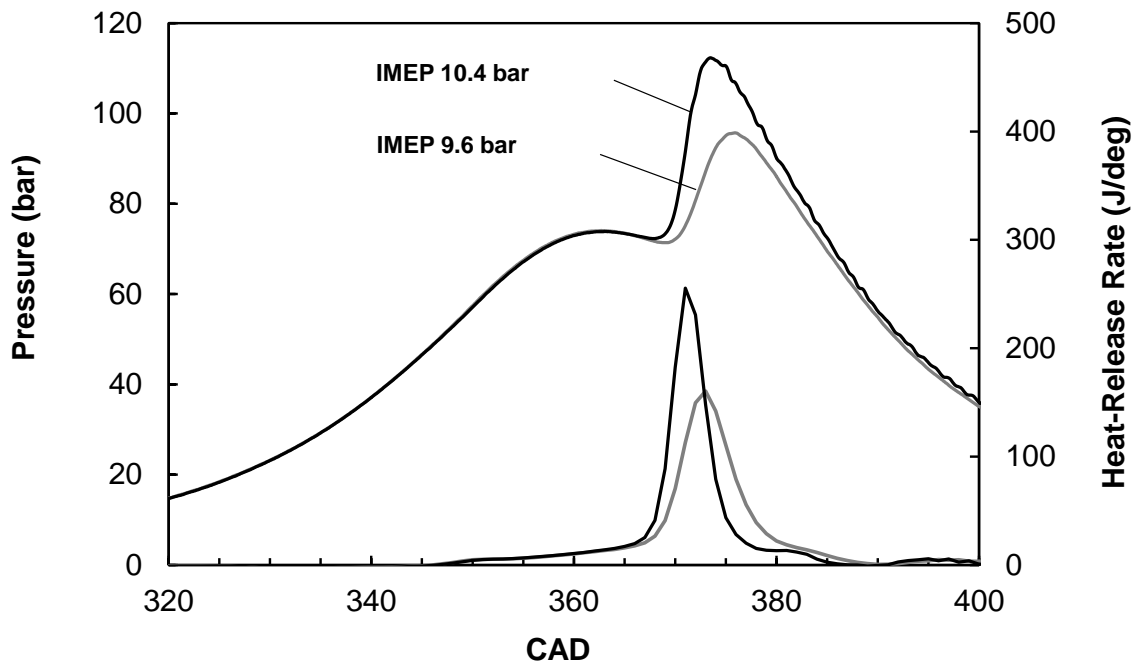


Figure A-2: Gasoline-only HCCI-type combustion

Figure A-3 shows the effect of such a compression ratio increase to 18.2 on the HCCI combustion of gasoline. The higher compression ratio allowed the operation at much lower load levels, down to 2 bar IMEP. The negative effect is significantly higher peak pressure rise rates, even at relatively mild loads of 6 bar IMEP. A significant contributor to the severe peak pressure rise rates is the combustion phasing in advance of TDC. This early combustion can be moderated using EGR as will be shown in Figure A-9.

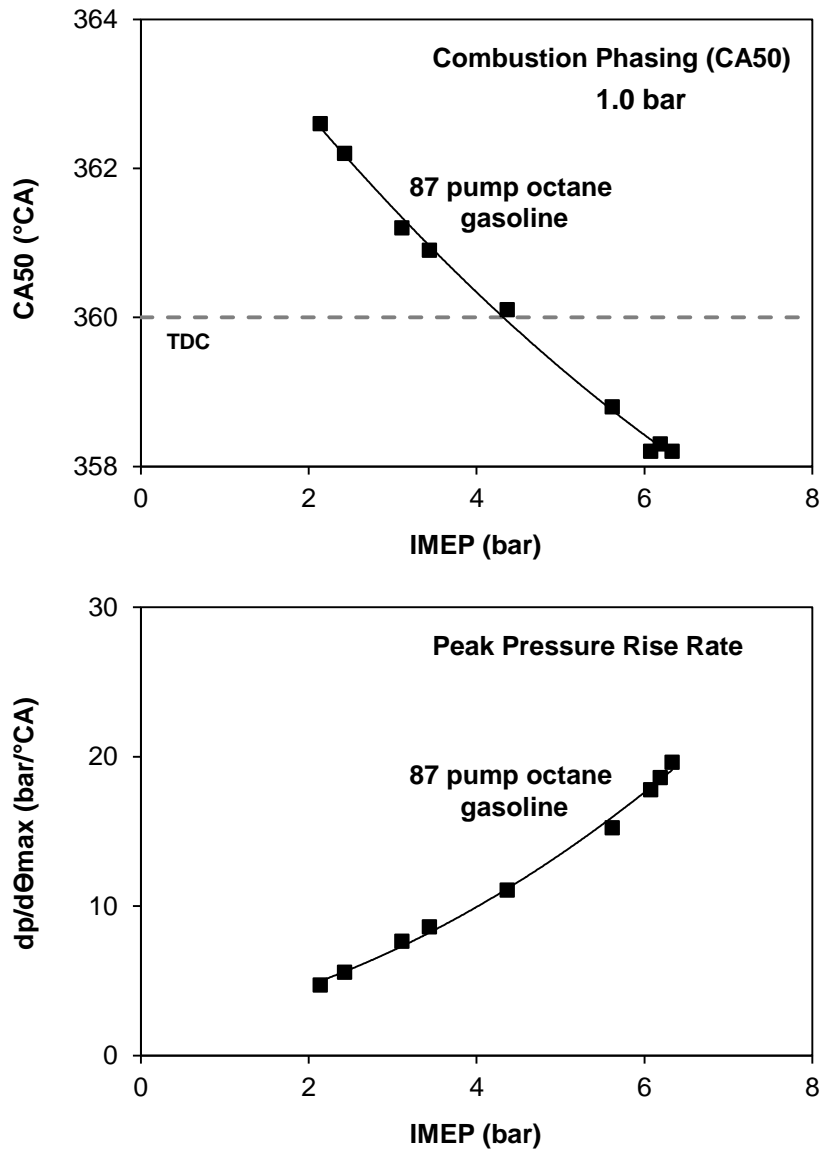


Figure A-3: Gasoline-Only HCCI-type Combustion at Higher Compression Ratio

For lower load operation, the use of EGR allows the engine fueling to increase while staying within engine nominal peak pressure rise rate limitations. Starting from a moderate EGR condition with an intake oxygen concentration of 16.4%, the engine load improves as EGR is increased to reduce the intake oxygen down to 12.9% as the combustion phasing is improved from excessively early conditions. Further increases in EGR, however, result in a decrease in engine load and an increase in unburned emissions.



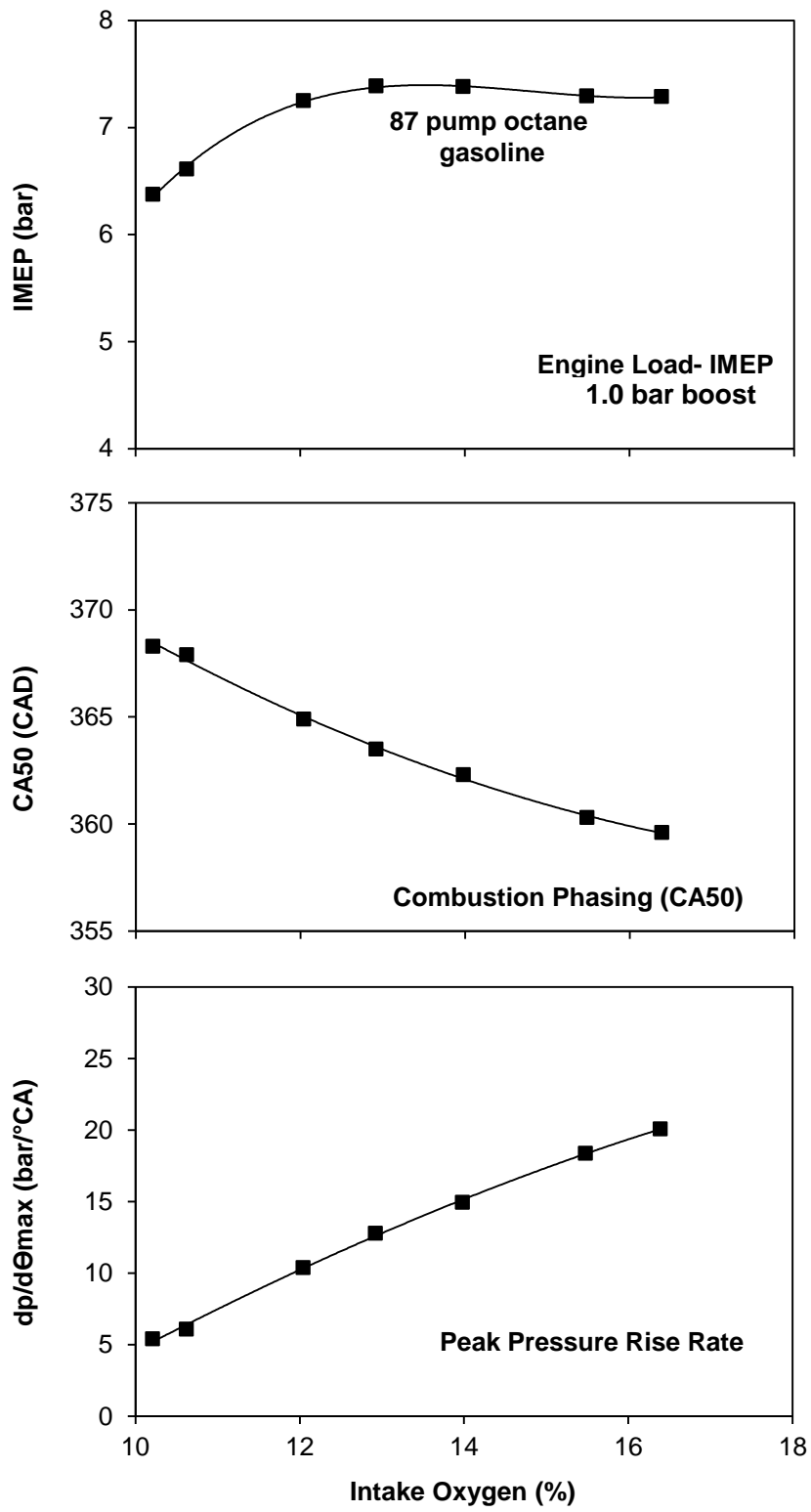


Figure A-4: Gasoline-Only HCCI-type Combustion With EGR



## APPENDIX B: NUMERICAL SIMULATION OF DIESEL AUTO-IGNITION

Zero-dimensional kinetic simulations of n-heptane ignition under constant-pressure conditions were performed to gain insight into the chemistry of the ignition process. The kinetics mechanism used was the n-heptane reduced mechanism from [71] computed using the Cantera solver running on the Python platform [72].

### B.1 Chemical Description of Ignition

The temporal evolutions of the temperature and bulk species are shown in Figure B-1 below. Figure B-2 shows the evolution of key chemical species. The initial conditions of the simulation were the same used in the kinetic analysis by Musculus [73]. The simulation conditions are initialized at a temperature of 787 K, pressure of 50 bar, and oxygen molar concentration of 12.7%. The balance gas is nitrogen. The n-heptane concentration is stoichiometric with respect to the available oxygen. The results show that the earlier reactions consists hydrogen abstraction of the n-heptane fuel by  $O_2$  molecules. The buildup of radicals continues with  $HO_2$  and  $OH$  participation. A key class of species, ketohydroperoxide (KHP) species, form as a result of alkyl peroxy radical undergoing a second  $O_2$  addition, subsequent isomerization, and then decomposition. The KHP species are relatively stable and continue to build up to 0.9 ms after the start of the simulation. This process is truncated when the KHP decomposes at approximately 850 K, resulting in a rapid surge of radicals. This causes an increase in the heat release and reaction rates that constitute the first stage of ignition. After the KHP pool depletes, the heat release rate decrease dramatically. Some CO is generated during and after the first stage of ignition. Most CO, however, is generated prior to and during

the second stage of ignition. The conversion of CO into CO<sub>2</sub> is minimal until the second stage of ignition.

An important species that build up during the dwell between the first and second ignition stages is hydrogen peroxide (H<sub>2</sub>O<sub>2</sub>). The production rates of hydrogen peroxide exceed its destruction rates until about 1000 K. At this point, the release of OH radicals from the decomposition of H<sub>2</sub>O<sub>2</sub> cause an increase again in the overall reaction rate and lead to the second stage of ignition at 1.7 ms after the start of the simulation. The second-stage ignition generates a large amount of OH that oxidizes the remaining hydrocarbons and CO.

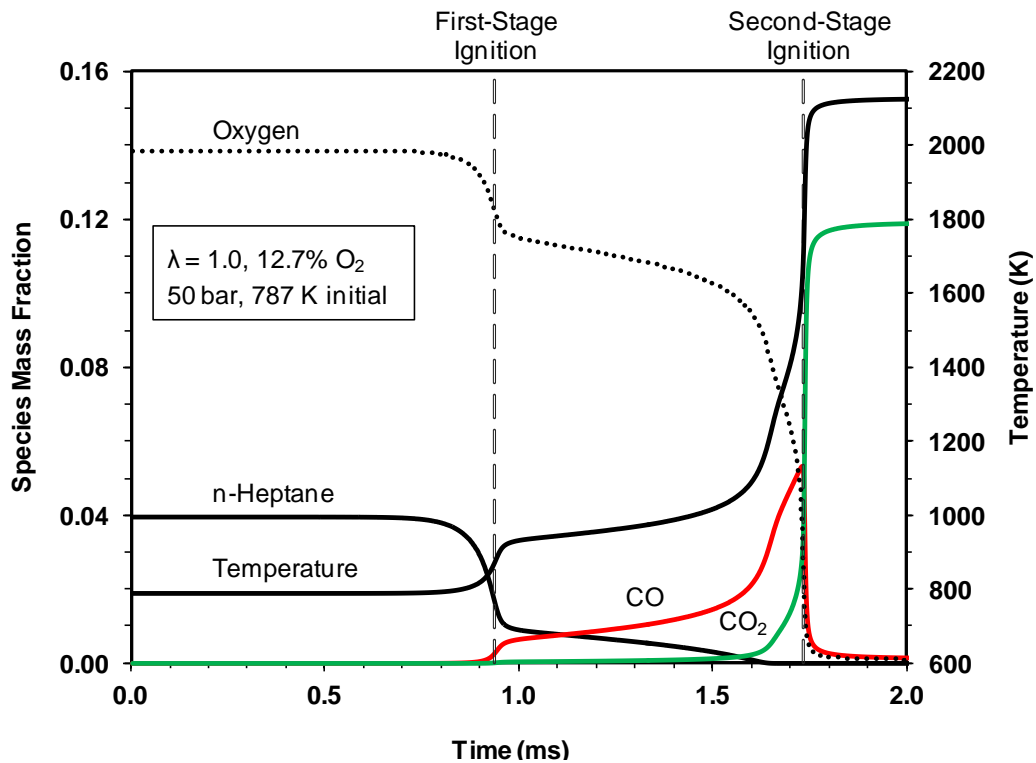


Figure B-1: Evolution of Bulk Gas Species During Ignition Process

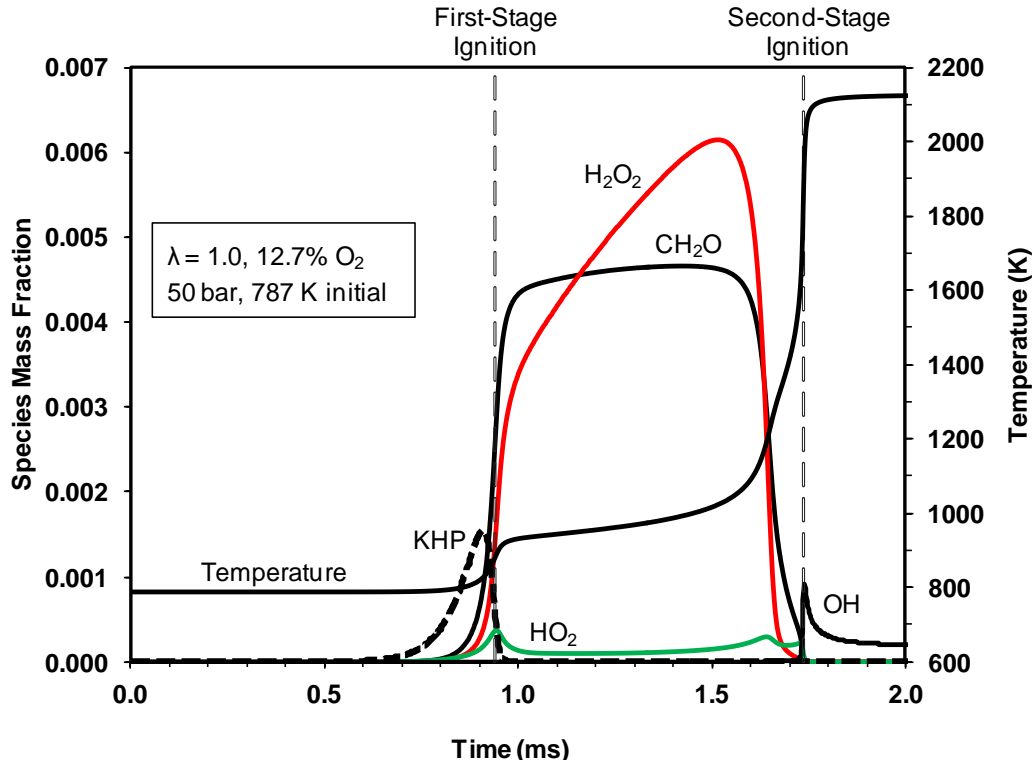


Figure B-2: Evolution of Key Species During Ignition Process

The ignition delay to the first and second stages of ignition are presently quantified by the local peaks of the change in temperature with respect to time ( $dT/dt$ ). The modelled sensitivity of the ignition delays to different parameters are discussed in the next section.

## B.2 Sensitivity of Ignition to Physical Parameters

The effect of temperature on the ignition characteristics was explored with a series of simulations of varying initial temperatures ranging from 727 K to 1047 K. The computed ignition times are plotted in Figure B-3. In addition to the local maxima of  $dT/dt$  as a parameter to indicate the onset of ignition, the time to five percent cumulative heat-release ( $HR_{5\%}$ ) is plotted. This parameter is analogous the pressure measurement based apparent heat-release commonly in engine tests to indicate the start of combustion.

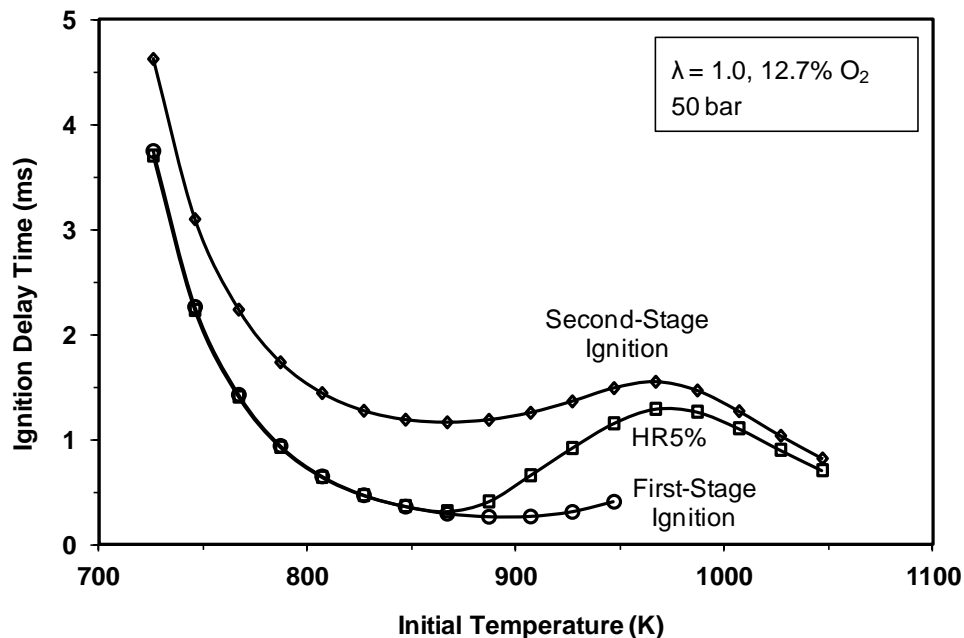


Figure B-3: Temperature Effects on of Ignition Delay

The simulation results indicate that the ignition delay decreases with increasing temperature up to 850 K. This is the start of the negative temperature coefficient (NTC) regime for n-heptane. In this regime high initial temperatures causes the KHP species to decompose prior to significant build-up, thereby limiting the availability of radical species to for the early reactions. This effect is clear in the plot of the HR<sub>5%</sub>, which coincides with the first-stage ignition timing up to temperatures of 867 K. At higher temperatures the HR<sub>5%</sub> shifts closer to the timing of the second-stage ignition. This indicates that the relative quantity of the early heat-release is diminished and the overall shape of heat release is shifted later and towards higher temperatures.

The effect of pressure on the ignition timing is shown in Figure B-4. Increases in pressure decreases the computed ignition delays, but sensitivity of the first-stage ignition to pressure is small in the range of 30 to 150 bar. The effect on the second-stage ignition is more pronounced. The ignition delay shortens from 2.6 ms to less than 1 ms by the

increase in pressure. This shortening of the ignition delay has implications for fuel-air charge preparation in highly boosted engines that is the trend for research and production engines.

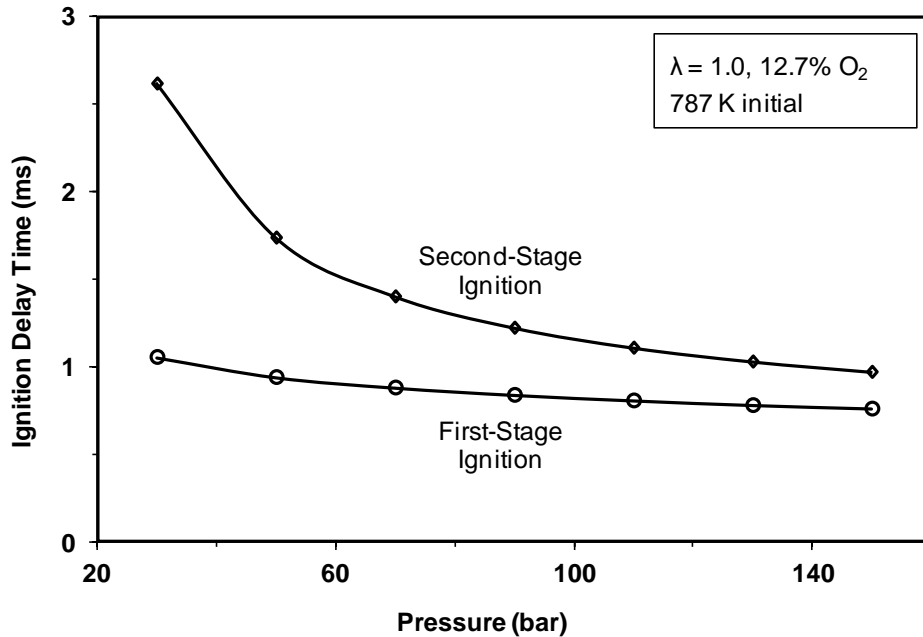


Figure B-4: Pressure Effects on Ignition Delay to Pressure

The effect of stoichiometry on the ignition process is shown for two types of conditions. The effect of changing the oxygen concentration at constant fuel quantity is shown in Figure B-5. Over the oxygen range of 9.2% to 20.8%, the effect on the first-stage ignition is minimal and the effect on the second-stage ignition is slight. This indicates that for homogenous conditions, oxygen availability has only a small impact on the ignition behaviour.

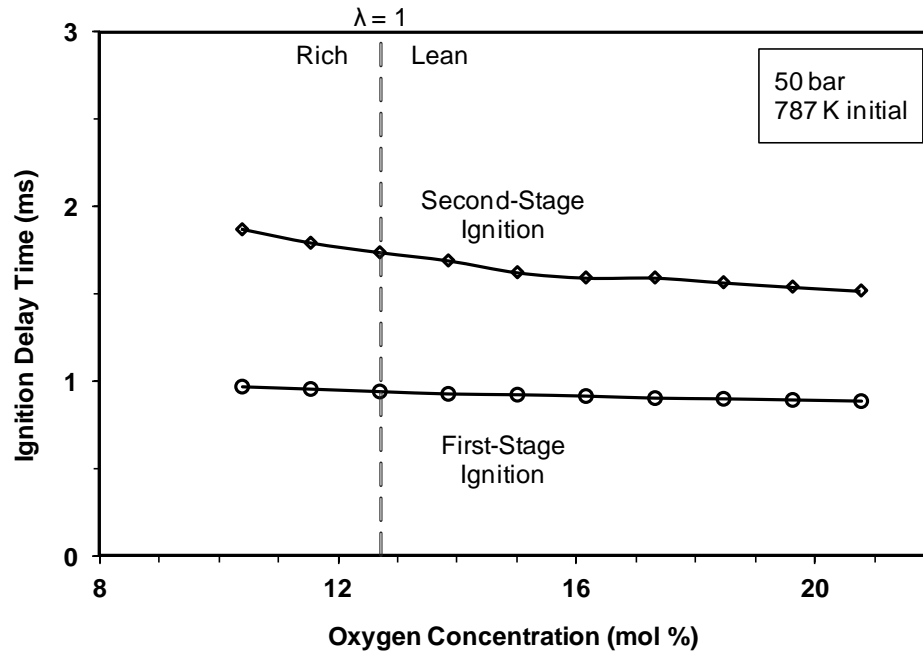


Figure B-5: Oxygen Availability Effects on Ignition Delay

The effect of changing the fuel quantity at constant oxygen quantity is shown in Figure B-6. Contrary to the previous case, the effect of fuel quantity has a significant effect on the second-stage ignition. Decreasing the fuelling to lean conditions has the effect of increasing the ignition delay. Under rich conditions, the second-stage ignition advances and approaches the timing of the first ignition stage. This behaviour is caused by the more rapid temperature rise at higher fuel concentrations, which can be seen in Figure B-7. Richer mixtures experience progressively higher temperature profiles, leading to faster reaction rates.



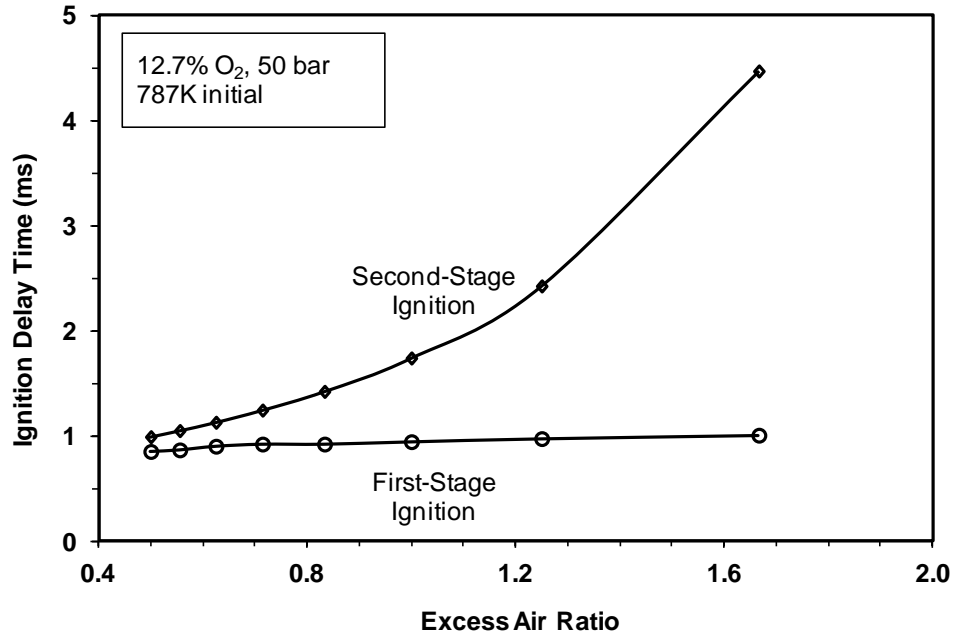


Figure B-6: Excess Air Ratio Effects on Ignition Delay

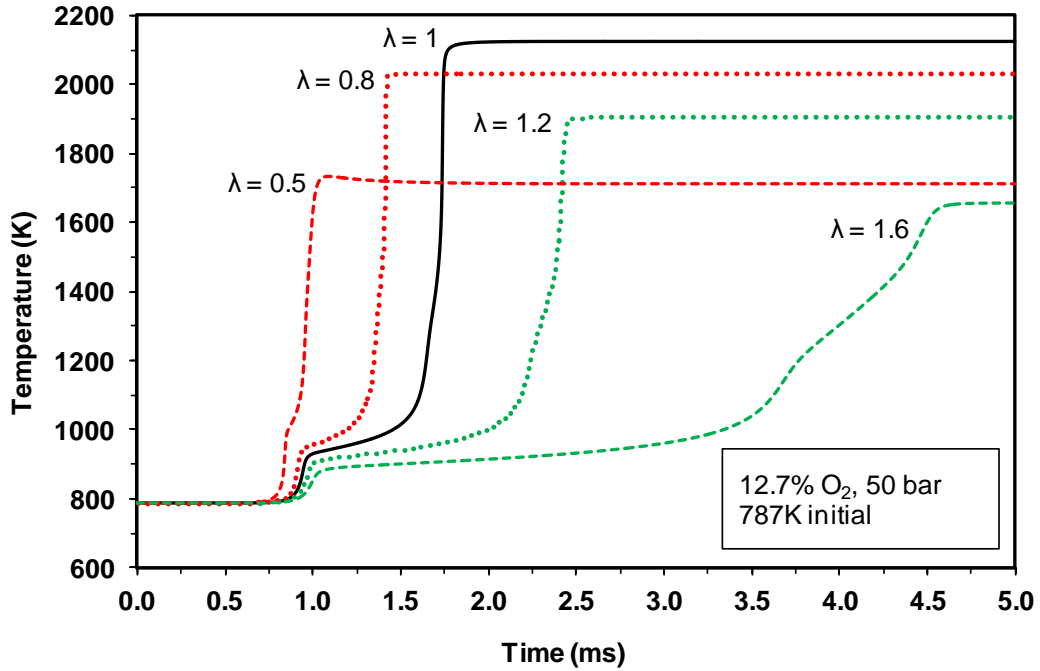


Figure B-7: Excess Air Ratio Effects on Temperature Profile

In summary, the simulations show that the temperature is the most important parameter governing the ignition process. The pressure and fuel quantity are secondary parameters that influence the ignition behaviour. The availability of oxygen, in the range that is of practical concern for combustion engines, has limited influence on the ignition event.

## APPENDIX C: NUMERICAL SIMULATION OF LAMINAR FLAME SPEED

One-dimensional kinetic simulations of a flat methane-air premixed flame with multi-component transport properties were performed to gain insight into the effect of stoichiometry and initial thermodynamic conditions on the fundamental laminar flame speed. The kinetics mechanism used was the GRI-Mech 3.0 [74] and computed using the Cantera solver running on the Python platform [72]. Available empirical data from [65-67] is overlaid on the simulation results in Figure C-1. The effect of temperature and pressure on the computed laminar flame speed is shown in Figure C-2.

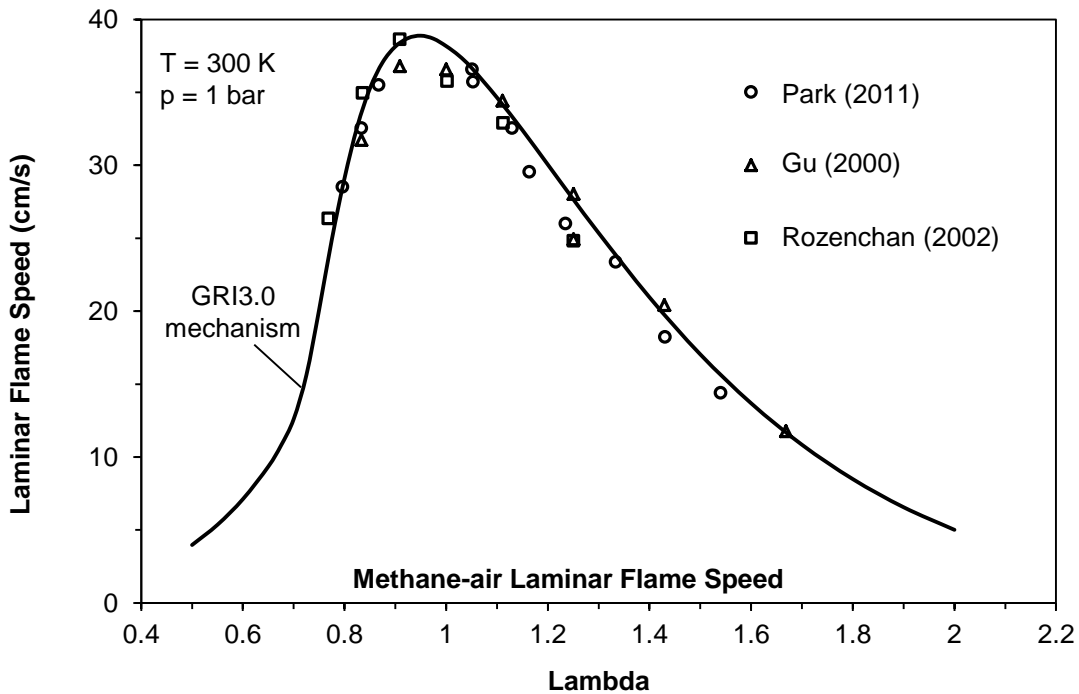


Figure C-1: Computed Laminar Flame Speed

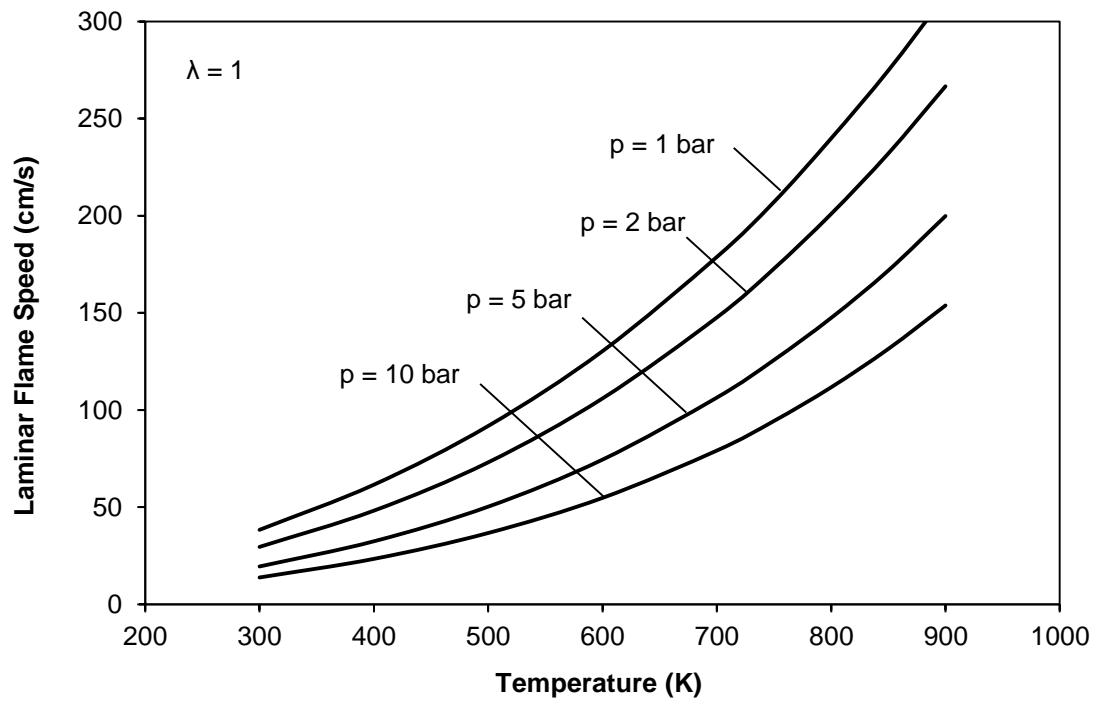


Figure C-2: Effect of Temperature and Pressure on Laminar Flame Speed

## **APPENDIX D: NOX GENERATION UNDER ELECTRICAL DISCHARGE**

The generation of NO and NO<sub>2</sub> species from the reaction of atmospheric nitrogen and oxygen were quantified by FTIR measurement under conventional spark discharge and under corona discharge. The tests were conducted with a constant flow sweeping through the combustion vessel CV-1, with the pressure held at 1 bar gauge. Results with an air residence time of 12.5 seconds and spark frequency of 20 Hz are shown Figure D-1 for a range of coil charging durations. A comparison for the corona discharge is shown in Figure D-2. As the air residence time of the corona discharge case was only approximately half of the spark discharge case, the level of NO<sub>x</sub> production was considerably higher under the corona discharge. However, the energy input, discharge power, and effective discharge duty cycle were also significantly higher. When the NO<sub>x</sub> production is normalized against the discharge power, the NO<sub>x</sub> production of the spark discharge was found to be an order of magnitude higher than that of the corona discharge. This is shown in Figure D-3, where the NO<sub>x</sub> production is expressed in units of nanograms NO<sub>x</sub> per second per watt of discharge power. The results confirm that while the discharge power of the corona discharge could be significantly higher than that of the spark discharge, the degree of molecular fragmentation and rearrangement is significantly lower, corresponding to a lower plasma density.

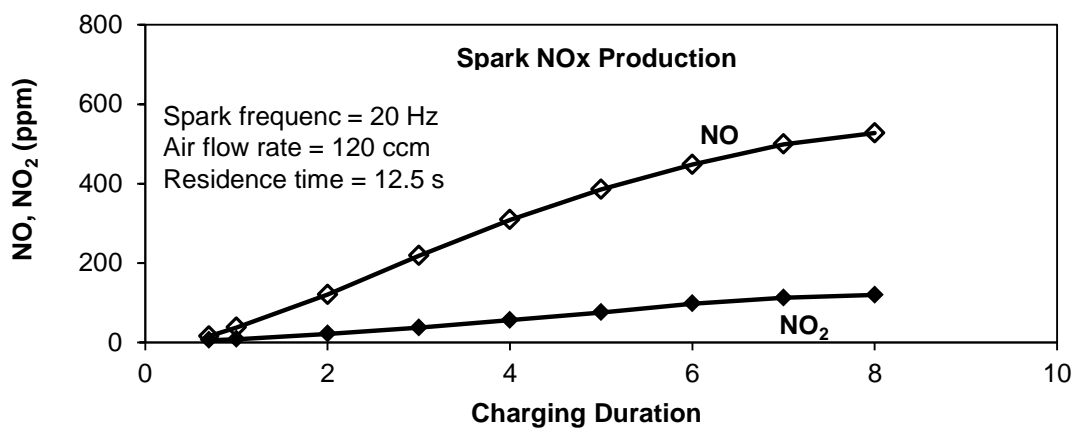


Figure D-1: NOx Production Under Spark Discharge

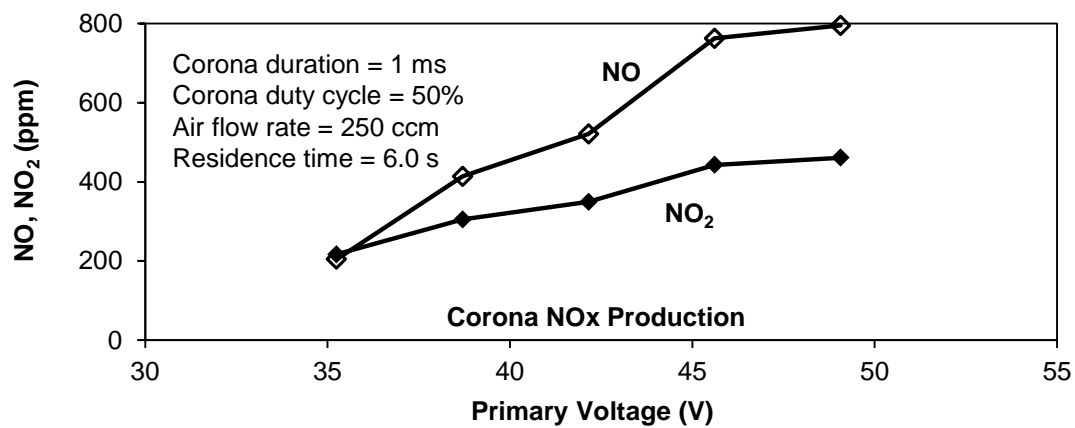


Figure D-2: NOx Production Under Corona Discharge

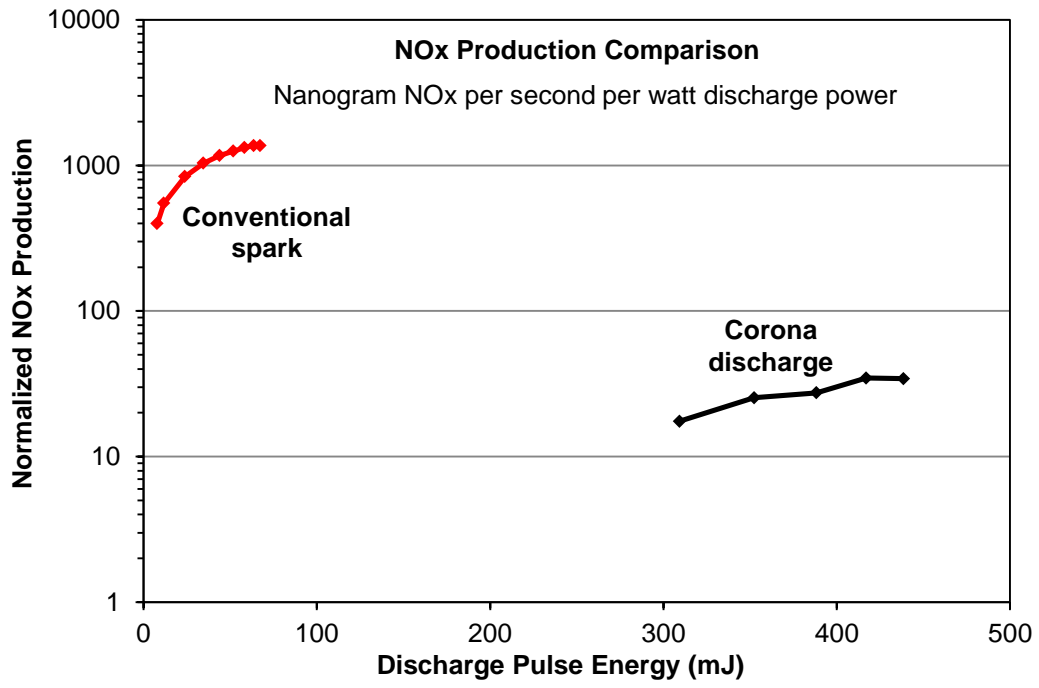


Figure D-3: Normalized NOx Production

## APPENDIX E: EFFECT OF SPARK GAP SIZE ON KERNEL FORMATION

A series of spark ignition tests were performed to evaluate the effect of the spark gap size on flame kernel formation. These experiments were performed in the constant-volume combustion chamber CV-1 under laminar conditions using methane-air mixtures at 1 bar gauge initial pressure and ambient temperature. The spark plug used was a NGK R5672A-9 V-groove non-resistive spark plug. Figure E-1 shows the flame kernel growth at lambda 1.3 for five different spark plug gap sizes of 0.5, 0.8, 1.1, 1.4, and 2.0 mm. The initial kernel expansion is obscured by the electrodes, but the later growth rate beyond approximately 5 mm in width could be accurately tracked.

A continuous increase in the flame kernel size was observed as the gap size increased from 0.5 mm up to 2.0 mm. A quantitative comparison of the flame kernel areas as a function of time after the spark is shown in Figure E-2. The result of a similar test at lambda 1.0 is shown in Figure E-3, with the same trend of faster early flame kernel development with larger gap sizes. The results concur with work by Badawy using gasoline-air mixtures at 1 bar and 90 °C [69]. They extended the combustion vessel work to an optical engine and observed larger gap sizes increased the turbulent flame speed and mass fraction burn rate. The engine IMEP increased and cyclic variations decreased when the spark plug gap size was increased from 1.0 mm to 1.4 mm. The increase in performance was attributed to decreased heat loss to the electrodes and increased discharge power at larger gap sizes. This increase in discharge power was also observed under flow across the spark gap as reported in Chapter 5.1.2.



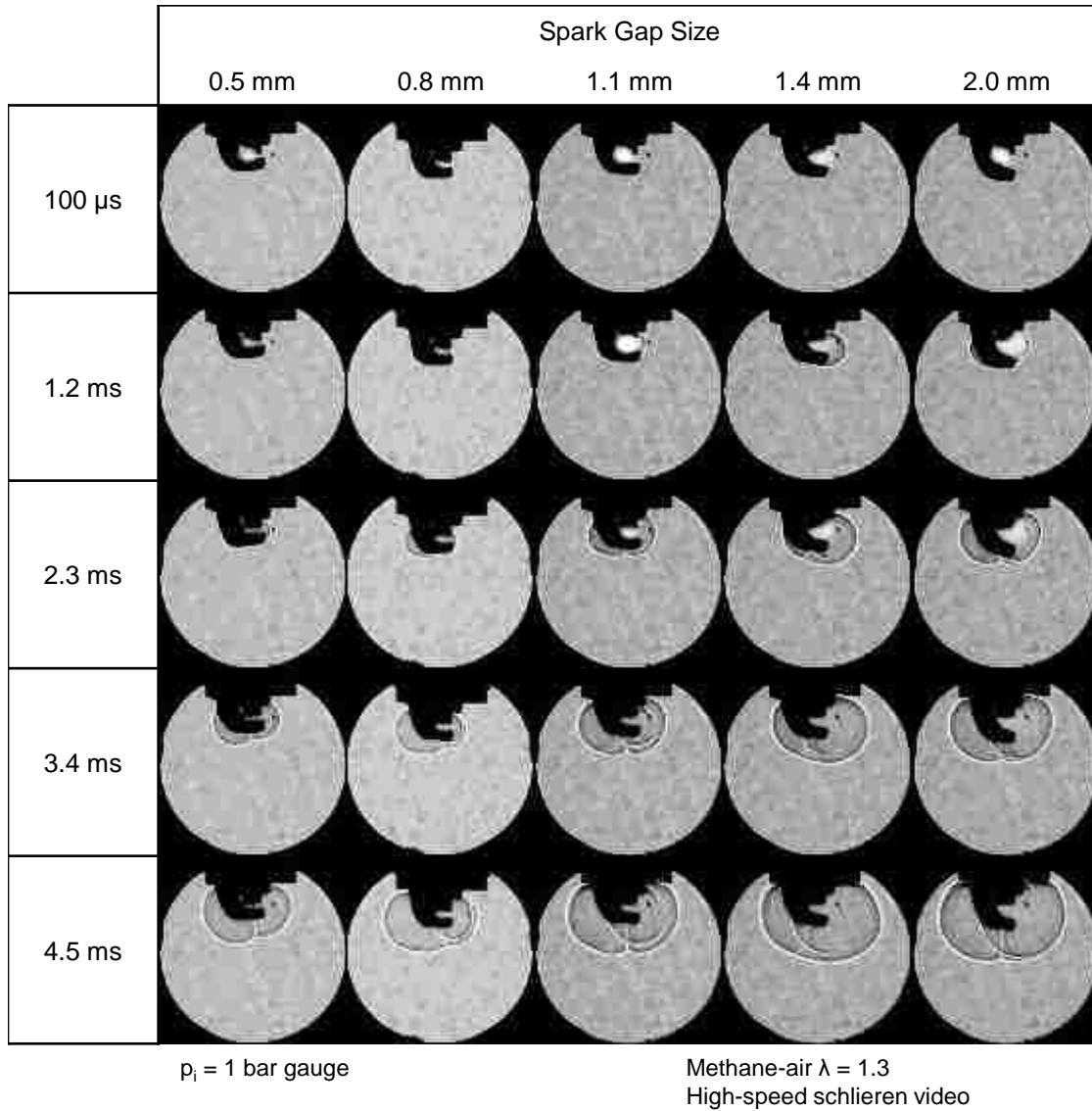


Figure E-1: Shadowgraph Images of Spark Gap Size Effect on Ignition

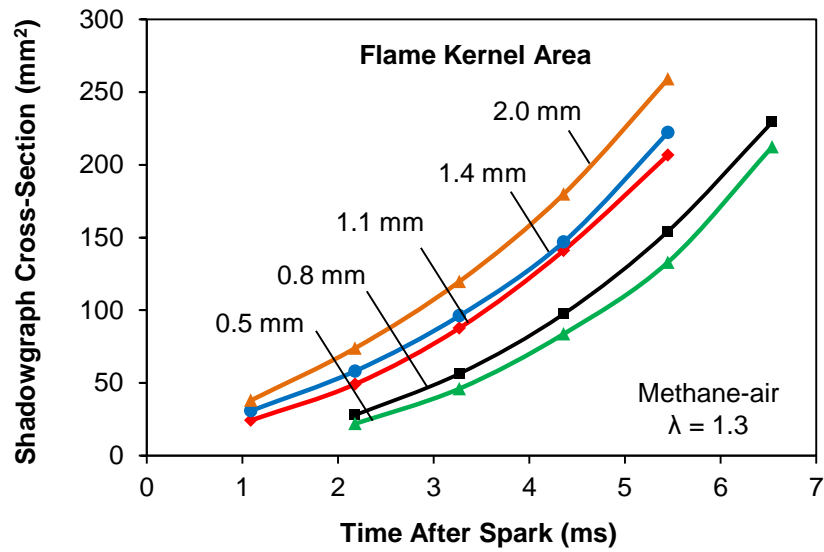


Figure E-2: Shadowgraph Area of Flame Kernel at  $\lambda = 1.3$  under Different Gap Sizes

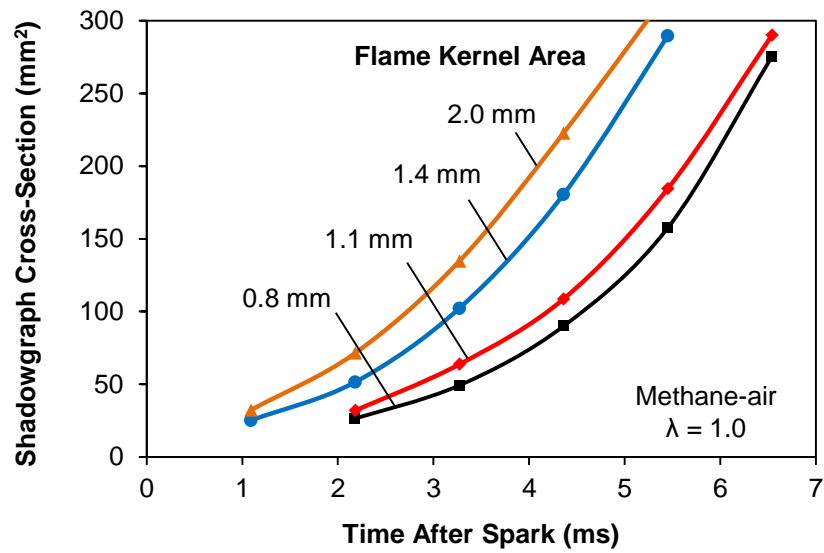


Figure E-3: Shadowgraph Area of Flame Kernel at  $\lambda = 1$  under Different Gap Sizes

While the improved ignition performance observed in the previous section is desirable, a consequence of the increased spark gap sizes is the increase in breakdown voltage required. This is of particular concern in turbocharged engines, where the increased in-cylinder pressures under high boost conditions requires a much higher

breakdown voltages in the range of 30 – 40 kV [70]. This places higher demands on the dielectric strength and design of the components to prevent leakage or abnormal discharge. The breakdown voltage in this test increased from 5 kV at 0.5 mm gap size to 8 kV at 2.0 mm gap size, as shown in Figure E-4.

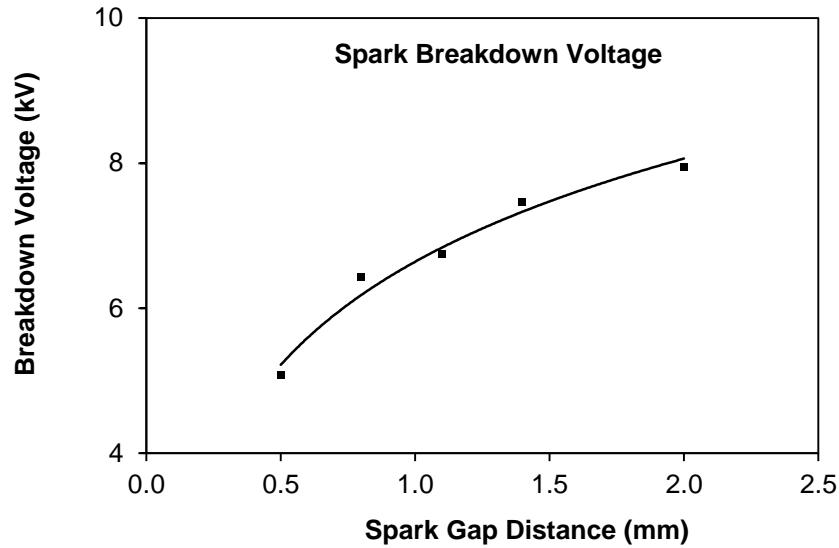


Figure E-4: Increase of Breakdown Voltage with Increase of Spark Gap Size

## VITA AUCTORIS

NAME: Kelvin Xie

PLACE OF BIRTH: Beijing, China

YEAR OF BIRTH: 1986

EDUCATION: University of Toronto, B.A.Sc., Toronto, ON 2009

University of Windsor, M.Sc., Windsor, ON, 2012

University of Windsor, Ph.D., Windsor, ON, 2018

## LIST OF PUBLICATIONS

### *Refereed Journals:*

1. Xiaoye Han, Kelvin Xie, Jimi Tjong, and Ming Zheng. “Empirical Study of Simultaneously Low NO<sub>x</sub> and Soot Combustion With Diesel and Ethanol Fuels in Diesel Engine,” J. Eng. Gas Turbines Power 134, 112802 (2012).
2. Shouvik Dev, Prasad Divekar, Kelvin Xie, Xiaoye Han, Xiang Chen, and Ming Zheng. “A Study of Combustion Inefficiency in Diesel LTC and Gasoline-Diesel RCCI Via Detailed Emission Measurement,” J. Eng. Gas Turbines Power 137 (12), 121501 (2015).

### *Refereed Conference Proceedings:*

1. Kelvin Xie, Xiaoye Han, Graham T. Reader, Meiping Wang, and Ming Zheng. “Light Hydrocarbon Emissions from Diesel Low Temperature Combustion,” Proceedings of the ASME 2010 International Mechanical Engineering Congress & Exposition, ASME IMECE2010-39191, November 16, 2010, Vancouver, British Columbia, Canada.
2. Kelvin Xie, Xiaoye Han, Usman Asad, Graham T. Reader, and Ming Zheng. “Empirical Study of Energy in Diesel Combustion Emissions with EGR Application,” 2011 JSAE Powertrain, Fuels, and Lubricants Conference, JSAE 20119354, SAE 2011-01-1817, August 31, 2011, Kyoto, Japan.
3. Marko Jeftic, Usman Asad, Xiaoye Han, Kelvin Xie, Shui Yu, Meiping Wang, and Ming Zheng. “An Analysis of the Production of Hydrogen and Hydrocarbon Species by Diesel Post Injection Combustion,” Proceedings of the ASME 2011 Internal Combustion Engine Division Fall Technical Conference, ASME ICEF2011-60135, October 3, 2011, Morgantown, West Virginia, USA.
4. Usman Asad, Arturo Mendoza, Kelvin Xie, Marko Jeftic, Meiping Wang, and Ming Zheng. “Speciation Analysis of Light Hydrocarbon and Hydrogen Production During Diesel Low Temperature Combustion,” ASME ICEF2011-60130, October 3, 2011, Morgantown, West Virginia, USA.

5. Shui Yu, Kelvin Xie, Xiaoye Han, Marko Jestic, Tongyang Gao, and Ming Zheng. "Preliminary Study of the Spark Characteristics for Unconventional Cylinder Charge with Strong Air Movement," ASME ICEF2011-60132, October 4, 2011, Morgantown, West Virginia, USA.
6. William de Ojeda, Yu, Zhang, Kelvin Xie, Xiaoye Han, Meiping Wang, and Ming Zheng. "Exhaust Hydrocarbon Speciation from a Single-Cylinder Compression Ignition Engine Operating with In-Cylinder Blending of Gasoline and Diesel Fuels," 2012 SAE World Congress & Exhibition, SAE 2012-01-0683, April 24, 2012, Detroit, Michigan, USA.
7. Xiaoye Han, Kelvin Xie, Graham T. Reader, Xiang Chen, Jimi Tjong, Meiping Wang, and Ming Zheng. "The Impact of Fuels and Fuelling Strategy on Enabling of Clean Combustion in a Diesel Engine," The Eight International Conference on Modeling and Diagnostics for Advanced Engine Systems, COMODIA 2012 FL2-1, July 24, 2012, Fukuoka, Japan.
8. Xiaoye Han, Kelvin Xie, Ming Zheng, and William de Ojeda. "Ignition Control of Gasoline-Diesel Dual Fuel Combustion," 2012 SAE Commercial Vehicles Conference, SAE 2012-01-1972, October 2, 2012, Chicago, Illinois, USA.
9. Shui Yu, Xiaoye Han, Kelvin Xie, Meiping Wang, Liguang Li, Jimi Tjong, and Ming Zheng. "Multi-coil High Frequency Spark Ignition to Extend Diluted Combustion Limits," FISITA F2012-A01-040, November 27, 2012, Beijing, China.
10. Shouvik Dev, Prasad Divekar, Kelvin Xie, Xiaoye Han, Xiang Chen, and Ming Zheng. "A Study of Combustion Inefficiency in Diesel LTC and Gasoline-Diesel RCCI Via Detailed Emission Measurement," Proceedings of the ASME 2014 Internal Combustion Engine Division Fall Technical Conference, ASME ICEF2014-5656, October 21, 2014, Columbus, Indiana, USA.
11. Tongyang Gao, Kelvin Xie, Shui Yu, Xiaoye Han, Meiping Wang, and Ming Zheng. "Characterization of n-Butanol High Pressure Injection from Modern Common Rail Injection System," Proceedings of the ASME 2015 Internal Combustion Engine Division Fall Technical Conference, ASME ICEF2016-1129, November 10, 2015, Houston, Texas, USA.

12. Kelvin Xie, Tadanori Yanai, Zhengyi Yang, Graham Reader, and Ming Zheng. Emission Analysis of HCCI Combustion in a Diesel Engine Fueled by Butanol,” 2016 SAE World Congress, SAE Technical Paper 2016-01-0749, April 13, 2016, Detroit, Michigan, USA.
13. Shui Yu, Kelvin Xie, Xiao Yu, Meiping Wang, Ming Zheng, Xiaoye Han, and Jimi Tjong. “The Effect of High-Power Capacitive Spark Discharge on the Ignition and Flame Propagation in a Lean and Diluted Cylinder Charge,” 2016 SAE World Congress, SAE Technical Paper 2016-01-0707, April 12, 2016, Detroit, Michigan, USA.
14. Kelvin Xie, Shui Yu, Tongyang Gao, Xiao Yu, Ming Zheng, and Liguang Li. “Investigation of Multi-pole Spark Ignition on Flame Kernel Development and in Engine Operation,” Proceedings of the ASME 2016 Internal Combustion Engine Division Fall Technical Conference, ASME ICEF2016-9474, October 11, 2016, Greenville, South Carolina, USA.
15. Shui Yu, Kelvin Xie, Xiao Yu, Meiping Wang, Ming Zheng, Xiaoye Han, and Jimi Tjong. “High Energy Ignition Strategies for Diluted Mixtures via a Three-Pole Igniter,” 2016 SAE International Powertrains, Fuels & Lubricants Meeting, SAE Technical Paper 2016-01-2175, October 24, 2016, Baltimore, Maryland, USA.
16. Kelvin Xie, Shui Yu, Xiao Yu, Geraint Bryden, Ming Zheng, and Mengzhu Liu. “Investigation of Multi-Pole Spark Ignition Under Lean Conditions and with EGR,” 2017 SAE World Congress, SAE Technical Paper 2017-01-0679, April 5, 2017, Detroit, Michigan, USA.